Quantitative nanoscale analysis of polymeric materials and their interactions with solvents using scanning force microscopy

By Sharifah Alharthi

Department of Chemistry, The University of Sheffield, Sheffield, S3 7HF, UK

Supervised by Professor Graham J. Leggett

A Thesis Submitted to the University of Sheffield for the Degree of Doctor of Philosophy

June 2024

DECLARATION

This work described in this thesis was undertaken at the University of Sheffield between November 2019 and June 2024 under the supervision of Professor Graham J. Leggett. Unless otherwise stated, it is the work of the author and has not been submitted in whole or in part for any other degree at this or any other institute.

Signed: .....

Sharifah Alharthi

Department of Chemistry,

Dainton Building,

University of Sheffield,

Brook Hill,

Sheffield, UK.

S3 7HF

ACKNOWLEDGEMENTS

During my PhD, I have had the privilege of working with some truly talented, inspirational, and friendly people. I would like to take this opportunity to express my gratitude to them:

1extend my sincere thanks to Professor Graham Leggett, for granting me the unique opportunity to work in their research groups and for their invaluable advice and guidance throughout this project.

I am grateful to the University of Sheffield and everyone in the Chemistry Department. Special thanks go to our group members, both past and present, particularly Dr. Ed and Deborah.

Lastly, I want to thank my family my mother, my father, my brothers, sisters, and my children. I couldn't have achieved this without their unwavering support.

ABSTRACT

The goal of this project was to study the frictional and adhesive interactions between AFM probes and surfaces. Poly(2-dimethylamino)ethyl methacrylate) (PDMA) and poly(glycerol penta(ethylene oxide)methacrylate) (PAGEO5MA) polymer brushes were synthesized to investigate them and examine the impact of grafting density on the constant formation of hydrogen bond complexes in different medium.

This study comprehensively examines the frictional behaviour of PDMA brushes fabricated across various scales, from nanometers to micrometers, using Friction Force Microscopy (FFM). The investigation reveals how solvent interactions influence frictional properties, with water promoting adhesion-dominated, sublinear friction-load relationships, while ethanol induces polymer collapse and linear friction-load relationships governed by molecular ploughing. The findings highlight that smaller PDMA features exhibit reduced adhesion and lower friction coefficients in water, whereas ethanol causes densely packed, collapsed polymer structures, increasing resistance to mechanical deformation, and enhancing the ploughing effect. These insights deepen our understanding of the frictional dynamics of polymer brushes and their dependence on environmental conditions and polymer characteristic.

This research examines the synthesis of PDMA brushes via Surface-Initiated Atom Transfer Radical Polymerization (SI-ATRP) and their frictional behaviours as influenced by varying grafting densities. The brush conformation was found to be significantly dependent on grafting density and the surrounding environment. Friction forces were analysed into load-dependent and shear-dependent components, revealing how normal and lateral forces affect the interactions between an AFM tip and PDMA surfaces. At high grafting densities, extensive contact leads to adhesive sliding, while lower densities result in fewer contact points and ploughing mechanisms. These findings, supported by modelling the friction-load relationship, indicate shifts in polymer chain conformations and underscore the complex relationship between grafting density and frictional properties.

This research explores the fabrication of PAGEOMA brushes through Surface-Initiated Activator Regenerated by Electron Transfer Atom Transfer Radical Polymerization (SI-ARGET ATRP) and their frictional behaviours across varying grafting densities. The brush conformation significantly influences grafting density and the surrounding environment, which in turn affects the physical properties of PAGEOMA brushes. Friction forces between an AFM

tip and the PAGEOMA surface are categorized into load-dependent and shear-dependent terms, determined by normal and lateral forces, respectively. High grafting densities lead to extensive contact and adhesive sliding, while lower densities result in fewer contact points and a transition to ploughing mechanisms. Variations in surface shear strength (τ) indicate shifts from brush-like to mushroom or pancake configurations. These findings are crucial for optimizing PAGEOMA brush-based materials for applications in coating, surface treatment, and medical materials by understanding the relationship between grafting density and frictional properties.

ABBREVIATIONS

AFM = Atomic force microscope

CFM = Chemical force microscopy

FFM = Friction force microscope

F_F = Frictional force

F_N = Normal force

JKR = Johnson, Kendall, and Roberts

DMT= Derjaguin, Muller and Toporov

SAMs = Self-assembled monolayers

ATRP = Atom transfer radical polymerization

SI-ATRP = surface-initiated atom transfer radical polymerization

DTBU = bis[2-(2-bromoisobutyryloxy)undecyl] disulfide

MUD = 11-mercapto-a-undecanol

NPPOC= 2-(2-Nitrophenyl) propoxycarbonyl

PCysMA = Poly(amino acid methacrylate)

Bipy = 2,2,-bipyridyl

UHV = Ultra high vacuum

PDMA = Poly(2-dimethylamino) ethyl methacrylate)

TFAA = trifluoroacetic anhydride

($NaCNBH_3$) = sodium cyanoborohydride

(TFEA) = 1,4 dioxane and 2,2,2-trifluoroethylamine

NPPOC-APTES = 2- nitrophenylpropyloxycarbonyl-3- aminotriethoxysilane

BIBB-APTES = bromoisobutyryl amidotriethoxysilane

POEGMA = poly(oligo ethylene glycol) methacrylate)

IL = interference lithography

DCM = dichloromethane

PMMA = poly(methyl methacrylate)

UV = ultra-violet

THF = tetrahydrofuran

(PMDETA) = N, N, N′,N″,N″-pentamethyldiethylenetriamine

Bipy = 2,2’-bipyridyl

RAFT = reversible addition fragmentation chain transfer

PDMA = poly(2- dimethylamino)ethylmethacrylate)

P3HT = poly(3-hexylthiophene)

PMMA = poly(methyl methacrylate)

(PAGEO5MA) = poly(glycerol penta(ethylene oxide)methacrylate)

FWHM = full width at half maximum

MUA = 11-mercaptoundecanoic acid

(VdW) = Van der Waals

(QCM) = Quartz Crystal Microbalance

(XPS) = X-ray Photoelectron Spectroscopy

TABLE OF CONTENTS

LIST OF SCHEMES

LIST OF FIGURES

CHAPTER 1 INTRODUCTION

1.1 Intermolecular Forces

The four essential forces occurring in nature seem to be: those acting among elementary particles such as strong and weak nuclear forces and those that are accountable for atoms and molecules interaction such as the gravitational and electromagnetic forces. The forces responsible for the binding of atoms to form compounds or molecules in the form of ionic and covalent bonds are called intramolecular forces. These forces are relatively more robust compared to intermolecular forces, yet, are impossible to be active between sliding surface interactions. The forces that act among molecules are essential in the tribological study of both the adhesion and friction. There are many categories of intermolecular force, such as dipole-dipole (Keesom), induced dipole-induced dipole (London dispersion) diplexer-induced dipole (Debye) forces which are typically referred to as Van der Waals interactions [1–3], charge-charge (Coulomb), charge-induced dipole and charge-dipole interactions [4]. In addition, several special forces exist, including hydrogen bonding (a specific form of dipole-dipole interaction) as well as hydrophilic and hydrophobic interactions.

Measuring the forces among atoms and molecules can reveal their composition and the essence of their interactions. Forces between the atoms can be defined as the potential of Lennard-Jones, as shown in (1.1):

$$V(r) = 4E\left[\left(\frac{\sigma}{r}\right)^{12} - \left(\frac{\sigma}{r}\right)^{6}\right] \quad \textbf{(1.1)}$$

where E is the energy of contact which has the lowest value at equilibrium distance r0, and σ is the distance when V(r) = 0.

At distances larger than r0, the potential is controlled by attractive long-range interactions which decrease as a factor of $1/r^6$, whereas at smaller distances Interaction is strongly impacted by repulsive short-range interactions that correlate with $1 / r^{12}$.

In terms of macroscopic bodies, single interactions of atoms are substituted via interactions between greater collections of atoms or molecules, with a slightly different mathematical [4]. The energy of interaction is provided for a molecule that interacts with a surface within a plane at a distance D, as seen in (1.2) (Figure 1.1):

$$W(D) = -\frac{A_H}{12\pi D^2} \tag{1.2}$$

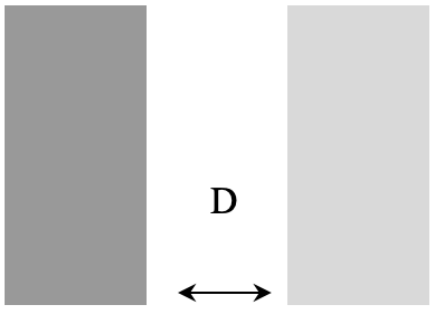

Figure 1.1: The energy of interaction for a molecule within a plane interacting with a surface at distance D.

If a hemisphere replaces the molecule – a rational estimate to the tip of a traditional probe for AFM – so this relation results to (1.3) (Figure 1.2):

$$W = -\frac{A_H R}{6D} \tag{1.3}$$

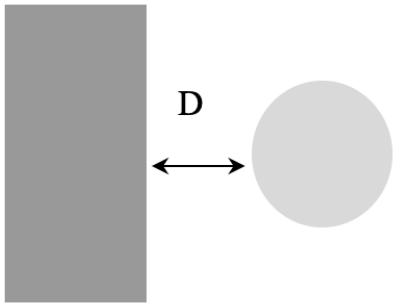

Figure 1.2: The energy of interaction for a molecule between a surface and a hemisphere at a distance D.

where A_H is the Hamaker constant and R is the sphere radius. Apparently, the energy of the interaction differs with mutual separation.

For two cylinders which are crossed the force becomes, shown in (1.4):

$$W = -\frac{A\sqrt{R_1 R_2}}{6D} \tag{1.4}$$

This equation is significant since the surface forces apparatus (SFA) has been able to successfully quantify forces on surfaces for more than three decades.

1.2 Lifshitz Theory

For a Van der Waals (VdW) particle-particle interaction, the Hamaker constant A can be described in (1.5):

$$A = \pi^2 \times C \times P_1 \times P_2 \tag{1.5}$$

where C is the Coefficient of interaction between particle-particle pairs, P_1, and P_2 are the number densities of the two types of particles which interact [5], [6]. The magnitude of this constant describes the strength of the VdW occurring between two particles, or between the surface and a particle [5]. The Hamaker constant offers a way for calculating the interaction parameter C from the potential of the VdW pair, shown in (1.6):

$$W(D) = -\frac{C}{r^6} \tag{1.6}$$

Hamaker constant ignores the effect of a medium that intervenes between the two contact particles. In 1954, Lifshitz established a description of the vdW energy but considering the dielectric properties of this medium (continuous phase) [7]. Lifshitz theory suggests that van der Waals interactions are the consequence of irregularities in the electrical and magnetic fields, which produce a force among interacting particles. Different processes contribute to the movement of charges within systems containing electrically neutral particles, which leads to the production of electromagnetic waves including the: rotational and vibrational molecular motions, ion displacements and movements of electrons. Waves spread through space (when interacting with the medium), generating a reaction on the opposing body's electromagnetic

arrangement. Finally, bodies are experiencing a force that seeks to reduce the system's energy (through methods such as repulsion and attraction) attempting to bring them to a separation of minimal energy (figure potential Lennard-Jones).

Lifshitz theory provides a quantum mechanical model for understanding van der Waals (vdW) interactions, which are primarily driven by fluctuating electromagnetic fields resulting from electron motion within molecules. These fluctuations generate temporary dipoles that induce similar dipoles in nearby molecules or surfaces, leading to an attractive force between the particles. The strength of this interaction is highly dependent on the distance between the molecules, with the attraction becoming more significant at larger separations due to retarded interactions, which refers to the delay caused by the time it takes for dipoles to influence one another. Additionally, the interaction strength is also governed by the dielectric properties of the materials involved, particularly their ability to polarize in response to electromagnetic fields. Lifshitz theory highlights the role of thermal fluctuations and dispersion forces, providing a comprehensive explanation of the long-range vdW forces that arise between electrically neutral molecules.

The composition of Lifshitz 's work requires the knowledge on the continuum theory and quantum electrodynamics; thus, the basic concepts of continuum theory must be summarised to provide the reader with some information regarding the formulas utilized in this theory. Phases interacting with each other are supposed to contain a set of quantum oscillators that produce and respond to electromagnetic field fluctuations. The interaction between all oscillators and electromagnetic fields are based on the bulk material's frequency-dependent electrical permittivity, $\varepsilon(\omega)$, and magnetic susceptibility, $\mu(\omega)$. The former can be used to calculate a range of different imaginary frequencies (often known as Matsuba Frequencies), $\zeta_n = 2\pi\, k_B\, Tn/\hbar \qquad (n = 0, 1, 2, \ldots..)$.

In order to calculate the system's total free energy in terms of the separation of the surface W(D), the free energies must be summarized for each oscillation, $g(\omega_j)$. Since the system provides a set of oscillators with energy levels actually rise in quantized steps ($\hbar\omega$) from the zero-point energy, ($\frac{1}{2}\hbar$), each oscillator 's free energy is determined by (1.7) [8]:

$$g(\omega_j) = k_B\, T \ln\left[2\, sinh\left(\frac{\hbar\omega_j}{2k_B\, T}\right)\right] \tag{1.7}$$

These surface modes ω_j represent a subset of the Matsubara frequencies given by (1.8):

$$\omega_j = i\zeta = i\frac{2\pi\, k_B\, Tn}{\hbar} \tag{1.8}$$

where $n = 0, 1, 2, \ldots..$

The frequencies produced depend on both the separation of the surfaces and the dielectric properties (the electric permittivity, $\varepsilon_{1,2,3}\,(i\zeta)$, and the magnetic permeability, $\mu_{1,2,3}(i\zeta)$ of all three interacting materials which are body 1 and 2, and the intermediate phase [7]. Therefore, the free energy depends on the dielectric properties of objects for each oscillator surface mode; thus, the system's total free energy is given through summation shown in (1.9):

$$W(D) = \Sigma_{\omega j} g(\omega j[\varepsilon_{1,2,3}\,(i\zeta), \mu_{1,2,3}(i\zeta), D]) \tag{1.9}$$

It can be combined this expression by $W(D) = -\frac{A_H}{12\pi D^2}$ providing the function of free energy in terms of separating two half-spaces using a constant Hamaker, as shown in (1.10):

$$W(D) = \frac{A_H[\varepsilon_{1,2,3}\,(i\zeta), \mu_{1,2,3}(i\zeta), T, D]}{12\pi D^2} \tag{1.10}$$

This demonstrates the strength of Lifshitz theory, which enables the measurement of a system's Hamaker coefficient from the dielectric properties of the interacting materials. Obviously, the theory of Lifshitz is mainly concerned with dispersion forces resulting in electrically neutral surfaces from the mutual polarisation. It thus cannot clarify the existence of interactions in more complicated systems.

Despite the limitations, it was shown to offer an exceptionally reliable estimate of the interactions in several systems [4], [9], [10], [11] and was therefore chosen for further research but with some modifications. The data for numerous mediums or surfaces to be analyzed is not easily obtainable.

Therefore, an approximate version developed by Israelachvili [4] can be used. In a simple relation like this, both the dielectric constants and refractive index of interacting materials define the interaction itself. When two bodies 1 and 2 interact with a third medium (3), the Hamaker constant, A_{123}, is defined as the sum of both a term with a zero frequency ($A_{(v=0)}$), and a higher than zero frequency ($A_{(v>0)}$). $A_{(v=0)}$ refers to the dipole- induced dipole (Debye) and dipole-dipole (Keesom) interactions. Dielectric constants Є of all materials in the reaction medium (1,2, and 3) are contributing factors to the $A_{(v=0)}$. In contrast, $A_{(v>0)}$ refers to the interactions via dispersion. Furthermore, it is a function of the refractive indexes (n) of the interacting materials (1,2 and 3), and the Hamaker constant of the system can be approximated using (1.11):

$$A_{132} = A_{v=0} + A_{v>0} \approx \frac{3}{4}kT\left(\frac{\varepsilon_1 - \varepsilon_3}{\varepsilon_1 + \varepsilon_3}\right)\left(\frac{\varepsilon_2 - \varepsilon_3}{\varepsilon_2 + \varepsilon_3}\right) + \frac{3h\nu_e}{8\sqrt{2}} \frac{(n_1^2 - n_3^2)(n_2^2 - n_3^2)}{(n_1^2 + n_3^2)^{1/2}(n_2^2 + n_3^2)^{1/2}[(n_1^2 + n_3^2)^{1/2} + (n_2^2 + n_3^2)^{1/2}]} \quad \textbf{(1.11)}$$

where n_x and ε_x are the refractive index and static dielectric constant of medium x, T is the absolute temperature at (298.15 K), k is the Boltzmann's constant with a value of (1.38065 9 10^{-23} J K^{-1}), , h is the Planck's constant with a value of (6.62608 9 10^{-34} J s), and ν_e is the UV's principal electronic absorption frequency, assuming that it is unique and equal at the same time for all the material (has a value of 3 $\times 10^{15}$ s^{-1}).

After calculation the Hamaker constant, the eq. $W(D) = -\frac{A_H}{12\pi D^2}$ can be used in the calculation of the system's adhesion work.

1.2.1 Hunter Model

Hydrogen bonding, as its names indicate, pertains to the hydrogen atom and electronegative atom interactions, such as halogens, O, or N. Hydrogen bond is a unique type of dipole-dipole

interaction. It appears to have strong values ranging from 4 to 16 kT, which made it known as relatively stronger than Van der Waals interaction (almost one kJ mol^{-1}), but less potent than ionic and covalent bonds (> 200 kJ mol^{-1})[12]. An enhanced version of the model previously suggested by Hunter in 2004 was utilized to decide whether these interactions could estimate the energy of adhesion between the bodies.

This solvation thermodynamic model was successfully applied to different solvation effects,[13], [14] and was also utilized in the simulation of adhesive interactions among surfaces that are polar by nature [15]. The fundamental principle of the model is focused on the identification of the hydrogen bond donors and acceptors, which are achieved via experimental or analytical methods of determining the set parameters [16]. From these, the different thermodynamic properties of the solvated molecules system in equilibrium can then be calculated.

Abraham et al. (2001) introduced the application of hydrogen bond parameters to determine the system's equilibrium constant [17]. The study suggested that equilibrium constant (K) can be solved using (1.12), which is highly accurate for an interacting system containing simple hydrogen bonds:

$$log\ K = c_1 \alpha_2^H \beta_2^H + c_2 \quad \textbf{(1.12)}$$

Where *log K* represents the logarithm of *K*, which describe a process, such as an equilibrium constant, rate constant, or a thermodynamic property. β_2^H and α_2^H are constants of functional groups related to hydrogen bond basicity (acceptor) and acidity (donor), respectively, c_1 is a term specific to a solvent which indicates its inverse relevance to the polarity of the medium, while c_2 is a constant representing a baseline level of *K* independent of β_2^H and α_2^H , with an approximate value of -1.0.

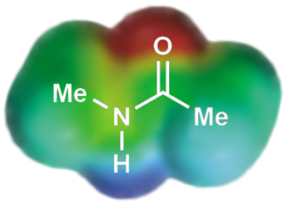

Figure 1.3: MEPS in the N-methyl acetamide radius of van der Waals, indicating sites referring to parameters of (Emax) and (Emin). The colours indicate the increase in density of electrons from the blue to the red [16]**.**

The Hunter model's primary presumption is that the hydrogen bonding occurs typically on the interacting molecules only at particular locations. Defining the molecular electrostatic potential surface (MEPS) in any molecular system (showing the closest distance of two nonbonded atoms), the maximum is most often placed close a hydrogen; whereas, the minimum is normally above a lone pair or any other large-electron density area. Figure 1.3 shows an illustration of a surface marked with maximum and minimum. The maxima and minima energies, E_{max} and E_{min}, has been characterized via linear correlation with $\alpha_{(2)}^{H}$ and $\beta_{(2)}^{H}$ values, causing new hydrogen bond strength parameters to be obtained concerning the two factors, given in (1.13) and (1.14) [16]:

$$\alpha = E_{max} / 52\, kJmol^{-1} = 4.1(\alpha_2^H + 0.33) \quad \textbf{(1.13)}$$

$$\beta = -E_{min} / 52\ kJmol^{-1} = 10.3(\beta_2^H + 0.06) \quad \textbf{(1.14)}$$

where the donor of hydrogen bond is α and the acceptor is β, of the corresponding molecule.

Then, study the possibility of a system that has reached equilibrium with two molecules in solution: the donor and acceptor of hydrogen bonds. Figure 1.4 suggests a potential competition for a solvent-solvent, solute-solute, and solvent-solute interactions at any given time. Each interacting molecule has a corresponding hydrogen bond parameter; thus, the free energy (ΔG°) of solvation can be described in (1.15) [16]:

$$\Delta G^{\circ} = -RT log\ K = -(\alpha - \alpha_S)(\beta - \beta_S) + 6\ kJmol^{-1} \quad \textbf{(1.15)}$$

where α and β are constants related to the hydrogen bond donor and acceptor abilities of a functional group or a molecule, respectively. α_S and β_S are the solvent's Hunter hydrogen bond parameters. T is the absolute temperature (298.15 K), R is the universal gas constant with a value of (8.314 J K^{-1} mol^{-1}), and K is Equilibrium Constant. The addition of 6 $kJmol^{-1}$ corresponds to bimolecular complexation's adverse free energy.

Hunter's model provides a theoretical approach for understanding hydrogen bonding interactions between molecules. It uses statistical parameters (α and β) to quantify a molecule's ability to donate (α) or accept (β) hydrogen bonds, which are important to determining molecular interactions. The model also accounts for the solvent's impact on these abilities through solvent specific parameters (α_S and β_S). By combining these factors, Hunter's model helps predict the strength and nature of hydrogen bonds, which is essential for understanding solubility, reactivity, and other physical properties of substances in different solvents.

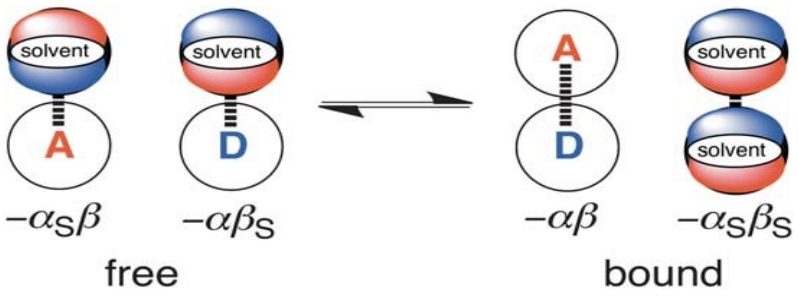

Figure 1.4: The solvent competition system for the complex established here between the H-bond solutes, D, and the H-bond solute, A[16]**.**

The discrepancy between the donor and acceptor's hydrogen bond for both the solvent and solute increases the interaction between solutes. In effect, the equilibrium starts to lean on the bimolecular complexation. Consequently, more significant donor and acceptor bonds and their higher affinity towards complex formation are caused by their stronger hydrogen bond parameters [16].

Interestingly, this method provided reliable estimates to various related studies concerning the interaction within the system containing mixed solvents [14]. Besides, it has been accurately predicting the polar solvent's critical concentration over which changes in the adhesive and frictional forces across polar surfaces are observed [10], [15], [18]. It was obtained by suggesting that the maximum and minimum interactions of a MEPS are located at the end group

of the molecular. Besides that, the power of the expanded method to simulate the non-polar type of interactions [19], the Hunter model is essential in the description of forces occurring on surfaces.

1.3 Study of Surface Interactions

It is noteworthy that the comprehensive study of surface interactions can be carried out not only with AFM but also with other instruments, such as the surface force apparatus (SFA), invented by Tabor and Winterton [20]. Further innovations were done by Israelachvili and Tabor,[21] and Israelachvili and Adams, allowing the measurement of liquid samples [22]. Both the SFA and AFM are not considered as imaging tools, and that is an important concept that must be pondered. In the SFA approach, two smooth cylindrical surfaces of mica are contacted perpendicularly with each other. Optical interferometry is used to measure the surfaces of two substrates. Whereas, deflection of the cantilevered spring holding is used to measure the expended forces. The quantitative measurement of various surfaces is made possible using this apparatus. They have mainly consisted of mica sheets, whether unmodified [20], [22] or even modified with self-assembled monolayers [23]. It means that the SFA requires smooth samples on a molecular level, which are only compatible with the mica surfaces or substances immobilized to mica. However, the downsides of SFA focus on the quantification of weak forces and interactions between single asperities since micrometer-scale is used in measuring the area of contact [24], [25]. The emergence of scanning probe microscopy, specifically in the case of AFM [26] and FFM [27], has emphasized the interaction occurring on single-asperity contact. This is because the contact area between the tip and the substrate is measured on a nanometer-scale, and much higher resolution is considered for all three axes compared to SFA. Thus, this results in a great deal of effort that has been achieved in nanotribology to study the behavior of adhesion effectively [28], [29], [30] friction [25], [31], [32] wear, and lubrication [33], [34], [35]. These natural phenomena on a nano-level have become extremely significant to investigate, in turn, working on developing several nanotechnology systems, including micro and nanoelectromechanical systems (MEMS / NEMS), that has a wide range of applications since discovery.

1.4 Force-Distance Measurement

Besides imaging, another primary function of AFM is the measurement of the mechanical properties of the surface, including adhesion and stiffness using force versus distance plots. In

1988, the pioneering study on the use of force versus distance plots extracted from an AFM focus on the characterization of LiF and forces on the graphite surface [36]. The cantilever deflection could be measured both perpendicular to the planer and parallel to the surface. The most basic form of quantitative measurement is the force-distance measurement (also recognized as a "force spectroscopy" or "force curve").

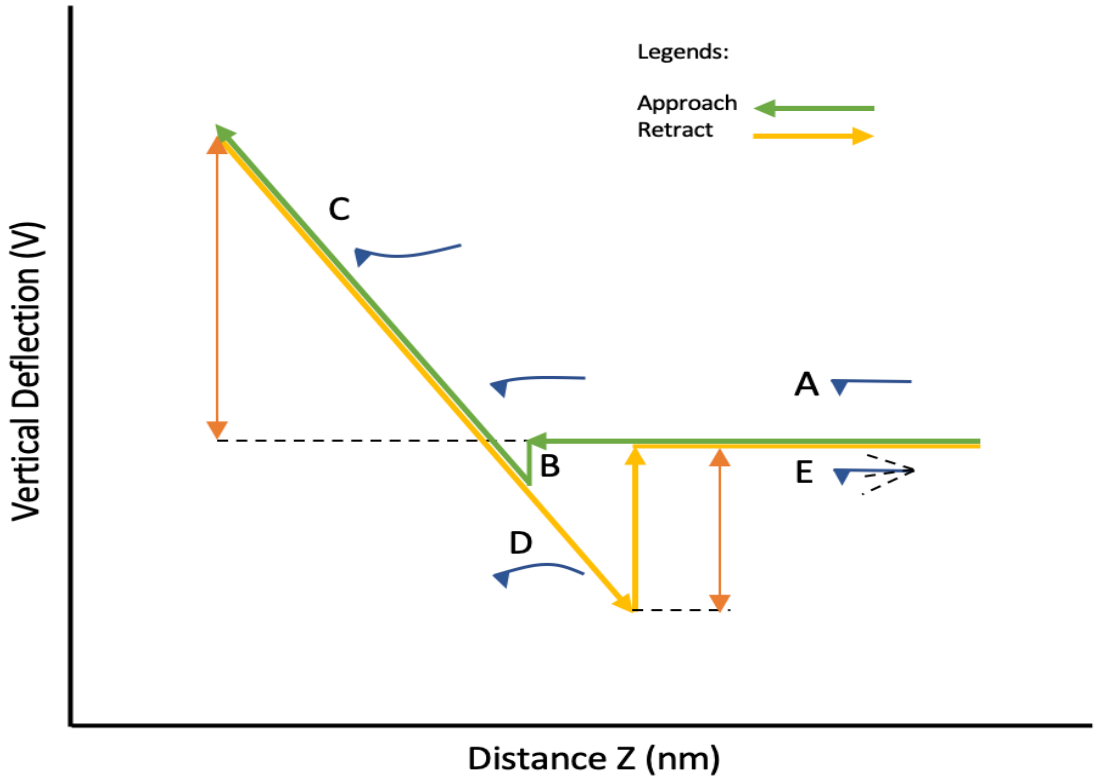

Figure 1.5: Variation in the interaction force as a function of distance during a force-distance measurement.

Figure 1.5 shows a diagram of the entire process. The simple force-distance curve has a complete cycle, including the curve of approach and retraction curve. The probe is placed above the surface of the sample, so the tip does not reach it. Then, the cantilever is being dropped slowly onto the surface (A). Mechanical instability causes the "jump to contact" (B) as the probe approaches the surface. The surface is now in close contact with the tip. The repulsive force is being measured as a result of pressing the tip into the surface (C) with further advancement in the piezoelectric scanner. The cycle is stopped at some predetermined point, and the tip is drawn back (D). The adhesion of the tip onto the surface causes hysteresis, wherein the retraction and approach directions are not the same. To separate it, the tip should be raised much farther compared to its initial point of contact. At this rate, the force measured

is negative in value (corresponds to attractive force), which indicates the effective dragging of the tip onto the sample surface. Finally, a non-contact position is achieved by snapping the tip off the surface. The adhesion (F_{adh}) is measured as the distance between the non-contact position and the minimum point in the plot, which is often called the pull-off force. Also, with a quantitative calibration of detector sensitivity (nm / V) and a cantilever spring constant k (N / m), the measured cantilever deflection can be converted to force using Hooke's Law (1.16). Hooke's Law is used to convert the cantilever deflection into force equivalent using the calibration done for the detector quantitatively (nm/V) and its spring constant (N/m). This equation is shown in (1.16).

$$F = -kx \tag{1.16}$$

where F is the force, k is the spring constant, and x is the distance. Interestingly, a different technique has been introduced, which involved functionalized tips. For example, selective adhesion of a particular molecule onto the tip is done to measure the forces acting on it using the force versus distance plot.

1.5 Contact Mechanics

For contact area measurement and analysis of the correlation of interactive forces with other parameters, it is essential to establish a model describing the behavior between surface and tip. FFM has emerged as an effective means of analyzing contacts for single asperity, according to the knowledge that a single asperity classification could be considered for a very sharp tip. Several years have passed since contact mechanics has been utilized in many applications. Furthermore, it became significantly crucial in the extraction of various information such as the contact area's molecular interaction, contact stiffness, elastic types of indentation, and stress-strain characteristics for loaded asperities [36-38].

In 1880, even though several models have been developed, there is still doubt about which model is suitable for different circumstances. Hertz introduced the first and simplest contact mechanic model. According to this, the circular contact area was attributed to material elastic deformation. In addition, this theory described the characteristics of single sliding contact without adhesion. According to this concept in an elastic contact, the correlation of F_N and the area of contact A is given by (1.17):

$$A = \pi \left(\frac{R}{K} F_N\right) ⅔ \tag{1.17}$$

where R is the hemisphere's radius, and K is the modulus of elasticity. The Hertz model is totally elastic in wherein surface attraction is completely neglected [39].

Although the Hertz model has become successful for inorganic materials, other materials show strong probe adhesion. In this way, the Hertz model could be improved. Notably, two models have taken a significant interest. Johnson-Kendall- Roberts model suggests that adhesion is applied at the tip-sample contact as an interfacial free energy γ. Based on this model, forces of adhesion lead to hemispherical deformation even without external force being applied. The contact area between the tip (assuming spherical with R as radius) and the surface is given by (1.18):

$$A = \pi \left(\frac{R}{K}\right) ⅔ \left(F_N + 3\pi\gamma R + \sqrt{6\pi\gamma RF + (3\pi\gamma R)^2}\right) ⅔ \tag{1.18}$$

where R is the radius of the probe, γ is the free energy at the interface, and K is the modulus of elasticity. When γ = 0 this equation is transformed to Hertz equation at the absence of load.

Furthermore, at zero loads, the contact area is limited and given by (1.19) [40]:

$$a_0 = \left(\frac{12\pi R^2 \gamma SV}{K}\right)^{\frac{1}{3}} \tag{1.19}$$

During a force measurement, the lifting of the tip from the sample surface causes hysteresis (probably non-reversibility) to assume that the tip is poked onto the surface after the initial point of fracture. As a result, necking occurs on the tip and continuously develops while the tip is removed from the surface. The stability of necking ends at its critical point concerning the contact area radius in the absence of load, as described in (1.20):

$$as = ao/4⅓ = 0.63ao \tag{1.20}$$

The neck is unstable at this point, and the tip is separating from the surface. Adhesion force (pull-off force or critical load) is the minimum load required to achieve the separation of the interacting bodies, as shown in (1.21)[41]:

$$F_s = -3\pi R\gamma SV \tag{1.21}$$

This force is equivalent to adhesive force extracted from force versus distance plots. The previous equation suggests that the adhesion force is proportional to the (i) the free energy at the interface at the tip-surface contact and (ii) area of contact between the tip and the surface. No adhesion occurs in non-contact areas. The area of contact at zero loads is observed as non-zero used in the JKR model, created by attractive forces. JKR model is useful at short range strong adhesive force between the surfaces [29], [51].

In contrast, The Derjaguin-Muller-Toporov model (DMT) is utilized for weaker, long-range interactions [29], [51]. The Derjaguin-Muller-Toporov (DMT) theory suggests that the surface follows the Hertz theory at deformation. Aside from the external load F, consideration is also given to the forces observed on the surface not included in the contact area [44]. It means this model considers the effect of Vander Waals Forces (attractive force) outside the area of contact. It leads to the establishment of a finite area of contact. External load causes a dramatic increase in the contact area. In terms of negative load, the contact region approaches zero. This instance maximizes the pull-off force. The relation between the load and the contact area radius is determined by (1.22):

$$A = \pi(\frac{R}{K})^{2/3}(F + 4\pi\gamma R)^{2/3} \tag{1.22}$$

And the pull-of force is given by (1.23):

$$F_S = -2\pi\gamma R \tag{1.23}$$

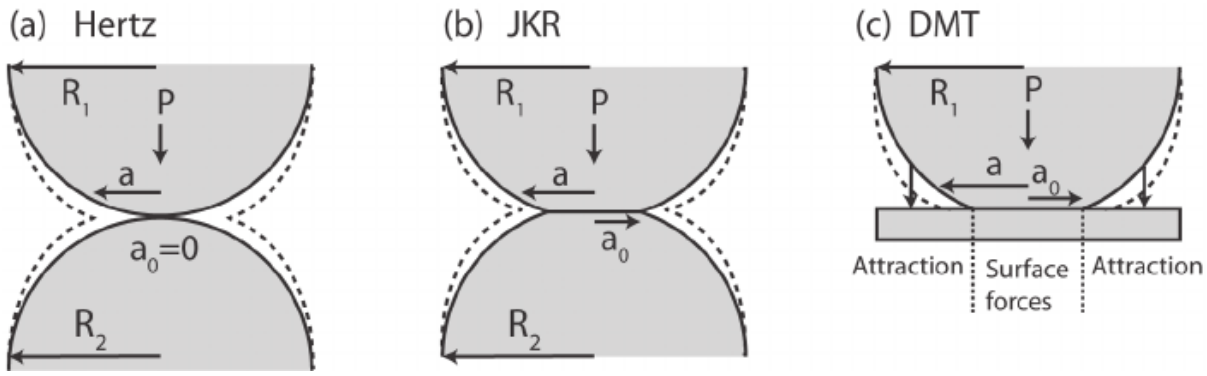

Figure 1.6: Cross-sectional diagram of the interaction for (a) Hertz, (b) JKR, and (c) DMT models between two elastic spheres [45]**. Clear lines signify zero-load contact region at zero-load, while dotted lines signify contact region for the load applied, *P*.**

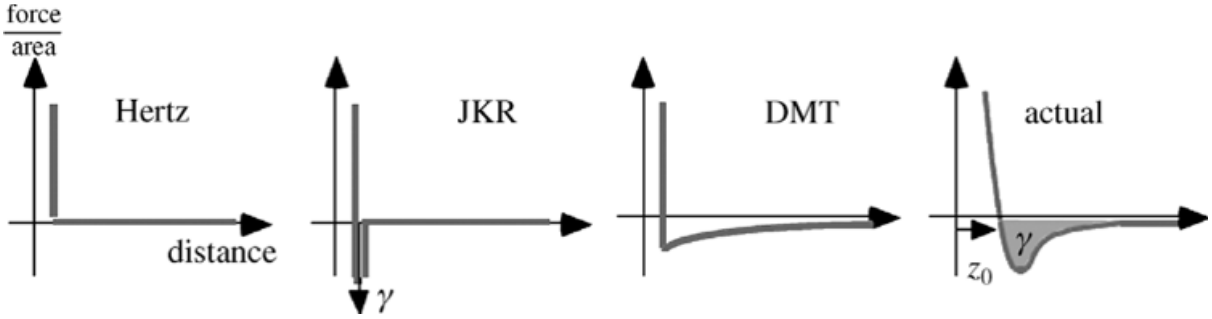

Figure 1.7: Schematic illustration of attraction force for the Hertz, JKR, and DMT models with in comparison to real contact between the AFM tip and the sample surface [46]**.**

Comparing these models, no interactions (adhesion) are considered for the Hertz theory (as seen in Figures 1.6 and 1.7). It is evident that the adherence is present in the JKR and DMT models with various reliance on separation. The theory of Johnson-Kendall-Roberts (JKR) ignores surface force (long-range forces) outside the area of contact and treats surface force (forces at short ranges) within the area of contact. However, The DMT Theory considers both surface forces within and forces of attraction on the outside of the area of contact. Also, The JKR model is correct in the case of soft materials; whereas, the DMT model is dominant for the stiff materials and less powerful adhesion [47], [48].

Since their publication, DMT and JKR theories became questionable both on experimental and theoretical perspectives. Between 1971 to 1984, this debate continued until it was slowly understood that the two ideas applied to two very different circumstances. These theories have been followed by many theories that attempted to understand the relationship between the

contact area and surface force. The Maugis theory has seen to be the most comprehensive and practical concept since it is applicable toa wide range of substances (i.e., large and small spheres with large and small surface energies, respectively) [49].

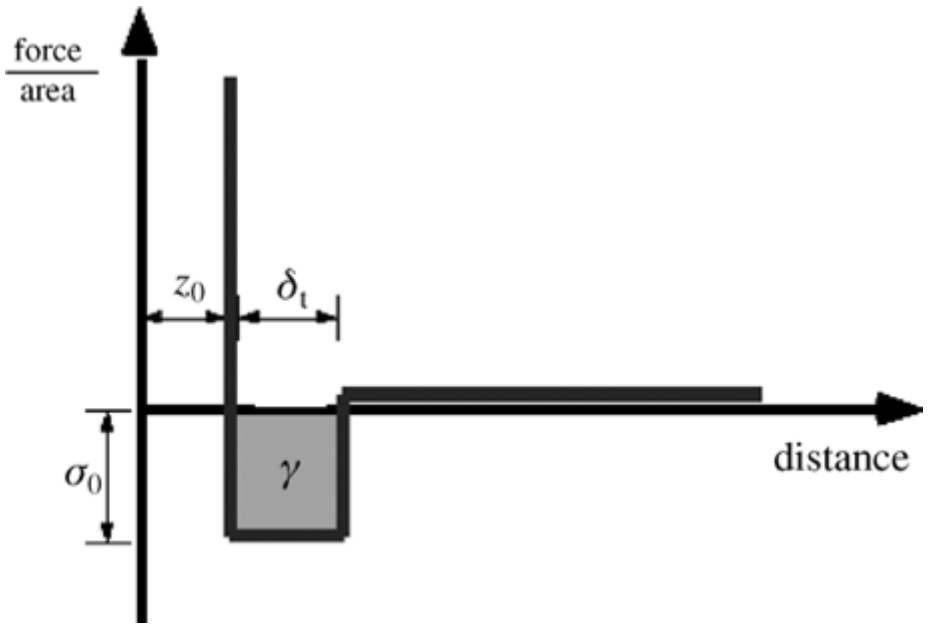

Figure 1.8: The schematic diagram demonstrates the relationship between force and distance used by Maugis [48]**.**

Maugis has attempted to link JKR and DMT theories to formulate a flexible model capable of calculating the pull-off force and contact area at a provided load (Figure 1.8). The full range of surface properties are defined by λ in (1.24):

$$\lambda = 2\sigma_0 \left(\frac{R}{\pi\gamma K^2}\right)^{1/3} \quad \textbf{(1.24)}$$

The constant stress of adhesion σo operates through a span of separation $\delta 1$ and then reduces to zero at great distances; consequently, adhesion work is $\gamma = \sigma_o$. A large λ usually present for fully compliant, soft, and adherent materials; whereas, small λ takes place for small, stiff, low-energy objects. The JKR model is accurate at $\lambda > 5$; whereas, the DMT model is valid at $\lambda <$ 0.1. At a range of 0.1 and 5, a similar transition regime is observed on both JKR and DMT.

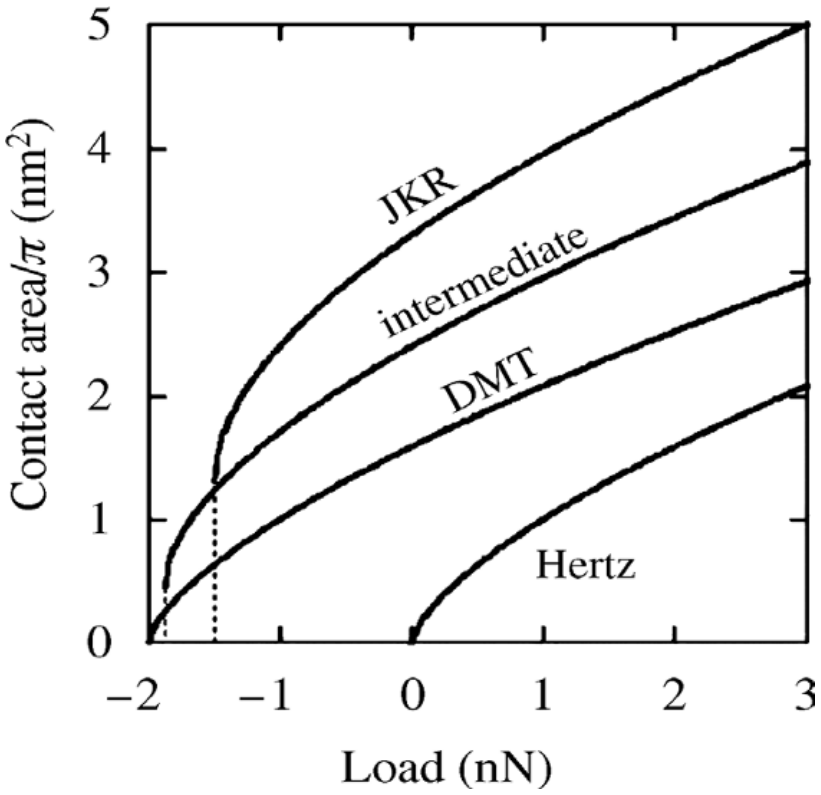

Figure 1.9: The expected load depends on the area of contact for different contact mechanics models [48]**.**

In many of these cases, the difference in area of contact with load can be seen in Figure 1.9. Hertz's theory can be utilized without forces of attraction $\gamma = 0$. Even though the Maugi model has been significant in recognizing the restrictions of various contact mechanics models, it is somehow challenging to utilize. A decade later, therefore, Carpet, Oligotree, and Salmeron created another approach (pointed to it as the COS equation) [50]. In 1999, they developed the Maugis principles and produced a simplified equation for estimating the contact radius by (1.25):

$$a = a_0(\alpha)\left(\frac{\alpha + \sqrt{1 - \frac{F}{F_{C(\alpha)}}}}{1+\alpha}\right)^{\frac{2}{3}} \tag{1.25}$$

where $a_0(\alpha)$ is contact region at load equal zero, $\alpha$is a parameter of transition. This equation connects both the applied load and the area of contact to the transition parameterα. When α = 0, the DMT is exactly applicable, and when α = 1, the JKR model is exactly applicable.

Moreover, for middle circumstances ($0 < \alpha < 1$), the transition equation relates accurately to the transition regime of the Maugis equation ($0.1 < \lambda < 5$). Consequently, an estimated formula is used for the connection between α and λ by (1.26):

$$\lambda = -0.924 \ln(1 - 1.02\alpha) \quad \textbf{(1.26)}$$

They have described a step in the process-by-step to match this formula in measuring the contact regime for applications on the AFM or SFA.

Models of contact mechanics can be an essential instrument in obtaining fundamental quantities from contact surface experiments. However, they must be used with caution, with careful consideration being given to the correct limitations and expectations that they involve.

1.6 Chemical Force Microscopy (CFM)

Chemical Force Microscopy (CFM) works by chemically modifying both the AFM tip and the sample surface to have certain functional groups, such as carboxyl (-COOH), amine ($-NH_2$) or methyl ($-CH_3$). This enables researchers to study molecular interactions such as hydrogen bonding, hydrophobic interactions and covalent bonding by allowing the tip to interact with the complementary or reactive groups on the surface. In force-distance measurements, the AFM cantilever is driven towards and away from the surface, and it senses the attractive or repulsive forces based on the chemical nature of the interactions. The adhesion force is quantified from the force-distance curves and higher adhesion force indicates higher chemical affinity while low adhesion is an indication of low or no interaction. Also, in scanning mode, CFM creates a chemical contrast image that shows the chemical composition of the surface and the distribution of the functional groups. This technique finds its application in the study of surface properties at the molecular level and hence finds its application in the fields of material science, biochemistry and nanotechnology. This is because CFM provides information on the local chemical composition of the sample surface.

CFM uses chemical reactions between both the functionalized tip and the sample surfaces. It is noticeable that AFM probes commercially available are constructed based on either silicon nitride or silicon. However, chemical modification of the probe gives the opportunity of recognizing the fundamental identity of nanoscale chemical interactions. It is appropriate for studying numerous developed systems, including nanosensors, conductivity, adhesion,

tribology, and polymers [51], [52], [53]. Different methods have been used, including attaching a wide range of molecules to a tip to investigate unique interactions between the tip and the sample. For example, the most attractive method for analyses of friction at the nano-level, and adhesive force on molecular substances might be the adsorption of a monolayer of functionalized organic compounds. Nakagawa et al. indicated the first modification of the AFM probe process[54], [55]. They immersed alkylsilane monolayers onto the silicon nitride tip and determined adhesive forces between enhanced tips and methyl monolayers located on silicon with various lengths of the alkyl chain. Noticeably, although the adhesive force for a bare cantilever was nearly insignificant, a larger magnitude was observed for functionalized tips and improved with the length of the alkyl chain, which was seen to be absorptive the silicon substrate due to non- covalent interaction. Similarly, Ito et al. found that a broader span of tip performances could also be obtained by adsorption of trichlorosilane, which could be transformed into polar functions [56].

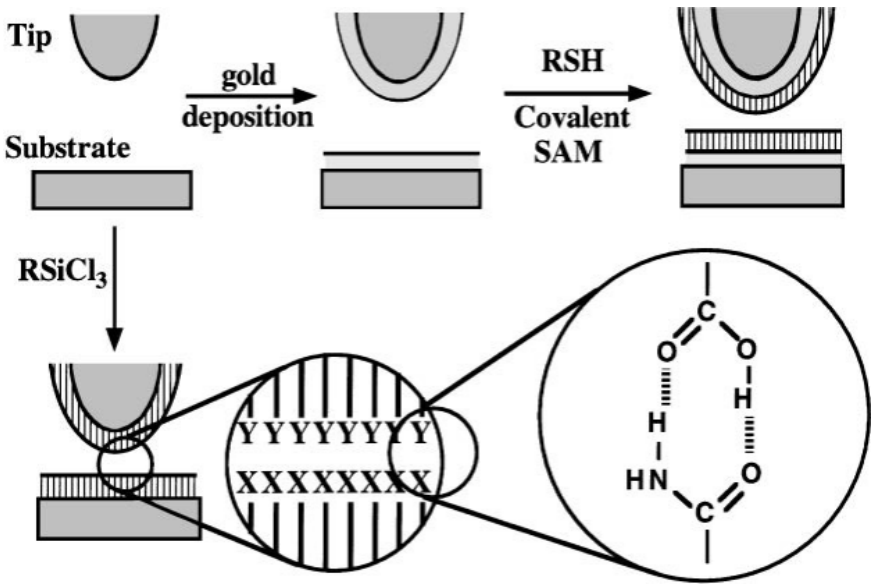

Figure 1.10: Chemical modification scheme in tips and sample substrates. The R in RSH and $RSiCl_3$ describes an organic alkyl chain ending with a functional group X (X = COOH, CH_3, NH_2, CH_2OH, etc.) [57].

Lieber and other researchers developed an alternative technique in 1994. They evaporated gold on the tip surface and immersed it in a solution of R-SH thiols, R becoming the functional interest group [52], [56]. It is obvious that the silane could be directly adsorbed to the tip of silicon nitride, while the attachment of alkanethiols needed the gold layer to be deposited before

its happening Figure 1.10. The functionalized tip in CFM is contacted with the sample surface and is pulled to determine the adhesion force (F_S) at which separation happens. For example, adhesion forces have been determined from force-distance measurements with different functional groups such as COOH-COOH, CH3-CH3, and CH3-COOH that were carried out in ethanol. Interestingly, polar interactions are considerably stronger than interactions with non-polar; similar functional interactions are significantly stronger than interactions with dissimilar ones Figure 1.11.

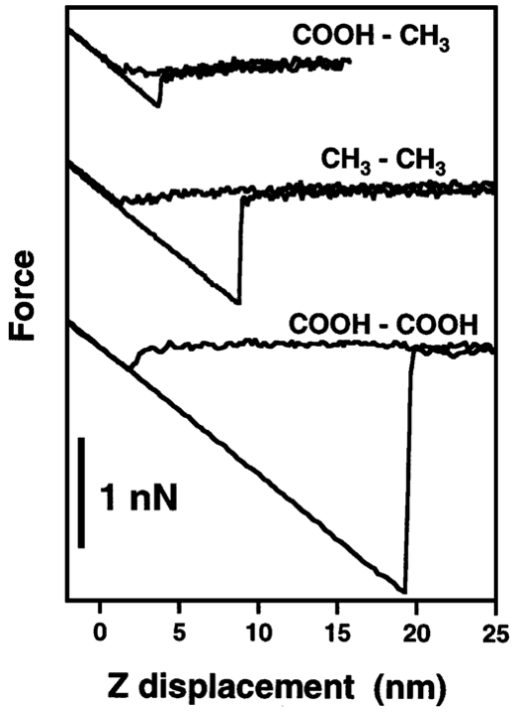

Figure 1.11: Representative F-D curve in ethanol reported for COOH-COOH, CH3-CH3, and CH3-COOH tip-sample surface modification [57]**.**

Van der Vegte and Hadziioannou have determined adhesive forces for a variety of functional group pairs of tip-surface [28]. It was found that the forces of acid-acid interaction were high at lower pH because they were still undissociated. With the dramatic increase in pH values and dissociation of molecules into carboxylate anions, the adhesive force decreased significantly due to repulsion between similar anions. The opposite has happened at lower pH for amines groups that were generally charged positively, resulting in repulsive interactions and uncharged at high pH. Vezenov *et al*. also determined adhesive forces with different pH [48]. Similarly to Van der Vegte and Hadziioannou's measurements, Vezenov et al. also observed that the interaction forces among groups of acids were strong at low pH. In contrast, those among groups of amines were strong at high pH.

Many researchers have measured the adhesive forces for a span of alkanethiol arrangements and polymers surfaces in various media, and considerable differences were found in the measurements provided in the different liquids. Clear and Nealey, for instance, found that the most significant adhesive force in water is observed between methyl-tips and methyl-monolayer interactions. In contrast, the adhesive force decreased in ethanol, hexadecane. In contrast, they found the lowest adhesive force in the water. The strongest in hexadecane is observed between a carboxylic acid-tip and an oxidation monolayer of alkene-trichlorosilane interactions.

1.7 Friction Force Microscopy (FFM)

Friction force microscopy (FFM) is a useful method for providing surface data on chemical compositions, molecular structure, and mechanical properties. Additionally, FFM has high sensitivity with nano-scale resolution and can be used to access quantitative data [42], [43], [58].]. FFM is based on calculating the lateral force of interaction between the tip and the surface of the sample when it scans through the surface Figure 1.12. These forces present on the surface of the sample could be measured via SFM instruments that use four-quadrant photodetectors. For the traditional constant force mode, the lateral cantilever deflections are determined via a laser beam, which is reflected accurately from the cantilever back to a measurement device (photodetectors)[42], [43]. Lateral deflections are the consequence of the load applied on the surface plane and the frictional interaction among both the tip and sample. After that, the forward and backward images (scans obtained with opposing tip movement directions) are recorded and subtracted from each other To eliminate the topographical impacts [29]. After deducting the forwards and reverse images, the produced image displays the surface friction spatial distribution (see Figure 1.12). This technique is called lateral force microscopy (LFM) or friction force microscopy (FFM).

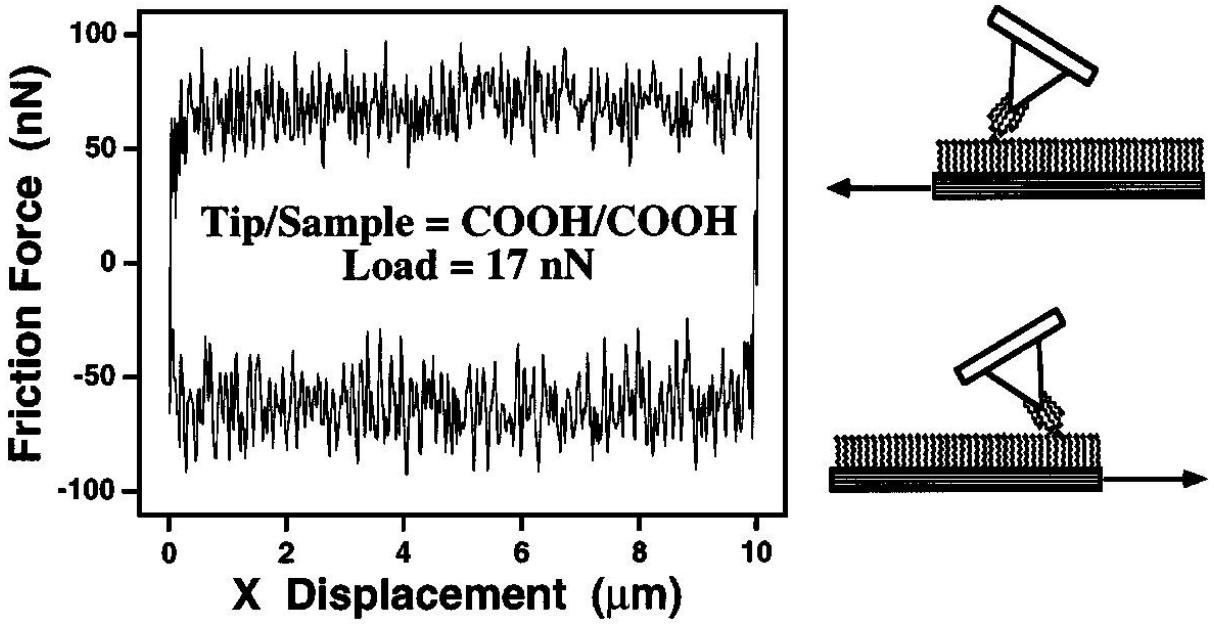

Figure 1.12: A standard friction loop that is tracked using a COOH-modified tip in EtOH solution on a COOH-terminated sample [57].

The chemical structure of the tip is modified (e.g., via a self-assembled monolayer) for the chemical force microscopy, so the differences in friction force can be calculated in contrast to differences in chemical composition. For instance, if the tip (polar) has a strong engagement with polar surface domains more than nonpolar domains, the deflection of the cantilever leans towards the lateral direction when crossing polar domains, and a more significant lateral signal will be registered on photodetector [42], [59]. In general, a bright region may refer to a larger deflection amplitude, so that stronger bonding refers to brighter regions in the CFM image (Figure 1.13a). In contrast, when the tip functionalization is switched (nonpolar tip), the tip is bent when crossing nonpolar domains of the surface. Instead, the different picture is observed (Figure 1.13b). The response of the frictional force to the amount of perpendicular load provided by the tip on the surface is demonstrated in Figure 1.14.

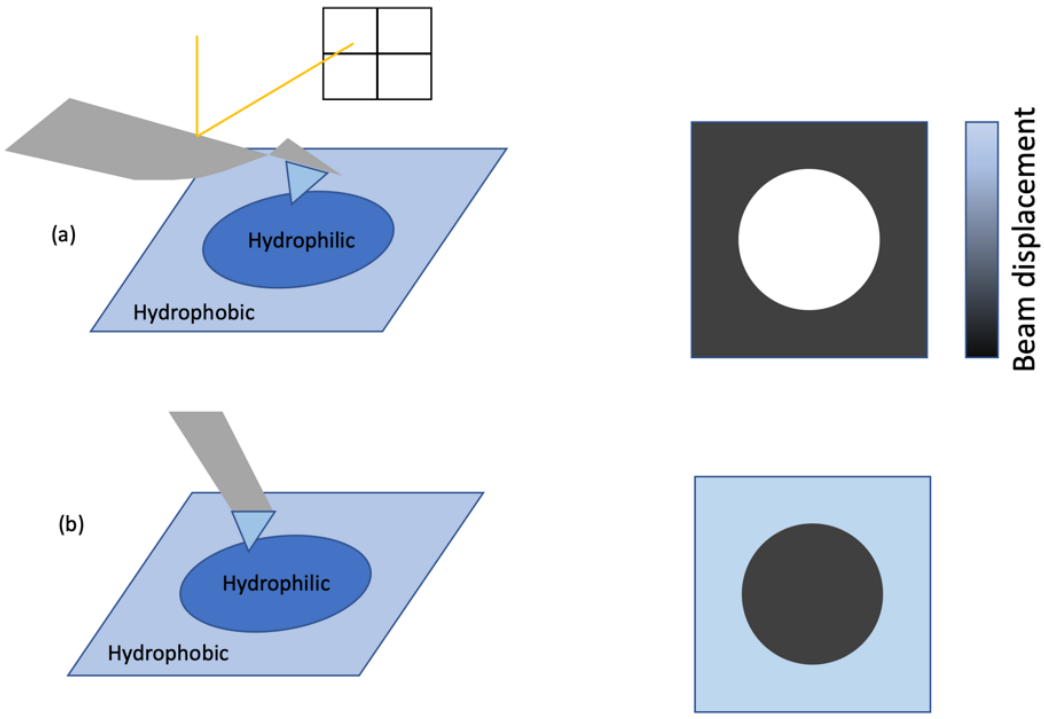

Figure 1.13: A) A hydrophilic tip on the functionalized hydrophilic location on the surface causes the cantilever to bend thanks to massive interactions detected by laser deflection thus producing a surface chemical profile image. B) Cantilever functionalization is modified in such a way that the tip is bent instead when hydrophobic surface areas are encountered

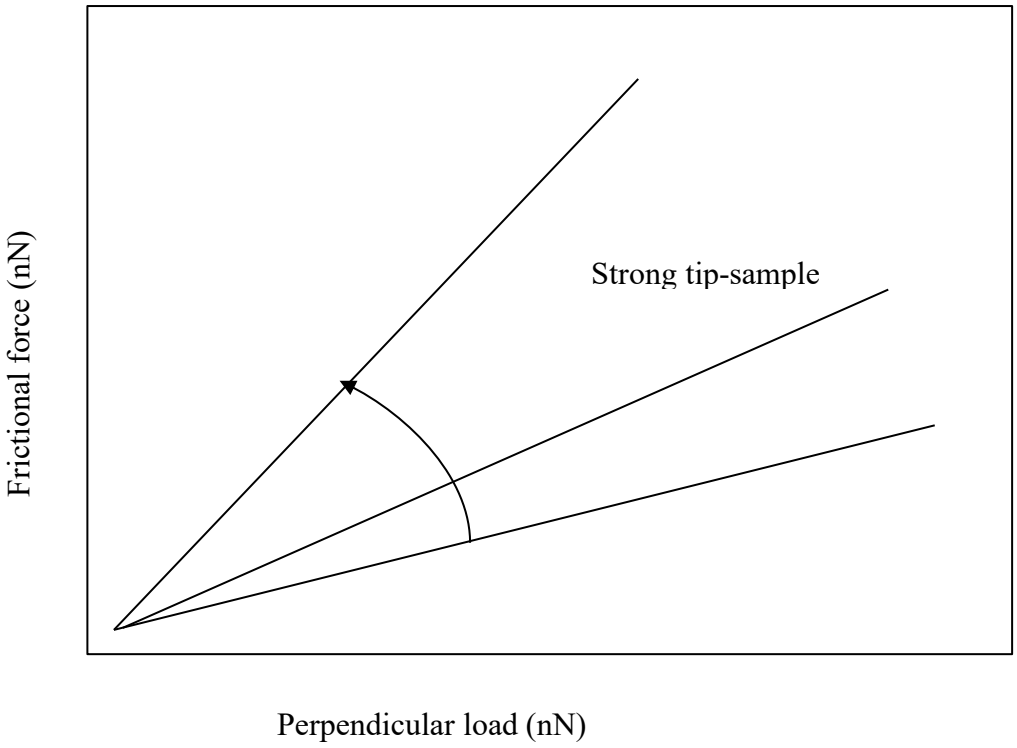

Figure 1.14: Frictional Force Typical Response to The Load Applied by The Tip.

Capillary force is a significant issue in the determination of frictional force as it efficiently improves the interaction between tip and surfac (4×10^{-7} N on mica in the air). It is usually caused by adsorbed moisture from the air, which is surrounding substrates. Consequently, FFM could be used under a suitable liquid to eliminate capillary water between tip and surface [29], [67], [68].

The ability of FFM to image the distribution of the various functional surface groups is shown in Figure 1.15. A patterned SAMs, consisting of more extensive lines of methyl terminated adsorbents divided by narrow lines of carboxylic acid terminated adsorbents has been observed. On the polar areas, there is an observable brighter contrast compared to the non-polar regions. It is due to the variation between the tip and the sample in the intermolecular forces that occur at the interface. As a general principle, like usually attracts like in intermolecular interactions (as contrasted to electrostatics, in which complete opposites attract). For this reason, a silicon nitride probe commercially available was used, which consists of an outer layer of silicon dioxide (polar). As a result, a reasonably strong attraction between the polar tip and the carboxylic acid areas on the surface is observed. It has relatively weaker interactive forces with the methyl terminated areas. Subsequently, there is a strong adherence of tip to the terminated

areas of carboxylic acid, under a higher energy dissipation rate. Therefore a greater frictional force, since the tip moves through those surface's areas.

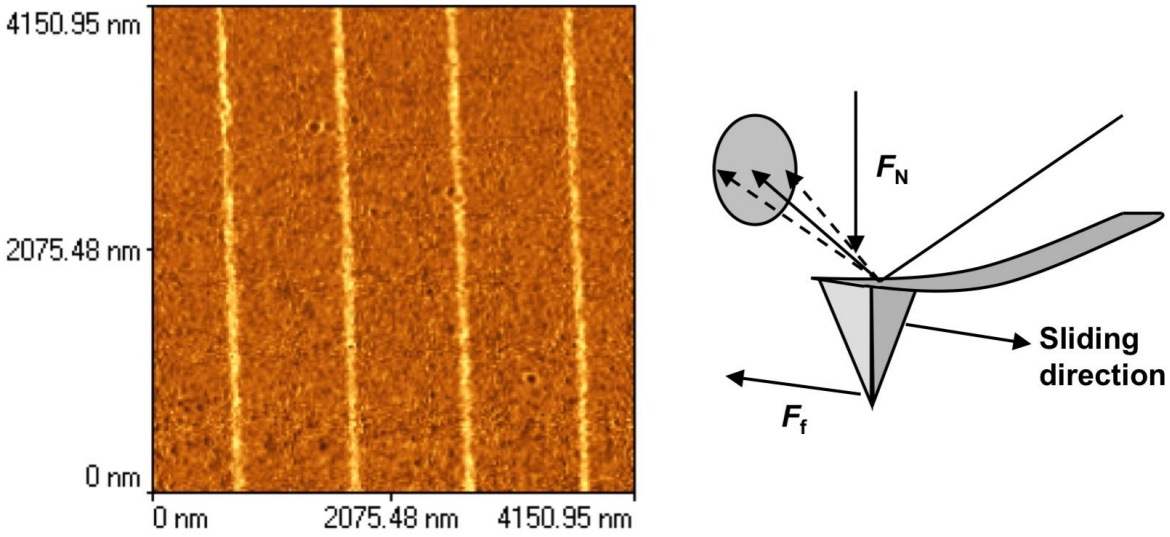

Figure 1.15: Demonstrate the power of FFM to image the distribution of the different functional surface groups [63]**.**

FFM is not just able to get many qualitative details. Indeed, the frictional interaction strength between the tip and the sample can be quantified by studying the relation of the frictional force and load. To achieve this, it is crucial to choose a suitable model of contact mechanics. The law of Amonton indeed has been described as the first classic friction theory. It has been commonly utilized to fit the data between friction (F_F) and applied load (F_N), which can often lead to a linear relationship, and the proportionality constant is the friction coefficient (μ), shown in (1.27) [59], [64]:

$$F_F = \mu F_N \tag{1.27}$$

Besides, the line that suits the data does not move across the origin in many circumstances at which a linear friction-load relationship is usually linear due to the effect of adhesive interaction between the tip and the sample. Thus, Deraguin was the first to propose a modification of the previous equation, given by (1.28):

$$F_F = F_0 + \mu F_N \tag{1.28}$$

where F_0 is the friction zero load.

Numerous attempts have been made since it was suggested to explain this law not only theoretically but also experimentally, often by taking into account the roughness and topographical characteristics of the shearing materials. In 1950 Bowden and Tabor suggested a second hypothesis as a consequence of these frictional uncertainties. The study found a linear proportionality of lateral friction F_L with the actual contact area A and shear strength, as seen in (1.29) [65]:

$$F_L = A\tau \tag{1.29}$$

This concept varies from the idea of Amontons due to nonlinear frictional relationship. Bowden and Tabor assumed the load among two shearing surfaces associates the actual contact area.

It has been shown that by using FFM in various conditions, several studies have investigated the micrometer and nanometer-scale measurement of friction-load associations. It was further noted that SAMs and polymer brushes had been used to provide a beneficial method for modifying substrates and producing various surfaces with various functional groups. Indeed, there have been indications of both linear and sublinear relationships between friction and load. Leggett et al. described the combined SAMs of methyl, and carboxylic acid samples terminated thiols. They observed an excellent fit of friction data to the law of Amonton, and a defined correlation among surface composition and energies [65]. These techniques were based on the theories at the macroscopic level for understanding friction at mechanical contact between multiple asperities. Nevertheless, sublinear friction-load relationships were also found for singly contacted asperities, and were designed via HRTZ, JKR, and DMT (a single asperity contact mechanics technique). For example, the JKR model may seem likely in circumstances where there can be strong adhesion among tip-surfaces. Also, the friction between two moving surfaces could be equivalent to the contact area based on the study of Tahor, and from the JKR is given by (1.30):

$$F_F \, \alpha \, \pi \left(\frac{R}{K}\right)^{2/3} \left(F_N + 6\pi\gamma R + \sqrt{12\pi\gamma RF + (6\pi\gamma R)^2} \right)^{2/3} \tag{1.30}$$

It is evident that the JKR model has been commonly applied to inorganic materials in the measurement of FFM, but it has been less broadly used on the molecular materials. However, the Amontons law has been used even more extensively for polymers and organic monolayers.

Recently, there has been a precious contribution from Gao et al. on this topic [66], who published some realistic friction findings on numerous samples (i.e., adhesives and non-adhesives) obtained from the SFA and FFM surface force instruments. They concluded that linear friction versus load plot is natural in cases of existing non-adhesive sliding, and non-linearity is a different condition only when there is a strong adhesive effect between two slides. This theory is supported by recent studies from the author's laboratory. Leggatt and co-workers have measured the friction force for poly (ethylene terephthalate) (PET) in two different mediums (perfluorodecalin and ethanol) [58]. They found that measurement in perfluorodecalin, a liquid with depressed dielectric constant, which produces excellent adhesion on tip and sample, fits the JKR model behavior. However, studies in ethanol, a liquid having a large dielectric constant, create linear friction versus load correlation according to the Amontons law. This scenario explains the presence of linear friction versus load correlation, provided that ethanol is commonly used as a medium for FFM measurements. A number of researchers found that the environment strongly supports determining suitable contact mechanics [15], [67]. The relation between friction-load changes based on the type of interactions (e.g., the tendency to donate or accept a hydrogen bond between substrate adsorbents and liquid molecules). Commonly, with rising adhesion the relation among friction and load becomes sublinear. It is worth pointing out that the results could be interpreted by considering friction as the total of adding both a load-dependent term (molecular ploughing) measured by a coefficient of friction and a shear-dependent term determined by shear strength, as seen in (1.31):

$$F_F = \mu(F_N + F_a) + \pi \left(\frac{R}{K}\right)^{2/3} \tau (F_N + F_a)^{2/3} \quad \textbf{(1.31)}$$

where μ is the frictional coefficient, F_N is the force normal to the surface (load), Fa is the pull-off force, R is the tip radius, K is the modulus of elasticity. In contrast, the shear strength becomes negligible for low adhesion systems. Linear friction load is superior in which energy dissipation occurs via molecular ploughing. The results will be perfectly governed by the Amonton law the equation (shown in (1.32)) converts to:

$$F_F = \mu(F_N + F_a) \quad \textbf{(1.32)}$$

1.8 Calibration of Forces

1.8.1 Normal Forces

Owing to the different physical properties of various cantilevers and the reason that signal is registered in volt from the photodetector, it is vital to calibrate these variables in quantitative analyses. Calibration of Normal force can be achieved by determining the sensitivity deflection and then normal spring constant. Hooke's law shows how the cantilever diffractions depend on force F, as shown in (1.33):

$$F = -kx \tag{1.33}$$

Even though manufacturers give the spring constant for the probes, they are likely to be inaccurate [68], [69]. The spring constant is affected by many factors such as the cantilever geometry, Young's modulus, and tip mass. In the literature, several different cantilever calibration methods have been published. For example, one approach based on the assembly of a recognized mass to the cantilever and calculation of the shift in resonance frequency [70], analysis on the deflection of cantilever in contact with second, standard reference cantilever [71], determination of k from cantilever oscillation observations attributable to thermal noise [72], [73]. Hutter and Bechhoeffer developed the last approach in 1993. It has been commonly used as it provides a range of benefits. This method's implementation is relatively straightforward, not entirely reliant on the shape and chemical composition of the cantilever [72]. Also, Matei *et al.* reported that this procedure is between 5 and 10 percent accurate [74].

To calibrate the normal force, the response of the photodetector (voltage) must be calibrated first. Distance units are used to interpret the voltage magnitude from photodetector so that deflection could be quantified. It uses a transformation factor, deflection sensitivity, which refers to the photodetector response to z-piezo displacement. This factor is obtained using a force curve when approaching the tip against a hard sample (mica, for example) [42]. All deformation occurs at the cantilever if it has relatively lower stiffness compared to the sample. Subsequently, the deflection cantilever can be considered to equate the distance in which the z-piezo moved, hence the registered photodetector voltage correlates linearly with the cantilever deflection. This linear relation could be derived in the repulsive regime from the slope of the force V / nm (see Figure 1.5).

After determining deflection sensitivity, the spring constant for the normal force (kN) must be determined. The Normal Force is then given by (1.34):

$$F_N = -k_N \Delta z \quad \textbf{(1.34)}$$

The calculation of normal, as well as spring constant for forces at the lateral direction, are provided respectively by $k_N = Ewd^3/4l^3$ and $k = Gwd^3/3h^2l$; in which d, w, and l are the thickness, width, and length of the cantilever, h is the height of the tip and E and G are the Young modulus and shear modulus of the components from where the cantilever is made [75]. Experimentally the method of thermal fluctuation is perfect, a harmonic oscillator with Hamiltonian influence is used in the estimation of the cantilever. It includes both terms for kinetic and potential energies in the equation. According to the theory of equipartition, thermal energy (k_BT) is equally divided between the two terms of the Hamiltonian cantilever, and hence the potential energy could be described in (1.35):

$$\langle \frac{1}{2} kx^2 \rangle = \frac{1}{2} k_B T \quad \textbf{(1.35)}$$

where T is the temperature (absolute), kB is the Boltzmann constant, k is the spring constant for forces normal to the cantilever, and x is the cantilever displacement. a reordering of the equation will result to (1.36):

$$k = \frac{k_B T}{\langle x^2 \rangle} \quad \textbf{(1.36)}$$

A correction factor X is required due to sources of error exist [72]. The photodetector signal voltage fluctuations are registered during the time and transformed by a Fourier transform into the frequency domain, presenting a power spectrum, a frequency-to-power spectral density (PSD) relationship, the last one describing the spectral energy distribution within time units. According to Parseval's hypothesis, which defines the form of Fourier transforms,[76] the first form integral, P, is equivalent to the deflection over the time domain$\langle x^2 \rangle$. Thus, the spring constant can be determined from the PSD integral at the cantilever oscillation frequency, as seen in (1.37):

$$k = \frac{k_B T}{p} \tag{1.37}$$

Many of the assumptions made are often not entirely accurate, but a cantilever shape-based correction factor is required. It is noteworthy that an element of 0.972 is provided for tipless force-calibration cantilevers [74], In contrast, Stark *et al.* found the value closer to 0.963 for V-shaped cantilevers [77](while more current experiments have shown that it ranges between 0.93 – 0.99 [78]). In practical application, most advanced AFM controller software enables the cantilever spring constant to be quickly and effortlessly determined, combining several of the corrections and allowing users to change parameters as necessary.

To achieve the calibration process for cantilevers in Atomic Force Microscopy (AFM) experimentally, two key steps are required to ensure accurate measurements:

The first step is to determine the deflection sensitivity, measured in nanometers per volt (nm/V). This value is essential for converting the voltage signal from the AFM detector into a physical deflection measurement. To determine this sensitivity, the slope of the linear section in the force curve is examined, specifically in the repulsive regime where the cantilever contacts the surface (Figure 1.5). For this calibration, a flat mica surface is used due to its smoothness and uniformity, making it ideal for accurate measurements.

The next step is to determine the spring constant of the cantilever, which reflects its stiffness and is vital for understanding its mechanical response during experiments. This is achieved by analyzing the thermal fluctuations of the cantilever. By examining its power spectral density, the spring constant value can be extracted. This analysis is performed at room temperature using the advanced MultiMode VIII AFM.

These steps are critical for accurate force measurements in AFM, ensuring that the cantilever's response is well-characterized and reliable for subsequent experimental analysis.

1.8.2 Lateral Forces

It is necessary that as with normal forces, the lateral photodetector signal in volts requires a conversion factor to provide friction force in newtons. The calibration factor at lateral direction α_c (N / V) is often special for each cantilever being used and influenced by the shape and stiffness of the cantilever. A multiplicity of different lateral stiffness calibration techniques

has existed [79]. However, the wedge calibration approach is the most utilized in multiple studies since its emergence. It was preferred mainly because of its relative ease of implementation, as it does not demand detailed tip geometry information [80]. However, it is worth noting that although the model expects a linear friction-load relationship, this is not necessarily expressed in reality [15], [81], [82], and is thus a possible cause of the systematic error. Initially designed by Ogletree et al.,[83] and enhanced by Varenberg et al. [84] for experimental process streaming, topographical properties are necessary for obtaining α_c for the model calibration method. Friction loops are obtained over flat and angled areas of the surface via commercial silicon test TGF11, in which the slope exactly is known (54.7°), between the flat 100 and 111(Figure 1.16). While the cantilever is transferred laterally across the test grating surface, the quantified horizontal torsion is reliant on the surface slope and travel direction, leading to the force curve (Figure 1.17).

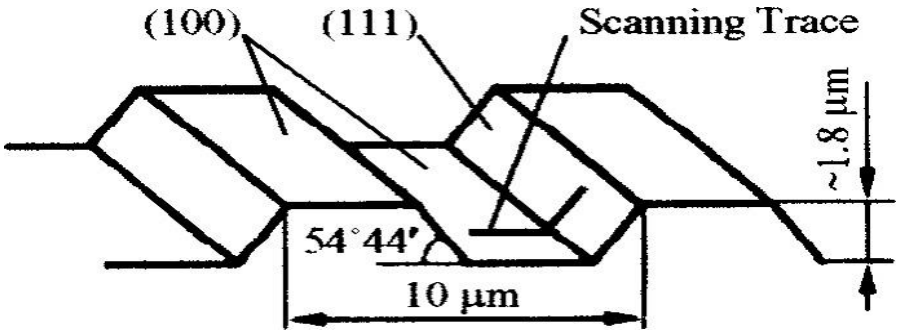

Figure 1.16: Shows the calibration diagram TGF11, the pich valuation is 10 µm, step height is 1.8 µm, and the edge angle is 54.44 [85]**.**

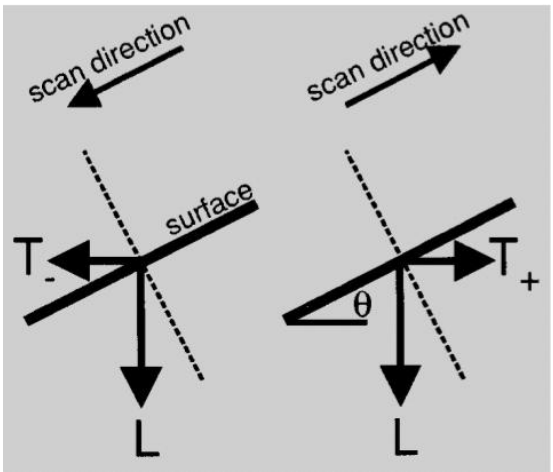

Figure 1.17:Shows forces as the tip moves over a sliding surface [85]**.**

From this data, the adjustments made by Varenberg et al. [84] offer the opportunity to modify the inaccurate recorded sloped torsion offset $\Delta_{\circ}^{\bullet}$ by deleting the corresponding recorded torsion offset from the flat section $\Delta_{\circ}^{flat}$, as seen in (1.38):

$$\Delta \circ = \Delta_{\circ}^{\bullet} - \Delta_{\circ}^{flat} \tag{1.38}$$

where $\Delta \circ$ is the modified torsion loop. Then, using half-width of the torsion loop ($W_{\circ}$), and the surface adhesion (A) achieved from force spectroscopy, the calibration factor at lateral direction will be determined by (1.39):

$$\alpha_c = \frac{\mu(L + A\cos\theta)}{W_0(\cos^2\theta - \mu^2\sin^2\theta)} \tag{1.39}$$

where θ= 54.7° and μ is the friction coefficient of the sloped area.

To achieves the calibration process experimentally, the wedge calibration method is utilized to determine the lateral stiffness of the cantilever. In this approach, the cantilever moves across a silicon grating (TGF11), which is commercially available from MikroMasch, Tallinn, Estonia. As the cantilever travels across the grating, friction signals are recorded under different applied loads. To ensure accurate measurements, the lateral force calibration is conducted separately for each solution used in the experiments.

1.9 Self-Assembled Monolayers (SAMs)

Numerous fabrication methods have utilized self-assembled monolayers (SAMs) for the fabrication of micro- and nanomaterials [86], [87]. SAM molecules have a particular and robust affinity head group for material making up the substrate, functional groups at a terminal position located outside the substrate, and alkyl chain connecting between terminal functional and head groups (Figure 1.18). Head groups binding different substrates vary, including the metals, oxides of metals, and semiconductors [86], [88]. Alkanethiols are widely utilized on gold, palladium, silver, and platinum to fabricate SAMs [89], [90]. Besides, alkyl siloxanes were extensively used to produce SAMs on a variety of substrates, such as glass, silicon oxide, titanium oxides, and aluminum oxides [86], [88]. It is worth pointing out that the chain length may have a noticeable influence on multiple interfacial properties [33], [91].

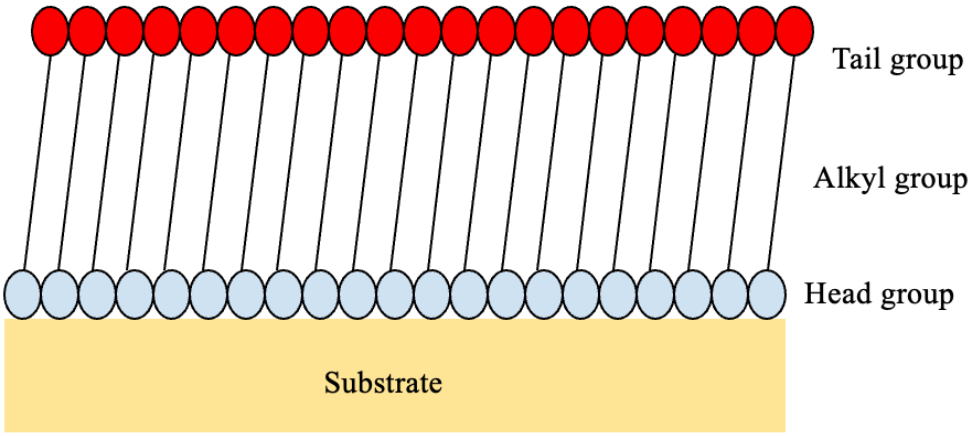

Figure 1.18: Schematic showing essential SAMs film components

The SAMs field has indeed been established when Nuzzo and Allara reported the formulation of SAMs of alkane thiolates on gold from an aqueous solution of di-n-alkyl disulfides in 1983 [92]. It is noticeable that SAMs' features have provided an effective instrument in surface investigations [88]. They are often utilized as model structures for a variety of purposes, such as enhancement of the surface [93] and treatment of biocompatible materials [94], [95]. Additionally, SAMs as model surfaces can be used to study the influence of intermolecular forces and forces at the interface in natural phenomena, including adhesion and wetting. Interestingly, they can also be aligned on scales of both micrometer and nanometer, [96], [97] making them attractive for further modifications.

1.9.1 SAMs of thiols

Mica, glass, and silicon wafers seem to be the most widely recognized planar substrates utilized to assist thin metal films for alkanethiol SAMs, such as gold copper silver palladium, platinum, and nickel [90], [98], [99], [100], [101]. These surfaces can be designed using several techniques, such either Vapour deposition or electrodeposition [88], [102]. Some nanometers of either a titanium, chromium, or nickel adhesion layer is deposited and then followed by a metal layer of interest. The adhesion layer metallic is significant for various metals that could hardly form oxide compounds (e.g., gold) [88].

Monolayer production via alkanethiols or dialkyl disulfides adsorption onto gold has been examined extensively, [86], [88], [90], [98]. The thiol is often transformed into gold thiol in a reduction of hydrogen elimination (1.40) [86]:

$$R - S - H + {Au_n}^0 \rightarrow RS^- Au \cdot {Au_n}^0 + \frac{1}{2} H_2 \quad \textbf{(1.40)}$$

Even though the final monolayer quality depends on various factors, including the solvent environment [103] and the cleanliness of the surface, it is entirely unaffected by other conditions (i.e., concentration and temperature). Considering this, monolayers of thiol continue to be susceptible to light. In the presence of oxygen, these are vulnerable to photooxidation [104] Thus, it must be stored in a dark atmosphere for 48 hours, which is free of oxygen.

1.9.2 SAMs of silanes

Silane SAMs are typically applied in altering the characteristics of different oxide surfaces (i.e., glass or mica) [86], [105], [106]. Alkylsilane is an organosilane subset which has a generic chemical structure of R-Si-R' where R is an alkyl chain and R' could be OMe (–trimethoxysilane), OEt (–triethoxysilane), Cl (–trichlorosilane), or others. Although the detailed formation mechanism for the monolayers of silane was the topic of debate, [107] the entire mechanism for oxide substrates is typically approved. The involvement of water in forming silane SAMs has been extensively studied. It has been observed that higher surface hydration could lead to more excellent quality monolayers [108], [109]. Water, whether in solution or on the surface,[110] helps to hydrolyze the head groups to silanol ($R\text{-}Si\text{-}O_3^{(3-)}$). The activated head groups are then partly cross-linked to build smaller molecular clusters linked by Si-O-Si bonds. Hence, these aggregates interact with the surface of the silanol groups, covalently binding to it and forming smaller islands. This process will continue once entire surface treatment is achieved (see Figure 1.19). Regardless, every head group is capable of linking chemically onto the surface.

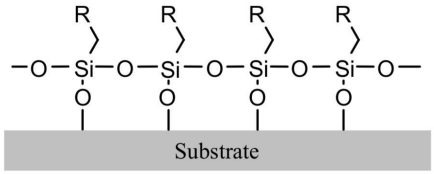

Figure 1.19: Crosslinking of SAMs in silane.

It should be noted that because of the formation mechanism, self-assembled monolayers of silane appear to have much-compromised quality (i.e., relatively low order) compared to their thiol counterparts. Nevertheless, they show more excellent stability (i.e., mechanical and thermal) than the monolayer form mentioned above because of their strong connections to the surface and the cross-linking of neighboring molecules. Also, during their formation, they are often more sensitive to the environmental factors, as such, higher care is needed to select a suitable solvent, temperature, concentration, and time of formation[111], [112], [113], [114].

1.10 Polymer brushes

There are many different types of surface-grafted polymer films, each with unique characteristics and applications. Specifically, brushes, refer to a particular kind of grafted-polymer films in which shear forces or repulsive forces cause the grafted polymer to stretch away from the surface, creating a highly extended, brush-like structure[115], [116]. When the grafted density is low, however, collapsed (mushroom) or beancake morphologies result, where the chains adopt a more compact configuration close to the surface. The stability and formation of polymer brushes is governed by elastic energy and entropic effects that play the key role in determining the conformation and behaviour of the system. Steric hindrance causes the polymer chains to extend themselves when they are densely grafted to a surface, which increases the elastic free energy because of the entropy penalty that comes with departing from the coiled state that the chains would otherwise prefer to adopt. This stretching produces a repulsive force that is part of the energy balance of the system as well. At the same time, entropy plays the key role in the stabilization of the brush. Free polymer chains are randomly coil in configuration in solution to achieve maximum entropy. However, in polymer brushes, the stretching of chains reduces their entropy. To counter this entropy loss, chain swelling and brush stabilization is favoured by favourable polymer solvent interactions in a good solvent. In a poor solvent however, polymer interactions are dominant and cause the brush to collapse through phase separation. The structure and behaviour of polymer brushes is therefore determined by elastic energy and entropy.

It is apparent that owing to their possible uses in material science and nanotechnology, and there was a growing interest in polymer brushes. It has been shown that brush formation involves two main techniques which are “grafting from” and “grafting to”. During grafting from, there is a growth of polymer molecules taking place on a surface originating from initially immobilized initiator sites. This method is especially useful, as it can regulate the growth

density of the polymers by controlling the density of the initiator positions. It could also provide a versatile, flexible, and controllable technique to form high-density polymer brushes. Other applications use approximately all available polymerization methods, such as surface-initiated atom transfers radical polymerization (SI-ATRP) [117], reversible addition-fragmentation chain transfer (RAFT) [118].

In contrast, polymer molecules that are pre-synthesized are positioned on the surface in the 'grafting-to' technique. Grafting techniques have shown various disadvantages despite its notable success, especially in the polymer chain's useful characterization prior to the primary process. Such is low grafting density since the initially attached molecule and the approaching macromolecule are sterically hindered, resulting in surface stability reduction [119].

It is worth pointing out Matyjaszewski et al. first reported ATRB, which is recognized as a highly potent method for controlled radical polymerization (CRP) approaches[120], [121]. It enables the scientist to design a substance with several detailed formulations, structures, and molecular configurability. ATRP includes the transformation of free radicals from alkyl halide to the monomer with a very constant value of K_act activation and K_deactdeactivated to actively growing polymers [122] (Scheme 1.1). This system must be controlled to prevent a termination reaction. The rapid transfer of initiators facilitates the uniform distribution of all polymer chains, maintains a constant growth of polymer chains, and is equivalent to the original initiator concentration. The exchange occurs in ATRP between the active and the inactive system changes depending on the catalyst [122], [123]. ATRP generally occurs effectively under particular conditions, such as monomer selection, concentration, temperature, and catalyst [122], [123]. The catalyst is the most significant aspect of an ATRP system since it specifies the location of the equilibrium of the transition of an atom (i.e., the exchange among the inactive and the active species) [124]. Several considerations should be recognized when selecting the catalyst. There must be at least two available oxidation numbers divided by an electron for the transition metal. Bonds between both the halogen atoms and the center of metals should also be constructed. The coordination spheres across the metal center should be extensible upon oxidation to accommodate the halogen atom [122], [125]. Several of the transition metal complexes that are used as catalysts for ATRP including Mo, Zr, Cu, Rf, Ru, Ni,Hf, Re, Pd, Co,Fe, Rn Ti, and Os [125], [126], [127]. There are indeed some examples of monomers that have already been polymerized efficiently and effectively utilizing ATRP such as styrenes, methacrylates, acrylonitrile, acrylates, vinyl pyridine, and acrylamides

(Matyjaszewski and Xia, 2001). Additionally, for their active and inactive species, every monomer has a different equilibrium atom transfer constant. The amount of equilibrium constant ($K_{eq} = K_{act} / K_{deact}$) influences the quantity of polymerization. As a result of this, polymerization will not occur or occur much more slowly, at a minute Keq value, while the rate will increase with the Keq value increasing.

Matyjaszewski et al. have designed the Electron Transfer Regenerated Activator (ARGET) as well as the Continuous Activator Regeneration Initiators (ICAR) 1. These methods minimize catalyst concentration at parts per million (PPM) rates, decreasing material and post-processing costs, and can significantly simplify the separation and processing of catalysts, making the ATRP technique industrially interesting [128]. In ARGET ATRP, there is an addition of an excessive quantity of reducing agent through both initial polymerization and converting deactivator, which has produced because of radical termination that returns to the activating species. There are already some appropriately used reducing agents, such as glucose, hydrazine, ascorbic acid, tertiary amines, and phenol [129]. Nevertheless, the ligand should be supplied at 3 to 10 times molar excess so that polymerization could be controlled, which has been identified as one of the downsides of the electron transfer-generated activator. The excessive ligand allows the catalyst to remain stable and prevents it from a destabilizing side reaction, as seen in Scheme 1[128]. Wang et al, (2012) [130] investigated alcohol as a useful reduction agent for $CuBr_2$ / bipyridyl because of its stability. ICAR ATRP used a minimal quantity of radical initiators that are thermal-free for copper (II) to copper (I) activator reduction.

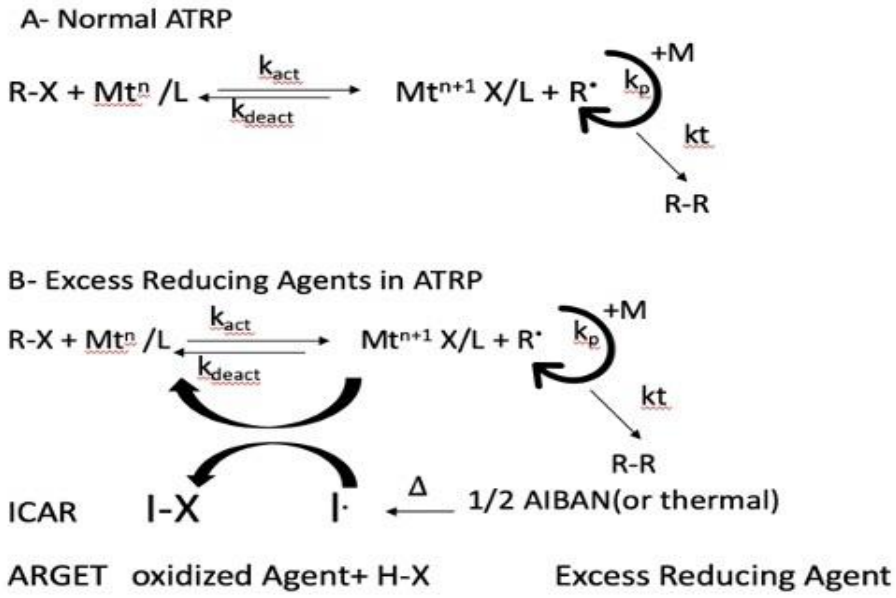

Scheme 1.1: Mechanism suggested for the ATRP methods according to Matyjaszewski et al, (2006).

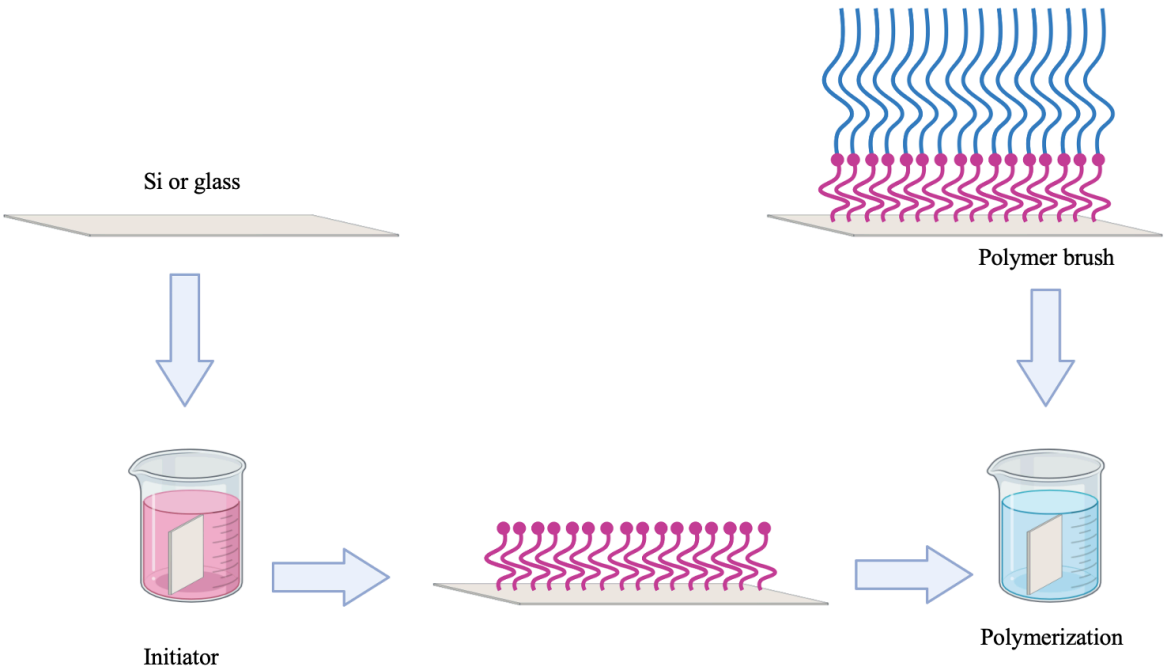

Scheme 1.2: The process of grafting Polymerization.

1.10.1 Stimulus-responsive brushes

Several studies have stated that polymers' stimulus-responsive behaviour in different conditions makes them particularly attractive for nanotechnology. Solvents, temperature, pH, and light are typically called stimuli that alter their physical characteristics by affecting polymer conformation [131].

1.10.1.1 pH responsive

There are two main types of pH or ion responsive polymers, strong polyelectrolyte brushes (strong acid or base, for example) or weak polyelectrolyte (such as weak acid or base) [132], [133], [134]. The pH or ion strength difference does not influence the number of charges in a strong polyelectrolyte brush; therefore, the brush charge density remains fixed [132], [133].

In contrast, the brushes are more susceptible to changes with both pH and ionic strength in a weak polyelectrolyte [132], [135]. A polymer with weakly basic groups, for example, starts to swell at low pH owing to the repulsive interaction among charged groups [136], [137]. However, due to the reduction in the electrostatic interaction between the polyelectrolyte brushes [132], [136], [138], a polymer composed of weak acidic groups collapses at low pH values.

1.10.1.2 Solvent-responsive polymer brushes

The polymer chain structure varies depending on the solvent condition. For instance, polymer brushes tend to expand in a suitable solvent so that polymer-solvent interactions could be increased; whereas its chains disintegrates into an environment with weak solvent to reduce the polymer and solvent interactions [132]. Polymer brushes that are responsive to solvent depend entirely on each component's quality in copolymer brushes; for example, a suitable solvent for a co-monomer may be ineffective towards monomer of different kinds. However, in a homopolymer, the response to the change depends on the polymer chains' grafting density. For instance, the response of low-grafting density (mushroom regime) grafting chains is small in comparison to that of the bulky polymer solution [131], [132]. In contrast, the brush forms a thinner homogeneous layer in a poor solvent than being in a suitable solvent with high grafting densities, and the collapsing becomes weak because there is no space available for conformational adjustment in the highly stretched polymer chains, owing to the very crowded surface of the polymer chains [131].

1.11 Patterned SAMs and Polymer Brushes

In many areas, the capability of nanoscale monitoring of structure will present novel opportunities to various applications (e.g., molecular electronics, medical, catalytic reactions) [139]. Nanoscale structures can be created from a wide range of techniques. These can usually be categorized under two major headings [140], [141]. Top-down methods include materials being physically changed to implement spatial organization [141], [142]. Lithographic techniques in this field are being used to pattern surfaces [141], [142]. Bottom-up approaches, on the other hand, are derived from the chemical modifications to combine atoms and molecules to produce highly structured ones [140], [143].

1.11.1 Photolithography

The fundamental concept of photolithographic procedures is introducing a surface to electromagnetic radiation so that the molecular structure of substrates could be modified [144]. Photolithography systems are typically used for patterning surfaces in industries. Numerous researchers focused on improving photolithographic techniques to obtain structural resolution under 100 nm [141]. Various patterns in photolithography are acquired by irradiating the substrate with a mask [144]. Photolithography is an effective patterning strategy for flat structures of large areas with excellent conformity, regulated topography, and a wide variety of forms. Photolithography, however, is insufficient for samples with surface irregularities (e.g., curved) [145]. The photolithographic accuracy improves as the wavelength of light used during exposure is decreased [143]. Two primary issues arise when using photolithography for polymer patterning: (1) identifying a process that is cost effective with a high resolution and (2) avoiding destructive patterning, especially for functionalized polymers. A major issue is that direct photoirradiation can lead to polymer degradation, especially in π-conjugated polymers, which have reactive side chains that make them sensitive to photochemical damage. This degradation can significantly affect the electronic properties of the material, which is impractical for organic electronics and flexible displays. In general, photolithography, photoresists, such as PMMA, photochemically react to UV light[146]. In positive resists the polymer is degraded by the exposure while in negative resists the areas to be exposed are made more resistant to solvents by cross linking. However, when using π-conjugated polymers like poly(3-hexylthiophene) P3HT, the exposure to UV light can break the conjugated system, leading to a decrease in electrical conductivity[147]. Alternative patterning techniques, such as

soft lithography or nanoimprint lithography, are investigated to avoid direct photodegradation and maintain the material's functionality.

1.11.2 Micro-scale UV lithography

UV lithography is efficient for a micron-scale modification of sample surfaces. Masking via photoresist is placed on the substrate consisting of monolayers of the polymer during the macromolecule modification, the irradiated with light afterward. A photoresist is a light sensitive material employed in photolithography and other patterning processes for imprinting a geometric pattern on a substrate. It is often an organic polymer that changes chemically when exposed to ultraviolet (UV) radiation, allowing for selective etching or deposition. Upon exposure, resistance with a positive tone is diminished; whereas, those that have negative tones are crosslinked instead (Figure 1.20) [148]. For instance, the photolithography technique has been used to adjust nitro group SAMs to obtain amines that were eventually bonded mostly with acid anhydrides [141].

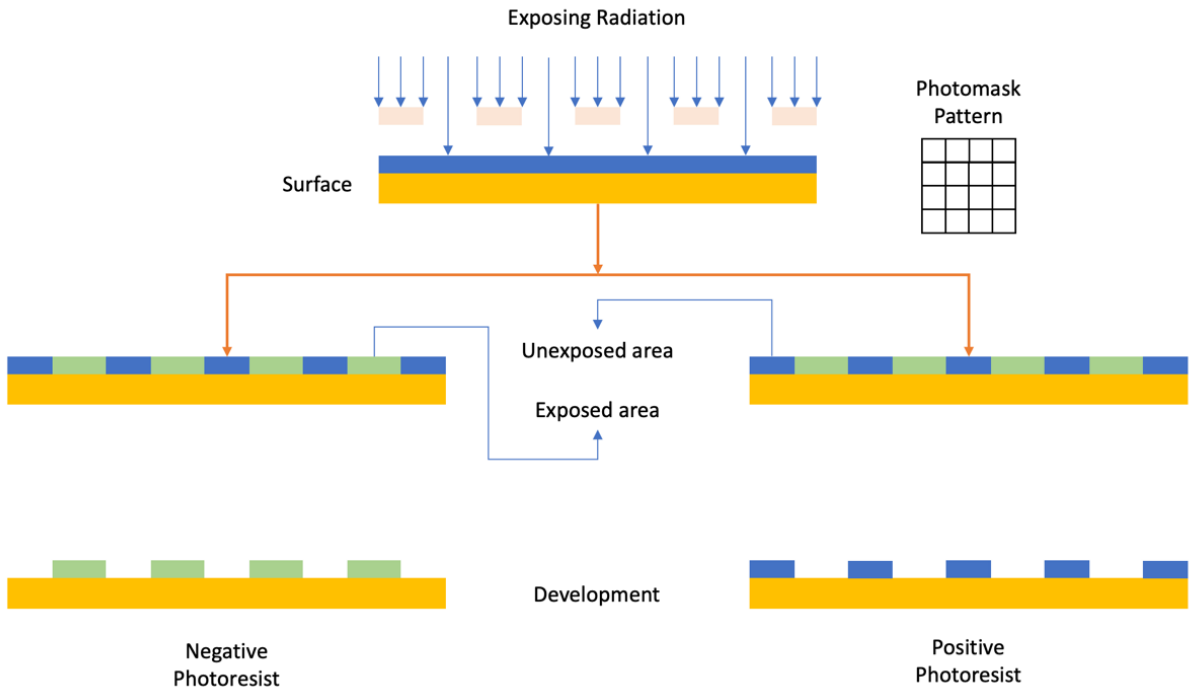

Figure 1.20: Chart demonstrating the photolithography process using a mask.

Also, Leggett et al. reported that oxidation of SAMs of thiolates on a gold-based structure to weakly bound sulfonates occurs upon exposure to UV light [149]. Furthermore, samples are patterned via mask exposure; oxidizing species are further removed from the sample by

subjecting it to a contrasting alkanethiol-containing solution. Then, the conversions were confirmed with the use of friction force microscopy (FFM). They also investigated N-NPPOC 3-aminopropyltriethoxysilane photoprotection using 325 and 364 nm UV light [148]. Micropatterning was obtained by presenting the sample through a mask to UV light, leading to the amine-functionalized surface production.

UV irradiation was found out to be effective in the generation of brushes of patterned polymers after using various methods. One strategy is to pattern the substrate-bound initiator, and then allow the polymer to grow. This means that utilizing UV light, functionalized surfaces with ATRP initiator can be patterned to replace the initiator so that the whole polymer brush only grows out of the masked places. Kamitani et al. observed that UV irradiation can also be utilized in the design of (3-Aminopropyltriethoxysilane) (Self-Assembled Monolayers) APTES SAMs; therefore, the unexposed areas (remaining surface amino groups) may be changed to generate ATRP initiators [150]. Finally, the polymer brush was developed from immobilized initiators to establish carbohydrate arrays. A wavelength of 244 nm for the UV light has been utilized to remove the active halogens from the silicon dioxide films of 3-(2-Bromo isobutyramide) propyl-triethoxysilane chloromethyl phenyl trichlorosilane [151]. Micropatterning was completed by irradiating the organic films across a mask, which includes the use of SI-ATRP in the production of micro-structured brushes. POEGMA brushes were grown from unaffected halogenated regions. The UV light (at 244 nm wavelength) has been used by exposing the film across a photomask to pattern the polymer brush at a micrometer scale. Also, Zhou et al. have been using this technique to pattern brushes of PMMA by UV light exposure of samples via a mask[152].

1.12 Aim

The aim of this project is to investigate the frictional and adhesive interactions between AFM probes and PDMA and PAGEO5MA brushes at different grafting density. It can be discovered how the association constant for hydrogen bond-forming complexes are influenced by changes to the composition of the medium in which they interact by modelling tip-sample interactions in sliding contacts. This opens the way to a new, quantitative method for analysis at the nanoscale. This project investigated nanomechanics properties include polymer brush systems, where the interactions are made more complex by the deformability of the polymer chains.

An important consideration in choosing to work with PDMA and PAGEO5MA brushes is their distinct physicochemical properties, which influence their behaviour and applications in various environments. PDMA is a tertiary amine-containing, stimuli-responsive, polybasic polymer that exhibits a range of conformational states depending on solvent environment and pH. In water and polar solvents, PDMA adopts a hydrated, extended conformation due to favourable polymer-solvent interactions, while in less polar or organic solvents, it collapses due to reduced solubility and weaker hydrogen bonding. Its dual responsiveness to both pH and solvent environment allows customizing surface properties, making it particularly valuable in drug delivery, biointerfaces, and switchable coatings, where environmental changes cause conformational shifts. Furthermore, PAGEO5MA a novel acrylic polymer with aldehyde-functional bonded groups, it can be readily functionalized by reaction with a wide variety of amines, enabling further modification for specific biomedical and material applications. This polymer is particularly useful in biosensors, biomedical coatings, and controlled drug delivery systems, where surface hydration and resistance to non-specific interactions are essential. Additionally, its adjustable brush architecture allows for accurate control over surface properties, making it a valuable material for designing adaptable and responsive biointerfaces.

Chapter 3 and 4 describe fabrication of PDMA micro- and nanostructures and analysis of their behaviour in relation to feature size.

Chapter 5 analysis the behaviour of PAGEOMA and based on grafting density in various environments.

CHAPTER 2 EXPERIMENTAL

2.1 Materials

Silicon wafer with a (100) orientation, test grade, thickness 380 nm, were obtained from Compart Technology (Peterborough, UK) and PI-KEM (Tamworth, UK). 1000-2000 mesh copper electron microscope grids for micrometre-scale patterning were obtained from Sigma-Aldrich (Gillingham, UK). α-Bromoisobutyryl bromide (BIBB) (98%), paraformaldehyde (>95%), (3-aminopropyl) triethoxysilane (APTES) (≥99%), benzoyl bromide (BB) (98%), triethylamine (≥99%), 3-(trimethylsilyl) propyl isocyanate (95%), benzyltrimethylammonium, known as Triton B, with a concentration of 40 wt. % in methanol, (>99%), and potassium dihydrogenphosphate with a purity of over (99%) were acquired from Sigma-Aldrich (Gillingham, UK (Gillingham, UK). Hydrochloric acid (>30%), sulfuric acid (≥95%), hydrogen peroxide (30% v/v), toluene (HPLC grade), ammonia solution (s.g. 35%), ethyl acetate (HPLC grade), dichloromethane (DCM, HPLC grade), ethanol (HPLC grade), methanol (HPLC grade), diethyl ether (HPLC grade) and hexane (HPLC grade) were obtained from Fisher Scientific (Loughborough, UK). Dry toluene was acquired from an onsite Grubbs dry solvent system. Deionized water with a resistivity of 15 MΩ cm was obtained from an Elga PURELAB system. High-performance liquid chromatography (HPLC) grade dimethylformamide (DMF) and tetrahydrofuran (THF) and basic alumina were sourced from Fisher Scientific (Loughborough, UK). 1,1,4,7,10,10-hexamethyl- triethylenetetramine (HMTETA, 97%), 2-(dimethylamino) ethyl methacrylate (DMA, 98%) and Copper(I) bromide (>99%) were obtained from Sigma-Aldrich (Gillingham, UK).

GEO5MA monomer was produced at GEO Specialty Chemicals (Hythe, UK) by Dr. C. Jesson and was employed in its as-synthesized state without additional purification processes. Copper (II) chloride ($CuCl_2$; purity: 99%) was procured from Acros Organics (UK). 1-Pyrenemethylamine hydrochloride (95%), sodium periodate ($NaIO_4$; >99%), sodium cyanoborohydride ($NaCNBH_3$; 95%),1,4 dioxane and 2,2,2-trifluoroethylamine (TFEA; 99.5%) were all acquired from Sigma-Aldrich (UK). N, N, N′,N″,N″-pentamethyldiethylenetriamine (PMDETA; 98%) and tetrahydrofuran (THF) were supplied by Fisher Scientific (UK).All chemicals employed in the experiments were of analytical reagent grade and utilized in their original state without further purification. Prior to use, Copper(I) bromide underwent storage under vacuum conditions to ensure its stability and

integrity. This precautionary measure was implemented to minimize any potential degradation or contamination that could affect experimental outcome.

2.2 Cleaning Glassware and Substrates

The glassware and substrates were initially washed with acetone and water and then dried. Substrates were separately placed into sample tubes. To further eliminate contamination, all glassware and substrates were also washed with ~~a~~ piranha solution,~~-~~a mixture of hydrogen peroxide (30 %) and sulfuric acid (70 %). Piranha solution is a strong oxidising agent and should be used with caution. A face shield and thick rubber gloves should be used in addition to following good chemical laboratory practice. Hydrogen peroxide was transferred first to the glassware and substrates; sulfuric acid is added afterwards. The glassware and samples were decided to leave in the solution until they became cool. The solution was thrown into a dilution tank. After that, the glassware and substrates were cleaned multiple times with deionized water and stored in a 120 ∘C oven.

2.3 Sample Handling

To ensure experimental integrity and prevent potential contamination, careful protocols were employed in sample handling and substrate preparation. In all cases, sanitized tweezers were utilized for sample collection, which involved sequential immersions in acetone and ethanol. This process effectively eliminated particles or residues that might compromise experimental outcomes. Subsequent drying of the tweezers with nitrogen gas ensured the removal of residual solvent traces, reducing the risk of introducing moisture onto the samples, which could negatively affect experimental accuracy.

Care was taken to ensure that samples were handled with careful~~-~~to prevent sample damage or contamination. Where necessary, samples were cut very carefully using a diamond scribe and metal ruler and rinsed with ethanol and dried under a stream of nitrogen to eliminate any remaining particles or contaminants. Glass substrates were divided into standardized 1 cm^2 sections to facilitate uniform treatment. Each section received thorough ethanol rinsing to eliminate surface impurities, followed by nitrogen gas drying to ensure substrate dryness, hence minimizing interference with subsequent experimental procedures~~.~~

2.4 Synthesis

2.4.1 Synthesis of 2-nitorphenypropyloxycarbonyl-3-aminopropyltriethoxysilane (NPPOC-APTES)

A previously described procedure was used to synthesize 2-Nitrophenylpropyloxycarbonyl-3-aminotriethoxysilane (NPPOC-APTES) [153]. There were two main steps in the synthesis (Scheme 2.1). The first stage was the synthesis of 2-(2-nitrophenyl) propan-1-ol. 2-Ethyl nitrobenzene (5400 μL, 40.0 mmol) was added to a 40% solution of benzyl trimethylammonium hydroxide (triton B) in methanol (7 g, 40.6 mmol). Paraformaldehyde (183 mg, 61 mmol) was added,-and the mixture was refluxed at 80°C for 24 h. On completion of the reaction, the solution was cooled, and solvents removed under reduced pressure. A solution of 1 M aqueous HCl was added to the mixture to adjust it to pH 7, after which the product was extracted three times with 60 mL of EtOAc each time. After filtering, the resulting solution was evaporated under reduced pressure to produce a brown oil, which was then dried using $MgSO_4$.

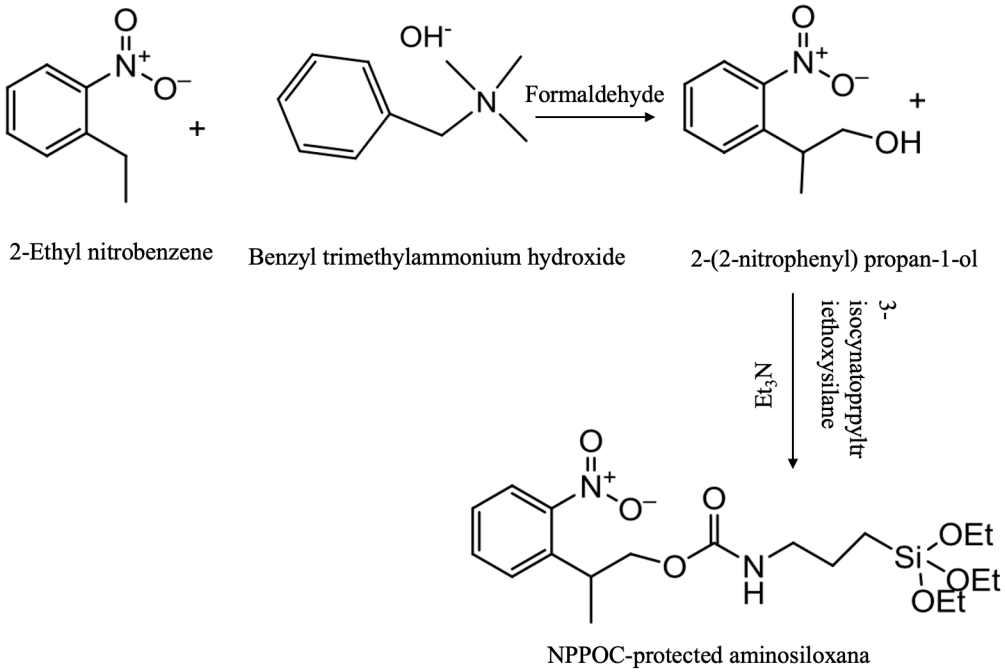

Scheme 2.1: The schematic illustrates the basic steps involved in the synthesis of APTES-NPPOC: synthesizing 2-(2-Nitrophenyl) propan-1-ol, which is then reacted with isocynatopropyltriethoxysilane to obtain NPPOC-APTES.

Purification of the brown oil was carried out using flash column chromatography (a 4:1 & 2:1 mixture of hexane and EtOAc) to obtain a deep orange oil (3.524 mg). ; R*f* 0.11(hexane/EtOAc 2:1); δH (400 MHz, $CDCl_3$) 1.34 (3H, d, *J* 7, CH_3CH), 1.70 (1H, s(br), OH), 3.52 (1H, m, CH_3CH), 3.81 (2H, m, $CHCH_2O$), 7.39 (1H, dd, *J* 8 and 8, 5-Ph), 7.50(1H, d, *J* 8, 3-Ph), 7.59 (1H, dd, *J* 8 and 8, 4-Ph), 7.76 (1H, d, *J* 8, 6-Ph)

In the second stage of the synthesis, a 2-nitrophenylpropyloxycarbonyl-3-aminopropyl troethoxysilane was prepared by adding 3518 mg (19.42 mmol) of 2-(2-nitrophenyl) propan-1-ol to 15 mL dichloromethane. To this solution, 5 mL (20.2 mmol) of 3-isocynatoprpyltriethoxysilane and (235µL, 1.7 mmol) of Et_3N were added and the mixture was refluxed for 24 h at 60ºC. On completion of the reaction, 0.1 M potassium buffer pH 7 was added to the mixture after it had been refluxed for 24 hours at 60°C, and the product was extracted three times with 20 mL of Et_2O. As a result of drying the separated. The organic layer

was separated with $MgSO_4$, and evaporating the solvent was removed under reduced pressure, the solvent was removed. A flash column chromatography method was used to purify the final product (yellow oil). As a protection against UV light and to prevent the final product from oxidizing, both flash column chromatography and evaporation were performed in a dark area. Rf 0.50 (hexanes/EtOAc, 1:1); ν_{max}(neat)/cm^{-1} 3337 (OCONH), 2971 (alkyl), 2928 (alkyl), 2881(alkyl), 1718 (OCONH), 1526 (NO_2), 1356 (NO2), 1074 (SiOEt), 954 (SiOEt); δH (300 MHz, $CDCl_3$) 0.59 (2H, t, *J* 8, CH_2Si), 1.21(9H, t, *J* 7, OCH_2CH_3), 1.34 (3H, d, *J* 7, CH_3CH), 1.58 (2H, tt, *J*7 and 8, $CH_2CH_2CH_2$), 3.12 (2H, td, *J* 7 and 6, $NHCH_2$), 3.70 (1H,m, CH_3CH), 3.81 (6H, q, *J* 7, $SiOCH_2$), 4.10 (1H, m, $CHCH_2O$), 4.23 (1H, m, $CHCH_2O$), 4.85 (1H, s(br), $CONHCH_2$), 7.36 (1H,dd, *J* 8 and 8, 5-Ph), 7.47 (1H, d, *J* 8, 3-Ph), 7.56 (1H, dd, *J* 8 and8, 4-Ph), 7.73 (1H, d, *J* 8, 6-Ph); δC (100 MHz, $CDCl_3$) 7.9 (CH_2Si),17.8 (CH_3CH), 18.7 (OCH_2CH_3), 23.6 ($CH_2CH_2CH_2$), 33.6(CH_3CH), 43.7 ($NHCH_2$), 58.8 (OCH_2CH_3), 68.9 ($CHCH_2O$), 124.4(6-Ph), 127.6 (5-Ph), 128.3 (3-Ph), 132.9 (4-Ph), 137.9 (2-Ph), 151.1(1-Ph), 156.5 (OCONH); m/z (ES+) 451 (100%, [M + Na]+); HRMS found 451.1875 [M + Na]+, requires 451.1871, δ 0.9 ppm.

2.4.2 Formation of NPPOC-APTES film

In a dry, clean Schlenk tube, a 2 cm × 3 cm slice of a clean silicon slide was placed. The tube was evacuated and refilled with dry nitrogen roughly three times, to eliminate any moisture present. Nitrogen was injected into Schlenk tubes and sealed with a septum. A solution of 1.0 mM NPPOC-APTES in dry toluene was supplied to a Schlenk tube, and then the tube was covered with foil to prevent any light. About 48 hours were required for the reaction to proceed under nitrogen. The physiosorbed surfactants were removed from the substrate by rinsing and sonicating it in a mixture of toluene and ethanol (1:1), followed by ethanol. The substrate was dried by blowing nitrogen gas over it. For annealing, the silane-coated film was positioned in an evacuated Schlenk tube fitted with a septum, wrapped in foil, and then placed in an oven for 30 min at 120°C. Once annealed, the sample was cleaned with ethanol and covered with aluminium foil before being stored in the dark.

2.5 Photolithography

Patterning of NPPOC-APTES films at the micrometre and nanometre scales was conducted using a Coherent Innova 300 C FreD frequency-doubled argon ion laser (Coherent UK, Ely, UK) with an emission wavelength of 244 nm. A laser power of 4.5 mW was used for

micrometre-scale patterning, a copper electron microscopy grid (1000-2000 mesh, Agar, Cambridge, UK) was used as a mask. Samples of NPPOC-APTES coated substrates were exposed at 244 nm at a dose of zero, 0.2, 0.5, 0.8, 1.0, 1.5, 2.0, 2.5 and 3.0 J cm^{-2}. The diameter of the region illuminated by the light source was accurately measured to be 0.5 cm^2, indicating the extent of the area effectively exposed to light or radiation during the experimental procedure. After photomodification, it is necessary to rinse the surfaces samples were rinsed with ethanol and dried under nitrogen to remove any residue from the photodeprotection process.

Interferometric lithography (IL) was performed using a Lloyd's mirror interferometer. A coherent beam from a uv laser was directed through a pinhole, with one half directed onto a mirror and the other onto the photoresist. The resulting interference between the reflected and direct beams on the substrate surface generated a sinusoidal intensity pattern, which was caused modification of the film. A laser power of 1.2mW was used. The rotation stage, responsible for orienting the mirror and sample at an angle of 2θ, facilitated the control of the angle between the two parallel beams. By varying the angle between the interfering beams, it was possible to change the pitch and full width at half maxiumu height (FWHM) of the resulting nanostructures. Patterns with periods of 690, 350nm were fabricated using angles of 10º and 25ø, respectively. Following exposure, the irradiated samples were thoroughly washed with ethanol and were subsequently dried using a stream of nitrogen to eliminate all photodegraded substances.

2.6 Functionalization of NPPOC-APTES films with by reaction with BIBB

Bromine initiators were introduced to deprotected NPPOC-APTES films by reaction with α-bromoisobutyryl bromide (BIBB). Initially, the patterned NPPOC-APTES substrates were subjected to derivatization, a critical process to enable further chemical modification. s Samples were placed in a solution comprising 2-bromoisobutyryl bromide (0.37 mL, 3 mmol) and triethylamine (0.41 mL, 4 mmol) dissolved in dichloromethane (DCM; 60 mL). The immersion time was carefully controlled and set at 40 minutes to ensure adequate reaction kinetics. Following derivatization, the samples were subjected to a thorough cleansing step to remove any residual reagents and byproducts. This cleansing process involved immersing the samples into sonication for 5 minutes in a solvent of DCM and ethanol. Finally, to eliminate

any remaining solvent and achieve complete dryness, the samples were dried under a gentle stream of nitrogen. This comprehensive preparation protocol ensured the substrates were suitably primed for subsequent polymerization reactions, thus facilitating the precise control and manipulation of surface chemistry and morphology.

2.7 Preparation of APTES films

To produce silane films formed by the adsorption of APTES, dry silicon wafers were immersed in 2% v/v APTES solution in ethanol for 5 minutes before use. After 60 minutes of reaction, the samples were sonicated for 5 minutes. Following the formation of the film, the wafers were washed with ethanol for a period of 5 to 10 minutes and then dried using nitrogen gas. An annealing step of 40 minutes was then performed on the samples in a vacuum oven (120°). To prepare for atom-transfer radical polymerization, the functionalized silane substrates underwent a process of derivatization. This involved immersing them in a solution containing 2-bromoisobutyryl bromide (0.37 ml, 3 mmol) and triethylamine (0.41 ml, 4 mmol) in 60 ml of dichloromethane (DCM) for 60 minutes. A final sonication in DCM and ethanol of 5 minutes followed by nitrogen drying was performed on the samples.

2.8 Preparing films with different initiator densities of BIBB using Benzoyl bromide

To facilitate atom-transfer radical polymerization with varying initiator density, the functionalized silane substrates were subjected to a process of derivatization. This procedure involved the preparation of two solutions. The first solution consisted of 2-bromoisobutyryl bromide (0.37 mL, 3 mmol) and triethylamine (0.41 mL, 4 mmol) dissolved in 60 mL of dichloromethane (DCM), which was allowed to react for 60 minutes. The second solution comprised Benzoyl bromide (0.37 mL, 3 mmol) and triethylamine (0.41 mL, 4 mmol) in 60 mL of DCM, also reacting for 60 minutes. Mixtures of BIBB and BB initiator densities on APTES surfaces were created by immersing annealed APTES substrates into a solution containing different volume ratios of BIBB and BB for 60 minutes at 24°C. For instance, substrates consisting of 100% BIBB and 0.0% BB were generated by immersing APTES surfaces in a solution comprising 100% of 0.37 mL BIBB and 0.41 mL TEA dissolved in 60 mL DCM for 60 minutes at 24°C, followed by rinsing with DCM and ethanol and subsequent drying with nitrogen gas. In the same methods, substrates with a composition of 70% BIBB and 30% BB were fabricated by immersing APTES surfaces in a solution containing 70% of

0.37 mL BIBB and 30% of 0.37 mL BB, along with 0.41 mL TEA dissolved in 60 mL DCM for 60 minutes at 24°C. Following this, the substrates were rinsed with DCM and ethanol, followed by drying with nitrogen gas. Furthermore, substrates with mixed initiator densities, consisting of 0.0% BIBB and 100% BB, were created by immersing APTES surfaces in a solution containing 100% of 0.37 mL BB, along with 0.41 mL TEA dissolved in 60 mL DCM for 60 minutes at 24°C. Subsequently, the substrates were processed by rinsing with DCM and ethanol before being dried with nitrogen gas and subjected to characterization.

2.9 ATRP

In order for the synthesis of PDMA Brushes to be used, DMA (47.1 g, 30 mmol) was first dispersed in DMF (50 mL) and deoxygenated by passing nitrogen through it at room temperature for 20 minutes. Subsequently, it was stored under N_2. An amount of HMTETA (0.30 mL, 0.15 mmol) was introduced into the solution and deoxygenated for 10 minutes. After adding Cu(I)Br (0.14 g, 0.10 mmol), the solution was allowed to be deoxygenated for 10 minutes. Three-stage deoxygenation with nitrogen and vacuum was conducted on the initiator surfaces by placing them in Schlenk tubes. Under a nitrogen atmosphere, 5.0 mL of the mixture was injected into each tube. ATRP was carried out at 90°C for the appropriate duration of time. The polymerization process was ended by withdrawing the wafer from its Schlenk tube and rinsing it with copious amounts of IPA and ethanol to eliminate the possibility of excess material left on the wafer.-Micropatterned PDMA brushes were synthesised using the same method.

2.10 Surface characterization techniques

2.10.1 Contact Angle Measurements

The surface-free energy or surface tension of a chemical process-modified solid substrate can be determined by evaluating their contact at the interface with a drop of water. The contact angle is created between tangential solid and drop surfaces [154]. The liquid drop extends over the surface, and the contact point is measured by the three-phase equilibrium that occurs around the drop perimeter between solid, liquid, and vapor [155]. The Young's equation defines the relation among these tensions produced at the interface and the contact angle, as shown in (1.41):

$$\gamma_{SG} = \gamma_{SL} + \gamma_{LG} \, COS\theta \quad \gamma \tag{1.41}$$

where γ_{SL} and γ_{LS}, the solid to liquid and the liquid to air, respectively, γ_{LG} is solid to gas (air) tension, and (θ) is the angle of contact between both the solid to liquid and the liquid to air edges (Figure 2.1). It is noteworthy that surfaces for which $\theta < 90^{\circ}$ is seen as being hydrophilic, while hydrophobic surfaces are being the surface for θ>90°. Once the θ rises to 150 degrees, the surface is defined as super-hydrophobic.

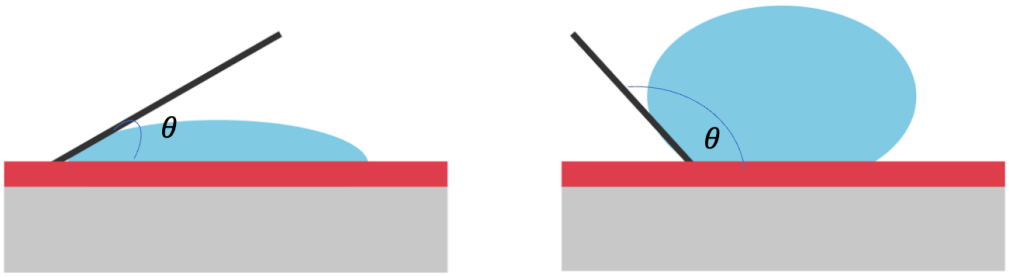

Figure 2.1: Shows (a) three lines of interface for the drop of water place on the surface and (b) the specific rough surface contact angle.

The Young's equation is valid determined on ideal surfaces whose characteristics are rigid, smooth, inert, and homogenous chemically. Actual surfaces like SAM substrates and polymer brushes could be rough and chemically heterogeneous. In turn, the actual and visible contact areas will vary and cause the contact angles to advance and recede, which is known as contact angle hysteresis [154], [156](Figure 2.1b).

2.10.1.1 Experimental procedure

In this investigation, the measurement of advancing sessile drop water contact angles was conducted employing a Rame Hart sessile-drop model 100-00 goniometer. This instrument was equipped with a microliter syringe, allowing precise injections to be administered. At the extremity of the syringe, a droplet of deionized water, precisely 2 μL in volume, was released. As the syringe was lowered, the water droplet encountered the sample surface, initiating the wetting process. Subsequently, the droplet was gently separated from the syringe by cautiously raising it. To ensure accurate and representative data, a standard protocol was followed wherein measurements were taken from five different positions on each sample. This procedure was repeated for three independent samples, and the resulting data were averaged to provide a reliable representation of the advancing sessile drop water contact angles for each sample.

2.10.2 Ellipsometry

A significant part of molecular film characterization is the use of ellipsometry as an optical surface analysis technique. Besides being easy to use, Ellipsometry also provides high accuracy and precision of 0.01 nm, regardless of the thickness of the film. During the reflection or transmission of linearly polarized light through a substrate or material, the ellipsometer determines its polarization change. As a general principle, the ellipsometer works by detecting linearly polarized light as it reflects or transmits across a substrate or material to determine polarization change during the reflection or transmission. A change in polarized light's amplitude ψ and phase Δ can be detected due to variations in surface thickness and refractive index [157], [158].

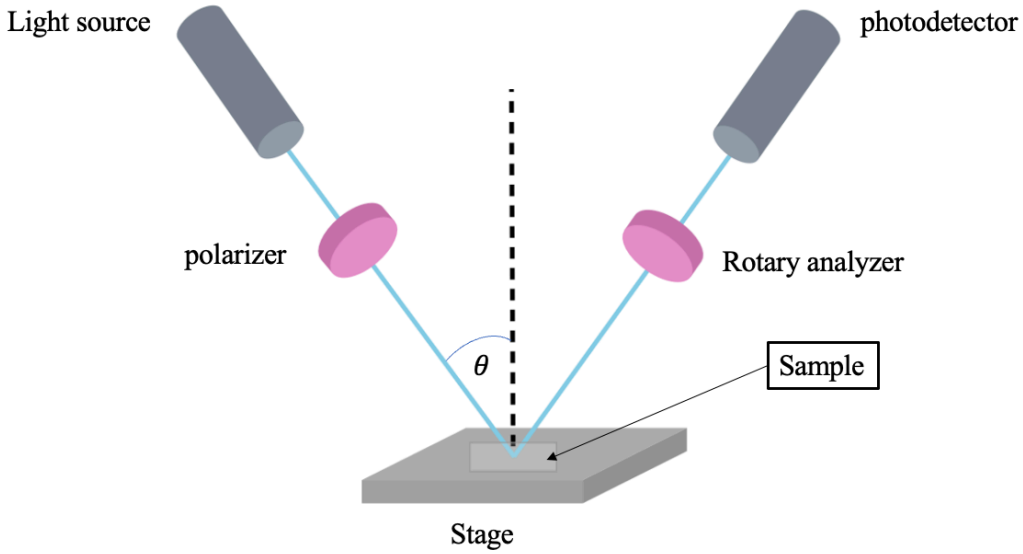

Figure 2.2: Ellipsometry schematic diagram illustrating basic principles.

A polarizer is used to polarize unpolarized light to ensure that elliptically polarized light is produced before entering the sample surface through a compensator Figure 2.2 In another analyser, polarized light is collected and transmitted to a photosensitive detector. Recently, the technique has gained a lot of attention to determine the thickness of polymer brushes[158], gradient polymer brushes [159]and responsive polymer [160]as a way of analysing growth thickness.

2.10.2.1 **Experimental procedure**

At various grafting densities, the thickness of PDMA brushes growing from ATRP initiators on silicon planar wafers was investigated. The ellipsometry measurements were performed using an M-2000 V ellipsometer (J.A. Woollam Co., Inc.) utilizing a white light source (370.5−998.7 nm) mounted on a 70° inclined angle. In ambient conditions, multiple measurements were performed for each sample (a minimum of two samples per exposure). In this study, the obtained ellipsometry data were modelled using a model consisting of PDMA brushes at various thicknesses on a flat silicon substrate, generated by the WVASE32 software from the J. A. Woollam Co. (USA). As part of the model, a one-layer Cauchy for a PDMA polymer brush was included, along with a one-layer initiator and silicon substrate.Too calculate

the accurate grafted polymer brush thickness, the silicon dioxide and initiator layer thickness were subtracted from the fitted layer thickness. It is important to note that the average value of the brush thickness was obtained from several measurements taken at different points on the two polymer-coated surfaces, which provided evidence of the brush uniformity.

2.10.3 X-ray Photoelectron Spectroscopy (XPS)

As part of surface analysis, one of the most essential instruments is X-ray Photoelectron Spectroscopy (XPS), commonly referred to as Electron Spectroscopy for Chemical Analysis (ESCA). It is a powerful analytical technique that facilitates compositional and ~~a~~ chemical structural analysis from a depth of only a few nm. In this technique, surface structures are quantitatively and qualitatively characterized by XPS non-destructively [161], [162], [163].

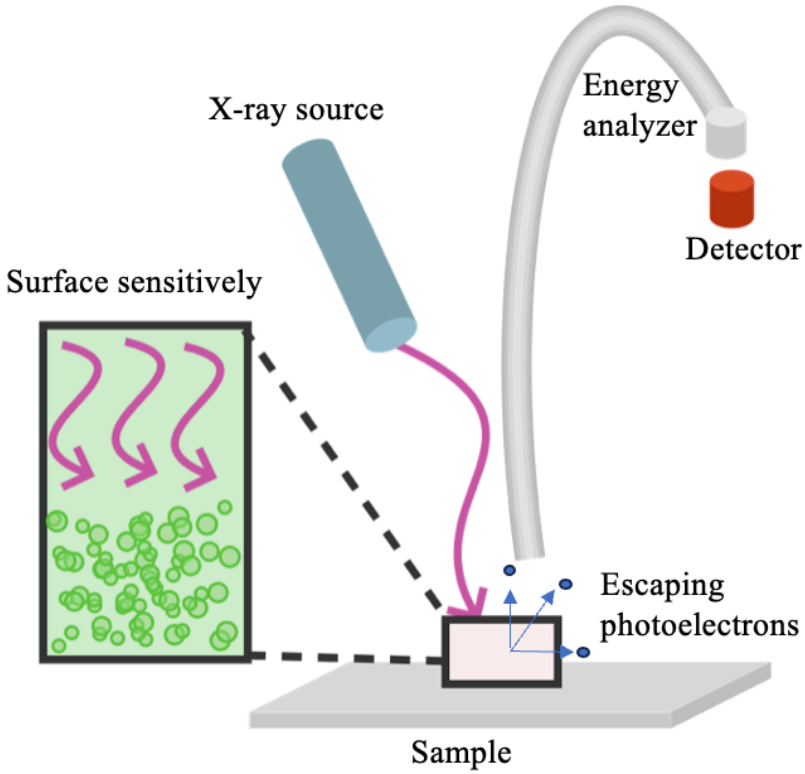

Figure 2.3: Illustrated the process of photoelectron emission on substrates.

In XPS, the sample is irradiated with X-rays, causing electrons in core shells to be ejected (Figure 2.3). These photoelectrons are collected in an analyser and the intensity is measured as a function of the photoelectron kinetic energy. It is mainly through XPS that electrons are

excised from the core shell (C1s, O1s, N1s,….). It is possible to calculate the binding energy by using the following formula:

$$BE = h\nu - KE - \emptyset$$

In this formulation, $h\nu$ represents the X-ray photon energy and $\emptyset$ represents the electron spectrometer work function.

It should be pointed out that, the BE measures the ionisation potential of the atom. However, the BE can be affected by the atomic chemical environment. Therefore, small chemical shifts in the BE can be noted because of changes in chemical bonding. To determine the non-homogeneity of the sample substrate, the width of the photoemission peaks requires to be measured [164], [165], [166].

The small sampling depth in XPS results from the inelastic scattering of photoelectrons in the solid[167]. The photoelectron travels a mean distance inside the substance known as the inelastic mean free path (λ). The inelastic mean free path is correlated with the kinetic energy of the electron, meaning that the inelastic mean free path is higher when the electron has high kinetic energy. The following equation can be used to determine the depth of the region sample:

$$I_d = I_\infty \left(1 - e^{-\frac{d}{\lambda} sin\theta}\right)$$

where the electron intensity from the thick layer is I_∞ and The XPS peak intensity is I_d. In most cases, solid surfaces have a known λ . The concentration of the surface element (CA) is directly related to peak intensity and this equation describes the relationship between them:

$$I_A = F\ K\ S\ \sigma_A\ C_A\ L(\theta)$$

An instrument factor is K and S refers to the sample area, while F refers to incident photon intensity. It is worth noticing that for a given spectrometer, these three factors remain constant. In this equation, $L\ (\theta)$ represents the angular symmetry factor and σ_A a represents the cross-section of the photoelectron emission.

2.10.3.1 **Experimental procedure**

A Kratos Axis Supra X-ray photoelectron spectrometer was used for XPS. The analytical chamber operatues under ultra-high vacuum. The instrument is equipped with a monochromatic Al Kα x-ray source and a hemispherical analyser fitted with a delay-line detector (DLD). It can be noted that the energy pass band of was set to 160 eV and 20 eV for the survey (wide) and narrow scans, respectively. The narrow scans reveal details about the bonding environment at the surface of molecules, while wide scans reveal details about the sample composition.

Samples for XPS analysis were prepared with 5x5 mm2 dimensions. Samples were rinsed with ethanol and dried under dry N2. After acquisition of spectera, the peaks in narrow scan spectra were extracted using CasaXPS software (Casa, http://www.casaxps.com, United Kingdom). All binding energies were calibrated relative to the C 1s saturated hydrocarbon peak at 285.0 eV, to correct for small shifts in the binding energy that can be caused by the accumulation of charge at the sample surface. a change in the bonding to the surface. A plot of obtaining data is generated against binding energy in eV as a function of intensity in counts per second (cps). The XPS samples were loaded, and the data were extracted by Dr Deborah B Hammond. An analysis of the XPS data was conducted by the author of this study

2.10.4 Atomic Force Microscopy (AFM)

Atomic force microscopy (AFM) is a type of scanning probe microscopy (SPM). It is noteworthy that SPMs are designed to identify local properties with a probe, including height, friction, electrical, and magnetic. In 1986, Binnig, Quate, and Gerber developed the atomic force microscope (AFM), only after the discovery of the scanning tunneling microscope (STM) [26]. The STM has been utilized in the analysis of conductor material surfaces; whereas AFM is mainly applied in the investigation of the material surfaces of various kinds [26], [57] that are present in different environments including air, liquids, or ultra-high vacuum (UHV) [168]. Being an electrical conductor is not a requirement for a sample. For this reason, AFM becomes unique and has given full attention to STM. (AFM) is essentially an imaging tool that provides information about the sample's surface by sliding a sharp tip across it [169]. The monitoring of flexible cantilever deflection determines the interactive forces present between the sharp tip and material surface [170], [171]. Thus, adhesion and repulsion forces between the sample and tip cause the deflection on the cantilever.

AFM consists of a cantilever with a sharp tip, photodetector, piezoelectric tube, and feedback system. The sharp tip in the cantilever is located at its apex and is usually at a size ranging from 10-100 nm. Furthermore, the deflection in the cantilever is measure using a sensitive photodetector. Scan motions are monitored using a piezoelectric tube. Whereas, the feedback system does the maintenance of cantilever deflection.

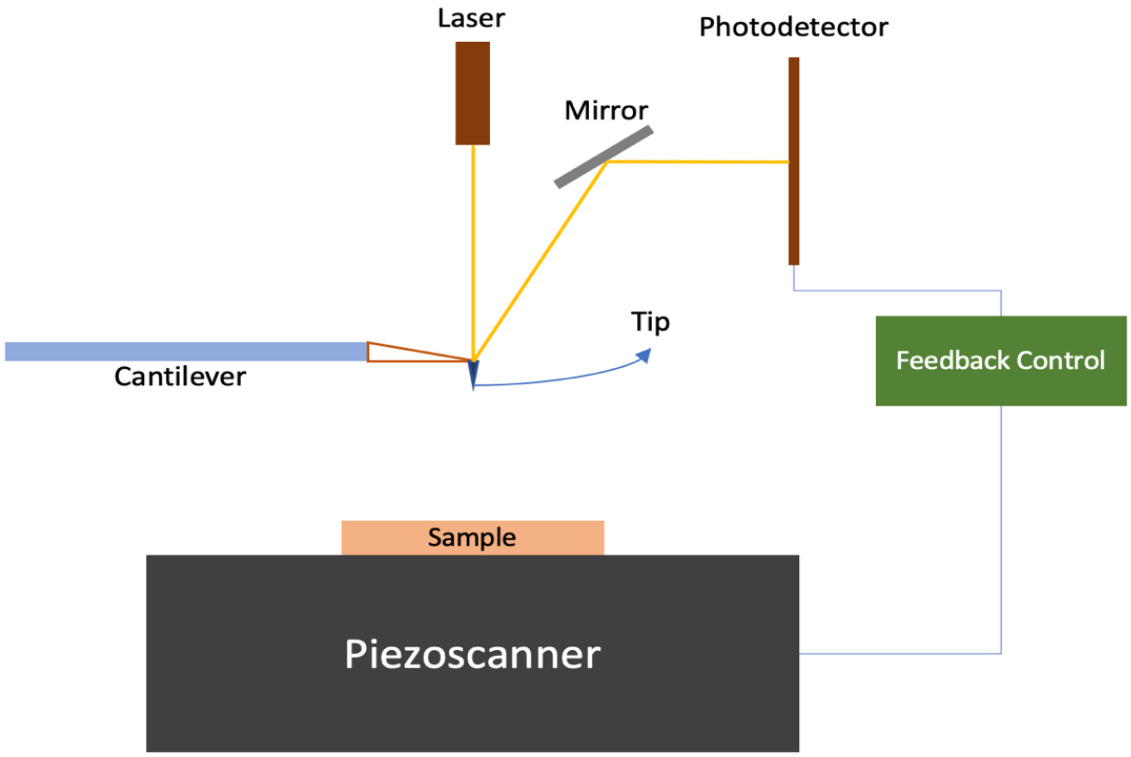

Figure 2.4: Schematic illustration of the atomic force microscopy (AFM).

Figure 2.4 illustrates the atomic for microscope representation wherein the cantilever is located parallel to the surface of the sample. The laser beam is located at precisely the center opposite of the cantilever tip, in which the sensitive photodetector directly receives the reflected beam [61], [172], [173]. The position of the laser spot and the fluctuation in the laser beam deflection is highly affected by the interacting force between the tip and the sample. A number of studies have shown that there is an excellent opportunity that AFM brings to measuring the local properties of a different material. Quantification of local characteristics such as topography and friction is done when the probe scans the sample's surface [43], [174], [175].

AFM provides three operating modes: contact mode (the most widely used), non-contact mode, and tapping mode. For the former, the sample surface is in mechanical contact with the tip; this allows the measurement of the repulsive forces occurring between them [176], [177]. However, this method is destructive due to direct contact between the tip and the sample surface. The material used for the cantilever in this mode is silicon nitride having a smaller spring constant. Instead, the non-contact method solves this issue, although it is more challenging when it comes to the application. Cantilever oscillation happens near the sample for the non-contact mode, allowing the measurement of the difference in the interactions between the tip and the sample surface [176].

On the other hand, technology has given more emphasis on the development of tapping mode to cope with the downsides of the prior methods discussed. This mode enables its application on biological samples and those made up of soft materials by reducing the surface contact and lateral forces acting between the tip and the sample surface[178]. Furthermore, the energy dissipation rate is minimized with the use of oscillating tip via utilization of high amplitude at its resonant frequency. Measuring the cantilever damping oscillation allows the production of phase images upon each run [178], [179]. However, this mode uses a silicon-based cantilever with higher spring constants than the contact mode [178].

AFM has been established as a great utility technique that is applied to polymer science, semiconductors, adhesive, electronics, manufacturing of biomaterials, and biology. Recently, it has been commonly used in classifying polymer brush-coated samples and the self-assembled organic molecules in different environments, either qualitatively or quantitatively. For instance, soft or physisorbed samples surfaces (e.g., polymer brush) greatly use tapping mode as the method of imaging [180], [181], [182], [183]. Other sample types include DNA [184], [185], protein[186], cells [187], and lipid bilayer support [44]. Morphology, ruggedness, and material patterns could be characterized by height image.

2.10.4.1 **Experimental procedure**

As ambient conditions prevailed in the air during the study, unpatterned and patterned surfaces were imaged using a Nasoscope V controller (Bruker, UK) in combination with a Dimension Icon atomic force microscope to scan images from tapping and contact modes. As part of the experiment, silicon cantilevers from Bruker, which have a spring constant of 42 N m^{-1} were used for the tapping of the air. In the topographical tapping mode, 0-degree scan angle images

were acquired at a 1.0 Hz scan rate. On the other hand, the contact mode had four cantilevers made from silicon nitride and tip radii in the 20-60 nm range. Friction images were collected from friction loops by obtaining forward-reverse scanning cycles along a single line using the contact mode microscope. The scan size was maintained at 1.0 μm and the scan angle at 90. The friction signal was obtained by subtracting in both directions the mean images, giving the resulting force twice the frictional force. In both tapping and contact mode, a dry sample was placed below the microscope on the sample stage. Then using a cantilever holder, the probe was placed above the sample. The laser was then centred at the end of the tip, horizontally and vertically relative to the photodetector. The tip was then tuned by using Nasoscope 8 software to detect the resonant frequency of the tip.

2.10.5 Friction force microscopy (FFM)

Among the most useful tools in the study of surface mechanical properties, chemical compositions, and molecular organization is friction force microscopy (FFM). Moreover, FFM is suitable for obtaining quantitative data with nanoscale resolution and high sensitivity[188], [189], [190], [191]. An FFM measurement determines the lateral interaction force between the tip and the surface of the sample as the tip scans across it. Measurement of the lateral deflections of the cantilever is performed by using a laser beam that is reflected from the cantilever's backside and detected by a photodetector[192], [193]. In addition to frictional interactions among the tip and sample, lateral deflection occurs from the load distributed in the surface plane. In this method, A topographical effect is eliminated by subtracting the trace and retrace measurements (scans performed with opposite tip motion directions) [194], [195]. In chemical force microscopy the chemical nature of the tip is modified (e.g., as monolayer assembly) to enable the magnitudes of specific types of forces to be measured. For instance, when crossing polar regions, a cantilever exhibits a greater deflection in the lateral direction. In this case, the photodetector will register a larger lateral signal as polar regions are more strongly interacting with the tip than nonpolar regions [193]. It is possible to reduce water capillary between the cantilever tip and the sample surface by employing the FFM method in the presence of an appropriate liquid [192].

Using the FFM approach, quantitative data can be generated and analysed [191], [195]. The determination of the normal force requires determining the cantilever spring constant and the photodetector signal. A contact mechanics model can incorporate frictional force data into it to find out the type of contact [189], [190].

2.10.5.1 **Experimental procedure**

2.10.5.1.1 **Pull-off Force Determination in liquids**

To assess the adhesion among two substrates, an Atomic Force Microscope (AFM) was employed to generate curves of force between a functionalized polymer sample and the AFM tip. These force curves represent the vertical deflection of a cantilever against the vertical displacement of the cantilever/tip (essentially the z-piezo displacement). Subsequently, the retract signal was analyzed to determine the type of adhesion among the substance and the tip. This analysis was facilitated utilizing the "Ramp" mode within the software Nanoscope following the microscope configuration into contact mode.

Figure 2.5 shows a typical force curve acquired for an AFM probe interacting with a poly (dimethyl aminoethyl methacrylate) brush. The probe begins from a position of non-contact, at the left-hand side of the diagram. The tip approaches towards the sample following the blue curve. Normally a “jump-to-contact” is observed in AFM as the tip approaches a hard surface. However, the swelling of the polymer in liquid creates a more diffuse interface, and the interaction force increases smoothly as the probe travels through the interface, eventually increasing steeply as it reaches the underlying substrate. On reversal of the process, the probe follows the red line. Because of adhesion between the tip and the surface, hysteresis occurs, and the tip must be pulled further than the point at which it first contacted the surface in order to separate it from the sample. In this example, the separation of the tip from the surface occurs in a series of steps, giving rise to a “sawtooth” unbinding curve. This type of behaviour is commonly reported for macromolecular systems, and it results from the separation of multiple molecular strands from the probe. It should be noted that in all cases, a scan range of 500 nm, a rate of 0.5 Hz and a trigger displacement of 30 nm were utilized. These settings ensured approach and retracted speeds of 500 nm s^{-1} to maintain stability since higher scans yield unstable readings.

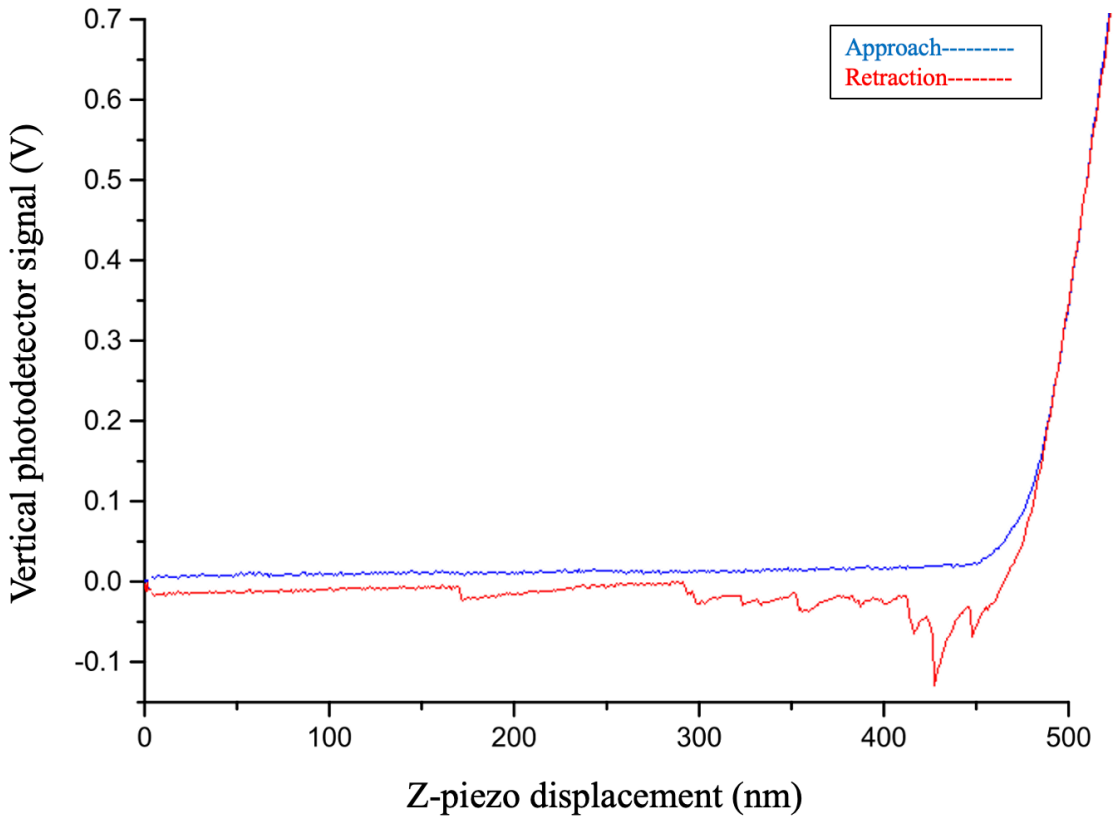

Figure 2.5: A force curve acquired for an AFM probe contacting a PDMA brush sample immersed in water. The approach signal is depicted by the blue line, while the red line represents the retract signal utilized to determine the pull-off force.

To ensure the validity of the results, force curves were systematically collected at 400 distinct locations across the samples, repeating the process for the purpose of ensuring the validity of the result, and utilising several probes and samples in every liquid. Subsequently, to provide a more efficient analysis, the raw NanoScope force curve data files were loaded into TToolbox. This allowed force curve files to be processed effectively while applying all tip parameters required to calculate the pull-off force. Even though Carpick's Toolbox force curve Matlab programme employs a similar concept, the algorithm underwent extensive optimization to increase calculations by up to 100 times, depending on the number of available CPU threads.

TToolbox computes the variation between the approach and retracts signals in the negative (adhesive) signal zone of the photodetector signal. Taking the force curve illustrated in Figure 2.5 as an instance, this difference was determined to be 0.502 V. Subsequently, for determining the force required to disengage the tip from the substrate, it is multiplied by the photodetector deflection sensitivity and the normal spring constant.

$$F_{Pull-off} = 0.502\text{V X } 0.123\text{N}m^{-1}\text{ X } 48.75\text{nm}V^{-1} = 3.010\text{nN}$$

The process involved performing this calculation individually for every force curve obtained. Each curve underwent the meticulous analysis described earlier to ascertain the force necessary to separate the tip from the surface. This step was crucial in ensuring a comprehensive understanding of the adhesive interaction among the surfaces under investigation. After calculating the pull-off force for each curve, the next phase entailed aggregating these values to derive an average pull-off force representative of the whole sample. This averaging process served to minimize the influence of any outliers or variations across different measurements, providing a more robust and reliable estimate of the adhesive forces at play. By systematically analyzing multiple force curves and synthesizing those findings into a single metric, researchers could gain deeper insights into the adhesive properties of the sample, enabling more informed conclusions regarding its behaviours in the given experimental conditions.

2.10.5.1.2 Friction force Determination in liquids

friction forces were generated utilising a Digital Nanoscope VIII multi-mode Atomic Force Microscope (Multimode VIII, Bruker, UK) performing in contact mode, employing an E-scanner and AFM tips. To conduct friction measurements across various liquids, an upgraded and recently designed glass liquid cell (MTFML-V2, Bruker, UK) was utilized. This cell boasted improved performance metrics, offering higher precision measurements with reduced noise levels. Additionally, an O-ring plastic (Bruker, UK) was incorporated into the setup to ensure optimal experimental conditions for friction analysis. Friction forces were obtained from the friction loop, which was derived from forward-reverse scanning along a single line. The friction signal was determined by subtracting the signal of the peak maximum from the signal of the peak minimum for micrometre and nanometer PDMA brushes patterns. Conversely, for unpatterned brushes, the mean signal of the forward scan was subtracted from the main signal of the reverse scan, and the result was halved. It's worth noting that all analysis procedures were conducted manually.

The measurements were conducted at a scan rate of 1 Hz, with 256 samples acquired per line and a scan angle of 90 degrees. The scan size was consistently maintained at 1 μm^2. To investigate the frictional characteristics of the samples, V-shape contact mode probes (model DNP) were utilized. These probes were crafted from non-conductive Silicon Nitride and featured nominal normal spring constants of either 0.06 or 0.12 N m^{-1}. The tips of these probes

ranged in radii from 20 to 60 nm. During experimentation, the normal load was gradually reduced in increments of 0.2 V, starting from 2.0 V, until the probe disengaged from the polymer brush surfaces. In the experimental procedure, three to five distinct locations were investigated on each sample. To enhance the consistency and validity of the findings, a minimum of three different samples were subjected to analysis. Furthermore, to prevent potential sources of variability and ensure comprehensive coverage, three distinct cantilevers were employed in each experimental stage.

The Normal calibration process for the cantilevers was conducted carefully, including two steps to ensure accuracy and reliability. Initially, attention was directed towards determining the deflection sensitivity (measured in nm V^{-1}) of the probes. This crucial parameter was derived by meticulously analyzing the slope of a linear section within the force curve, specifically focusing on the repulsive regime Figure 2.6. This analysis was appropriately performed on a flat mica surface, known for its uniformity and suitability for calibration purposes.

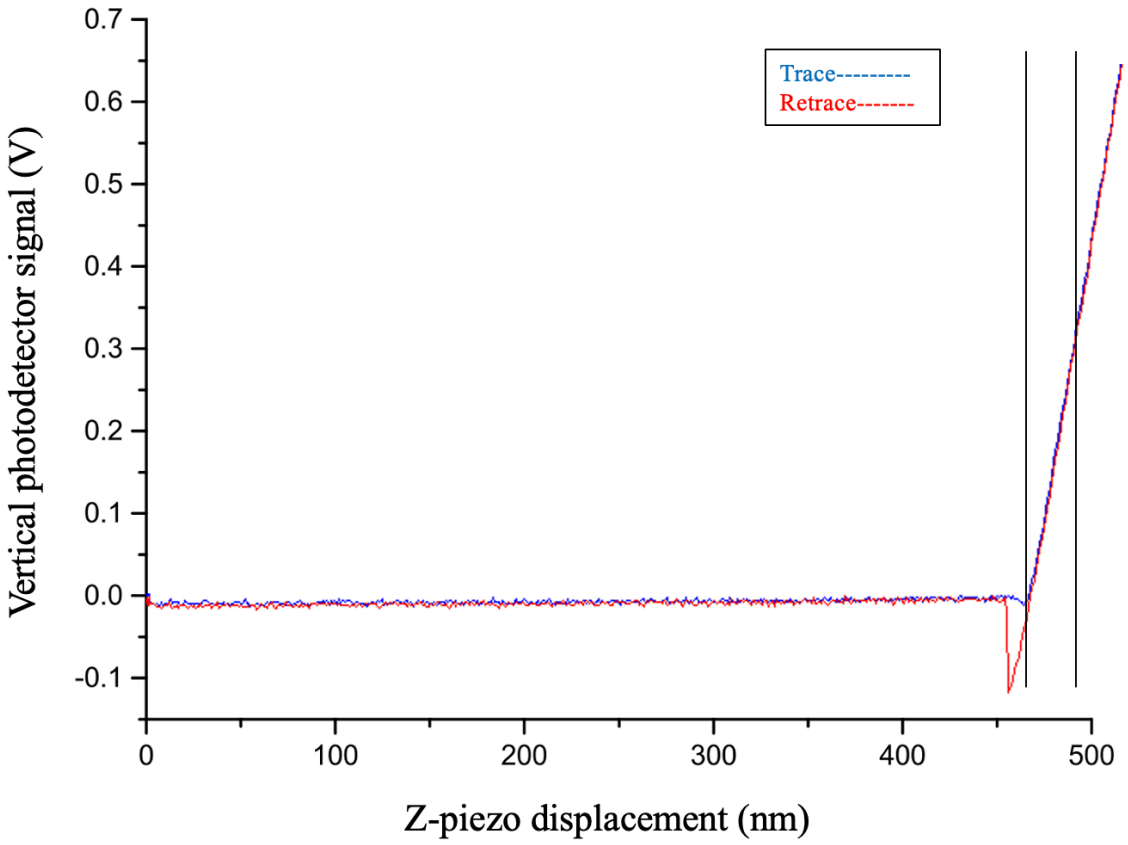

Figure 2.6: A typical force curve acquired in order to determine the deflection sensitivity of a cantilever by measuring its interaction with a flat mica surface. The approach signal is blue and the retract curve is red. The highlighted region is utilized for calculating the photodetector deflection sensitivity.

following the determination of the deflection sensitivity, the calibration process proceeded to the next stage, which involved determining the actual spring constant of the cantilever. This parameter is fundamental in understanding the mechanical properties and behaviours of the cantilever during atomic force microscopy (AFM) experiments. The calculation of the spring constant was completed by subjecting the cantilever to thermal fluctuations and analyzing its power spectral density Figure 2.7. This thermal spectrum analysis was thoughtfully conducted at room temperature, employing the advanced capabilities of the multi-mode VIII AFM instrument.

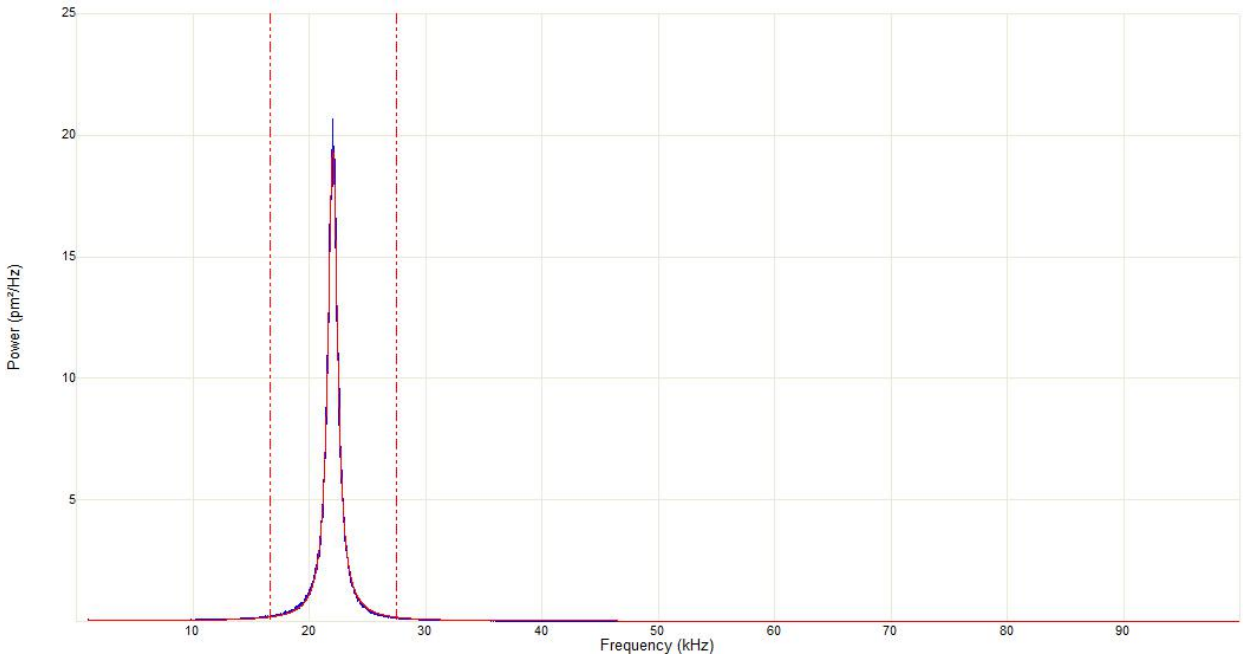

Figure 2.7: Illustrates determining the spring constant of the cantilever performed on a flat mica surface.

By carefully conducting these calibration steps, researchers ensured that the cantilevers were accurately characterized and optimized for subsequent AFM experiments. The demanding calibration process not only enhances the accuracy and reliability of the experimental results but also emphasises the careful consideration of detail inherent in the scientific methodology.

The wedge calibration method was utilised to ascertain the lateral stiffness, wherein the cantilever traverses over a silicon grating TGF11 that is available for purchase (MikroMasch, Tallinn, Estonia), and the resulting friction signals were recorded at varying applied loads Figure 2.8. Calibration of lateral force was conducted for each solution utilized in the measurements to ensure accuracy. By imaging a calibration grating TGG01 (MikroMasch, Tallinn, Estonia) at scanning angles of 0.0 and 90 degrees, the tip radius was determined. To prevent contamination and potential loss of tips, using the same solution used for the friction measurement tests, all calibrations were completed right away after each experiment.

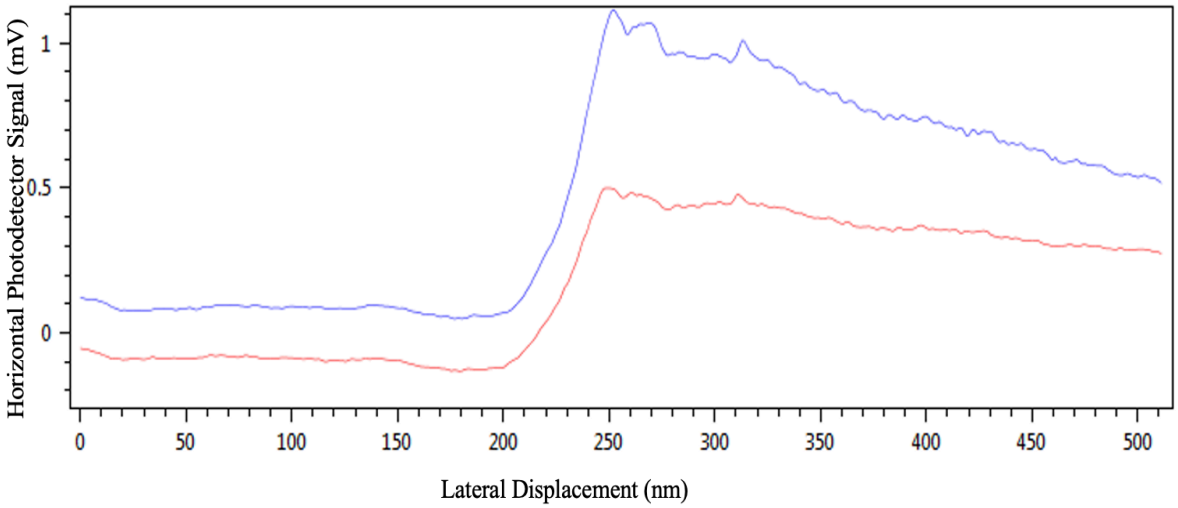

Figure 2.8: Illustrates determining the lateral force of the cantilever performed on the TGF11 surface.

CHAPTER 3 SOLVATION OF POLYMER BRUSH SYSTEMS

3.1 Introduction

Polymer brushes are surface-grafted polymers that are formed either by grafting from, in which the polymer chains grow from a surface-bound initiator, or by grafting to, in which a pre-formed polymer is attached to a surface. The work described in this thesis is focussed on surface-grafted polymers formed by surface-initiated atom-transfer radical polymerisation (SI-ATRP), in which polymers are grown from surface-bound bromine initiators. The conformation of a surface-grafted polymer depends on numerous factors. At low grafting densities, surface-grafted polymers collapse, and their dimensions are defined by the radius of gyration. The surface grafted polymers are referred to as mushrooms under these conditions. However, as the grafting density increases above a critical point, neighbouring chains experience steric repulsion, and they swell away from the surface. Under these conditions, the surface-grafted polymer is referred to as a brush. The degree of swelling increases as the grafting density increases. The degree of swelling is influenced by the nature of any solvent-polymer interactions (the polymer swells more in a good solvent, which solvates the polymer chain strongly, than in a poor solvent), charge-charge interactions (repulsive interactions cause increased swelling) and the temperature (brushes may become desolvated as the temperature is increased, leading to a decrease in the degree of swelling). Patterned polymer brushes have attracted considerable interest from engineers, materials scientists, and physicians [196], [197]for numerous applications, including devices based on cells[198], [199] and proteins[199] biosensors, and actuators[200]. A variety of lithographic techniques have been employed to design patterned polymer brushes with feature dimensions ranging from nanometres to micrometres, including photomask lithography, interference lithography, scanning probe and electron beam lithography[201]. Patterned polymers can be created via a combination of both methods, by patterning initiators at surface and then using surface-initiated atom transfer radical polymerization to grow polymers from these patterned initiators. By controlling the polymerisation conditions, for example the polymerisation time and the grafting density, it is possible to modify the conformation, thus, in turn, controlling the properties of the polymer film, such as its tribological characteristics, optical and electrical properties or interactions with biological systems.

There are many contributing factors which determine polymer chain performance and responsiveness in patterning systems including elastic free energy and entropy penalty. Polymer brushes can collapse sideways at the outer edges of a patterned surface, within a continuous brush layer, steric repulsion between neighbouring chains causes them to swell away from the surface. However, at the edge of a patterned structure, the free volume is greatly increased, and the polymer chain, if it interacts strongly enough with the substrate, will form a "train" in which it is bound to the substrate rather than projecting away from it. Aside from the environmental impact, the dimensions of the grafted area and the ungrafted region area are also anticipated to have a noteworthy influence on the morphology of nanopatterned polymer brushes[202] [203]The reduction in the size of the grafting footprint leads to a decrease in the thickness of the polymer brush, which in turn reduces the degree of crowding of the chains as a result[204]. Numerous methods have been employed to describe the conformations of polymer brushes, which involve examining how their behaviour changes based on their thickness and the properties of the surrounding environment. These environmental properties include factors such as ionic strength, pH, solvent quality, and temperature [205]. During the process of scanning a sample, the cantilevers' side-to-side movements are measured and recorded. Conformational changes in polymer brushes have been found to cause changes in their tribological properties. Leggett and co-workers investigated the relationship between the conformations of poly (2-methacryloyloxyethyl phosphprylcholine) brushes and their frictional properties using friction force microscopy (FFM)[206]. They found that, for thicker brushes, the friction coefficient decreased as the thickness of the brush increased. However, for thinner brushes, the friction coefficient became independent of thickness. In a good solvent, such as water, PMPC brushes are solvated and swell away from the surface to create brushes. Conversely, when placed in an unfavourable solvent, such as ethanol, surface-grafted PMPC chains collapse to form mushrooms[206]. Takahara et al. also studied the tribological properties of PMPC brushes[207]. They argue that the frictional properties and morphology of PMPC are significantly influenced by the composition of the solvent and the interaction between probe and brushes. Their research indicates that when the sample is immersed in an aqueous medium, the polymer chains are solvated, leading to the formation of swollen brushes. Conversely, in toluene, the polymer chains were found to be collapsed[207]. Additionally, studies have demonstrated that the coefficient of friction is heavily influenced by the density of the grafting. It has been shown through research that when the polymer grafting density is relatively low, the friction force is significantly higher in contrast to surfaces with greater polymer density [208]

To understand fully the data obtained using friction force microscopy, it is necessary to be able to model the mechanics at the tip-polymer contact. The Derjaguin-Muller-Toporov (DMT) and Johnson-Kendall-Roberts (JKR) models in continuum mechanics have been extensively utilized to study the interactions between AFM probes and solid surfaces. Recently, the proposed model considered that the friction force acting on the contact interface can be expressed as the sum of two separate contributions. The first contribution is load-dependent, meaning that it increases as the load or normal force on the contact interface increases. This component is associated with molecular ploughing, which occurs when the probe physically displaces molecules in the brush layer. The second contribution is shear-dependent, meaning that it increases as the shear force on the contact interface increases. This component arises from the dissipation of energy due to the shearing of adhesive interactions between the probe and the brush layer. By considering these two separate contributions, the proposed model aims to better understand the underlying mechanisms governing frictional forces in probe-brush interactions. Therefore, frictional force can be meddled by using equation (1.31).

In the past few decades, extensive research has been conducted to investigate the tribological characteristics of polymer brush films. Multiple studies have explored the nanoscale mechanical behaviour of polymer brushes[209], [210], [211]. However, the mechanical behaviour of nanostructured polymers is complex and remains poorly understood. Recent advancements in experimental techniques have provided deeper insights into the deformation mechanisms of polymer brush films under various loading conditions. Additionally, modelling has emerged as a powerful tool to complement experimental findings and predict polymer brush behaviour at the molecular level.

The aim of this chapter is to investigate the tribological characteristics of polymer brush layers fabricated from polymers with varying grafting densities. The nanomechanical behaviour of continuous brush layers will be compare with micro- and nanostructured polymers formed using mask-based photolithography and interference lithography, respectively. To enable production of micro and nano-patterns, nitrophenyl (propyl oxycarbonyl) protected aminopropyl triethoxysilane (NPPOC-APTES) films were used to form patterned initiator groups at the surface. Exposure of these films to UV light causes removal of the nitrophenyl protecting group enabling functionalisation by reaction with bromo (isobutyryl bromide) (BIBB) initiator. PDMA polymer brushes were grown from the Br initiators via SI-ATRP. Micrometre-scale patterns were formed by placing a mask over the sample during exposure, while nanopatterns were formed by using a Lloyd's mirror interferometer to carry out

patterning. Interference occurs when two or more coherent light beams overlap, creating an interferogram. The resulting intensity distribution is captured on a photosensitive film. There are two main approaches to generating interference patterns using laser beams. The first involves using optics to split a coherent beam into two beams (known as two-beam interferometry) or multiple beams (referred to as multiple-beam interferometry), which are then made to interfere with one another. The second approach involves passing light from a single coherent source through an optical element to produce an interference pattern. The aim was to compare the frictional properties of continuous brush layers with those of nano structure surface-grafted polymers, where the free volume is expected to be larger, creating greater conformational freedom.

3.2 Experimental Details

3.2.1 Preparation of NPPOC-APTES initiator

A description of the synthesis of APTES-NPPOC molecules was described in detail in section 2.4.2 In brief, clean silicon substrates were immersed in a solution of the adsorbate in toluene for 48 h. The substrate was rinsed and dried by blowing nitrogen gas over it. For annealing, the silane-coated film was positioned in an evacuated Schlenk tube fitted with a septum, wrapped in foil, and then placed in an oven for 30 min at 120°C. Once annealed, the samples were cleaned with ethanol and covered with aluminium film before storage in the dark place.

3.2.2 Photodeprotection and patterining of NPPOC-APTES films

The patterning of NPPOC-APTES films at micrometer and nanometer scales was achieved as describe in Section 2.5 at varying doses from 0 to 3.0 J cm². The illuminated area was precisely 0.5 cm². Post-photodegradation, surfaces were rinsed in ethanol and dried under nitrogen. For nanopatterned NPPOC-APTES films, Interferometric Lithography (IL) was utilized 1.2 mW laser power. Exposure dosages of 1, 3, and 6 J cm² were applied. The rotation stage adjusted the angle between the interfering beams to 10° and 25° using a rotation stage, producing patterns with periods of 690 nm and 350 nm, respectively. The Full Width at Half Maximum (FWHM) was 270 nm for a 10° angle and 190 nm for a 25° angle. After exposure, samples were washed with ethanol and dried with nitrogen to remove photodegraded residues

3.2.3 NPPOC-APTES film functionalization with BIBB

Photodeprotection of NPPOC-APTES films were executed as outlined in Section 2.6. Before initiating atom-transfer radical polymerization, the patterned silane substrates were derivatized by immersing them in a solution of 2-bromoisobutyryl bromide (0.37 mL, 3 mmol) and triethylamine (0.41 mL, 4 mmol) in dichloromethane (DCM; 60 mL) for 40 minutes. Subsequently, the samples were sonicated in DCM and ethanol for five minutes, followed by nitrogen drying.

3.2.4 The synthesis and polymerization of PDMA brushes

description of the procedure for synthesizing poly (2-dimethyliamino) ethyl methacrylate) and growing PDMA brushes on ATRP initiator samples can be found in experimental section 2.9. To ensure the fabrication of uniform brushes, consistent polymerization conditions were

maintained throughout the reaction. These conditions included a fixed monomer to catalyst molar ratio of [DMA]: [CuBr]: [HMTETA] = 300:1.0:1.5, as well as controlled polymerization time, solvent type, temperature and initiator density. All samples were prepared systematically under these standardized conditions. To compare the properties of patterned and unpatterned polymers, samples were designed to include extensive unpatterned areas (ranging from 1 cm to 4 cm), micropatterned structures, and nanostructures on a single substrate. This approach allowed for the growth of PDMA polymers under identical conditions across all types of structures.

3.3 An analysis of the surface

The analytical methods (XPS, spectroscopic ellipsometry, contact angle goniometry and atomic force and friction force microscopy) are described in detail in chapter 3.

3.4 Results and Discussion

3.4.1 Formation of SAMs

In this study, 2-Nitrophenylpropyloxycarbonyl-3-aminotriethoxy silane (NPPOC-APTES) was synthesized by reacting 2-(2-Nitrophenyl) propan-1-ol, which is then reacted with isocynatopropyltriethoxysilane to obtain NPPOC-APTES (Chapter 3) and then deposited on a glass surface (Scheme 3.1). To demonstrate the creation of an APTES-NPPOC film, contact angle measurements, XPS, AFM, and FFM were used to characterize the functionalized surface.

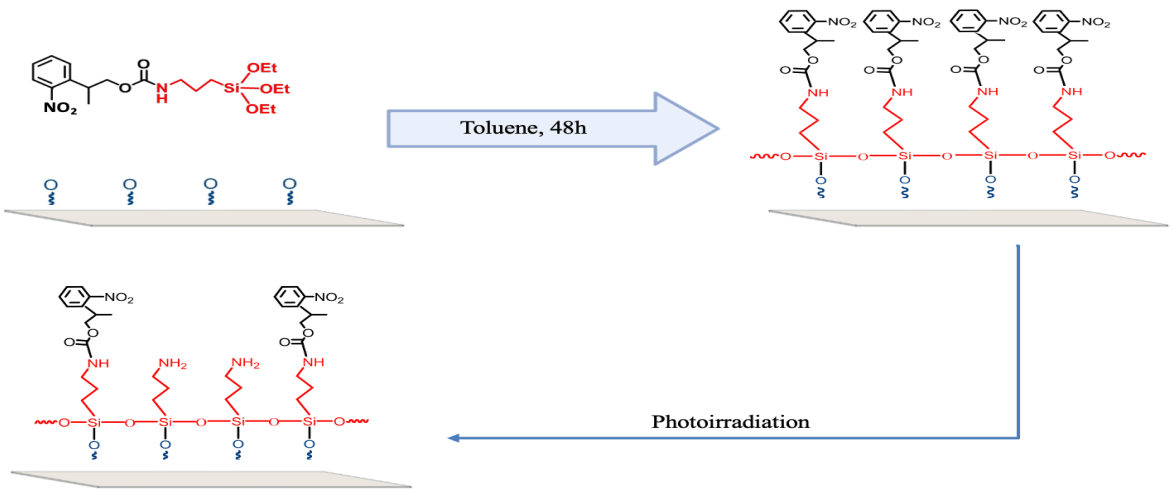

Scheme 3.1: Schematic diagram illustrating NPPOC-APTES monolayer formation on glass.

Siloxane films are generally intricate, and the quality of the materials produced is influenced by a wide variety of factors[114], [212], [213]. In the specific conditions of controlled moisture utilized in this study, the duration of substrate exposure to the silane solution plays a crucial role. To determine the duration required for achieving consistent surface coverage by the NPPOC-protected silane, the contact angle measurement was employed. The water contact angle of the untreated substrate was measured to be below 10°. In Figure 3.1, the contact angle varies as a function of the substrate's immersion time in 1.0 mM of NPOCC-APTES solution. At the start of the study, there was a significant increase in the contact angle, reaching approximately 67º with a deviation of 2 degrees after 5 hours. Subsequently, the rate of change exhibited a gradual decrease with extended immersion time. The contact angle continually rises and stabilizes at a consistent level of 76° within 48 hours. The change in contact angle was explained because of a progressively greater increase in surface coverage. A complete film covering the surface was required to attain a stable contact angle value. The extended deposition time, in this case, is due to the lower reactivity of triethoxysilane, which is hydrolysed in solution. This aligns with the findings of Dendane et al., reporting that trichlorosilane achieves faster and more comprehensive coverage compared to triethoxysilane[214].

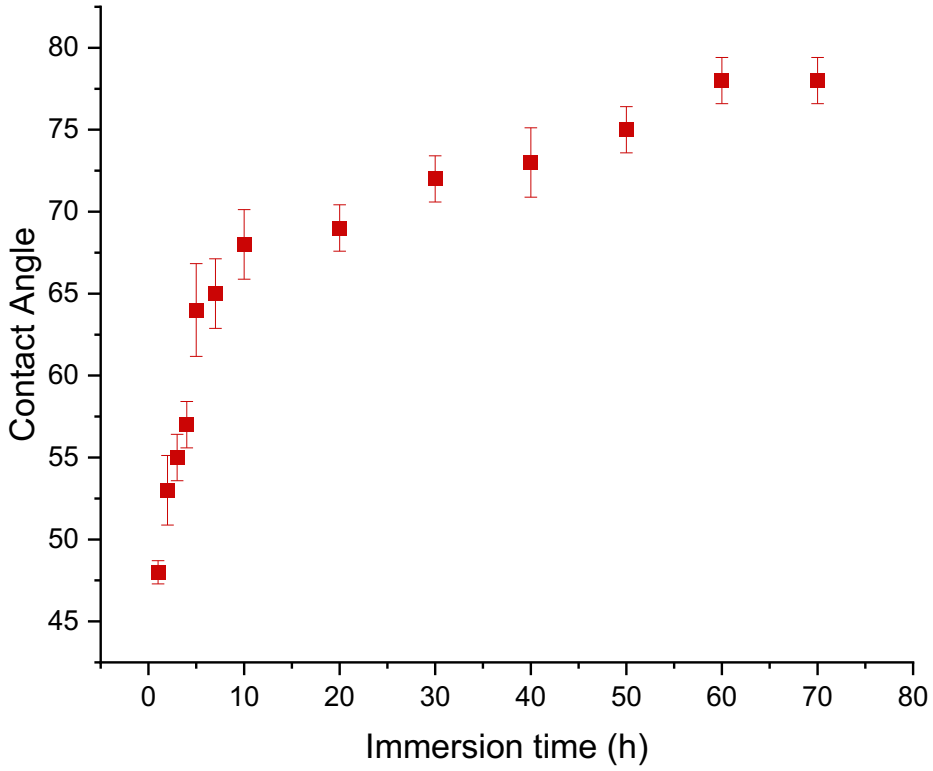

Figure 3.1: illustrates as the substrate is immersed in the NPPOC-protected silane solution, the water contact angle on the substrate changes over time.

X-ray photoelectron spectroscopy (XPS) was used to analyse and describe the properties of the NPPOC-protected films, which provided comprehensive coverage over the entire surface. The C1s and N1s spectra, which were obtained at high resolution, can be seen in Figure 3.2. The main peak in the C1s spectrum appeared at an energy level of 285.0 eV, indicating the presence of carbon atoms (-C-C-C-,). Additionally, there were carbon atoms bonded to nitrogen and oxygen (-C-N-/-C-O-), observed at 286.0 eV and a faint indication of the signal from carbamate carbon (NCOOR) at 289.3 eV (figure 3.2). It is evident from Figure 3.2 that there are two distinct bands present in the region of the N1s spectrum. The peaks located at 400.0 and 406.2 eV are attributed to nitrogen atoms present in the amine and nitro groups, respectively. These results align with both experimental observations and theoretical investigations [153]. Based on the fact that there are equal numbers of amino and nitro groups in the silane structure, the calculated ratio between them should be 1:1. Nevertheless, the measured ratio in the spectrum was found to be 1:0.89, indicating a deviation from the expected 1:1 ratio. The most plausible explanation for this discrepancy is that some of the NPPOC groups underwent deprotection

because of X-ray exposure within the XPS instrument. Research published in the past couple of years has concluded that the outcomes of these studies are in line with those found in previous studies.

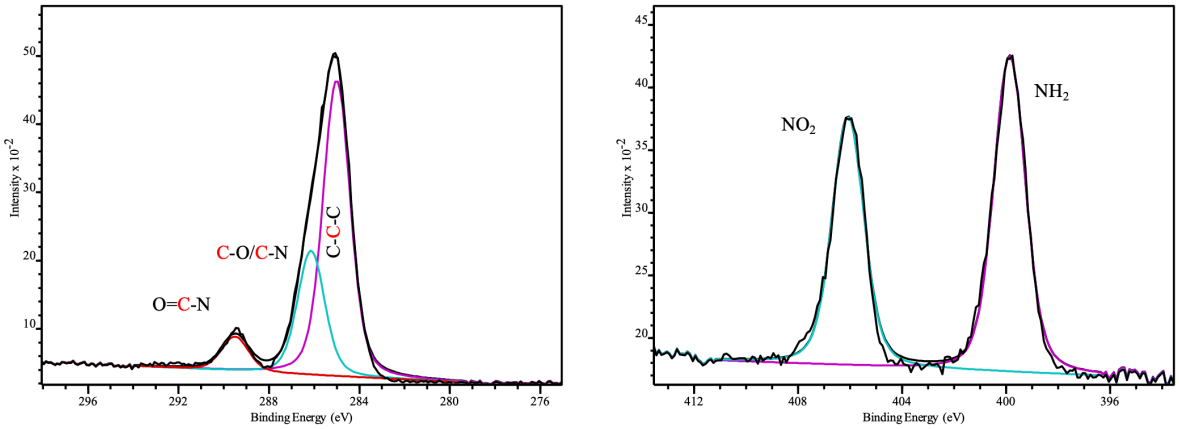

Figure 3.2: (a) representing the C1s spectrum and (b) representing the N1s spectrum of a film formed by the adsorption of NPPOC-APTES onto silicon dioxide

Following the creation of NPPOC-APTES films, the surface roughness was assessed through AFM measurements. After annealing, a smooth and continuous layer of silane was produced on the surface of the wafer. This was evidenced by a roughness of 0.451/0.458 nm (Ra/Rq) for the complete NPPOC-APTES monolayer (Figure 3.3).

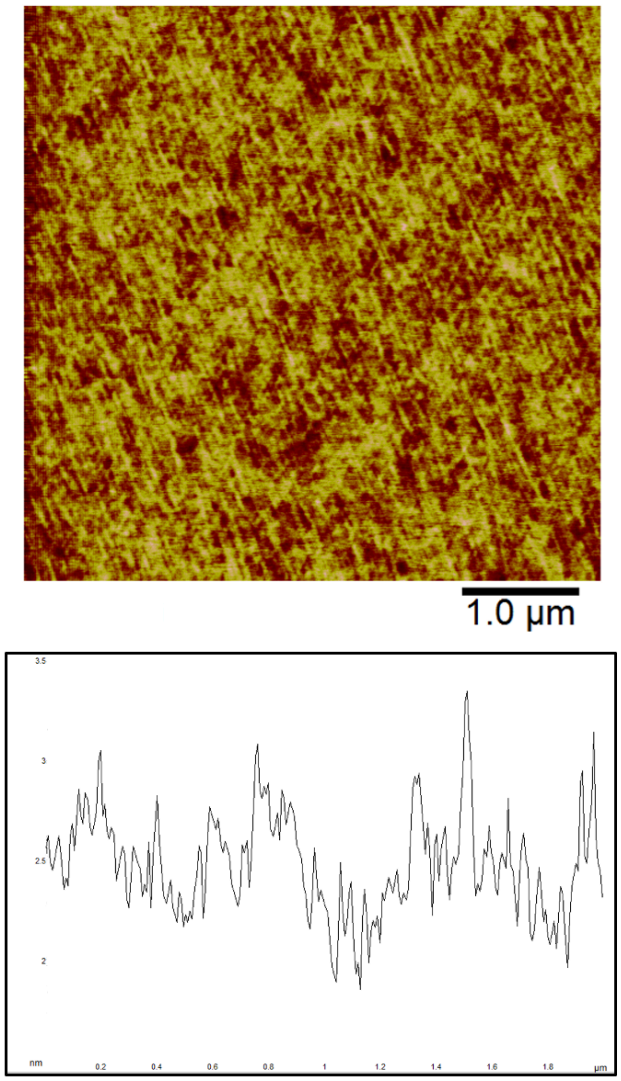

Figure 3.3: presents an AFM tapping mode hight image an NPOCC-APTES film formed on a silicon substrate, along with sample line section profile extracted from the same image.

3.4.2 Photodeprotection of NPPOC-APTES films (XPS, contact angles, FFM)

The elimination of the NPPOC protective group necessitates the use of light irradiation with a wavelength exceeding 320 nm[153]. Previous research performed by Alang Ahmed et al. investigated the kinetics of the photodeprotection process of NPPOC-APTES films on silicon surfaces under light sources with wavelengths of 325 nm and 365 nm[153]. It was anticipated that subjecting NPPOC-protected surfaces to UV light would lead to the formation of free amine groups on the surfaces. Simultaneously, this process would result in the liberation of the carbon dioxide and nitrophenylalkene byproduct (Scheme 3.2).

In the present work, a wavelength of 244 nm was employed, and contact angle measurements were utilized to measure the effects of photomodification on unpatterned samples by exposing the whole sample to UV irradiation. Figure 3.4 provides the correlation between contact angle and exposure for an NPPOC-APTES layer subjected to 244 nm irradiation, representing the relationship as a function of dose. It was noticed that as the exposure increased, there was a corresponding decrease in the contact angle. As a result, NPPOC groups are converted into more polar amines. At an exposure level of 3.0 Jcm^{-2}, the contact angle remained constant, indicating that the majority of the NPPOC group was eliminated.

The surface chemistry is influenced by UV wavelength, exposure time, and power, as these factors determine the energy delivered to the sample and the extent of photodeprotection. Shorter wavelengths, such as 244 nm, carry higher-energy photons, making them more effective at breaking chemical bonds like those in the NPPOC protective group. In contrast, longer wavelengths, such as 325 nm or 365 nm, have lower energy and require longer exposure or higher intensity to achieve the same level of NPPOC removal. Exposure time also plays a crucial role, as a longer duration allows more energy absorption, leading to increased NPPOC conversion into free amine groups. However, beyond a certain point, additional exposure does not cause further chemical changes, indicating that the process has reached completion. The power of the UV source affects the rate of reaction, with higher power delivering more photons per second, accelerating photodeprotection. If the power is too low, the process may be slow or incomplete, whereas excessive power or prolonged exposure could lead to material degradation. Therefore, optimizing these parameters is essential for efficient surface modification while minimizing unwanted side effects.

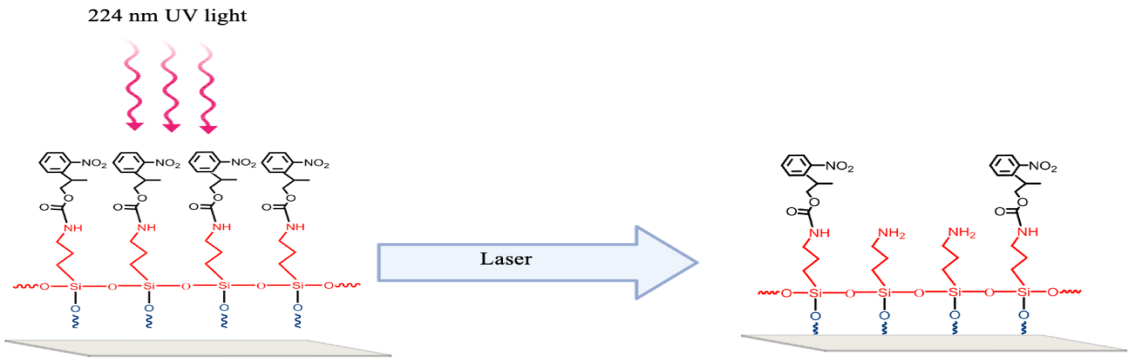

Scheme 3.2: Diagram illustrating the process of UV light-induced removal of NPPOC-APTES films through photodeprotection.

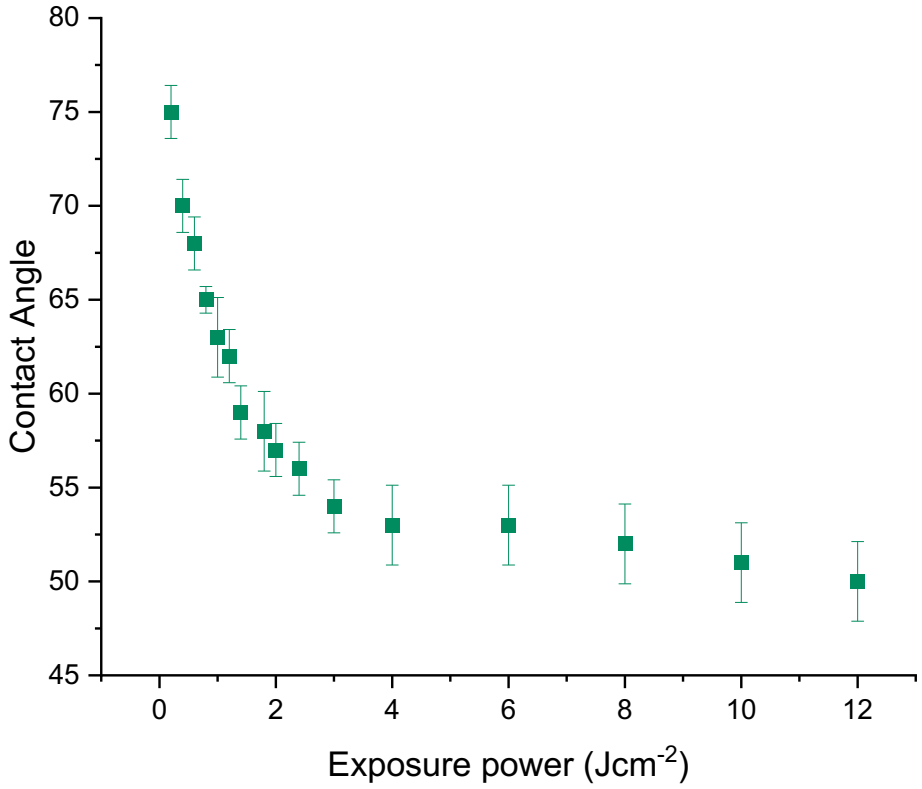

Figure 3.4: Contact angle of a photomodified APTAS-NPPOC film as a function of the dose.

Besides this, Figure 3.5 shows the utilization of X-ray photoelectron spectroscopy (XPS) to examine a sample of NPPOC-APTES film that was subjected to dose 3 Jcm^{-2}. The NO_2 peak was completely absent, indicating the complete removal of the NO_2 groups. Instead, a single component emerged at 400.5 eV, corresponding to NH_2 species. This observation confirms the successful completion of the photolysis reaction at the applied dose.

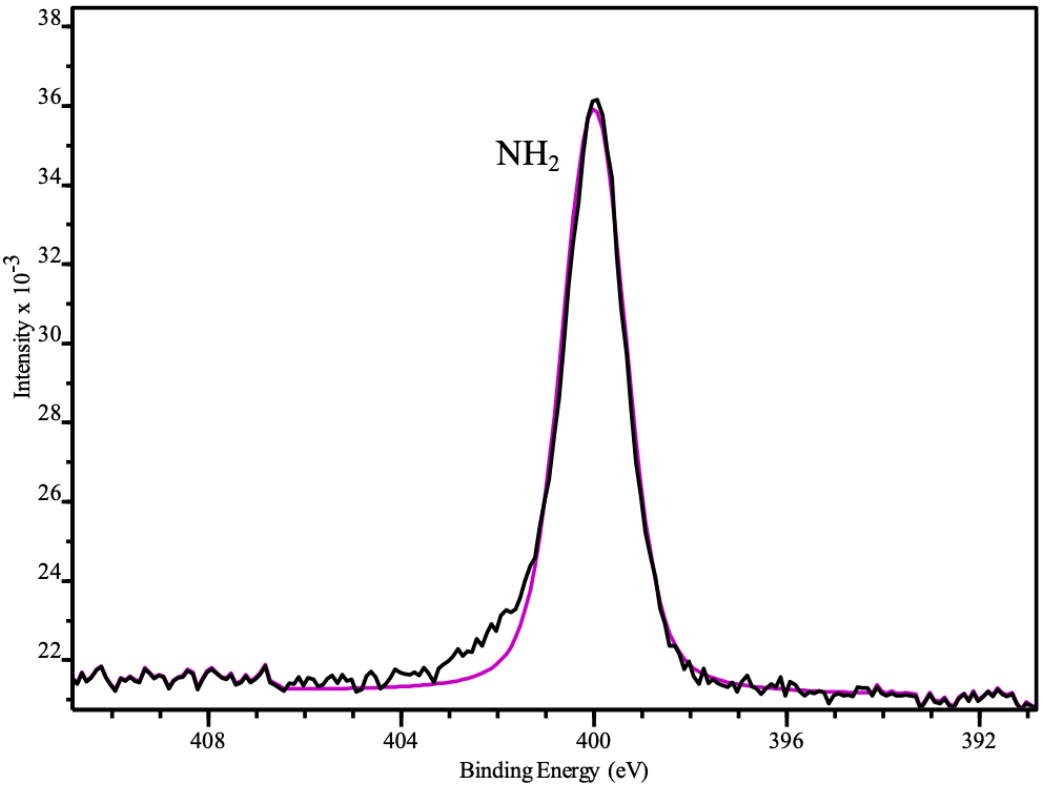

Figure 3.5: High resolution N1s XPS spectra of NPPOC-APTES monolayer following exposure to dose 3.0 Jcm^{-2}.

3.4.3 Micropatterning of NPPOC-APTES Monolayers

The siloxane films safeguarded by NPPOC were subjected to UV light exposure using masks to generate patterns at a micrometre scale. The impact of irradiation on surface composition was evaluated using friction force microscopy (FFM). The friction response was measured from friction loops acquired by performing forward and reverse scanning cycles along a single line using a contact mode microscope. The friction signal was obtained by subtracting in both directions the mean images, giving the resulting force twice the frictional force. Figure 3.6 demonstrates that the regions subjected to irradiation (squares) exhibited a more noticeable brightness contrast than those protected by masks (bars).

In the exposed areas, a greater contrast was apparent, which indicates an increase in friction force associated with an increased interaction among the AFM probe and amine groups generated during photodeprotection. This correlation agrees with a substantial amount of

research investigating the relationship between friction and surface-free energy in organic systems[191], [194].

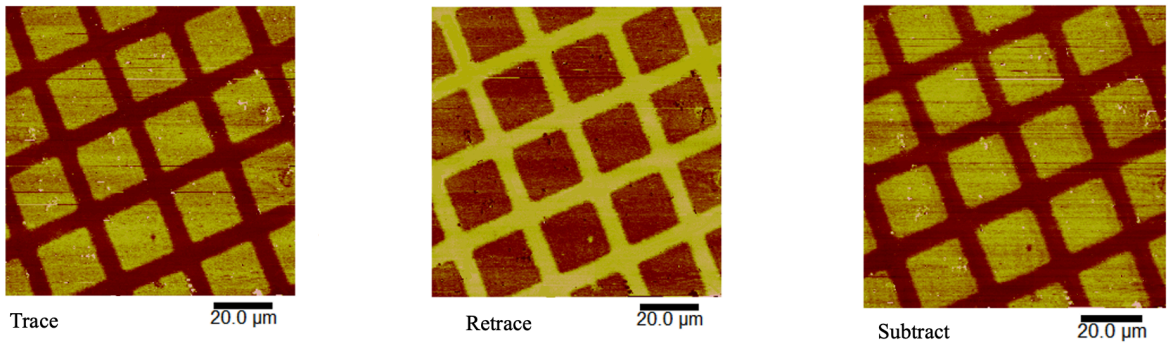

Figure 3.6: FFM scans of pattern modified NPPOC layers exposed to a laser 244nm, with (squares) indicating exposed areas and (bars) indicating masked areas.

3.4.4 Nanopatterning of NPPOC-APTES Monolayers

For the creation of nanopatterned NPPOC-APTES films, Interferometric Lithography (IL) was employed, utilizing a laser power of 1.2 mW. Various exposure dosages were administered, specifically 1, 3, and 6 J cm². The rotation stage was used to adjust the angle between the laser beams to 10° and 25°, resulting in the formation of patterns with periodicities of 690 nm and 350 nm, respectively. The Full Width at Half Maximum (FWHM) measurements indicated a width of 270 nm for the 10° angle and 190 nm for the 25° angle.

To evaluate the impact of irradiation on the surface composition, atomic force microscopy (AFM) and friction force microscopy (FFM) were employed. AFM was used to capture the topographical changes on the surface at the nanoscale, providing detailed imagery and surface height information (Figure 3.7). FFM, on the other hand, was utilized to assess the changes in frictional properties induced by the nanopatterning process. In Figure 3.8 the frictional response was systematically measured by acquiring friction loops through forward and reverse scanning cycles along a single line using a contact mode microscope. By subtracting the mean images in both scanning directions, the resulting force, which is twice the frictional force, was determined. The detailed procedure involved first aligning the laser beams to achieve the desired interference pattern. For a 10° angle between the beams, a pattern period of 690 nm was produced, while a 25° angle yielded a finer pattern with a 350 nm period. The FWHM values provided additional insights into the sharpness and resolution of these patterns, with narrower widths at higher angles indicating more defined nanopatterns.

After patterning, AFM analysis revealed the surface morphology changes, highlighting the periodic structures and any surface roughness alterations due to the varying exposure dosages. These images provided a visual confirmation of the successful patterning and allowed for the assessment of uniformity and precision of the nanopatterns. FFM further elucidated the impact of these patterns on surface friction. By performing forward and reverse scans, the frictional properties were mapped, showing variations corresponding to the different exposure dosages and patterning conditions. This detailed frictional analysis is crucial for understanding how nanopatterning influences the material's performance in applications where surface interactions play a critical role. Through this comprehensive approach, the study demonstrated how varying the exposure dosage and angle between the laser beams in Interferometric Lithography can accurately create the nanopatterns on NPPOC-APTES films. The combined use of AFM and FFM provided a reliable analysis of both topographical and frictional changes, offering insights into the material's behaviours and potential applications in fields requiring accurate surface engineering and control.

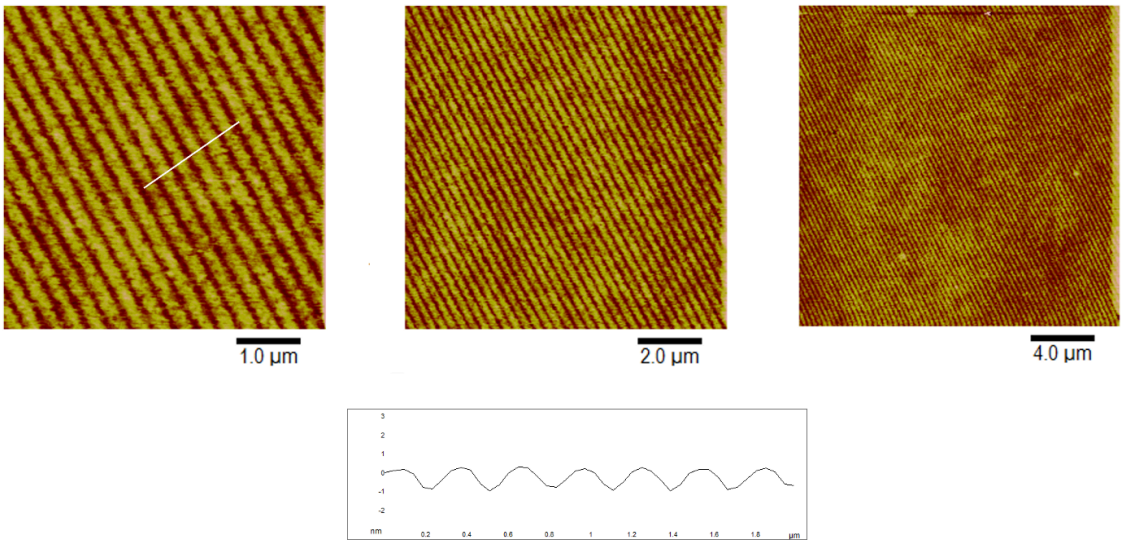

Figure 3.7: AFM scans of pattern modified NPPOC layers exposed to Interferometric Lithography (IL) at angle 25, with a sample line section profile showing peaks with a depth of 1 nm.

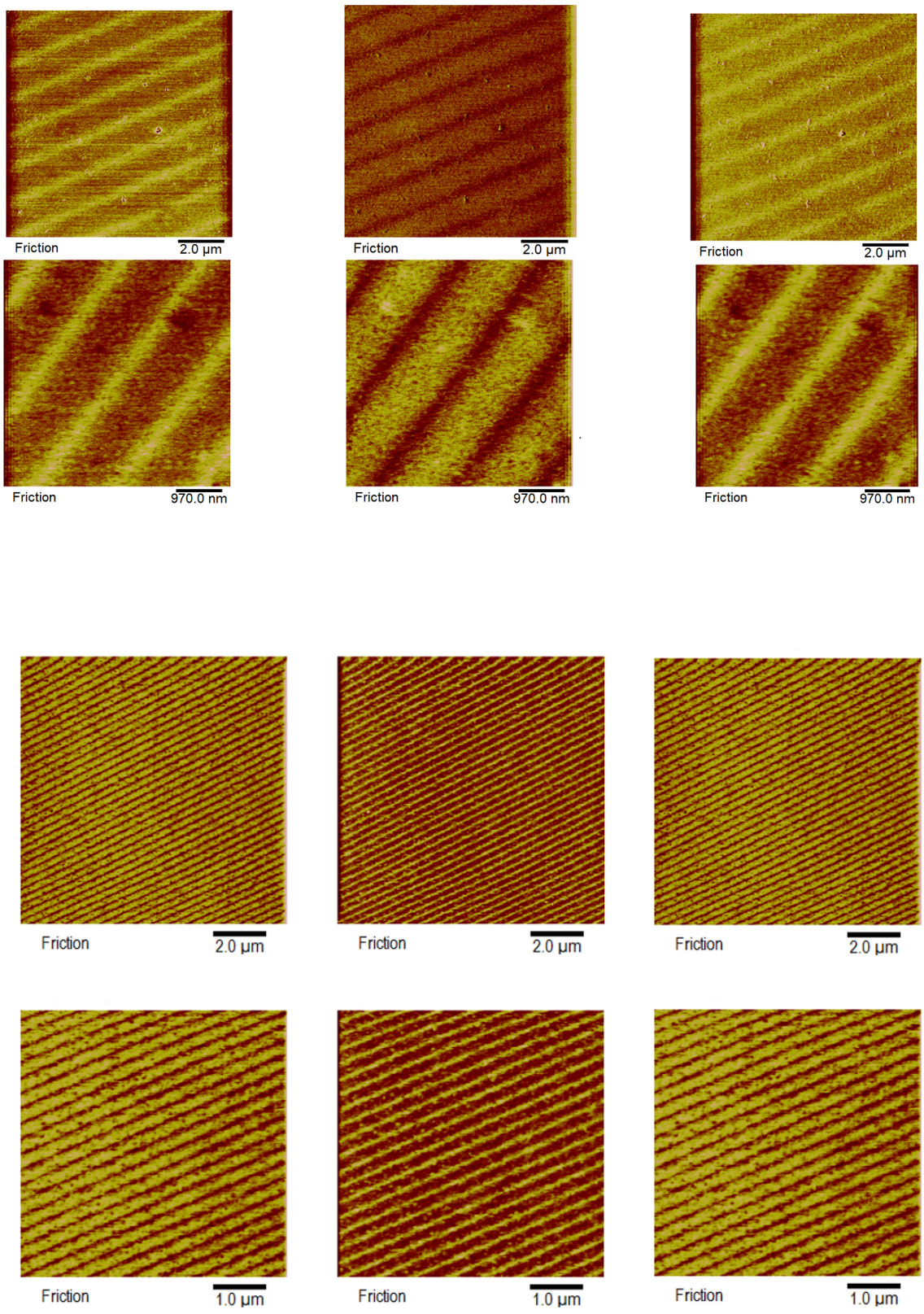

Figure 3.8: FFM scans of pattern modified NPPOC layers exposed to Interferometric Lithography (IL). 10 and 25

3.4.5 The derivatisation of deprotected NPPOC-APTES films by reaction with trifluoroacetic anhydride (TFAA)

A solution of trifluoroacetic anhydride (TFAA) in dry THF was applied to NPPOC-APTES surfaces after photodeprotection to provide trifluoroacetamide-functionalized surfaces, which were studied by XPS and contact angle measurements. As a result of this reaction, the anhydride would form an amide bond with the deprotected amine (Scheme 3.3). According to Figure 3.9, water contact angles of NPPOC-treated surfaces vary as a function of exposure time in a TFAA solution after deprotection, when presented with a dose of 3 J cm^{-2} at 224nm. In the beginning, the contact angle of the treated samples dramatically increased, followed by a gradual slowdown until they finally achieved a maximum angle of 95° after a period of three hours. In the three hours that followed, the contact angle remained unchanged. It is reasonable to conclude that the derivatization values obtained here are familiar with those found by other researchers [153]

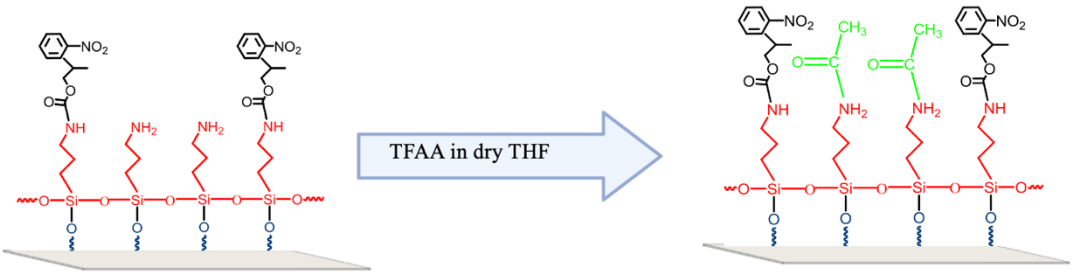

Scheme 3.3: Schematic diagram showing the selective modification of exposed regions in photopatterned NPPOC-APTES films.

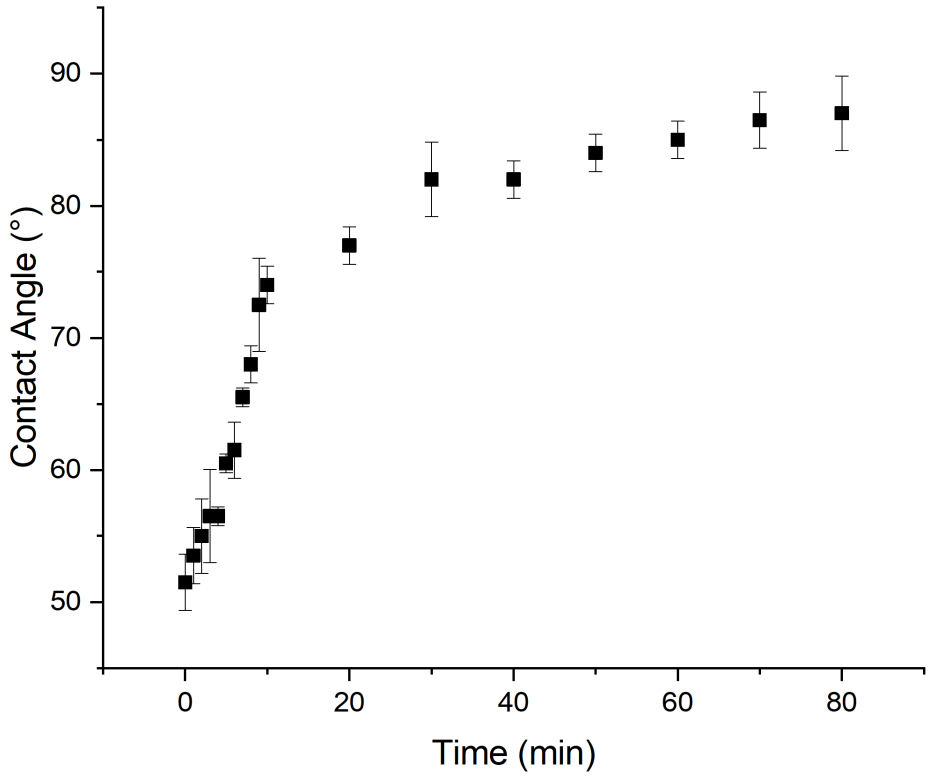

Figure 3.9: Variation in the water contact angle with the time of immersion of deprotected NPPOC-APTES films in a solution of TFAA in dry THF.

To further clarify, A C1s XPS spectrum has been collected for derived layers of NPPOC-protected silane after photodeprotection at 224 nm, which are shown in Figure 3.10. In this experiment, the binding energy peaks at 285.0 eV and 286.45 eV are due to alkyl carbon chains (-C-C-C-) and (-C-N-), respectively. Additionally, two peaks at 289.2 and 293.1 eV, occurring in a ratio of 1:1, are qualitatively correlated with amide (N-C=O) and (F-C-F) and indicate amine-anhydride reactions.

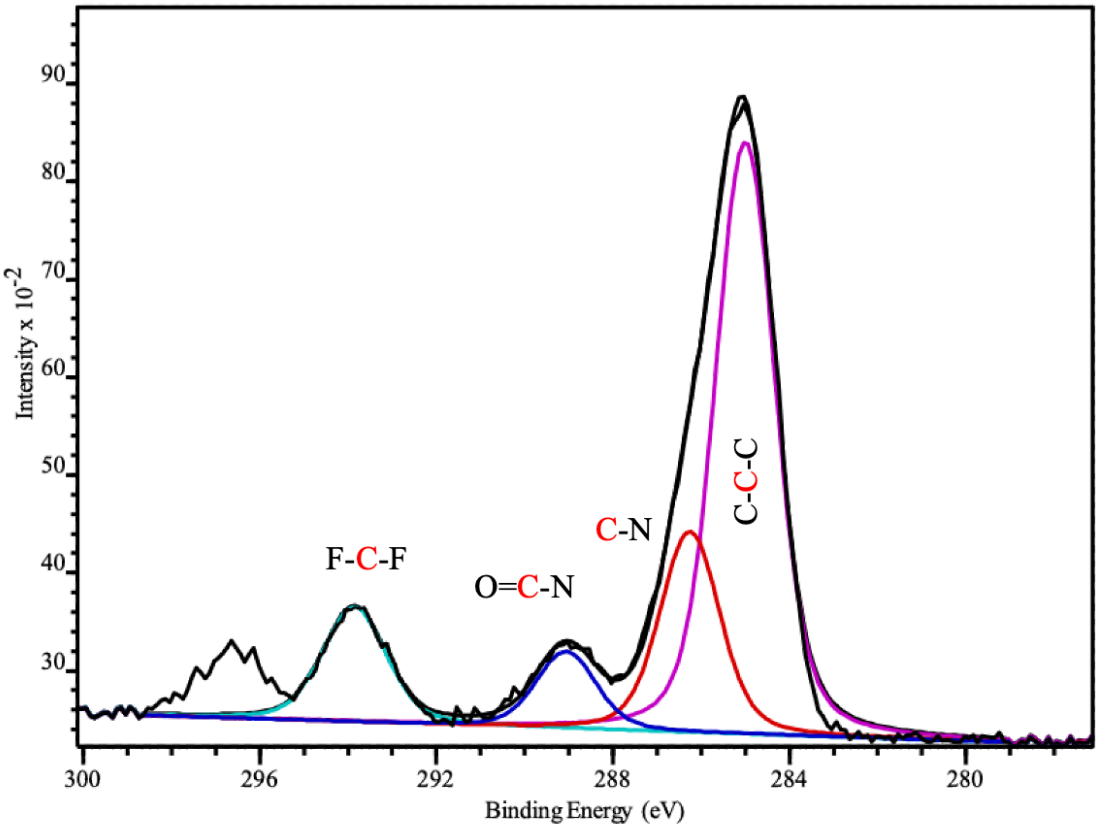

Figure 3.10: shows an analysis of the C1s XPS spectrum of deprotected NPPOC silane films treated with TFAA solution.

3.4.6 The derivatisation of deprotected NPPOC-APTES films by reaction with Bromo (isobutyryl bromide)

Following UV exposure, the NPPOC structure is split to produce a primary amine, which is extremely capable of reacting with electrophiles. In a specific case, the process of synthesis of 2-bromoisobutyramides through treatment of the amine with reacted 2-bromoisobutyric molecules is of great attention. The reason for this is that these can act as ATRP initiators (Scheme 3.4).

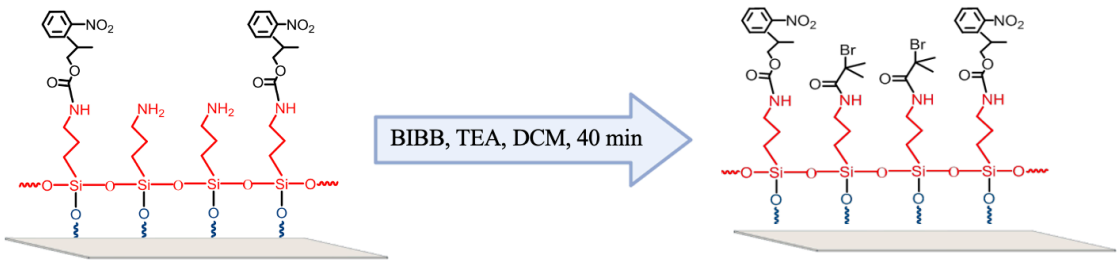

Scheme 3.4: The reaction of 2-bromoisobutyryl bromide with NPPOC-deprotection surfaces.

Under the influence of U.V. light at a wavelength of 244 nm with a dose of 3.0 J cm-2, NPPOC-APTES layers were completely deprotected in order to demonstrate that the free amine groups were functionalized in a successful manner with BIBB compounds. Both contact angle measurements and XPS were performed on the deprotected samples after derivatization with BIBB compounds. For a uniform surface, the contact angle was decreased from 78.0 to 57.0±3 following the photodeprotection, and then it was raised to 68.0±3 after the halogenation treatment.

There are three peaks in the high-resolution C1s spectrum at binding energies of 285.0 eV, 286.68 eV, and 288.65 eV, representing the (-C-C-C-), -C-N/-C-Br, and (N-C=O) bonds, respectively (Figure 3.11). In this case, the existence of an additional peak for the C-Br component indicates that BIBB has derivatized the NPPOC molecule. According to the results obtained here, the derivatization values are comparable to those previously [153].

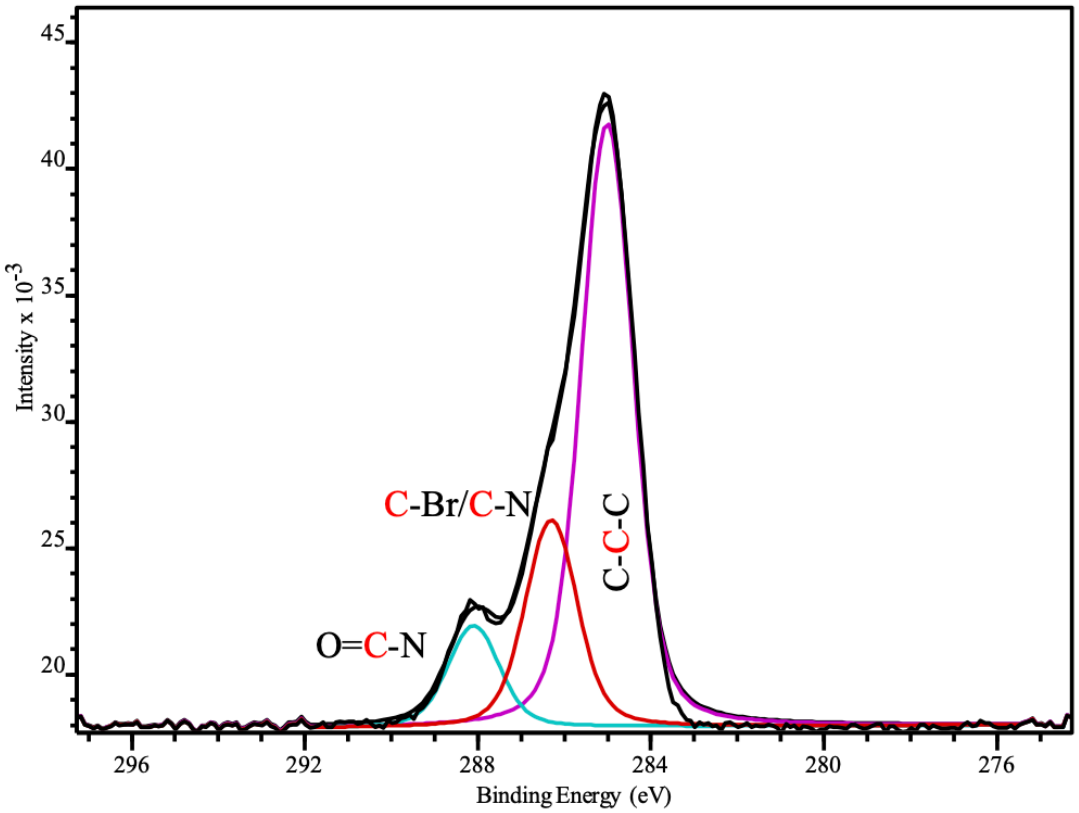

Figure 3.11: High-resolution C1s spectra was observed for a photo-deprotected NPPOC amino silane layer modified with BIBB compound.

The siloxane films protected by NPPOC were exposed to UV light using masks to create micrometer-scale patterns. Subsequently, these samples were immersed in a BIBB solution. The effect of this immersion on the surface composition was analyzed using friction force microscopy (FFM). The friction response was determined by friction loops obtained from forward and reverse scanning cycles along a single line with a contact mode microscope. The friction signal was calculated by subtracting the mean images in both directions, resulting in a force value that is twice the frictional force. Figure 3.12 illustrates that the regions exposed to UV light (represented by squares) displayed a more pronounced brightness contrast compared to those shielded by masks (represented by bars). This increased contrast in the exposed areas suggests a higher friction force, which is associated with the enhanced interaction between the AFM probe and the bromine groups generated during the immersion. This observation aligns with extensive research on the relationship between friction and surface-free energy in organic systems [215], [216]

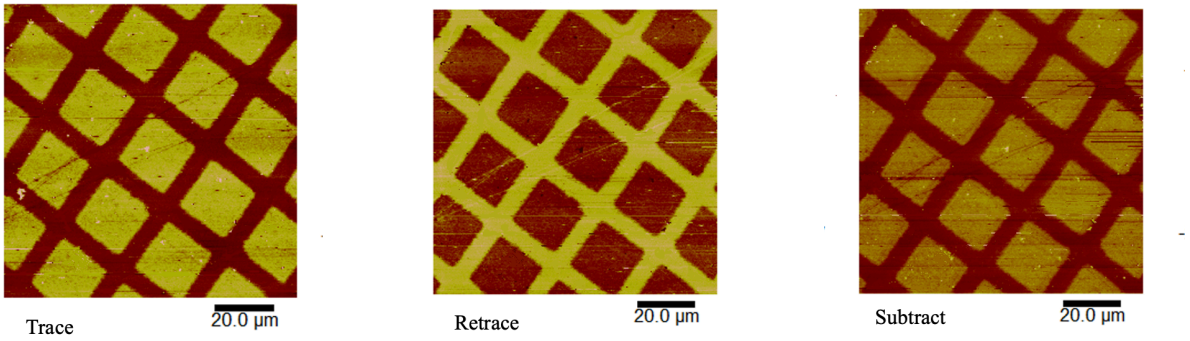

Figure 3.12: FFM scans of pattern modified NPPOC layers immersed in a BIBB solution.

3.4.7 Synthesis of PDMA and polymerization reaction

There were several literature reports that served as the basis for the brush synthesis protocol[217], [218]. The PDMA brushes were synthesized at 90 °C in DMF from NPPOC-Photodeprotection surfaces after being attached to a bromine initiator and polymerized via surface-initiated atom transfer radical polymerization. Schematic 3.5 illustrates the chemical reactions expected during PDMA polymer synthesis. The polymerisation conditions, which contained monomer to catalyst [DMA]:[CuBr]:[HMTETA] molar ratio = 300: 1.0: 1.5: ratio, solvent type, temperature, and initiator density remained constant. To determine the dry thickness of the PDMA brushes over polymerisation time, the kinetics of growth of the polymer brushes were examined using ellipsometry (Figure 3.13). This figure shows that polymer brush thicknesses of 13 to 24 nm can generally be reached within 10 to 30 minutes. Afterwards, the thickness of the PDMA polymer chains grew with the polymerisation time, extending to 36 nm after 1.5 h of the synthesizing process.

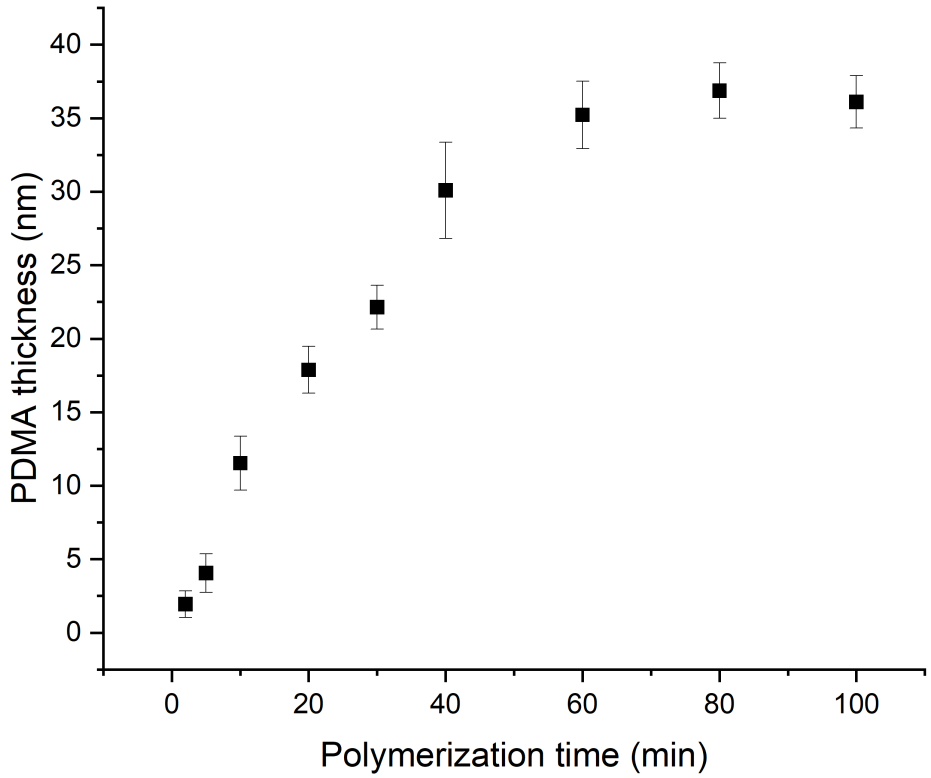

Figure 3.13: Variation in ellipsometry dry thickness of PDMA brushes with producted by SI-ATRP AS a function of polymerisation time.

Polymerization processing of PDMA brushes increased silicon's static water contact angle without modifications from 0° to 39° after 1.5 hours. An analysis of the C1s and N1s, XPS spectra of PDMA brushes 24nm in thickness was carried out in (Figure 3.14). The XPS C1s spectra were evaluated by fitting three components with binding energies of 285.0 eV, 286.3 eV, and 288.7 eV. These energy values relate to (-C-C-C-), (C-O/C-N), and (O=C-O), respectively. In this case, these energy values relate to C-C-C, C-O/C-N, and O=C-O, respectively. The calculated atomic ratios for these elements were 4.1:2.7:1, which is close to the theoretical prediction of 4:3:1. XPS O1s shows doublet single at 532.1 and 533.7eV which attributed to (C-O) and (C=O), respectively. As a result of the N1s spectra calibration, one peak was found at 400.0 eV. This peak was attributed to C-NH_2 in the PDMA brushes (Figure 3.14). The result indicates a good agreement with another research[219].

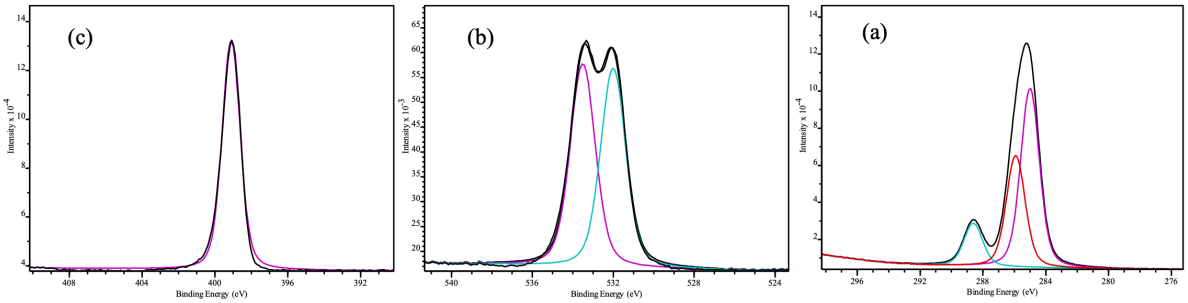

Figure 3.14: High-resolution (a) C1s spectrum, (b) O1s spectrum and N1s spectrum for PDMA brushes with a dry thickness of 24 nm.

The AFM tapping mode profile of unpatterned PDMA brushes with a dry thickness of 24 nm is shown in Figure 3.15. The PDMA polymer has grown uniformly across the substrate, as evidenced by the low surface roughness. The grafted PDMA polymer brushes had approximate roughness of 0.358 nm/0.265 nm, indicating smoothness and high grafting density.

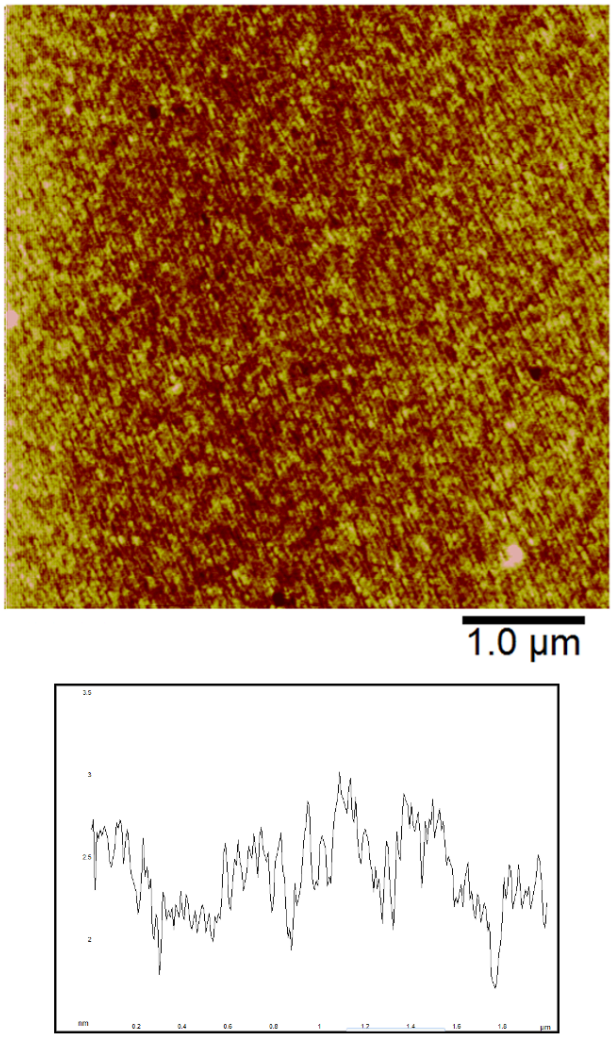

Figure 3.15: AFM tapping mode height image of unpatterned PDMA brushes with a dry thickness of 24 nm.

3.4.8 Growth of PDMA from uv-patterned surfaces formed by mask-based lithography

A photomask was utilized to expose NPPOC-APTES samples via a 2000 mesh grid to generate micrometre-sized patterns. To grow the PDMA brush, the exposed (square) areas were etched with BIBB and SI-ATRP was conducted (Scheme 3.5). Once that has been done, the PDMA pattern samples were measured by using tapping modes AFM and FFM (Figure 3.16). An analysis of cross-sectional images demonstrated significant height contrast between PDMA brush areas (squares) and NPPOC areas (bars), indicating PDMA polymer brush growth is

spatially selective. Figure 3.17 illustrates FFM's ability to represent the distribution of various functional surface groups. The images of the exposed samples show a clear pattern for friction forces. The strong contrast between the exposed and masked areas is owing to the variation in contact between the AFM tip and the tail groups of NPPOC-APTES and polymer molecules. Inside the squares, a SAM of the brominated initiator has formed and then grows the PDMA polymer from it. These tail groups have a significant interaction with the AFM tip, resulting in frictional resistance to the motion of the tip and therefore a bright contrast in the image is observed. During exposure, the area between the squares (bars) was masked, and the NPPOC-APTES molecules remained intact in these regions. The groups of the NPPOC-APTES tail showed lower friction than the polymer, therefore those regions appear darker.

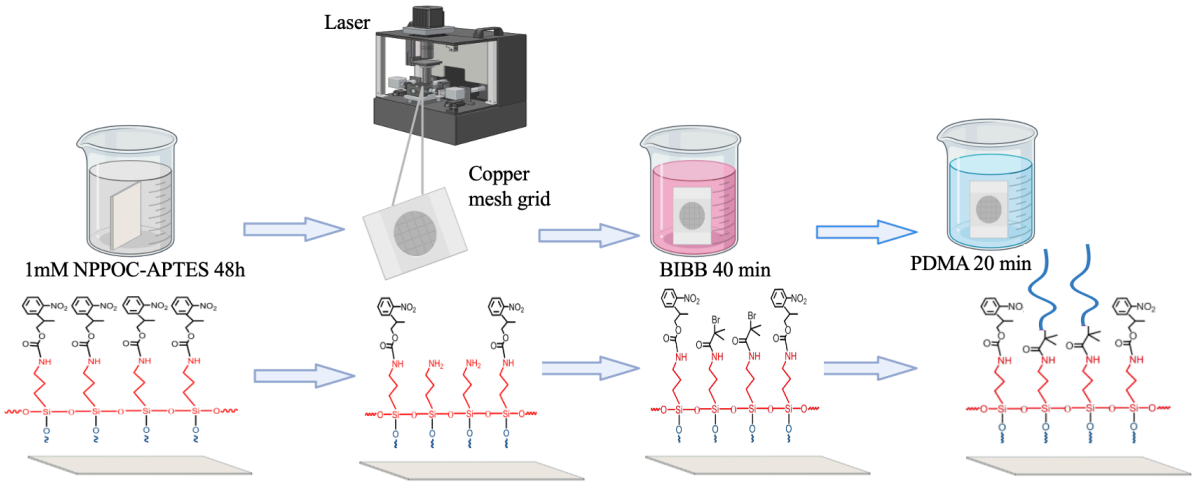

Scheme 3.5: Schematic representation of PDMA gown from a patterned NPOOC-photo-deprotected amino silane substrate. Through a mask, UV light was employed to eliminate the NPPOC groups from the exposed sections of the SAM. By derivatizing exposed amines with BIBB, PDMA brushes were synthesized from exposed regions.

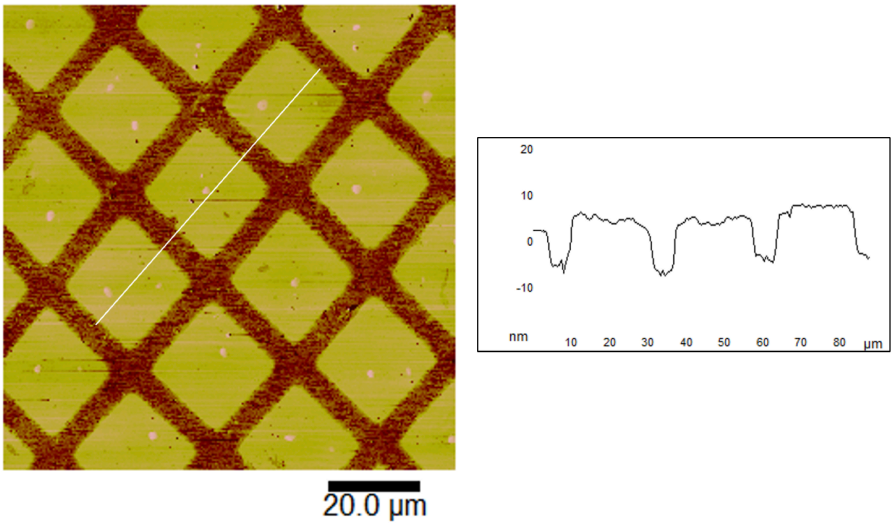

Figure 3.16: AFM tapping mode height image of a micropatterned PDMA brush generated on a patterned NPPOC-photodeprotected substrate utilizing SI-ATRP.

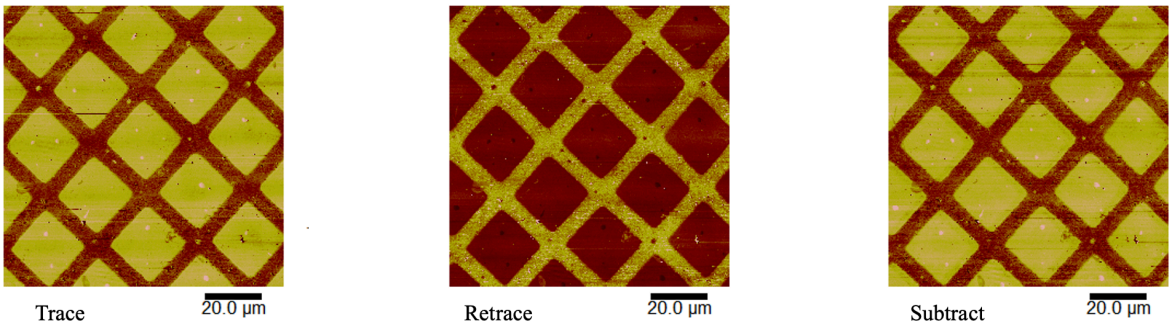

Figure 3.17: FFM contact mode profile of a micropatterned PDMA brush generated from a patterned NPPOC-APTES film by SI-ATRP.

3.4.9 Growth of PDMA from uv-patterned surfaces formed by interferometric lithography

In this study, Lloyd's mirror with a double-beam interferometer was utilized to fabricate nanometre-sized structures for PDMA brushes by employing interferometric lithography (IL). Through the rotation stage, different nanopatterns were fabricated by adjusting the angle between these beams. NPPOC films were exposed at angles of 10 and 25 to achieve nanometre structures. In Figures 3.18 and 3.19, it is shown that these PDMA nanopatterns are investigated using AFM to determine their chemical properties. The terminal NPPOC group was deprotected in areas subjected to a maximum in the interferometer. In the following stages,

PDMA polymer brushes formed from these areas after halogenation with BIBB. Additionally, in this AFM image, minimum exposure to the interferometer prevented polymer brush growth in areas that contained a protecting group. The PDMA polymeric sections in these patterns were broader than the unmodified areas, according to a cross-sectional measurement. For PDMA brushes nanopatterned at 10 and 25 angles, the feature periods were 690 nm and 350 nm, respectively.

According to Kaholek et al, brush height tends to decrease as the pattern's feature scale decreases 304. It was hypothesized by these workers that “at constant grafting density a polymer brush in good solvent adopts a vertically less ordered and laterally more extended conformation, induced by the lack of lateral restraint the brush experiences at its boundaries, leading to less chain crowding and thus less chain stretching.” Furthermore, it is possible for polymer structures generated from micropatterns to exhibit greater relaxation near the edges of the pattern. The results of the study indicated that PDMA brushes generated from such nanopatterns were considerably thinner than PDMA brushes generated from micropatterns under similar conditions. Topographical pictures demonstrate nanopatterned PDMA brushes for angles 10 and 25 with a line width (FWHM of 270 nm and 190 nm) (heights of 6 nm and 3.5 nm) respectively, while the height in the micropattern PDMA brushes, under similar circumstances, was 13 nm.

Angle 10, dose 3 Jcm^{-2}

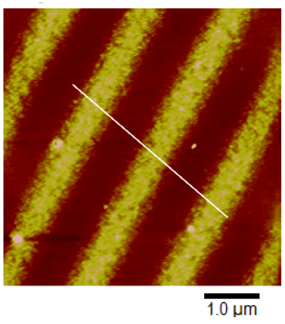

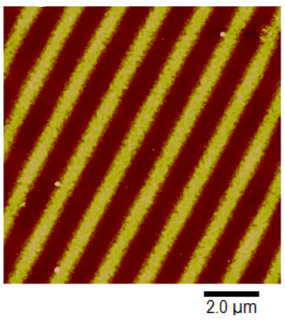

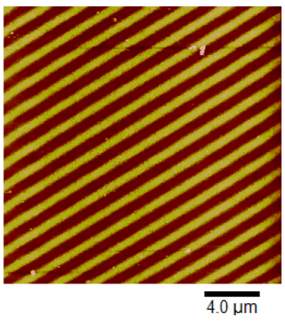

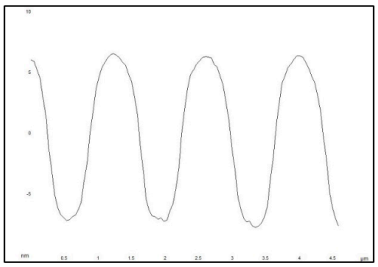

Angle 10, dose 6 Jcm^{-2}

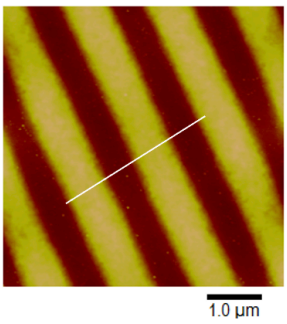

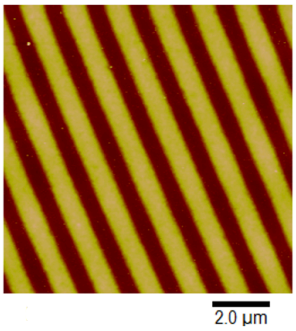

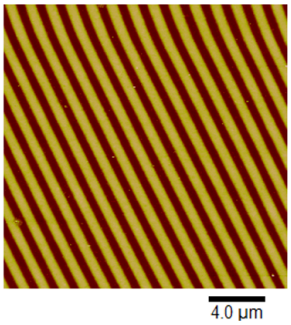

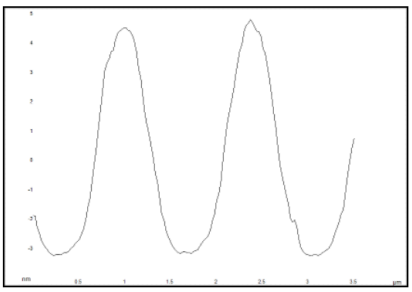

Angle 25, dose 3 Jcm^{-2}

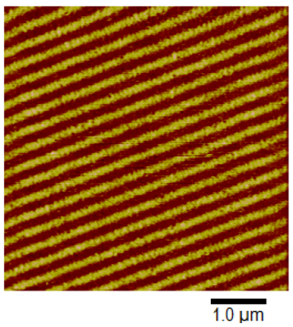

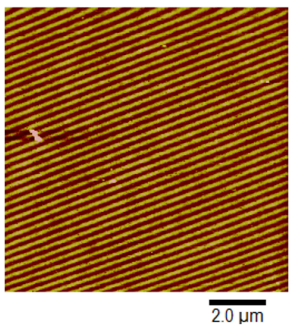

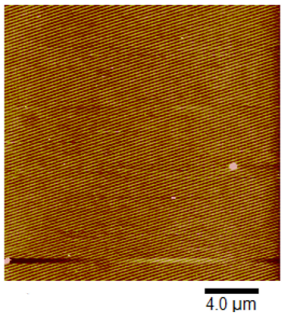

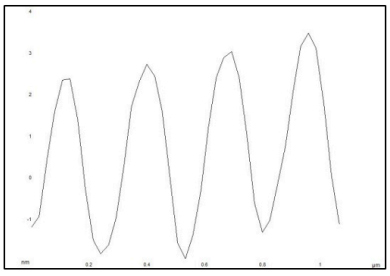

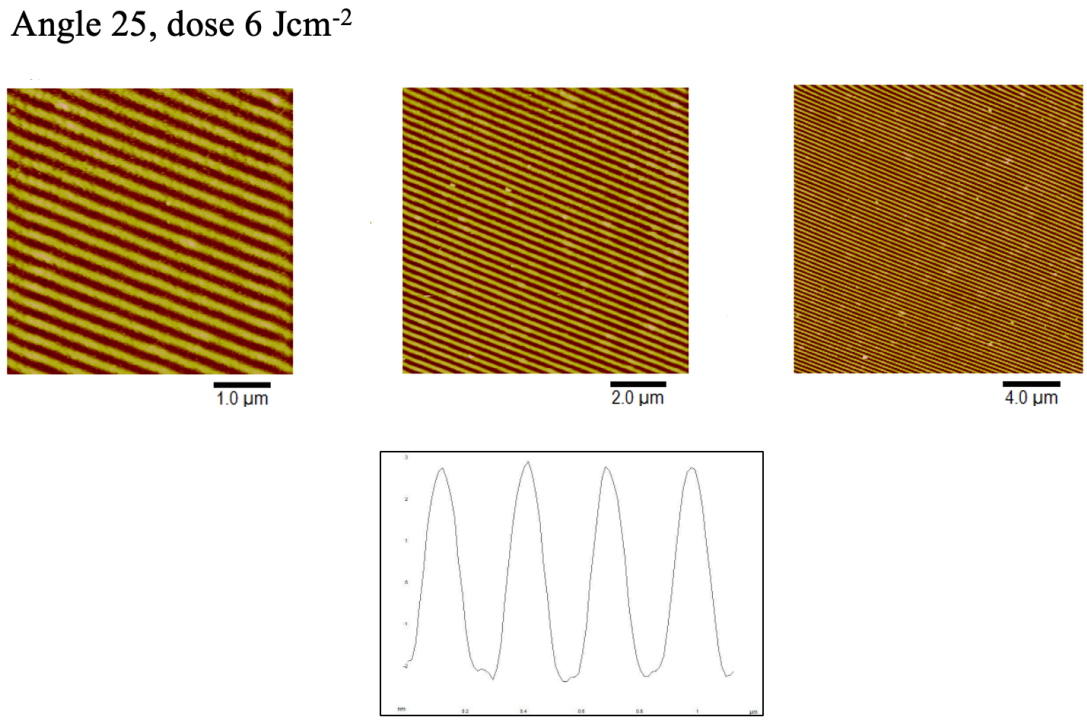

Figure 3.18: AFM hight image of a nanopatterned PDMA brush generated on a nanopatterned NPPOC-deprotected substrate utilizing an angle of 10 and 25.

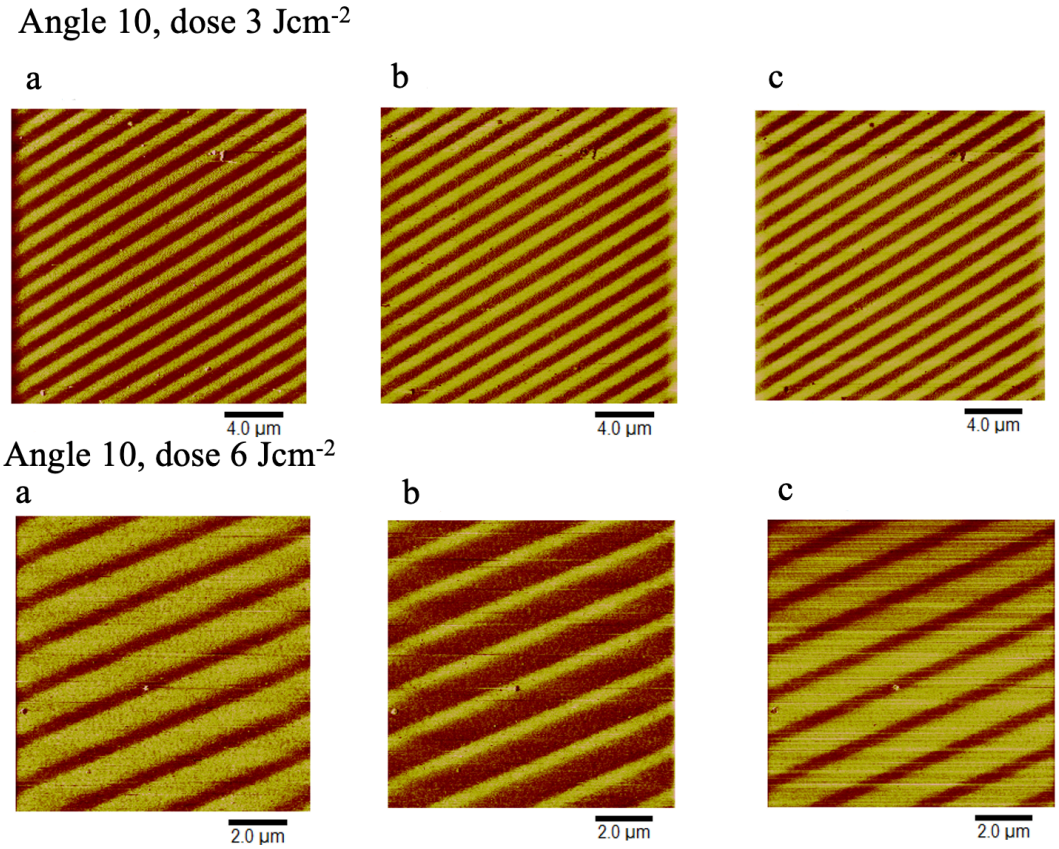

Figure 3.19: FFM contact mode profile of a nanopatterned PDMA brush generated on a nanopatterned NPPOC-deprotected substrate utilizing an angle of 10 a: lateral force forward, b: lateral force forward reverse and c: the subtract image.

3.4.10 Swelling behaviour of PDMA brushes in water

A friction force microscope was employed to investigate the frictional behaviour of PDMA brushes as a function of their diameters. To measure the performance of PDMA brushes, water was used as a solvent, which is considered a suitable solvent for the PDMA. Therefore, it would be reasonable to assume that hydrogen-bonded water molecules are responsible for solvating PDMA molecules. There should be a consideration for the fact that water bound to polymer chains can lead to steric hindrance and osmotic [215]

To enable quantification of friction data, friction loops were acquired in which the probe completed a complete forward/reverse cycle along a single scan line. The true friction signal

in such a friction loop is equal to half the difference between the friction force measured in the forward and reverse directions (Figure 3.20).

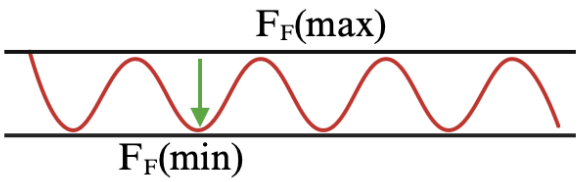

Figure 3.20: Friction loop as half the difference between the peak maximum and the peak minimum friction force.

During an FFM scan, the probe moves forward along a single scan line and then reverses along the same path. As the probe interacts with the surface, frictional forces cause variations in its lateral deflection, resulting in different signals for the forward and reverse directions. These variations are recorded and plotted, generating a friction loop that represents the lateral force as a function of scan position. The true friction force is determined by analysing the difference between the maximum and minimum lateral forces in both directions.

For the trace image (forward scan), the friction is given by:

$$\Delta FT = FF(\text{max})\text{T} - \text{FF}\ (\text{min})\text{T}$$

In this equation, F(max) represents the peak maximum friction force, and F(min) represents the peak minimum friction force.

In a similar manner, friction according to the reverse image (backward scan), can be calculated as follows:

$$\Delta\text{FR} = FF(\text{max})\text{R} - \text{FF}\ (\text{min})\text{R}$$

Consequently, the final friction force can be obtained as follows:

$$\Delta\text{FF} = \Delta\text{FT} - \Delta\text{FR}$$

This calculation removes offsets due to instrumental effects and provides the net friction force acting on the probe. The larger the difference between forward and reverse forces, the higher the friction. If the values of ΔFT and ΔFR are similar, the net friction force is small, indicating

a low friction surface. This method allows for quantitative comparison of friction on different materials or surface modifications.

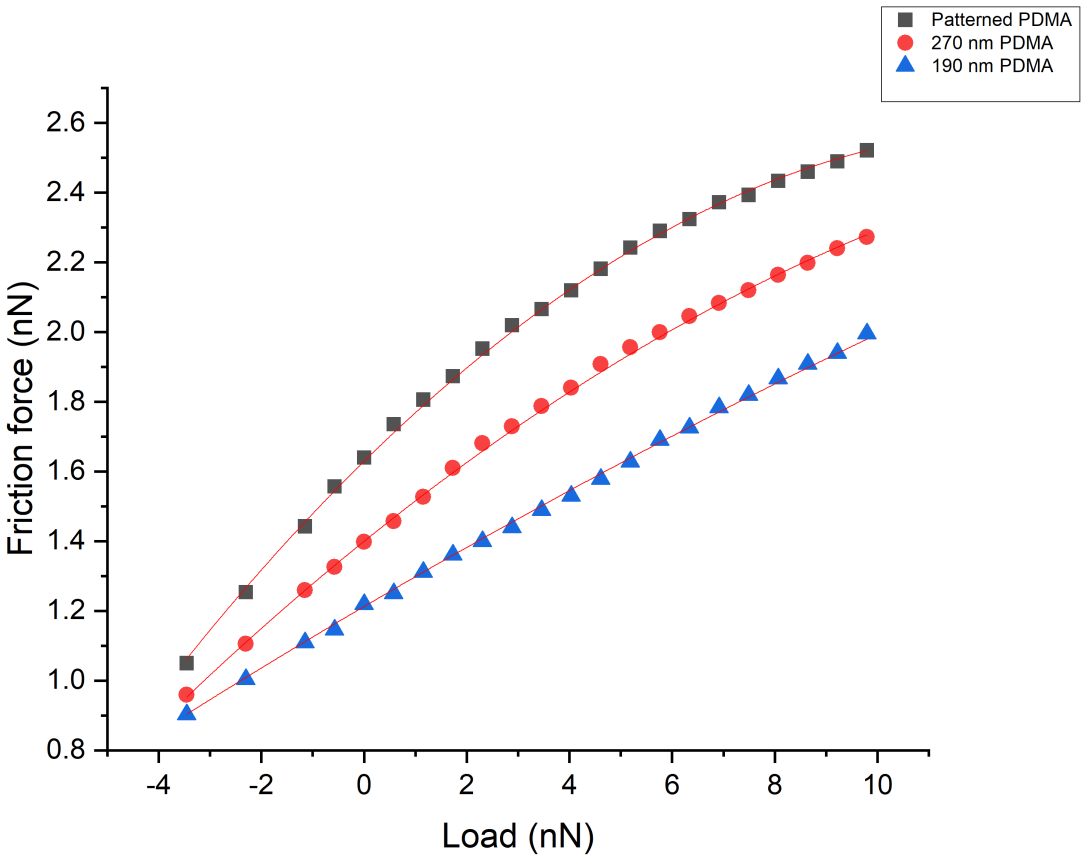

Figure 3.21: Dependence of the friction force on the load in water for micropatterned and nanopattern PDMA brushes.

It was necessary to perform all measurement procedures manually. The friction load data were interpreted by assuming that the friction force is the sum of a load-dependent term, due to molecule ploughing, combined with a shear term associated with sampling-tip adhesion interaction (equation 1.31). Figure 3.21 shows the friction force as a function of the applied load in water for PDMA brushes grown under identical conditions from three different patterned structures. Because the polymerisation conditions used were identical, the degree of polymerisation (the length of the surface-grafted polymer chains) should be similar in all cases; thus, differences in the friction-load behaviour are substantially attributable to differences in

the conformations of the polymer molecules grown from the different patterns. It can be seen from Figure 3.21 that there is a nonlinear relationship between the friction force and the load in water for all the PDMA samples that were examined. The largest friction force at a given load was obtained for the polymer grown from a micropatterned surface. In these structures, the polymer chains in the initiator-functionalised regions are expected to have the same conformations as polymers grown from an unpatterned initiator film. The friction force measured for the polymer grown from nanopatterned initiators is smaller and decreases as the feature dimensions decrease. For the narrowest lines studied, the friction-load plot approaches linearity. This indicates that as the polymer pattern width decreases, molecular ploughing begins to dominate the contact mechanics, whereas for the micropatterns, adhesive sliding is dominant (i.e., the shear term in equation (1.31) is dominant).

Adhesion forces for these samples are shown in Figure3.23. Consistent with the above explanation, the adhesion force is largest for the micrometre-scale pattern and smallest for the nanolines with the smallest line width.

While a swollen PDMA brush is expected to be highly solvated in water, and to have a small work of adhesion (defined as the work done in separating unit area of interface), the swollen brushes are expected to have low elastic moduli and the contact area may thus be large. Consequently, the net adhesion force may be larger despite the smaller work of adhesion. In contrast, the nanopatterned brushes are predominantly collapsed, and the net adhesion force is smaller because the contact area is also significantly smaller.

The data in Figure 3.21 were fitted using equation 1.31. By applying this equation, the friction force (F_F) is plotted as a function of the normal force (load) (F_N). The tip radius (R) was 20 nm, and the adhesion forces (F_a) was reported in figure 3.23. The surface shear strength (τ) was determined from the fits to the data (Figure 3.23). it can be seen that the surface shear strength obtained from modelling the friction-load data in Figure 3.23 is correlated closely with the adhesion forces. This supports the explanation given above, that for the micropatterned brushes, sliding is dominated by shearing, due to the enhanced area of contact between the probe and the surface grafted polymer layer. This explanation is consistent with earlier work by Zhang et al on PMPC layers, in which it was also concluded that fully swollen brushes yielded unexpectedly large adhesion forces, despite their being expected to have smaller works of adhesion, a phenomenon attributed to the small modulus of the swollen brush[220].

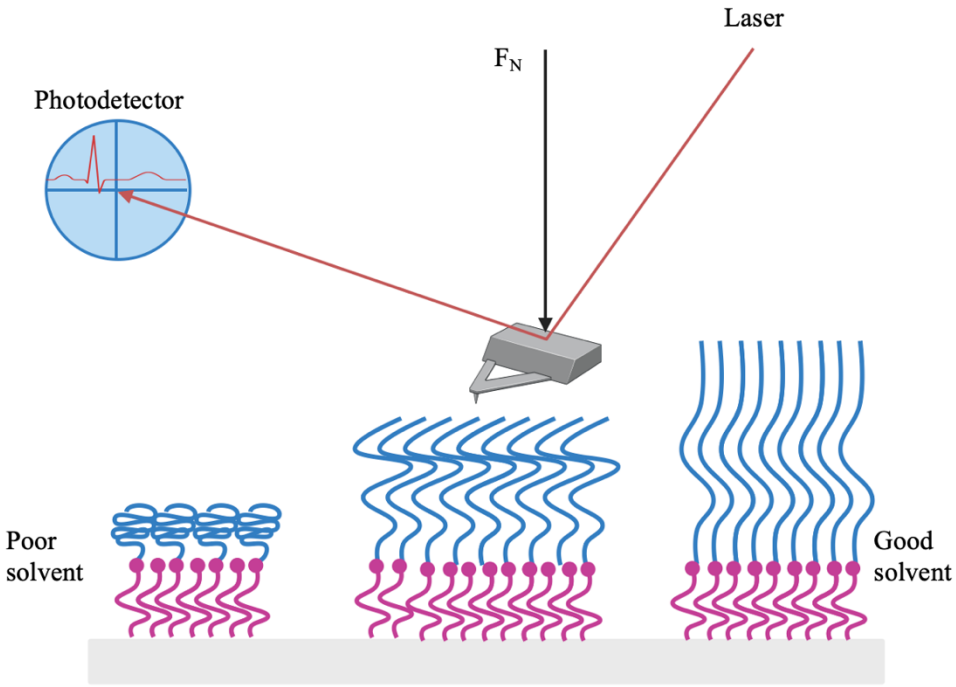

Figure 3.22: Schematic diagram showing how changes in swelling of the surface-grafted polymers lead to changes in their conformations in different solvents.

In general, the peak friction force of a polymer decreases as the size of its structure becomes smaller. As far as friction values are concerned, PDMA brushes with micropatterns recorded the highest values. As the feature size of PDMA brushes decreases, the friction formed changes in the following manner: ΔFF PDMA micrometre pattern > ΔFF 270 nm FWHM > ΔFF 190 nm FWHM. A variable conformation of the brush can be attributed to variations in the pattern dimensions of the PDMA brush. It is evident from Figure 3.21 that the frictional force measurements correlate directly with the feature size of PDMA brushes. A reduction in the contact area between the tip and surface is thought to result from a decline in the density of grafted polymer or the size of its footprint. Consequently, as the density of grafted polymer decreases, fewer PDMA polymer molecules are available to interact with the tip, leading to reduced contact between the tip and surface. Moreover, a decrease in footprint size limits the ability of the tip to contact the surface, thus diminishing the overall contact area. This behaviour is thought to be caused by the grafted chains on the boundary of the polymer lines shortening or stretching beyond the ungrafted regions, a phenomenon illustrated in Figure 3.22. In

consequence, the polymer thickness at the centre footprint has been reduced. Therefore, the contact area between a polymer chain and tip diminishes, reducing their interaction strength. Additionally, it is possible to physically interact between the overlapping brush sections and those without polymers. The tip-surface contact and the energy dissipation rate could also be affected due to this additional factor. There may be less crowding occurring in the polymer brush areas, particularly at the perimeter patterns, as the separation between the polymer chains increases (when chains collapse along the edges of the lines).

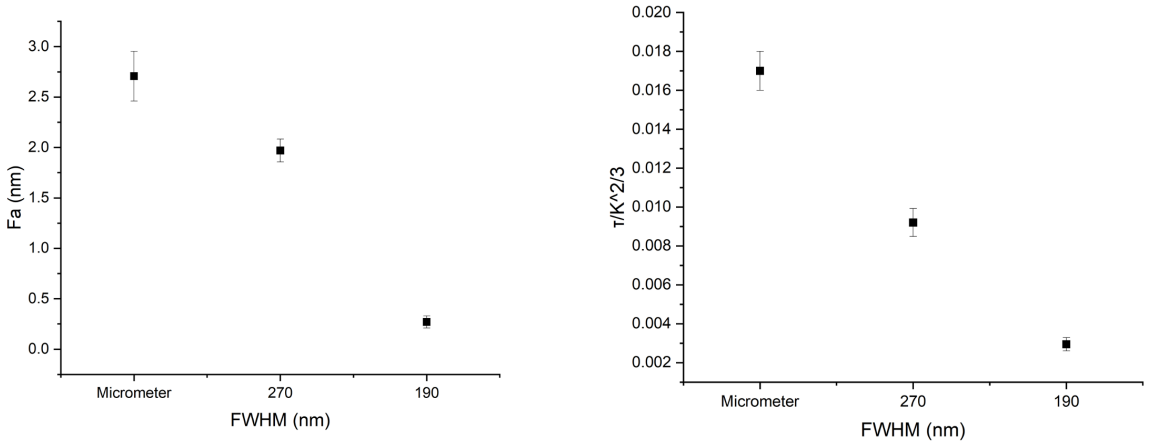

Figure 3.23: Depenendence on the pattern dimensions of the adhesion force and the surface shear stress calculated using the equation1.31.

There is a clear correlation between this phenomenon and the decreasing brush lines. In these situations, the tip may encounter fewer molecular units of the polymer on a small scale when it is scanning the surface of the polymer than on a larger scale. The contact mechanics of various PDMA configurations were carefully studied, with adhesion force and surface shear stress quantified using the Equation (1.31). This analysis encompassed both micrometer-scale and nanometer-scale PDMA patterns, specifically those with Full Width at Half Maximum (FWHM) values of 270 nm and 190 nm Figure 3.23. The results demonstrate a clear trend: the shear strength of a feature increases with its size. In practical terms, this means that the micrometer-scale PDMA patterns exhibited significantly higher adhesion forces and surface shear stress compared to their nanometer-scale counterparts. These behaviours can be attributed to the larger contact area available in micrometer-scale patterns, which facilitates stronger intermolecular interactions between the PDMA molecules and the AFM tip.

Among the nanometer-scale patterns, a distinct structure was observed. Patterns with an FWHM of 270 nm displayed higher adhesion forces and surface shear stress than those with an FWHM of 190 nm. The smallest nanometer-scale patterns (190 nm FWHM) recorded the lowest values for both adhesion force and shear stress. This is likely due to the reduced number of polymer chains available for interaction in the smaller features, which diminishes the overall contact area and, consequently, the frictional force. These observations are consistent with the principles of contact mechanics, where larger features provide more extensive contact interfaces, leading to enhanced mechanical stability and greater resistance to deformation. In summary, the study highlights the crucial role of feature size in determining the mechanical properties of PDMA patterns, with larger micrometer-scale and 270 nm FWHM nanometer-scale patterns offering superior adhesion and shear strength compared to the smaller 190 nm FWHM nanometer-scale pattern.

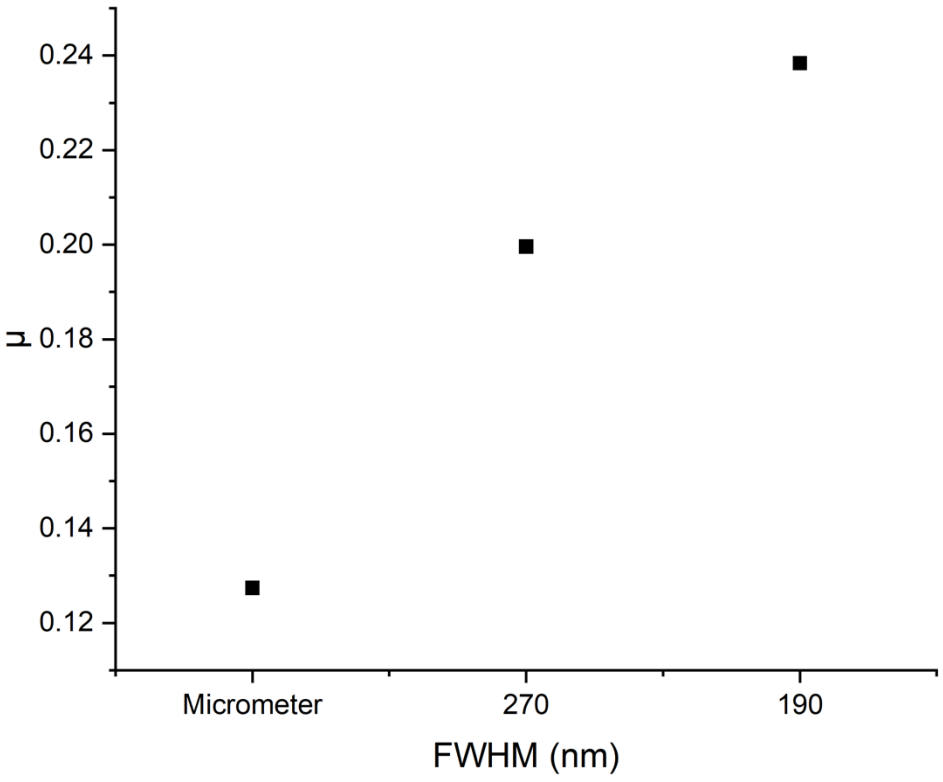

Figure 3.24: Dependence of the coefficient of the friction, calculation using equation (1.31) on the pattern dimensions.

The friction coefficient (μ) for each configuration was calculated using the Equation (1.31), providing a detailed understanding of how different feature sizes affect frictional behaviours. In Fig. 3.24, the coefficient of friction increases by a factor of ~2 from micrometre-scale patterns (fully dense brushes) to 190 nm-wide nanostructures. The findings reveal a clear trend: as the size of the PDMA features increases, the friction coefficient decreases. This inverse relationship is attributed to the changes in the density of polymer chains and the contact area between the AFM tip and the polymer surface. Specifically, larger micrometer-scale PDMA patterns exhibited significantly lower friction coefficients compared to their nanometer-scale counterparts. This is because larger features provide a more extensive contact area, which distributes the load more evenly and reduces the overall resistance to sliding.

Among the nanometer-scale patterns, friction coefficients (μ) exhibited a distinct order. Patterns with an FWHM of 270 nm demonstrated a lower friction coefficient than those with an FWHM of 190 nm. The smallest nanometer-scale patterns (190 nm FWHM) recorded the highest friction coefficients. This can be explained by the decrease density of polymer chains within smaller features, which leads to weak interactions with the AFM tip. Additionally, the smaller contact area in nanometer-scale patterns results in higher local pressure and greater resistance to movement, Therefore, increasing the friction coefficient. These results emphasize the importance of feature size in determining the frictional properties of PDMA brushes. In larger micrometer-scale patterns, the friction forces are distributed across a broader area, resulting in a smoother sliding interaction and a lower friction coefficient (μ). Alternatively, in smaller nanometer-scale patterns, the reduced contact area lead to higher frictional coefficient and greater resistance to sliding.

In summary, the study highlights that the friction coefficient is highly dependent on the size of the PDMA features. Larger features tend to have lower friction coefficients (μ) due to better load distribution and less localized pressure, while smaller features exhibit higher friction coefficients (μ) because of decrees chain density and higher local resistance. This knowledge is essential for developing polymer surfaces with customized frictional characteristics for a variety of applications.

3.4.11 Swelling behaviour of PDMA brushes in ethanol

The same experiments were also performed in ethanol. For all samples, friction-load correlations were determined and graphed in Figure 3.25. The Ethanol solvent is regarded as a

poor solvent for the PDMA chains. The polymer molecules are likely to collapse because of the decreased solvent binding. Hence, the contact area's energy dissipation process is caused predominantly by molecular deformation instead of adhesion. Moreover, the value of τ represents a negligible quantity, as molecular ploughing is responsible for most of the energy dissipation in the system. Based on a modelling analysis of this system, it has been shown that the friction force is linearly proportional to the load applied to the PDMA brushes Figure 3.25.

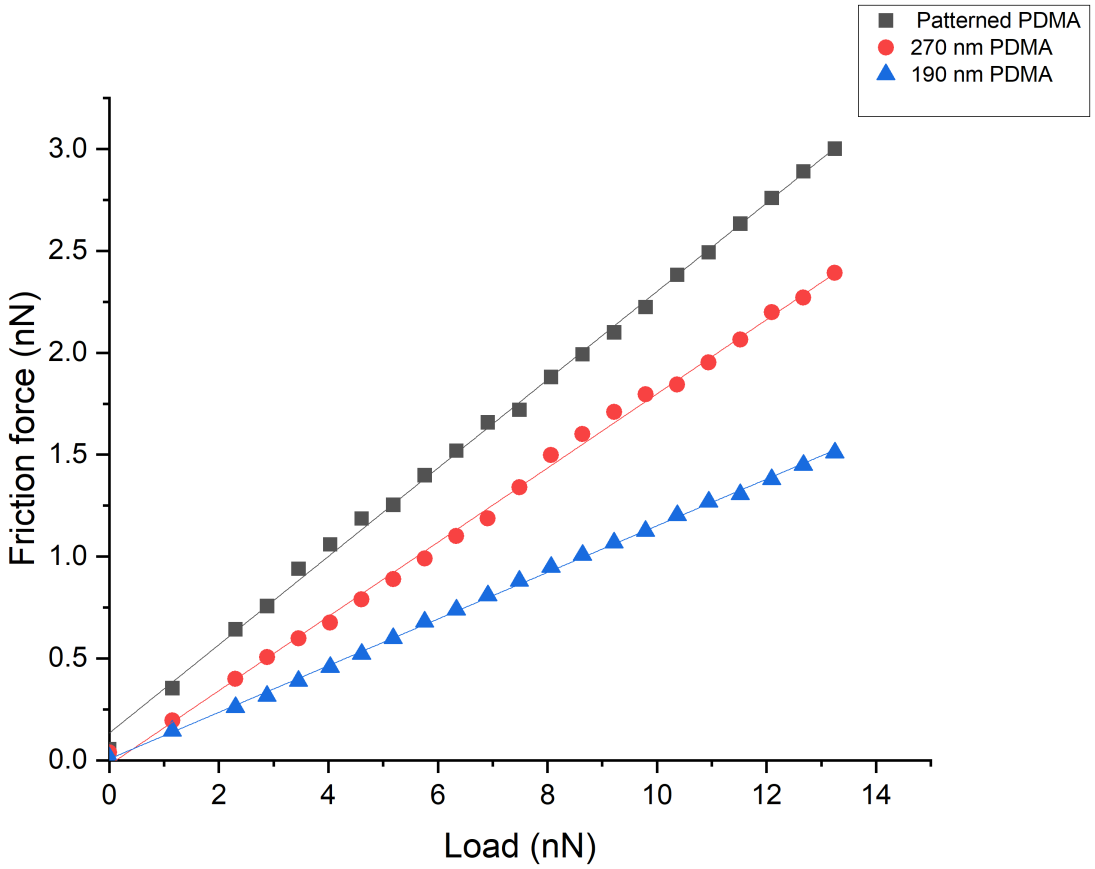

Figure 3.25: Friction-load plots for PDMA micropatterns and for PDMA nanopatterns with FWHM of 190 and 270 nm.

As a result of this, friction coefficients (μ) were determined from the friction-load graphs, illustrated in Figure 3.26. It has been found that there is a direct correlation between the friction coefficients of PDMA patterns and the dimensions of their structures. It can be explained by the fact that the number of collapsed PDMA polymer chains responsible for ploughing reduced as the scale size became smaller. Moreover, grafted polymer molecules are less susceptible to stretching at the edges of the pattern. In addition, they display fewer interactions and overlaps

between non-polymerized areas and the polymerized area, in this situation, the main explanation for diminishing (μ)values in response to feature size can be attributed to polymer grafting density.

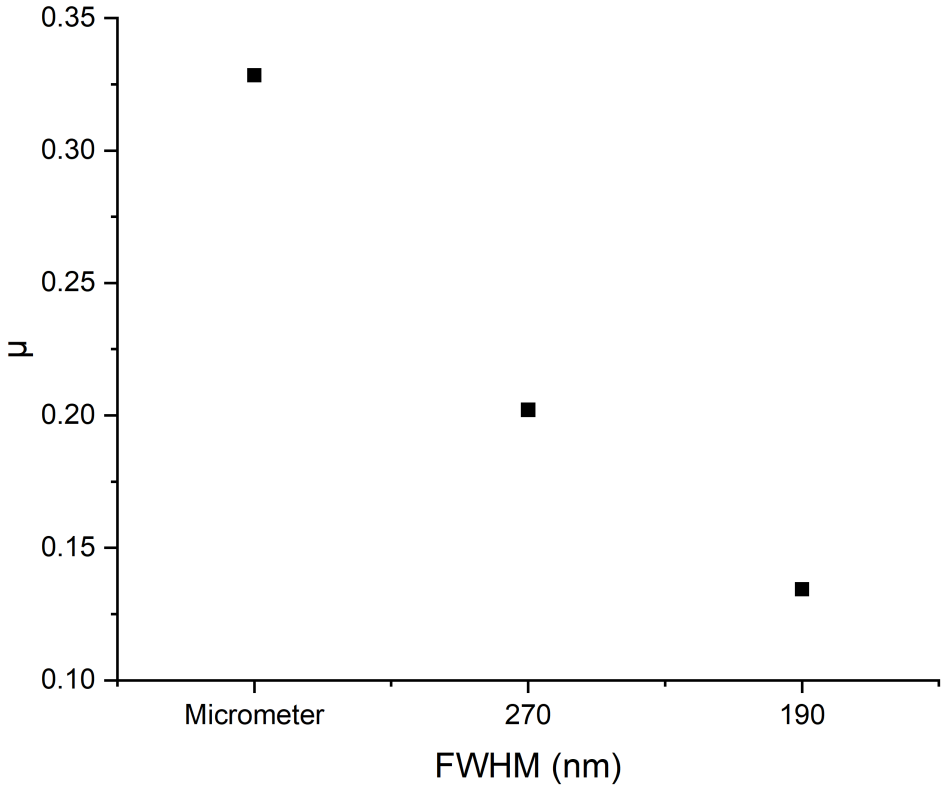

Figure 3.26: Coefficient of the friction for PDMA micropatterns and for nanopatterens with FWHM of 190 and 270 nm.

Based on the experimental results, In Fig. 3.26, the coefficient of friction decreases by a factor of ~3 from micrometre-scale patterns (fully dense brushes) to 190 nm-wide nanostructures. The coefficient of friction (μ) was found to be lowest for samples with the lowest grafting density. Specifically, this was observed in the PDMA nanopatterns with Full Width at Half Maximum (FWHM) values of 190 nm and 270 nm. Among these, the PDMA patterns with an FWHM of 190 nm exhibited the lowest friction coefficient, followed by those with an FWHM of 270 nm. Conversely, the highest coefficient of friction was recorded for the samples with the greatest grafting density, which corresponded to the PDMA micrometer-scale patterns.To qualitatively understand this phenomenon, it is essential to consider the concept of molecular

ploughing. Molecular ploughing refers to the energy dissipation that occurs between the PDMA brushes and the scanning tip during frictional interactions. This energy dissipation can be described in terms of the force differences (ΔFF) involved. The amount of energy dissipated during these interactions can be ordered as follows: ΔFF PDMA micrometre pattern > ΔFF 270 nm FWHM > ΔFF 190 nm FWHM.

This comparison highlights the significant influence of grafting density on frictional properties. In micrometer-scale patterns, the dense arrangement of polymer chains leads to substantial change in the chain mobility, resulting in a higher degree of molecular ploughing and greater energy dissipation. This increased resistance to sliding elevates the friction coefficient for these patterns.

In the other hand, in nanometer-scale patterns with lower grafting densities, such as those with an FWHM of 190 nm and 270 nm, the reduced density of polymer chains translates to fewer contact points and less extensive change in the chain mobility. Consequently, the molecular ploughing effect is minimized, leading to lower energy dissipation and a reduced friction coefficient. Among these nanometre patterns, the 190 nm FWHM samples have the least energy dissipation, indicating the smallest frictional forces at play. This comprehensive understanding of the relationship between grafting density, pattern scale, and frictional behaviour is crucial for designing PDMA brush surfaces adapted to specific applications. For applications requiring minimal friction, such as in lubrication systems or microfluidic devices, nanometer-scale patterns with lower grafting densities are ideal due to their reduced energy dissipation and lower friction coefficients. In contrast, for applications that benefit from higher frictional resistance, such as in adhesive surfaces or sensors, micrometer-scale patterns with higher grafting densities are more suitable, offering greater energy dissipation and higher friction coefficient. In conclusion, in ethanol, the trend is opposite to that in water, attributed to ploughing.The friction force is the sum of two terms: a shear term and a ploughing term. In a good solvent (water) the shear term is increased and dominates friction. As the free volume increases (in nanostructures) the shear term increases, and the coefficient of friction increases too. However, in a poor solvent (ethanol), the polymer chain collapses. The friction force is dominated by ploughing. The chains at the edges tend to form train on the surface rather than swelling away from the surface, the number of pathways for dissipation is reduced, leading to a reduction in the coefficient of friction. The study reveals that the friction coefficient of PDMA brushes is strongly linked to their grafting density and pattern scale. The concept of molecular

ploughing and the associated energy dissipation provide a qualitative explanation for the observed variations in frictional properties. This knowledge enables the strategic design of PDMA brush surfaces with adapted frictional characteristics, enhancing their performance and suitability for a wide range of technological applications.

3.4.12 Conclusion

In this comprehensive study, PDMA brush patterns were accurately fabricated across a wide range of sizes, spanning from nanometer scales of 190 nm to microscopic dimensions. Friction Force Microscopy (FFM) was employed to investigate the frictional behaviour of these PDMA brushes in various solvents, specifically examining how their dimensions influence friction. The friction force experienced by these brushes can be decomposed into two primary components: a load-dependent term associated with molecular ploughing and a shear term linked to adhesion interactions. When placed in water, a solvent well-suited for PDMA brushes, adhesion interactions predominantly govern the contact mechanics at the interface. This condition leads to a sublinear relationship between friction and applied load, which aligns well with predictions made by the Equation (1.31) model. This hypothesis is strongly supported by the calculated contact mechanics variables, which demonstrate that as the diameter of the polymer features decreases, there is a corresponding decrease in the work of adhesion. This indicates that smaller polymer features exhibit reduced adhesive interactions due to less contact area available for adhesion. The experimental results indicate that the behaviours of PDMA brushes in water is not only influenced by the solvent itself but also by the fundamental properties of the polymer, such as free elastic energy and the degree of lateral stretching of the polymer chains across the patterned regions. These factors collectively contribute to the observed frictional behaviours, with adhesion playing a critical role in determining the interaction at the contact points. As opposed to that when ethanol, a poor solvent for PDMA, is introduced, a significant change in the behaviour of the PDMA brushes is observed. Across the entire range of applied loads, the friction-load relationships become linear. This linearity can be attributed to the collapse of the PDMA brush structure in ethanol. In such a collapsed state, the polymer chains are densely packed, resulting in extremely low or virtually non-existent shear stress. Consequently, molecular ploughing becomes the dominant mechanism driving friction within the contact region. The friction coefficient (μ) of the PDMA brushes in ethanol was found to be directly proportional to both the grafted density and the footprint size of the polymer patterns. This means that as the density of grafted polymer chains or the period of the patterns decreases, the friction coefficient correspondingly decreases. The experimental data clearly demonstrated this trend, with PDMA brushes exhibiting lower friction coefficients for lower grafting densities or smaller periods. Specifically, the PDMA nanopatterns with Full Width at Half Maximum (FWHM) values of 190 nm and 270 nm displayed lower friction coefficients compared to the micrometer-scale patterns, which had the highest grafting density

and consequently the highest friction coefficient. The behaviour of PDMA chains in ethanol further clarifies these findings. In a poor solvent environment, PDMA chains are more likely to collapse rather than extend or overlap across non-polymerized areas. Near the edges of the patterns, the chains are unlikely to extend beyond the designated polymer regions, resulting in a compact and dense brush structure. This conformation minimizes the surface area of the polymer that is exposed to the solvent, thus reducing the frictional forces generated during contact with a sliding probe. The dominance of the ploughing mechanism in the frictional behaviour of collapsed PDMA brushes emphasize the significance of mechanical deformation in determining friction coefficients. In the collapsed state, the polymer chains are tightly packed, leading to greater resistance to deformation. As the contacting probe moves across the surface, it must overcome this dense packing, resulting in a ploughing effect that dominates the frictional response. This effect is more noticeable in brushes with higher grafting densities, where the dense packing enhances the resistance to mechanical deformation.

In summary, this study provides a detailed examination of the frictional behaviour of PDMA brushes in different solvents, highlighting the critical role of solvent-polymer interactions and polymer chain dynamics. The findings reveal that in water, adhesion interactions govern the frictional behaviour, leading to a sublinear friction-load relationship, while in ethanol, the collapse of the polymer structure results in linear friction-load relationships dominated by molecular ploughing. These insights contribute to a deeper understanding of the frictional properties of polymer brushes and their dependence on both environmental conditions and specific polymer characteristics.

CHAPTER 4 EFFECT OF GRAFTING DENSITY ON THE MORPHOLOGY AND MECHANICAL PROPERTIES OF PDMA BRUSHES

4.1 Introduction

The grafting density of polymer brushes refers to the number of polymer chains attached per unit area of the substrate. It is a crucial parameter influencing the brush conformation, frictional properties, and overall performance in different environments. The grafting density can be varied by adjusting several experimental parameters. One key factor is the initiator concentration in grafting-from techniques, such as surface-initiated polymerization, where the surface density of initiators determines the number of polymer chains that can grow. Polymerization time also plays a role, as longer polymerization generally leads to higher molecular weights; however, at high densities, steric hindrance may limit further growth. Additionally, monomer concentration affects grafting density, as increasing the monomer supply enhances polymer growth and chain extension. Surface functionalization is another important factor, as the type and density of functional groups on the substrate influence the number of available grafting sites for polymer attachment. By controlling these parameters, researchers can adjust the grafting density to achieve desired material properties. Once the grafting density is varied, several techniques can be used to verify and characterize it. Ellipsometry measures the thickness of the polymer brush layer, which correlates with grafting density, as higher densities generally result in thicker layers[221]. Contact angle measurements assess surface wettability changes, where a denser brush layer typically leads to a more pronounced shift in hydrophilicity or hydrophobicity[222], [223]. Atomic Force Microscopy (AFM) provides insights into surface morphology and roughness, distinguishing between sparsely and densely grafted regions, while friction force microscopy (FFM) can further evaluate grafting density by measuring frictional differences[223]. X-ray Photoelectron Spectroscopy (XPS) confirms polymer attachment by detecting characteristic elemental compositions of the polymer backbone[224]. Quartz Crystal Microbalance (QCM) quantifies mass changes upon polymer grafting, offering an indirect estimation of grafting density[225]. Spectroscopic techniques such as FTIR, UV-Vis, and NMR help identify chemical modifications associated with polymer attachment[226]. Fluorescence labeling can be used if polymers are tagged with fluorescent markers, allowing surface density estimation through

fluorescence microscopy[227]. Additionally, neutron or X-ray reflectivity provides detailed information about the polymer layer's thickness, density profile, and overall conformation[228]. These techniques together offer a comprehensive approach to characterizing grafting density and ensuring reproducibility in polymer brush fabrication.

There are a variety of applications for brushes with polymeric configurations, such as sensing, biomedical, polymer-coated materials, and others, all of which are highly dependent on the brush's conformation to function effectively[229], [230], [231], [232]. It is critical to understand that the behaviour and structure of polymer brushes can be affected by polymer chain embedding. In addition, they are affected by the density of the graft, the molecular weight, and the surrounding environment, for instance, ionic strength, pH, solvent and temperature of the substrate[233], [234], [235], [236], [237], [238]. It was further noted that A high grafting density is employed in the grafting process to ensure that adjacent polymer chains are closely spaced. Therefore, the chains are forced to extend toward the surface by steric repulsion, creating an architecture resembling a brush. The reverse is true, a pancake-shaped or mushroom-shaped configuration is created at low grafting density, in which neighbouring chains are separated by a greater distance than the polymer height, resulting in the chains growing laterally and covering the ungrafted region[216], [230]. Moya et al. found a direct correlation between the thickness of poly [[2-(methacryloyloxy)ethyl] trimethylammonium chloride] (PMETAC) brushes and the concentration of an initiator (ω – mercaptoundecyl bromoisobutyrate thiol) using ellipsometry and QCM-D to characterise the surfaces. The result was that in low densities of grafting, collapsing brushes were observed, while high densities yielded structured brushes[239]. Leggett et al. observed that a direct correlation between the thickness of [poly (cysteine methacrylate)] (PCysMA) brushes and the concentration of an initiator using photolithography to modify the surfaces. According to the results, high densities of grafting yielded structured brushes, whereas low densities yielded collapsing brushes[215]. An efficient method for fabricating highly conformable polymer systems is surface-initiated atom transfer radical polymerization (SI-ATRP). The major advantage of this technique is the capability to apply bottom-up and top-down approaches either together or independently, offering the opportunity to design highly structured brush systems for various biological purposes. In several studies, researchers have attempted to control the brush graft density by employing strategies that involve the formation of multiple monolayers [210], [236], [240], [241], brushes made of ester-linked polymer hydrolysed [242], controlling the parameters of polymerization (e.g., monomer concentration

and time required for reaction) [243], [244], [245], [246], ATRP initiator gradient density creation [233], [234], [235], grafted polymer chains hydrolysed [247], grafted polymer photodegradation [248], [249]. Nevertheless, most of these approaches have certain drawbacks, and they require to be enhanced.

A further contribution has been provided using photolithography in regulating grafting density in polymers. Photolithography is a valuable technique since it allows the design and manufacture of structures on a variety of spatial scales, ranging from macro to nanoscale [248], [249]. Yamamoto et al. used photolithography to irradiate 2-(4-cholorosulfonylphenyl)-ethyltrichlorosilane (CTCS) initiator to generate surfaces with different densities. Poly(methyl methacrylate) (PMMA) was grown from the unpatterned sites of the initiator using ATRP. According to the study, the thickness of the brush decreased as the amount of photodegradation increased. Based on AFM force-distance experiments, it was observed that the compression resistance reduced with a reduction in the density of the grafted brushes[250]. Currently, friction force microscopy (FFM) is one of the most promising technologies for studying brush structures by obtaining the amount of friction between the end-grafted polymer and the tip surface as well as the shear stress under a variety of conditions[215], [251]. It is important to realize that energy dissipation mechanisms at interfaces between tips and substrates account for friction forces, which are typically due to molecular adhesion or molecular deformation. It is important to take into consideration that various environmental factors surrounding both surfaces have an impact on the pathways. The steric repulsion between molecules of polymers in a good solvent leads polymer chains to assemble in a brush conformation. There is an increased possibility that a polymer structure will collapse when the solvent is poor. In this case, the energy dissipation process is influenced via the ploughing of molecules across the contact region between the tip and substance, leading to the friction force being dominated by load terms [252], [253]. There may be a more complicated correlation between brush conformation and tribological behaviour in the case of swollen brushes.

Here a unique methodology is employed for the investigation of the relationship between brush characteristics and grafting density. The process involves introducing a controlled initiator of brominated substrates to fabricate brushes having uniformly varying attachment densities, The density of grafting decreases continuously during debromination of the initiator with diluted molecules, causing variations in the polymer composition. In a variety of environments, FFM with cantilevers was performed to examine brush conformation and performance. A

rationalization of the friction measurements has been achieved based on the model suggested by Zhang et al.[206], who assumed that the friction force could be expressed as the combination of a load-dependent term and a surface shear term. Further support for this was provided using contact mechanic models for data evaluation.

4.2 Experimental Sections

4.2.1 Preparation of APTES-BIBB initiator

As described in the procedure in section 2.8, APTES molecules were adsorbing onto silicon surfaces and then derivatizing via BIBB molecules. The reaction between the amine groups of the APTES and the bromide groups of the BIBB facilitated the formation of initiator-functionalized surfaces, which are essential for subsequent atom-transfer radical polymerization (ATRP). During this process, the immersion time, concentration of reagents, and reaction conditions were carefully controlled to ensure uniform derivatization. The derivatized substrates were then thoroughly rinsed with DCM and ethanol to remove any unreacted BIBB and other byproducts. Finally, the cleaned substrates were dried under a stream of nitrogen gas, preparing them for the next steps in the polymerization process. This thorough preparation ensured the creation of well-defined, initiator-functionalized surfaces necessary for effective PDMA polymer brush growth.

4.2.2 Gradient ATRP initiator

To facilitate atom-transfer radical polymerization with varying initiator densities, functionalized silane substrates were derivatized using two solutions following the procedure outlined in section 2.9 The first solution included 2-bromoisobutyryl bromide (BIBB) and triethylamine (TEA) in dichloromethane (DCM), reacting for 60 minutes. The second solution consisted of Benzoyl bromide (BB) and TEA in DCM, also reacting for 60 minutes. Mixed initiator densities on APTES surfaces were created by immersing annealed APTES substrates in solutions with different volume ratios of BIBB and BB at 24 °C for 60 minutes. For example, 100% BIBB was achieved by immersing APTES surfaces in a solution of BIBB and TEA in DCM, followed by rinsing with DCM and ethanol, then drying with nitrogen gas. A 70% BIBB and 30% BB composition was prepared by immersing substrates in a mixed solution of BIBB, BB, and TEA in DCM, following the same rinsing and drying procedure. Similarly, 100% BB was obtained by immersing APTES surfaces in a solution of BB and TEA in DCM, followed by rinsing, drying, and characterization.

4.2.3 Synthesis of PDMA and polymerization reaction

The synthesis of poly (N, N-dimethylacrylamide) (PDMA) and the subsequent growth of polymer brushes through surface-initiated atom transfer radical polymerization (SI-ATRP) have been thoroughly detailed in sections 2.9. In this chapter, all experiments were carried out under uniform polymerization conditions to maintain consistency across the samples. To ensure that the PDMA brushes were composed of polymers with identical molecular weights, the polymerization process was conducted simultaneously for all samples. This approach was critical for achieving uniformity in the brush properties, particularly in terms of molecular weight distribution, which is essential for reliable comparative analysis of the experimental results. During the polymerization process, all samples were subjected to the same monomer to catalyst ratios, solvent conditions, temperature, and polymerization time. This meticulous control over the polymerization parameters was necessary to produce a well-defined and consistent polymer brush layer. Upon completion of the polymerization, the resultant PDMA brush films exhibited a dry thickness of approximately 35 nm. This thickness was confirmed through precise measurement techniques, ensuring that the polymer brushes formed a uniform and continuous film across the substrate. The careful synthesis and polymerization procedures were fundamental in producing high-quality PDMA brush films suitable for subsequent experimental investigations.

4.3 An analysis of the surface

Experimental procedures were conducted in accordance with the procedures outlined in experimental section 2.10. and included XPS, ellipsometry, as well as friction force microscopy (FFM). XPS (X-ray photoelectron spectroscopy) will provide information about the chemical composition and surface chemistry of the samples. Ellipsometry will be used to measure the thickness and optical properties of the PDMA brushes. Finally, friction force microscopy (FFM) will allow for the characterization of the surface topography and the measurement of frictional forces between the tip and Gradient PDMA brushes.

4.4 Results

4.4.1 The Preparation process and characterisation of ATRP initiator

In the present study, ATRP initiator substrates were created using silicon and glass films that have been functionalised with a 3-aminopropyl triethoxysilane (APTES) and then reacted with bromoisobutyryl bromide (BIBB), resulting in an APTES-BIBB structural arrangement. In Scheme 1, initiator substrates and PDMA gradient brushes are assembled using typical fabrication techniques. As a way of fabricating PDMA substrates with different grafting densities, Br dilution was used to selectively minimize the concentration of Br from the initiator surfaces (Scheme 4.1 and 4.2).

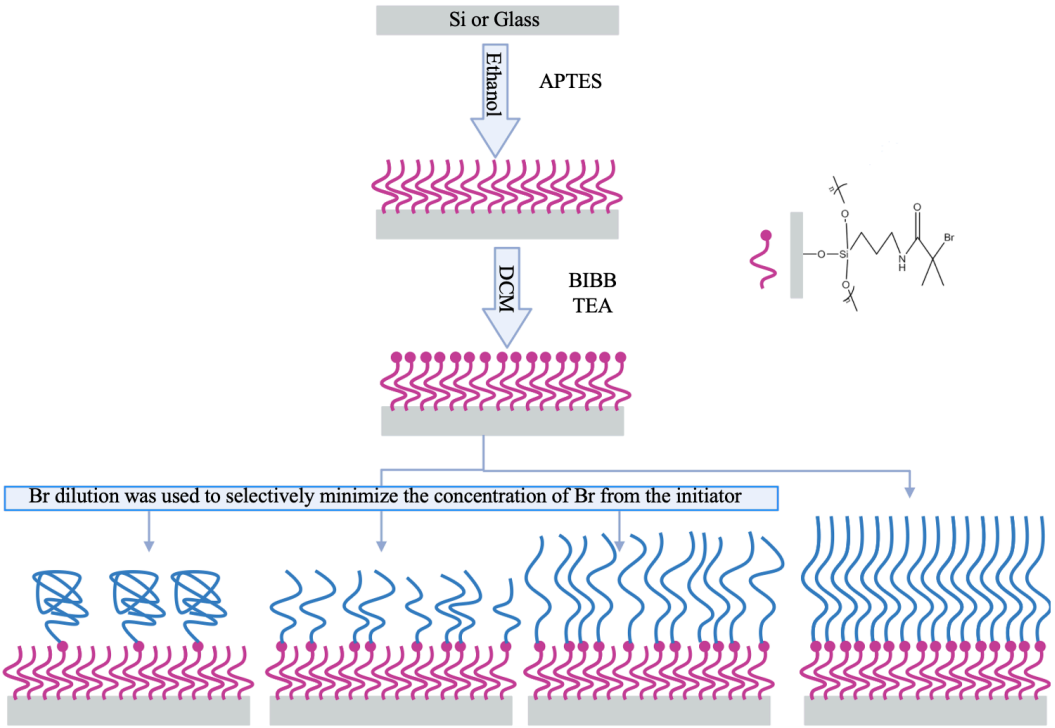

Scheme 4.1: A schematic diagram of the deposition of an APTES-BIBB film on a glass or silicon surface, and the fabrication of PDMA films of varying grafting density using Br dilution molecules.

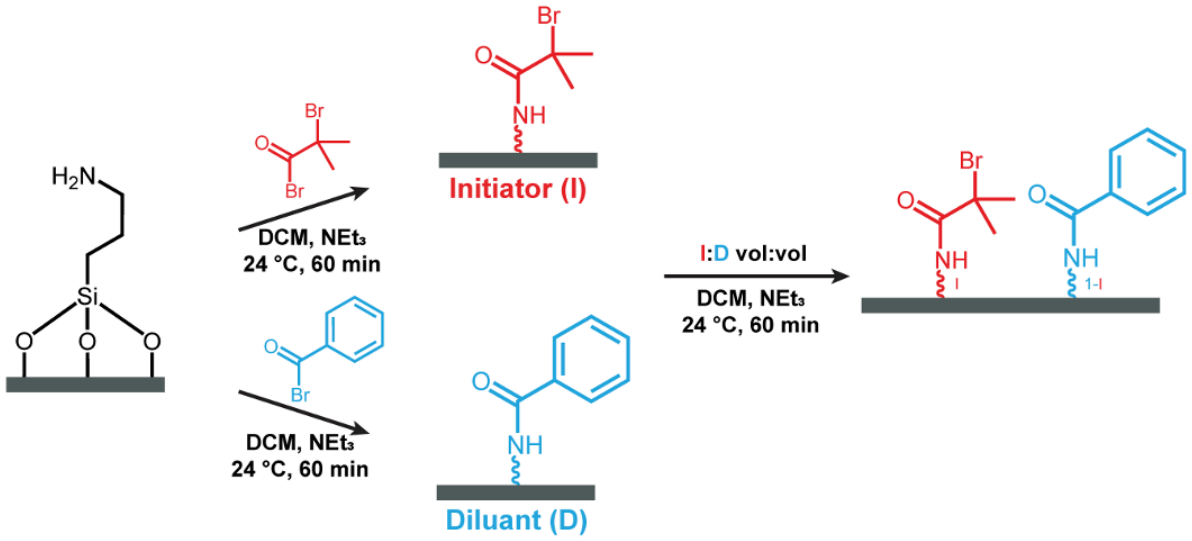

Scheme 4.2: A schematic representation of the deposition of an APTES-BIBB film on a glass or silicon surface at varying grafting density using Br dilution molecules.

The obtained APTAS, the composition of the unmodified initiator and modified initiator with dilution surfaces were characterised using XPS in silicon and glass substrates. The C1s spectrum for an APTES film displayed two peaks at 285.0 eV and 286.2151 eV (Figure 4.1), corresponding to saturated carbon and carbon adjacent to the amino group, respectively, as anticipated. The experimental ratio between saturated carbon and nitrogen-linked carbon was found to be 2.11:1.0, which is close to the theoretical ratio of 2:1. Additionally, a peak at 288.21 eV likely indicates the presence of an imide group (C=N) formed due to multilayer generation in the silane surfaces. This is further corroborated by the presence of a protonated amine group (NH^{3+}) peak adjacent to the N1s peak of free amine at 399.91 eV. The N1s spectrum for an APTES layer shows a peak at 399.856 eV, as expected (Figure 4.1).

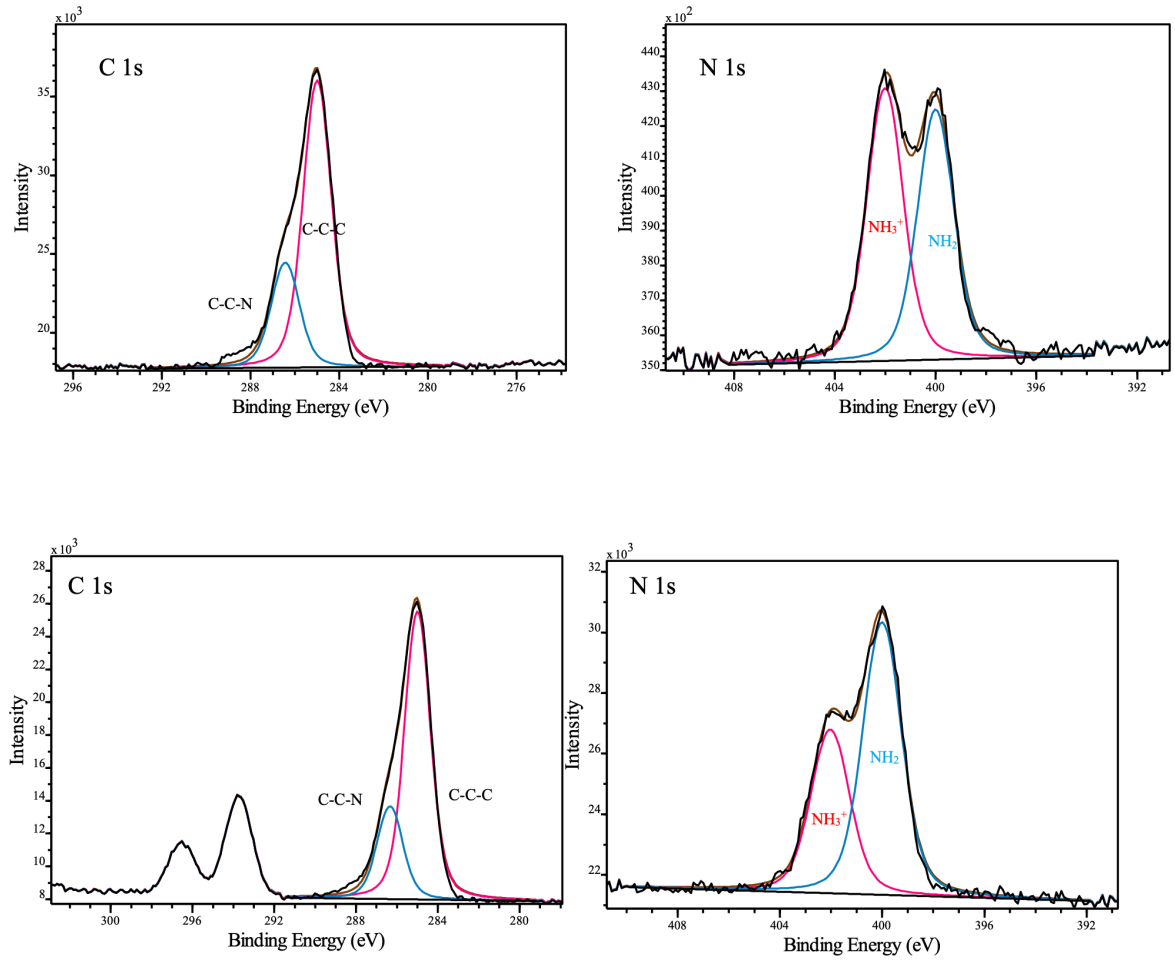

Figure 4.1: High-resolution XPS spectra for unmodified APTES: a) C1s spectra, b) N1s spectra.

In the spectrum of an unmodified substance, C 1s, N 1s, and Br 3d peaks were detected with high resolution. The XPS C1s spectra (figure 4.2) were assessed by fitting three components with binding energies of 285. eV, 286.2 eV, and 288.3 eV. This energy value is equivalent to C-C-C, C-O/C-N, and O=C-O, correspondingly. There is a close agreement between the calculated ratio of 4:2:1 for C-C-C, C-Br/C-NCO and O=C-N as the peak ratio was 3.95:1.99:1. Based on Figure 4.2, Br 3d peaks were detected at 70.0 and 72.0 eV, which corresponds to BIBB-APTES components.

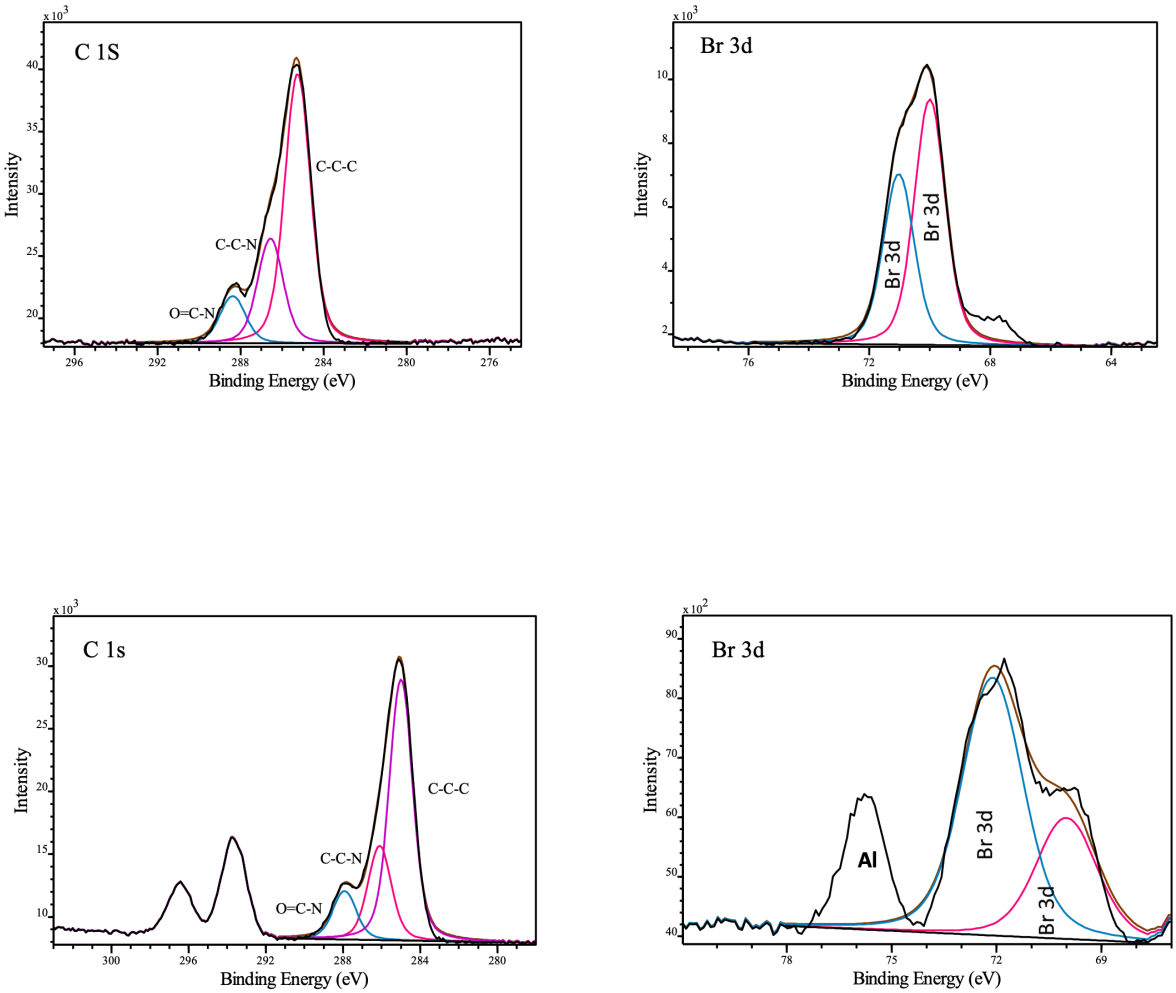

Figure 4.2: High-resolution XPS spectra for unmodified APTES-BIBB initiator: a) C1s spectra, b) Br 3d spectra.

The high-resolution XPS spectra provided illustrate the binding energy of the Br 3d peak for APTES-BIBB initiator films, modified with varying proportions of diluents (Figure 4.3). The graph on the left shows intensity (in units of 10^{-3}) plotted against binding energy (in eV), with several spectra corresponding to different diluent concentrations. The accompanying table on the right lists the specific ratios of initiator to diluent used for each spectrum. The spectra show the characteristic Br 3d doublet peaks around 70 eV and 72 eV, confirming the successful incorporation of bromine into the film. As the proportion of diluent increases, the intensity of the Br 3d peaks generally decreases, indicating a lower concentration of bromine in the films. This relationship suggests that higher diluent concentrations dilute the bromine content, thereby reducing the overall intensity observed in the spectra. This trend is essential for

understanding the impact of diluent ratios on the surface composition and chemical environment of the modified APTES-BIBB films.

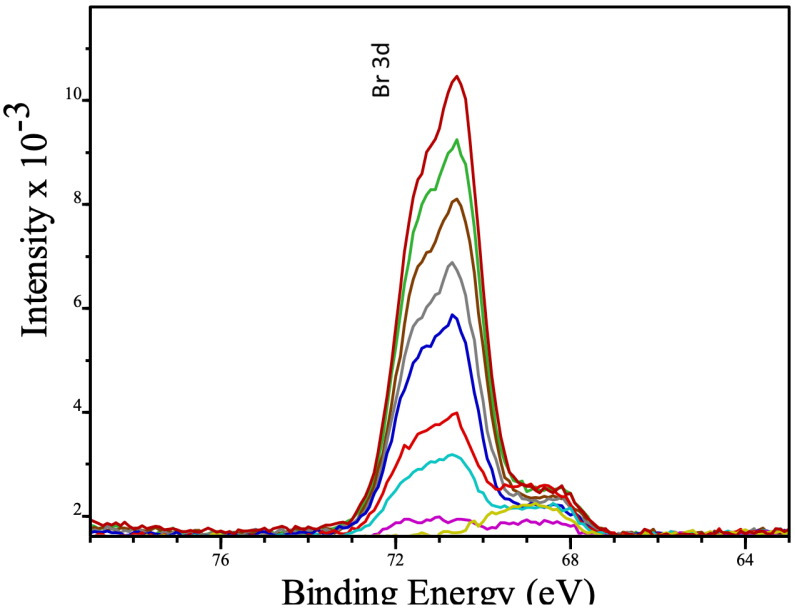

Initiator (I)	Diluante
100%	0%
70%	30%
50%	50%
30%	70%
20%	80%
10%	90%
5%	95%
1%	99%
0%	100%

Figure 4.3: High-resolution XPS Br 3d spectra for modified APTES-BIBB initiator with dilution molecules.

The composition dilution surfaces only without BIBB-APTES were examined through XPS in silicon and glass substrates. In this spectrum, C 1s, N 1s, and Br 3d peaks were characterized with high resolution. The XPS C1s spectra (figure 4.4) were determined by fitting three components with binding energies of 285.1 eV, 286.4 eV, and 288.3 eV. This energy value is comparable to C-C-C, C-O/C-N, and O=C-O, respectively. The calculated ratio of 4:2:1 for C-C-C, C-Br/C-NCO, and O=C-N is almost identical to the peak ratio of 3.96:1.95: 1. Based on Figure 4.4b, N 1s peak was detected at 400 eV, which corresponds to NH-group.

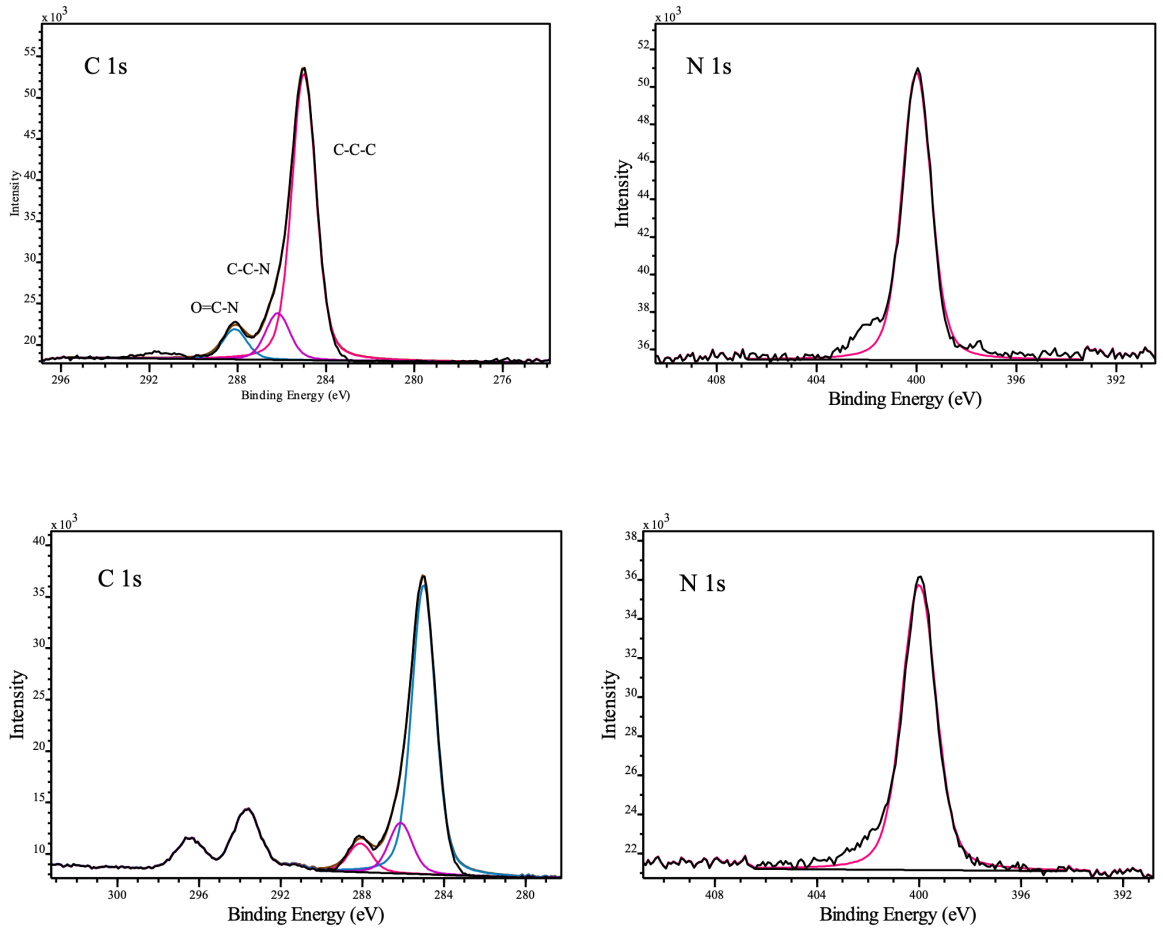

Figure 4.4: High-resolution XPS spectra for dilation surfaces only: a) C1s spectra, b) Br 3d spectra.

Following the creation of BIBB-APTES films, the surface roughness was assessed through AFM measurements. After annealing, a smooth and continuous layer of silane was produced on the surface of the wafer. This was evidenced by a roughness of 0.465/0.439 nm (Ra/Rq) for the complete BIBB-APTES monolayer (figure 4.5).

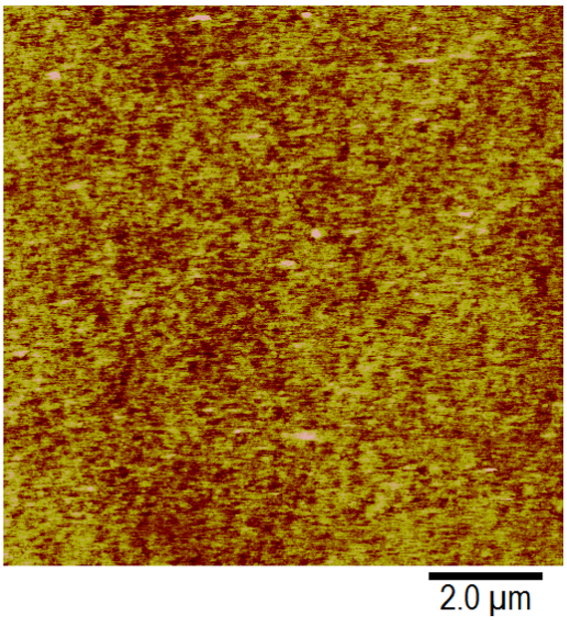

Figure 4.5: presents an AFM tapping mode hight image of monolayer BIBB-APTES

4.4.2 The growth of PDMA brushes and the effect of the initiator density

In this study, PDMA brushes were synthesized by SI-ATRP using APTES-BIBB initiators at a variety of graft densities, depending on the time and conditions of the polymerization process. An XPS and ellipsometry analysis of control samples were conducted to verify the efficiency of the polymerization reaction. As part of this experiment, a 24 nm dry thickness of PDMA brush on both silicon and glass surfaces was examined using high-resolution XPS spectra for C 1s and N 1s. The XPS C1s spectra were assessed by fitting three components with binding energies of 285.0 eV, 286.5 eV, and 288.3 eV. These energy values relate to (-C-C-C-), (C-O/C-N), and (O=C-O), respectively. The calculated atomic ratios for these elements were 4:3:1, which is close to the theoretical prediction of 3.9:3.1:1. XPS O1s shows doublet single at 532.1 and 533.7eV which attributed to (C-O) and (C=O), respectively. As a result of the N1s spectra calibration, one peak was found at 400.0 eV. This peak was attributed to C-NH2 in the PDMA brushes (Figure 4.6), these result in a good agreement with another research[219].

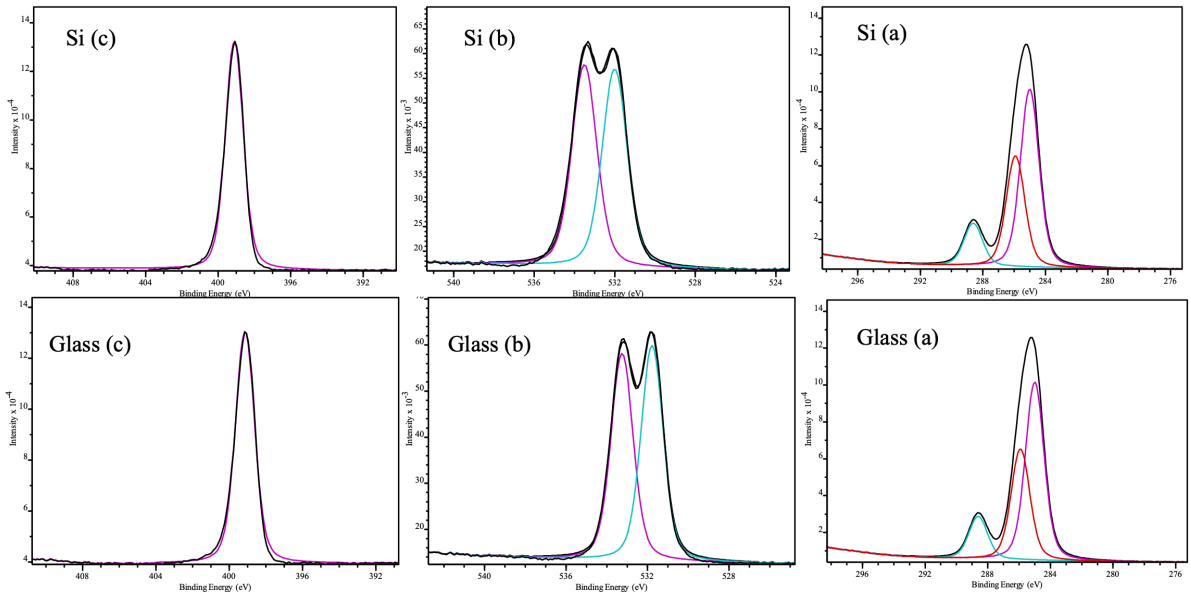

Figure 4.6: High-resolution (a) C1s spectrum, (b) O1s spectrum and (C) N1s spectrum for PDMA brushes subjected to varying initiator density on silicon and glass substrates.

The AFM tapping mode profile of unpatterned PDMA brushes with a dry thickness of 30 nm is shown in Figure 4.7 The PDMA polymer has grown uniformly across the substrate, as evidenced by the low surface roughness. The grafted PDMA polymer brushes had approximate roughness of 0.348 nm/0.254 nm, indicating smoothness and high grafting density.

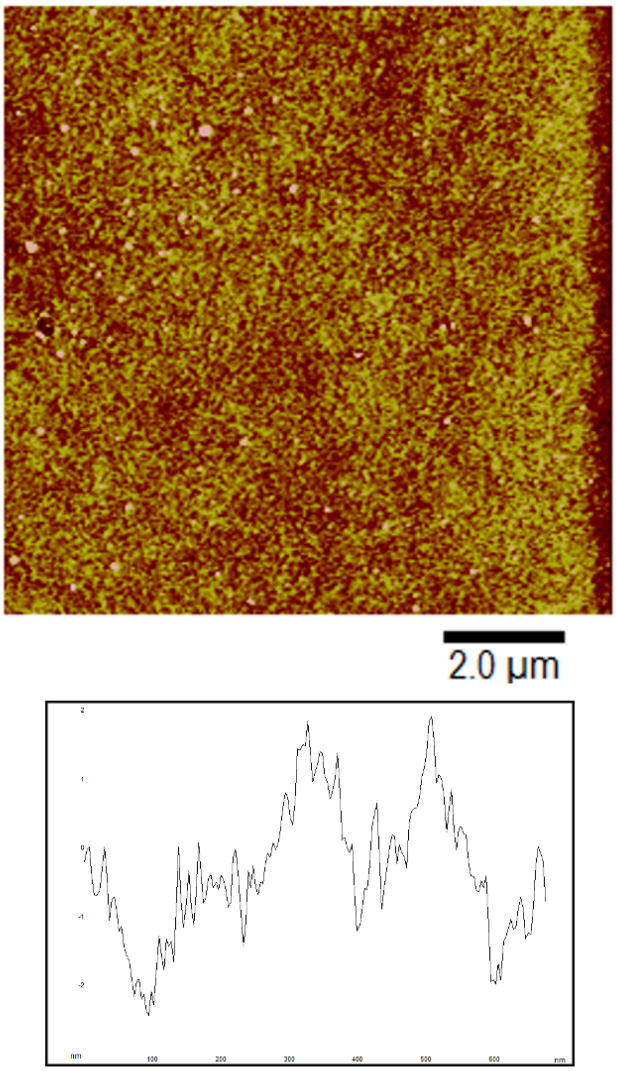

Figure 4.7: AFM tapping mode hight of PDMA brushes with a dry thickness of 30 nm.

APTES films are subjected to bromination via employing 100% BIBB, followed by the growth of PDMA brushes on these initiator-functionalized surfaces. The dry brush thicknesses were determined through ellipsometry measurements. As illustrated in Fig. 4.8, the ellipsometry brush thickness exhibited dynamic changes throughout polymerization time. Initially, a nearly linear correlation between the mean brush thickness and polymerization time was evident during the first 60 minutes. Subsequently, the rate of increase in brush thickness decelerated. To ensure consistency and efficiency, a fixed polymerization duration of 60 minutes was established for the subsequent investigations, resulting in a brush thickness of 30 nm. This period facilitated uniform and rapid growth of the brush, enabling reproducible film preparation. Due to the anticipated significant impact of polymerization degree on brush properties, precise regulation of polymerization conditions was considered essential.

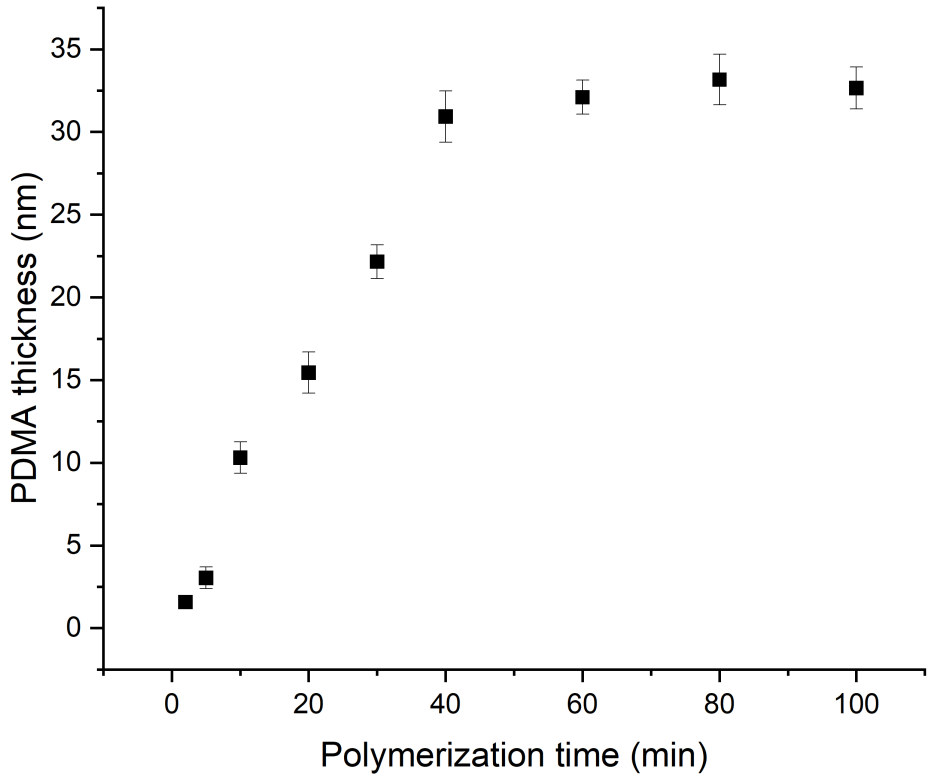

Figure 4.8: illustrates the variation in dry brush thickness over polymerization time for PDMA brushes, as determined by ellipsometry.

Furthermore, the brush thickness was assessed relative to initiator density with Br dilution, determined via ellipsometry, as illustrated in Figure 4.9. A non-linear correlation was discerned between these variables. The ellipsometry data exhibited agreement with XPS findings, illustrating a decrease in brush thickness with increasing dilution. Interestingly, a substantial reduction in thickness was observed upon the introduction of dilution, particularly evident at concentrations of 30% and 50%. Subsequently, the rate of thickness decline slowed, stabilizing within the concentration range of 70% to 99%. This phenomenon is attributed to the diminished presence of Br atoms with increasing dilution, resulting in greater separation (D) between adjacent end-grafted polymer chains (Figure 4.10). Consequently, the brushes exhibited an enhanced propensity towards adopting a mushroom conformation. This observation aligns closely with expectations from prior research in the literature, exemplified by studies conducted by Penn et al, Hess et al. [254].

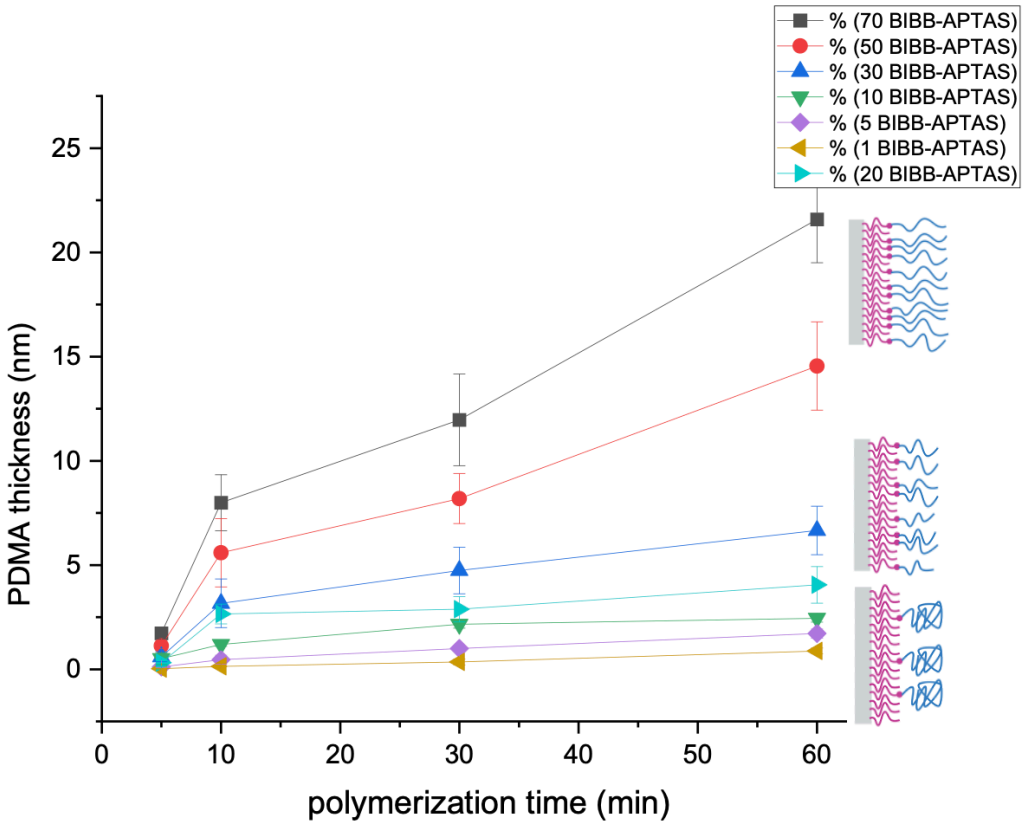

Figure 4.9: illustrates the variation in dry brush thickness over polymerization time for PDMA brushes with different initiator densities, as determined by ellipsometry.

Figure 4.10: The transition from a brush to a mushroom conformation for polymer brushes on a surface. D is the distance between two grafting points and h is the brush height. (a) D < h for brush structure and (b) D > h for mushroom structure.

4.4.3 Frictional behaviour of brushes of varying grafting density

Bromine-functionalized APTES were reacted with different concentrations of dilution to generate a range of surface initiator densities, ensuring uniform distribution across the entirety of the surface. Subsequently, PDMA chains were initiated from these surfaces through atom transfer radical polymerization (ATRP), resulting in the creation of a variety of brushes with differing densities. The frictional behaviour was subsequently assessed for each sample, with the applied load as the variable, in both water (considered a good solvent) and ethanol (considered a poor solvent) environments for PDMA brushes.

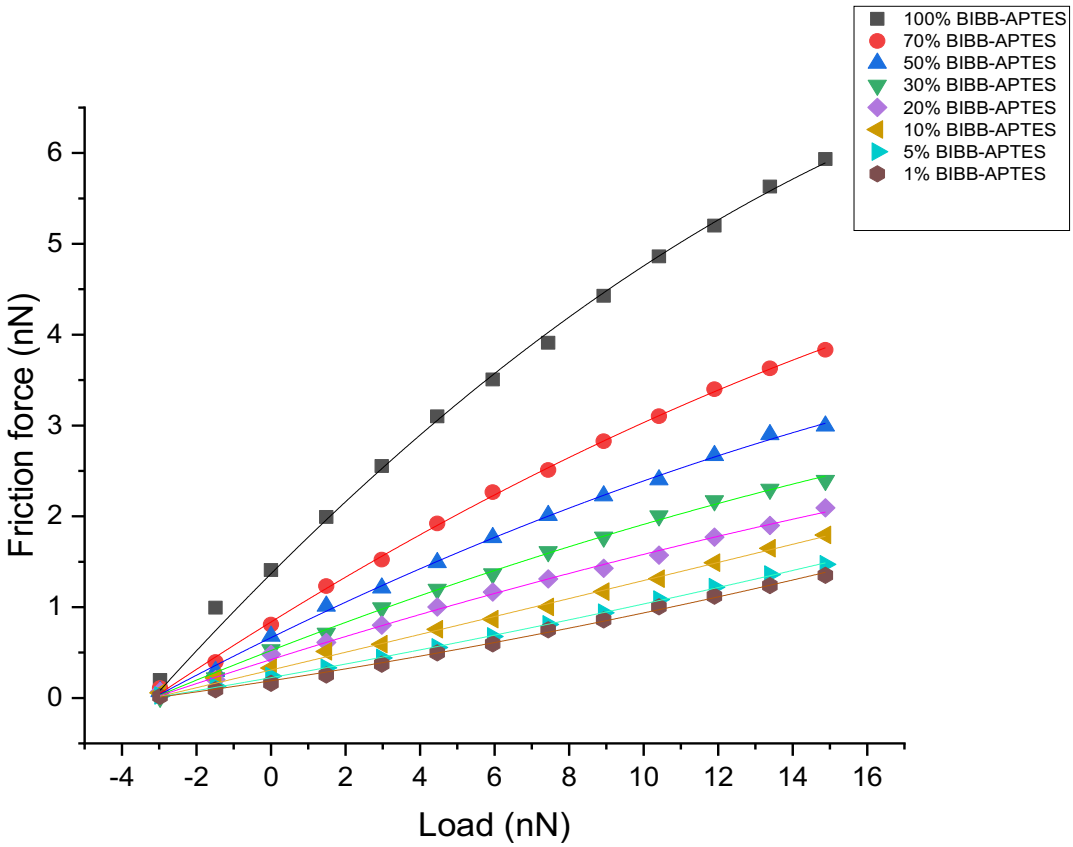

Figure 4.11: displays the typical friction-load plots obtained for brushes originating from the APTES-BIBB films, which were fabricated at different levels of initiator density in a water environment.

In the water environment, a non-linear relationship between friction and load was observed for higher initiator densities (see Fig. 4). Alternatively, a linear relationship was observed for lower initiator densities. This transition to linear behaviour is likely due to the decreased surface chain density, leading PDMA chains to form a collapsed "mushroom" conformation. In such

circumstances, the polymer experiences strong solvation by water, resulting in steric repulsion between adjacent chains, causing them to swell away from the surface. The high compressibility of the brushes, resulting from their small elastic moduli, allows the sharp tip to deeply penetrate the brush film, creating a large contact area. Despite the initial expectation of a low work of adhesion due to the solvated polymer, the polymer's low modulus leads to a substantial contact area, resulting in a significant net adhesive interaction. As a result, the frictional force shows a sublinear correlation with the applied load across the entire range, as illustrated in Figure 4.11. The friction-load relationship was effectively analysed and modelled using the Equation (1.31). By applying this equation, the friction force (F_F) is plotted as a function of the normal force (load) (F_N). The tip radius (R) was 20 nm, and the adhesion forces (F_a) was reported in figure 4.14. The surface shear strength (τ) was determined from the fits to the data (Figure 4.13).

However, as the density of the grafted brushes decreased, there was a notable alteration in this relationship. It is evident that the relationships exhibited nonlinearity for samples grown from initiators with concentrations of 100%, 70%, and 50%, whereas they became linear for those grown from initiators with concentrations of 30%, 20%, 10%, 5%, and 1%. Furthermore, as the polymer density decreases, a corresponding reduction in the net interaction strength is noted. This indicates the significant influence of polymer architecture on intermolecular interactions and overall material behaviour.

The reason that the friction force increases with the grafting density has to do with the contact mechanics of a nanometre scale asperity (the probe) interacting with a solvated polymer brush. At low grafting densities, the brushes collapse, forming random coil structures whose dimensions are determined by the radius of gyration. Friction in these systems is dominated by ploughing and the friction-load relationship is linear. However, as the grafting density increases, there is a transition to a non-linear friction-load relationship, suggesting an increasing shear contribution to friction, and the friction force increases with grafting density. As the grafting density increases, the brushes become increasingly swollen: solvent (water) molecules bond to the surface-grafted polymers and steric repulsion causes swelling.

In a microscopic or macroscopic contact (one in which the area of contact is somewhat larger than the spacing between the surface grafted polymer chains), this would be expected to yield an increase in lubricity (i.e., a decrease in friction). However, for a single nanoscopic asperity, such as an AFM probe, the reverse happens. AFM force curves for swollen brushes reveal

comparatively long approach curves before the probe eventually contacts the substrate, and correspondingly long retraction curves, often displaying the characteristic sawtooth behaviour associated with force spectroscopy of macromolecules[220], due to the separation of loops of the polymer from the probe. Adhesion forces for swollen brushes can be surprisingly large. Zhang et rationalised this behaviour as follows. The thermodynamic work of adhesion (i.e., the work done in separating unit area) for a solvated, swollen brush is smaller than for a collapsed random coil structure. However, elastic moduli of swollen polymer brushes are small, and the probe is very narrow; thus, the swollen polymer deforms substantially, and the area of contact becomes large; thus, while the work of adhesion is small, when multiplied by the large contact area, the net adhesion force is large.

Zhang et al reported that for poly(2-(methacryloyloxy)ethylphosphorylcholine) (PMPC) brushes, adhesion forces were larger in a good solvent than in a poor solvent, and friction-load data were best modelled in water by Johnson-Kendall-Roberts contact mechanics in water (a good solvent), whereas a linear friction-load relationship was observed in isopropanol, a poor solvent, consistent with the above explanation[220].

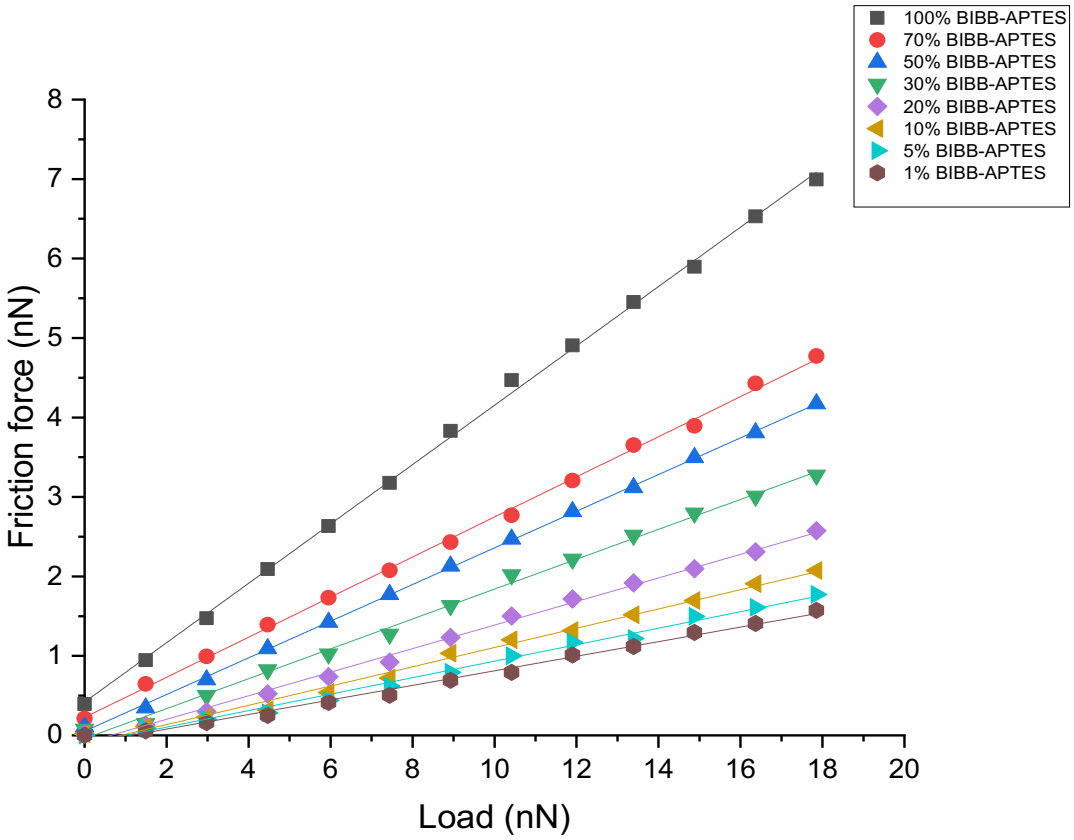

Figure 4.12: illustrates the changes in friction forces relative to applied loads across different grafted PDMA brushes in an ethanol environment.

In contrast, in a poor solvent such as ethanol, the potential for hydrogen bond interactions between the brush and the solvent is diminished. Consequently, the non-solvated brush tends to collapse, potentially forming mushroom-like structures. As a result, the friction-load relationship remained consistently linear despite the varying initiator density, as shown in Figure 4.12. Even in this solvent, the most extensively grafted polymer chains did not achieve fully swollen brush configurations. The sliding interaction is primarily determined by the dissipation of energy through molecular ploughing, caused by conformational changes in the polymer chains, with the friction force being dependent upon the applied load.

4.4.4 Impact of brush density on the friction-load relationships of the PDMA polymer brushes

Many researchers agree that the shape of a polymer brush is influenced by the density of polymer chains anchored to the surface. As the grafting density decreases, there is a shift from a brush-like structure to a mushroom-like conformation[188], [189], [192] . In this investigation, the influences of environmental factors and grafting density on the response and mechanical attributes of a PDMA brush, employing Force Microscopy (FFM) as the analytical technique, have been explored. The polymerization time and conditions were maintained consistently throughout the experiments. Thus, any observed variability in behaviour can be attributed to variations in the grafting density of the brushes. This controlled approach emphasizes the importance of carefully examining the effects of grafting density on the properties and performance of the polymer brushes, facilitating a comprehensive understanding of their behaviour under different conditions.

According to these findings, combining the initiator with varying concentrations of dilution proves effective in eliminating Br from the initiator. It was observed that as the dilution concentration increased, PDMA brush densities decreased, resulting in an expansion in the distance between two neighbouring polymer chains. Analysis of the figures indicates that samples grown from initiators with concentrations of 100%, 70%, and 50% exhibit a brush conformation in their polymer structure. Interestingly, these samples demonstrated sublinear friction-load relationships, suggesting a mechanical characteristic influenced by the initiator concentration. In comparison with previous samples, the examining samples grown from initiators with concentrations of 30%, 20%, 10%, 5%, and 1%, a noticeable shift occurred, revealing a linear friction-load relationship. This phenomenon can be attributed to a transition towards mushroom conformation. This transition occurs due to the significant distance among grafting points ($D > H$), encouraging polymer chains to extend across the engrafted region. Consequently, collapsed brushes are produced, causing friction-load relationships to be linear.

In contrast, the consistent linear friction-load relationship observed in ethanol, regardless of changes in the grafting density of PDMA brushes, can be attributed to the unique solvent properties of ethanol. It is recognized as a poor solvent for PDMA brushes, meaning it has a limited ability to interact with and swell the polymer chains. As a result, the solvent-induced changes in the conformation of the polymer brushes, which typically drive transitions in

friction behaviour, are minimized in ethanol. Consequently, the friction characteristics primarily reflect the fundamental properties of the polymer chains rather than being influenced by changes in grafting density.

4.5 Discussion

the data provided here emphasizes the critical influence of grafting density on the conformation of PDMA brushes on surfaces. However, it is equally imperative to recognize the significant impact of environmental conditions on brush behaviour. Especially noteworthy, a transition in PDMA brush structure, shifting from a brush to a mushroom or coil configuration, was observed specifically in a poor solvent environment, associated with a reduction in the density of end-grafted brushes. The comprehension of this transition can be achieved by examining the solvation behaviour of PDMA brushes in both favourable and unfavourable solvent environments. In a medium such as water, which represents a good solvent due to its strong affinity for the PDMA chains, the brushes exhibit an extended conformation like a brush structure. Here, the water molecules efficiently solvate the polymer chains, preventing their collapse onto the surface. Alternatively, in a solvent environment characterized by poor solvation properties, such as ethanol, where the interactions with PDMA polymer chains are limited, significant conformational alterations occur in the brushes. As the density of end-grafted brushes diminishes, the intermolecular interactions between adjacent polymer chains decrease significantly. Consequently, the polymer chains tend to aggregate and collapse onto the surface, adopting a more compact conformation in the style of mushroom or coil structures. Therefore, while grafting density plays an essential role in determining brush conformation, the contrasting solvation behaviours in good and poor solvent environments demonstrate the critical influence of the surrounding medium on the structural dynamics of PDMA brushes. The typical brush conformation of the polymer is primarily attributed to the extent of solvation and the minimal separation between grafted points along the polymer chains. Consequently, the addition of a small quantity of diluent to the initiator is not sufficient in creating a distance between grafting points that exceeds the brush height. The observed sublinear friction-load relationship in these circumstances correlates with the pathway of energy dissipation, which is governed by adhesion. While adhesion is diminished owing to the solvation state, the polymer's low elastic modulus results in a considerable contact area. As a result, the equation (1.31) exhibited a strong fit to the data (refer to Figure 4.11). Utilizing the Equation (1.31) model, the data were analysed, and the surface shear strength was determined as a variable dependent on

the concentration of initiators (Figure 4.13). This plot illustrates the change in shear stress (τ) concerning initiator concentration. Subsequently, τ experiences a substantial increase at high grafting densities (for samples with initiator concentrations of 100%, 70%, and 50%). However, beyond the 30% level, it exhibits a sharp decline and stabilizes at lower grafting densities, indicating a transition dominated by ploughing in the tip-sample interaction. This shift occurred as the distance between grafting points was wider than the brush height, causing the polymer chains to collapse and overlap with the non-grafted region. Friction forces exhibited a direct correlation with the applied loads, as exhibited in Figure 4.11 (for samples with initiator concentrations of 10%, 5%, and 1%). The calculated shear stresses (τ) were sufficiently small to be disregarded, as illustrated in Figure 4.13.

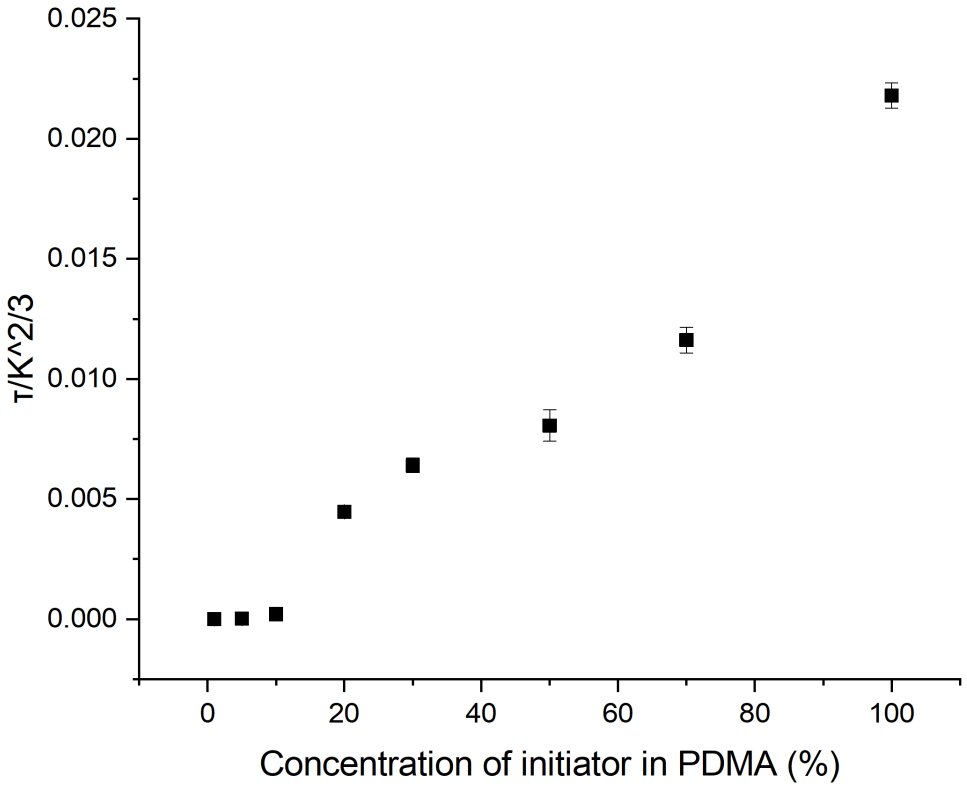

Figure 4.13: Analysis of correlation of friction-load measurements to equation (1.31) change in (τ) shear stress over PDMA brush with different grafting density.

In circumstances characterized by a high grafting density of PDMA brushes, the closely packed polymer chains on the surface lead to stronger intermolecular interactions, particularly

adhesion forces. These adhesion forces contribute significantly to the overall frictional behaviours by promoting adhesion between the contacting surfaces. As a result, the calculated shear stresses, which are measures of the resistance to sliding, become more significant and cannot be neglected. Therefore, investigating the influence of adhesion force on friction forces for PDMA brushes in water is essential for optimizing their performance in aqueous environments. Figure 4.14 illustrates the relationship between initiator density percentages for PDMA brushes and the corresponding adhesion forces observed in water. The adhesion results from the interaction between the surface functional groups on the tip (predominantly O silanols, which are weak acidic) and the basic pendant group (tertiary amine) on PDMA. A clear trend appears, indicating that as the percentage of initiator density decreases, the adhesion forces in water also decrease. however, higher percentages of grafting density correlate with higher adhesion forces. This finding suggests a direct influence of grafting density on the adhesive properties of PDMA brushes in aqueous environments. Understanding this relationship is valuable for customizing the adhesion characteristics of PDMA brushes to specific requirements in applications such as surface modification or adherence.

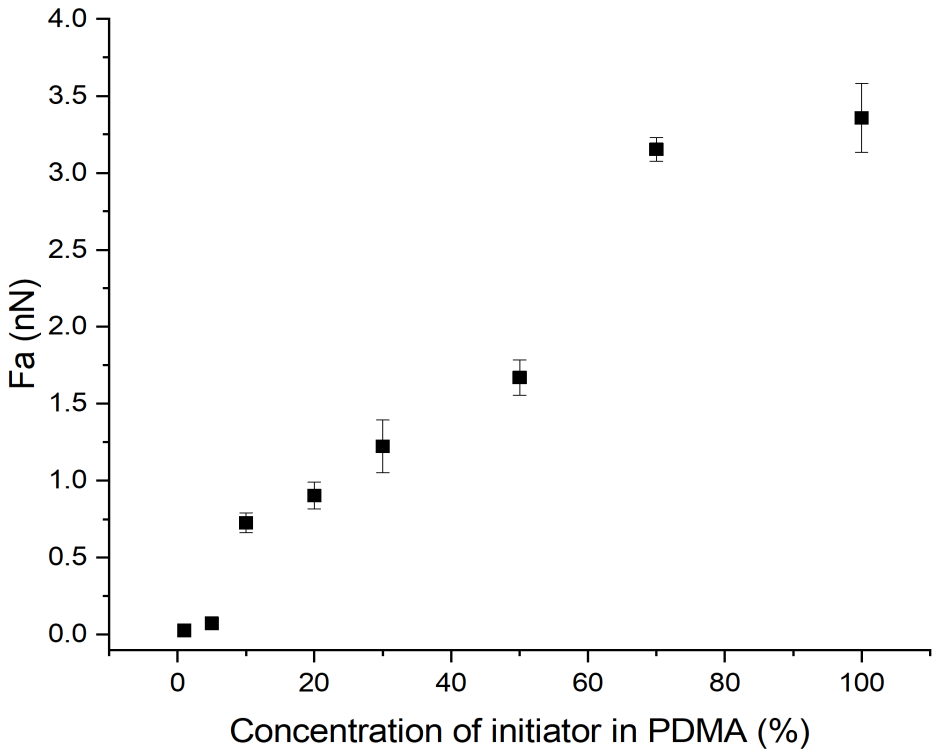

Figure 4.14: Relationship between adhesion forces and PDMA brush with different grafting density.

4.5.1 **The friction coefficient in water and ethanol**

In a sub-linear relationship between the friction force and load observed when studying PDMA brushes as a surface in water as a solvent, an increase in shear stress is typically accompanied by a decrease in the friction coefficient (figure 4.15). The friction coefficient (μ) is defined as the ratio of the friction force (F) to the normal load (N). In this sub-linear relationship, as the load on the PDMA brush surface increases, the shear stress (τ) also rises. Shear stress represents the force per unit area needed to initiate sliding or shearing motion between the PDMA brush surface and the water solvent. However, the rate of increase in the friction force diminishes relative to the increase in load. Consequently, the friction coefficient decreases because the elevated shear stress does not entirely offset the amplified load. This behaviour implies an enhanced efficiency in dissipating the applied load as the normal load intensifies, resulting in a reduced friction coefficient.

In addition to the previously described phenomenon, when considering PDMA brushes with increasing grafting density, the decrease in friction coefficient with increasing shear stress and load can be further explained. As the grafting density of PDMA brushes increases, there is a greater coverage of polymer chains on the surface. This denser coverage results in more molecular interactions between the polymer chains and the water molecules in the solvent. These interactions effectively reduce the ability of the water molecules to resist shear motion when the AFM tip slides over the surface. Consequently, the shear stress required to induce sliding or shearing motion between the PDMA brush surface and the water solvent decreases. Overall, the combination of increased shear stress due to higher grafting density and the smoother, more conformal surface of the PDMA brushes results in a decreased friction coefficient as the load increases. This phenomenon highlights the complex relationship between surface properties, molecular interactions, and mechanical forces in determining frictional behaviours at the nanoscale.

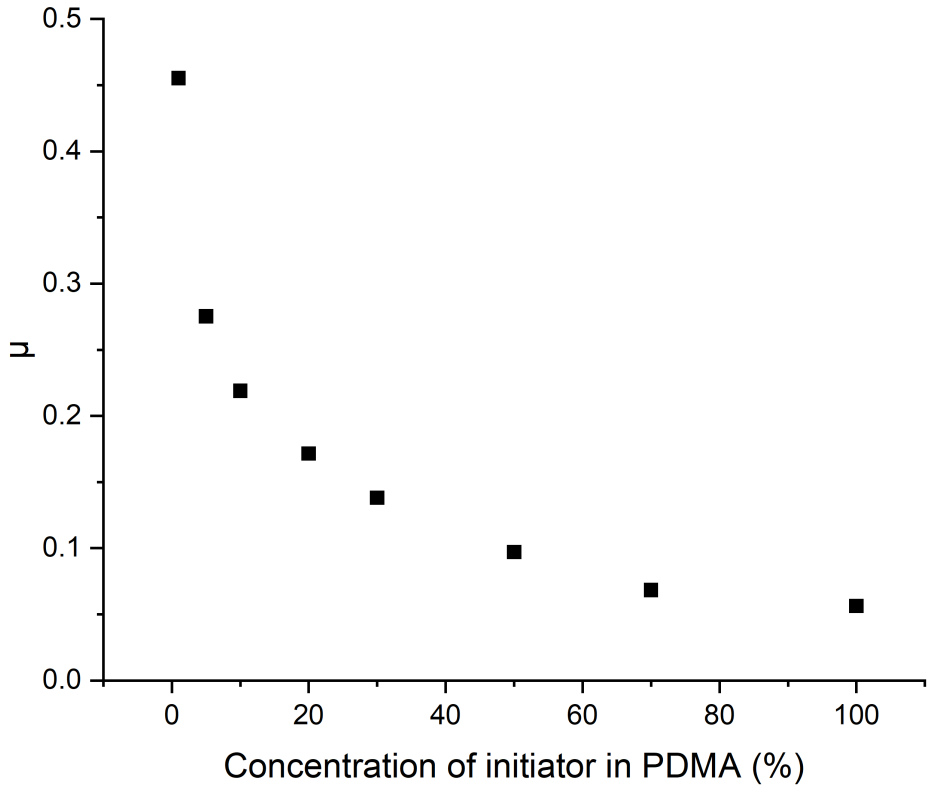

Figure 4.15: Analysis of correlation of friction-load measurements to equation1.31, change in (μ) over PDMA brush with different grafting density in water.

In a linear relationship between the friction force and load observed when studying PDMA brushes as a surface in ethanol as a poor solvent, there was an increase in the friction coefficient with increasing the grafting polymer density Figure 4.16. Based on the experimental results, the coefficient of friction (μ) was found to be lowest for samples with the lowest grafting density. Specifically, this was observed in the PDMA with concentration less than 30%. Among these, the PDMA brushes with a concentration 1% and 5% exhibited the lowest friction coefficient, followed by those with a concentration of 10%. Conversely, the highest coefficient of friction was recorded for the samples with the greatest grafting density, which corresponded to the PDMA 100%, 70% and 50%. To qualitatively understand this phenomenon, one must consider the concept of molecular ploughing. Molecular ploughing describes the energy dissipation occurring between the PDMA brushes and the scanning tip during frictional interactions, characterized by differences in force (ΔFF). This analysis emphasizes the substantial impact of grafting density on frictional behaviours. At high grafting densities, the densely packed polymer chains experience significant restrictions in chain mobility, resulting

in a noticeable molecular ploughing effect and greater energy dissipation. This increased resistance to sliding leads to a higher friction coefficient for these brushes. Therefore, at lower grafting densities, the thinner arrangement of polymer chains results in fewer contact points and less obvious changes in chain mobility. Consequently, the molecular ploughing effect is diminished, leading to lower energy dissipation and a reduced friction coefficient.

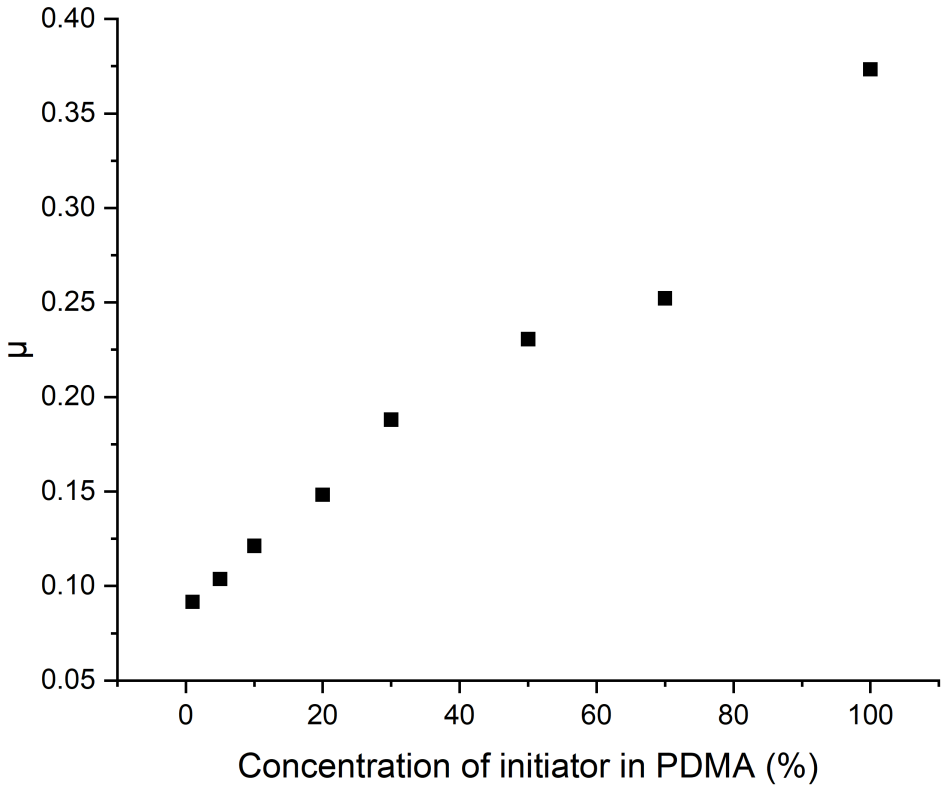

Figure 4.16: Analysis of correlation of friction-load using equation (1.31), change in (μ) over PDMA brush with different grafting density in ethanol.

4.6 Conclusion

In the synthesis of PDMA brushes through Surface-Initiated Atom Transfer Radical Polymerization (SI-ATRP) combined with dilution methods across a range of grafting densities, a significant dependence of the brush conformation on both the grafting density and their immediate surroundings was observed. This emphasizes the important relationship between the density of grafted polymer chains and the local environment in determining the structural characteristics of the PDMA brushes. the friction force experienced between the AFM tip and the surface of PDMA brushes can be dissected into two primary components: the load-dependent term and the shear-dependent term. The load-dependent term is contingent upon the normal load generated by the AFM tip onto the PDMA surface. Variations in the normal load directly influence the friction force experienced between the tip and the PDMA surface, with changes in the normal load leading to proportional alterations in the friction force. Essentially, the load-dependent term elucidates how the friction force adjusts in response to fluctuations in the force applied by the tip onto the PDMA surface. in contrast, the shear-dependent term of the friction force is governed by lateral or shear forces that arise between the AFM tip and the PDMA surface. These shear forces emanate from interactions between atoms or molecules at the interface between the tip and the PDMA surface. The magnitude of the shear-dependent term is contingent upon several factors, including the properties of the materials involved, surface characteristics, and the occurrence of sliding or shearing motion between them. A comprehensive understanding and quantification of these load-dependent and shear-dependent components of the friction force in AFM facilitate insights into the surface attributes, adhesion properties, and frictional dynamics of PDMA brushes at the nanoscale. Such insights are instrumental in various applications across fields like materials science, surface engineering, and nanotechnology. In a favourable solvent, sublinear friction-load correlations were obtained, indicating a complex association between the grafting density and the mechanical behaviours of the PDMA polymer brushes. At high grafting densities, the PDMA chains completely cover the surface, resulting in a significant area of contact between the brush and the tip surface. This extensive contact area, combined with the relatively small modulus of the polymer chains, contributes to adhesive sliding behaviours. The softness of the PDMA allows for deformation under load, leading to a reduction in the frictional force relative to the applied load.

However, as the grafting density decreases, the coverage of the surface by PDMA chains diminishes, resulting in fewer contact points between the brush and the tip surface. Consequently, the dominance of adhesive sliding diminishes, and ploughing becomes the primary mechanism governing the frictional behaviours. In this regime, the reduced density of PDMA chains leads to less extensive contact between the brush and the tip substrate, resulting in a transition to a linear friction-load relationship. Support for this conclusion comes from modelling the friction-load relationship using the Equation (1.31). It was observed that the surface shear strength (τ) exhibited variations corresponding to changes in the grafting density of PDMA. Specifically, τ increased with higher grafting densities but decreased noticeably at very low densities. This observation suggests a potential transition in the conformation of polymer chains, indicating a shift from brush-like structures to mushroom or coil configurations as the grafting density decreases. These observations highlight the complicated relationship between grafting density and frictional behaviours in PDMA brushes. Understanding how changes in grafting density influence frictional properties is crucial for the design and optimization of PDMA brush-based materials for various applications, including lubrication, surface modification, and biomaterials. Further investigation into the underlying mechanisms governing friction in polymer brushes across different grafting densities can provide valuable insights for improving their properties to specific application requirements.

CHAPTER 5 INVESTIGATION OF THE SURFACE CHEMISTRY AND NANOMECHANICS ON THE ATTACHMENT OF DYE MOLECULES TO PAGEO5MA POLYMER BRUSHES

5.1 Introduction

Polymer brush surfaces exhibit unique functionalities that make them highly suitable for various applications, including, lubrication[255], switchable wettability[256], selective fouling[257] and controlled gating in nano- and micropattern. A crucial feature in these contexts is the brush's permeability to dye molecular. These surfaces are formed by densely packed polymer chains that are anchored at one end, with permeability being significantly influenced by the conformation of these chains, which can range from fully extended to completely collapsed. This combination of permeability and brush thickness is often described as the hydrodynamic fingerprint of the polymer brush[258].

The attachment of dyes into polymer brushes is a strategic approach to modifying the chemical environment of the brush. Dye molecules can attach to polymer brushes through various mechanisms, such as electrostatic interactions, hydrogen bonding, or covalent bonding. These interactions can alter the conformation and flexibility of the polymer chains, as well as affect the absorption and emission properties of the dyes. Dye molecules can interact with the polymer chains and the surrounding medium, leading to changes in the physical and chemical properties of the surface. For example, incorporating fluorescent dyes into polymer brushes can enhance the surface's optical properties, allowing for applications in sensing and imaging[258]. On the other hand, incorporating hydrophobic dye molecules can make the surface more water-repellent, which can be useful in creating self-cleaning surfaces or preventing biofouling.

The diffusion of molecules through a polymer brush is governed by several factors, including the conformation and density of the brush, the solvent content, the size of the diffusing molecules, and the interactions between the molecules and the polymer chains. These factors collectively influence the brush's permeability. Studying attachment of dye molecules to polymer brushes provides a valuable mechanism for analyzing brush properties, offering insights beyond just measuring the average height of the polymer chains from the anchoring

surface. This method allows for a more detailed examination of the structure-property relationships of the brushes, ultimately leading to a better understanding of their physical solvation.

Depending on the architecture of the system being studied, quantifying the amount of dye molecules attached to polymer brush layers can range from relatively simple to quite challenging. One of the primary challenges in designing and fabricating polymer brushes with embedded inorganic or organic particles is achieving optimal dispersibility of the particles while preventing their aggregation and the formation of mesoscopic and microscopic clusters. Extensive research has focused on understanding how dyes attach to zwitterionic brushes that are immobilized on conductive substrates[259], [260], [261]. Techniques such as electrochemical impedance spectroscopy has been particularly useful in these studies[262].

Several studies have explored chemical modification techniques for polymer brushes[263], [264], [265]. For instance, poly (2-hydroxyethyl methacrylate) brushes can undergo esterification or oxidation to introduce specific functionalities[264]. In another approach, the epoxy groups within poly (glycidyl methacrylate) brushes can react with n-octylamine[266] or n-propylamine[267], while tertiary amine groups in poly(2-dimethylamino) ethyl methacrylate can be quaternized using different alkyl halides[266]. Zou et al. investigated the functionalization of periodate-oxidized poly[N-(2,3-dihydroxypropyl) acrylamide] (PDHPA) brushes with bovine serum albumin through reductive amination[268]. However, these derivatization protocols typically involve organic solvents and often result in relatively low degrees of functionalization. Leggett and colleagues synthesized a novel hydrophilic methacrylic monomer called GEO5MA [269]. This monomer features a pendent cis-diol group, which can be selectively oxidized with sodium periodate to produce an uncommon aldehyde-functional water-soluble monomer, AGEO5MA. Alternatively, GEO5MA can be homopolymerized to form PGEO5MA, which can then be easily transformed into PAGEO5MA by treating it with an aqueous sodium periodate solution under mild conditions. In their study, they utilized this chemistry to create new hydrophilic aldehyde-functional polymer brushes[269]. Literature suggests that these brushes are likely to attract significant interest for a range of bio-applications[267], [270], [271]. This interest stems from the potential of these brushes to facilitate easy conjugation of proteins or enzymes in aqueous solutions at room temperature. Additionally, these brushes can be easily derivatized with amino acids, such

as histidine, to create poly (amino acid methacrylate) brush through Schiff base chemistry. Both concepts were demonstrated in their previous study

In this study, Dr. C. Jesson conducted a similar reaction, substituting histidine with a methylaminopyrene molecule to synthesize a new PAGEO5MA brush. This modification enhances the range of functional groups attached to polymer brushes. By using methylaminopyrene, Dr. C. Jesson demonstrated the flexibility of the existing method to accommodate different amine-containing compounds, thus creating novel polymeric materials with unique properties. This approach not only highlights the robustness of the chemistry involved but also opens new possibilities for the design and development of advanced functional polymer brushes for bio-applications and beyond. The author investigated the nanomechanical properties of the PAGEO5MA brush both before and after attaching the brushes with varying concentrations of methylaminopyrene molecules.

The aim of this chapter is to investigate the functionalization of PAGEO5MA polymer brushes by attaching the dye molecule methylaminopyrene and to assess its impact on the brush's properties. This study explores the flexibility of the chemical modification strategy, enabling the attachment of various amine-containing molecules and expanding the functional potential of polymer brushes. This functionalization is particularly significant as it enhances the applicability of these materials in scientific and industrial fields. The study also examines the effect of dye attachment on the nanomechanical properties of polymer brushes using Friction Force Microscopy (FFM) to analyse changes in friction and stiffness. Understanding these modifications is crucial for optimizing polymer brush performance in fields such as biosensing, drug delivery, and nanotechnology. By evaluating the effect of different methylaminopyrene concentrations on the brush structure and behaviour, this research validates the modification approach and provides valuable insights into the design of advanced functional polymer materials.

5.2 Experimental Sections

5.2.1 Preparation of Silicon Wafers Functionalized with Initiator

Silicon (100) pieces were sectioned into squares approximately 1 × 1 cm^3 in size. These pieces underwent a 60-minute UV-ozone cleaning process at 103 Pa using a Bioforce Nanosciences ProCleaner. Subsequently, the cleaned wafers were inserted into test tubes, along with a 3 mL glass sample vial that contained about 100 µL of APTES. The test tubes were tightly closed

with rubber septa and heated in an oven at 100 °C for 60 minutes. After heating, the APTES-functionalized substrates were removed and allowed to sit so any excess APTES could evaporate. The wafers were then washed with THF and dried using dry air. Next, the wafers were immersed in a 0.1 M BIBB mixture in 1,4-dioxane for 18 hours at room temperature (22 °C). In the end, the substrates were thoroughly cleaned with 1,4-dioxane and water, then dried again under vacuum air.

5.2.2 Experiments on Polymerization Kinetics

SI-ARGET ATRP was employed to synthesise PGEO5MA brushes utilizing initiator-functionalized silicon wafers in an aqueous solution containing GEO5MA at a ratio of 45% v/v. The molar ratios of GEO5MA/Cu (II)Cl_2/PMDETA/ascorbic acid were maintained at 1000:1:5:3. The catalyst, ligand, monomer, and water were sequentially introduced to a 50 mL round bottom container supplied with a magnetic stir bar. The solution was shaken for 10 minutes before introducing ascorbic acid. Stirring continued for an additional 10 minutes to achieve active catalyst formation. Each initiator-functionalized silicon substrates were inserted in a sealed 1.5 mL vial, and the vial was injected with the reaction solution, minimizing the amount of air to less than 0.1 cm^3. After the desired polymerization period, each substrate was separated from the reaction solution, thoroughly washed several times with ethanol and deionized water, and dried using dry air.

5.2.3 Selective Oxidation of PGEO5MA Brushes Utilizing Sodium Periodate

Planar silicon wafers fabricated with PGEO5MA brushes have been submerged in a 3.0 $g \cdot dm^{-3}$ aqueous mixture of sodium periodate for 30 minutes at room temperature (22 °C). Afterward, each wafer underwent thorough rinsing with deionized water followed by drying with dry air.

5.2.4 Preparation of the PAGEO5MA Reference Brush via SI-ARGET ATRP

PAGEO5MA reference brush was synthesized with AGEO5MA using a ratio of 15% v/v, employing ascorbic acid according to the following procedure: AGEO5MA (0.87 mL, 3.1 mmol), water (4.79 mL), Cu(II)Cl_2 (0.92 mg, 6.84 μmol), and PMDETA (50 μL) were combined in a 7 mL sample vial. The mixture was mixed for 2 minutes to achieve complete mixture before adding ascorbic acid (0.15 mg, 0.85 μmol, 0.42 mM) and immersing the substrates. Each vial was filled with approximately 1 cm^3 of air, and the SI-ARGET ATRP of

GEO5MA proceeded for 1-2 hours at 22 °C. This process was halted by extracting the substrates from the reaction solution. Subsequently, each substrate was thoroughly washed with deionized water and dried using dry air.

5.2.5 Modification of PAGEO5MA Brushes with methylaminopyrene and Subsequent in Situ Reductive Amination

AGEO5MA brush-functionalized silicon wafers were immersed in an aqueous medium prepared with 3 $g \cdot dm^{-3}$ methylaminopyrene and 7 $g \cdot dm^{-3}$ $NaCNBH_3$ in methanol. The immersion was conducted at 50 °C for 16 hours. The concentration of the pyrene during the reaction was varied to target different degrees of functionalization (70%, 20% and 10%). The concentrations of pyrene to target these degrees of functionalization were 20 uM, 0.025 uM and 0.009 uM respectively. A 2.5 molar excess of $NaBH_3CN$ was used for all reactions. Afterward, each substrate was removed from the mixture, thoroughly cleaned with deionized water, and dried using dry air.

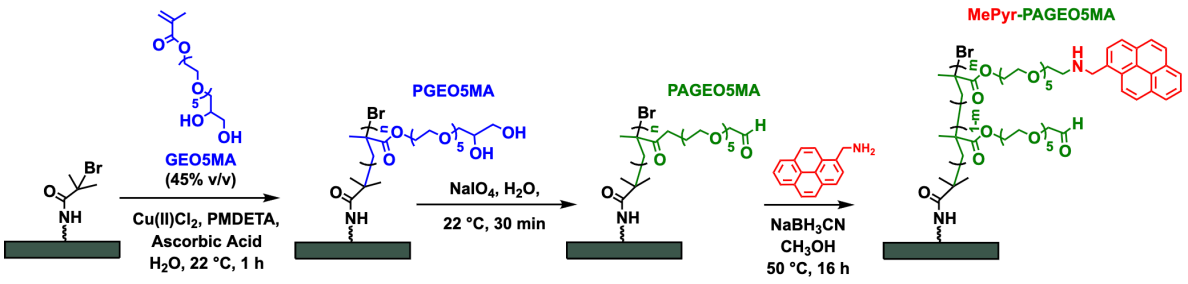

Scheme 5.1: A schematic representation of the Modification of PAGEO5MA Brushes with methylaminopyrene.

5.3 An analysis of the surface

Experimental procedures were conducted in accordance with experimental section 3 procedures and included ellipsometry, friction force microscopy (FFM). Ellipsometry will be used to measure the thickness and optical properties of the AGEO5MA brushes. Finally, friction force microscopy (FFM) will allow for the characterization of the surface topography and the measurement of frictional forces between the tip and AGEO5MA brushes.

5.4 Results and Discussion

5.4.1 Formation of PAGEO5MA Brushes with methylaminopyrene

SI-ARGET ATRP was employed to synthesise PGEO5MA brushes utilizing initiator-functionalized silicon wafers in an aqueous solution containing GEO5MA at a ratio of 45% v/v (Scheme 5.1). Planar silicon wafers fabricated with PGEO5MA brushes have been submerged in aqueous mixture of sodium periodate at room temperature. PAGEO5MA reference brush was synthesized with AGEO5MA using a ratio of 15% v/v, employing ascorbic acid according to AGEO5MA brush-functionalized silicon wafers were immersed in an aqueous medium prepared with different concentration of methylaminopyrene and $NaCNBH_3$ in methanol. Dr. C. Jesson studied the thickness of all polymers produced using Ellipsometry while the author examined their nanomechanical properties using FFM.

5.4.2 Swelling behaviour of PAGEO5MA brush brushes in methanol

PAGEO5MA brushes were treated with different concentrations of methylaminopyrene to produce a range of brushes with varying dye concentrations, ensuring uniform distribution across the entirety of the surface. The pyrene concentration was adjusted during the reaction to achieve different levels of functionalization, specifically targeting degrees of 70%, 20%, and 10%. These targeted functionalization levels corresponded to pyrene concentrations of 20 μM, 0.025 μM, and 0.009 μM, respectively, Subsequently, PAGEO5MA chains were initiated from these surfaces through Activators Regenerated by Electron Transfer Atom Transfer Radical Polymerization ARGET ATRP resulting in the creation of a variety of brushes with different degrees of functionalization. In addition to Friction Force Microscopy (FFM), several other techniques can be employed to characterize dye-functionalized polymer brushes. X-ray Photoelectron Spectroscopy (XPS) can be used to analyse the surface composition and chemical state of the dye-functionalized brushes, confirming the attachment of the dye and its interaction with the polymer. Additionally, Ellipsometry can measure the thickness and refractive index of the polymer films, providing data on the extent of functionalization (which has been studied by Dr. ED). While these techniques offer valuable complementary information, due to time constraints, this study primarily focuses on FFM to explore the nanomechanical properties and frictional behaviour of the dye-functionalized polymer brushes. The frictional behaviour was subsequently assessed for each sample, with the applied load as

the variable, in both methanol (considered a good solvent) and heptane (considered a poor solvent) environments for PAGEO5MA brushes.

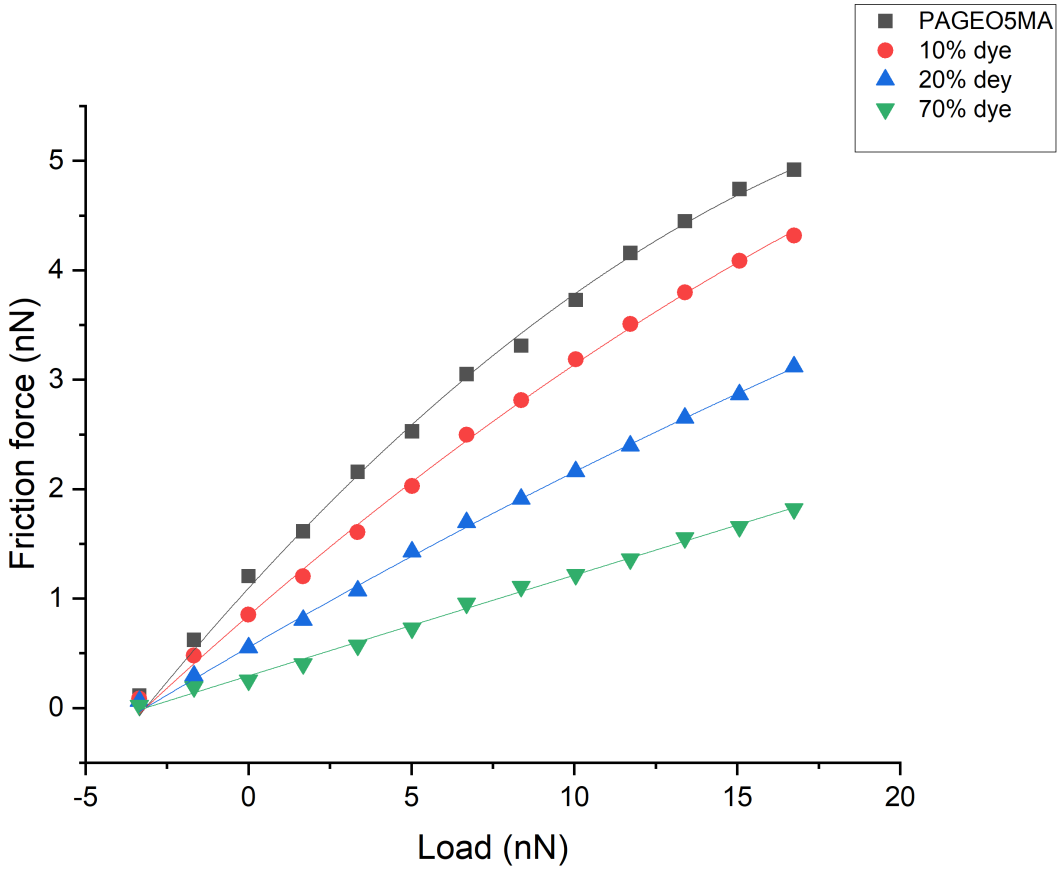

Figure 5.1: displays the typical friction-load plots obtained for PAGEO5MA brushes with different grafting density in methanol.

In the methanol environment, the friction behaviour at different dye concentrations is influenced by the extent of methylaminopyrene attachment, which alters the polymer brush structure and interactions (Figure 5.1). At higher dye concentrations, the brushes collapse, forming a random coil conformation. In this state, friction is dominated by ploughing, and the friction-load relationship is linear. However, as the dye concentrations decreases, there is a transition to a non-linear friction-load relationship, suggesting an increasing shear contribution to friction, and the friction force increases with grafting density. As the grafting density increases, the brushes become increasingly swollen, as solvent (methanol) molecules interact with the surface-grafted polymers and steric repulsion causes further swelling.

A non-linear relationship between friction and load was observed for higher grafting densities (see Fig. 5.1). Alternatively, a linear relationship was observed for lower grafting densities. As

the grafting density of PAGEO5MA brushes decreases, there may be a notable transition in the conformation of the polymer chains. Initially, at higher grafting densities, the polymer chains adopt a brush-like structure where they are densely packed and extend away from the substrate surface. This configuration typically results in a greater surface coverage and stronger interactions with the surrounding environment. However, as the grafting density decreases, fewer polymer chains are immobilized on the substrate surface. This reduction can lead to a transition in the conformation of the polymer chains from a brush-like structure to a mushroom or coil structure. In these configurations, the polymer chains are less extended and may become more collapsed or overlapping near the surface. This transition alters the surface properties significantly, affecting how the polymer interacts with its surroundings. Specifically, when methylaminopyrene is used to decrease the grafting density of the PAGEO5MA brushes, it influences how the polymer chains are tethered to the substrate. Lower concentrations of methylaminopyrene result in fewer initiation sites for polymer growth, thus reducing the number of polymer chains attached to the surface. This reduction in surface coverage and the alteration in chain conformation from extended brushes to more compact configurations can affect the surface energy, adhesion properties, and frictional behaviours of the modified surface. Under such conditions, the polymer experiences strong solvation by methanol, resulting in steric repulsion between adjacent chains. It is worth pointing that the steric repulsion between adjacent polymer chains due to strong solvation by methanol leads to increased polymer chain mobility and expansion. This causes the polymer to swell away from the surface, resulting in a larger contact area and altered physical properties. The high compressibility of the brushes, resulting from their small elastic moduli, allows the sharp tip to deeply penetrate the brush film, creating a large contact area. It obvious that elastic moduli refer to the measure of a material's ability to deform under stress and return to its original shape when the stress is removed. In the case of brushes with small elastic moduli, this means that they can easily be compressed and deformed, allowing the sharp tip to effectively pierce the brush surface and make maximum contact. This increased contact area enhances the efficiency of the brush in achieving its intended purpose. Despite the initial expectation of a low work of adhesion due to the solvated polymer, the polymer's low modulus leads to a substantial contact area, resulting in a significant net adhesive interaction. As a result, the frictional force shows a sublinear correlation with the applied load across the entire range, as illustrated in Figure 5.1. The friction-load relationship was effectively analysed and modelled using Equation (1.31).

There was, however, a notable change in this relationship as the density of the grafted brushes decreased with increasing methylaminopyrene concentration. It is noticeable that the relationships exhibited nonlinearity for pure PAGEO5MA, and brushes grown with concentrations of 10% methylaminopyrene, whereas they became linear for those grown with concentrations of 20%, and 70% dye. Moreover, the net interaction strength decreases as the density of the polymer decreases. There is clear evidence that polymer architecture influences intermolecular interactions and material behaviours in a significant way.

The contact mechanics of various PAGEO5MA configurations were studied, with adhesion force and surface shear stress quantified using the Equation (1.31). This analysis included both PAGEO5MA and PAGEO5MA with different dye concentration, specifically those with degrees of methylaminopyrene 70%, 20%, and 10% (Figure 5.2 and 5.3). The results demonstrate a clear trend: the shear strength of a feature improves with increases the grafting density. This means that the pure PAGEO5MA and PAGEO5MA with lower dye concentration (10%) brushes exhibited significantly higher adhesion forces and surface shear stress compared to their PAGEO5MA with mid (20%) and high (70%) dye concentration. These behaviours can be attributed to the larger contact area available in high grafting density, which facilitates stronger intermolecular interactions between molecules and the AFM tip. Among the low grafting density, a distinct structure was observed. Brushes with mid dye concentration displayed higher adhesion forces and surface shear stress than those with A high dye concentration. The PAGEO5MA with high dye concentration recorded the lowest values for both adhesion force and shear stress. This is likely due to the reduced number of polymer chains available for interaction in the smaller grafting density, which diminishes the overall contact area and, consequently, the frictional force. These observations are consistent with the principles of contact mechanics, where larger grafting density provide more extensive contact interfaces, leading to enhanced mechanical stability and greater resistance to deformation. In summary, the study highlights the crucial role of grafting density in determining the mechanical properties of PAGEO5MA, brushes with low methylaminopyrene concentration offering superior adhesion and shear strength compared to the brushes treated with mid and high methylaminopyrene concentration.

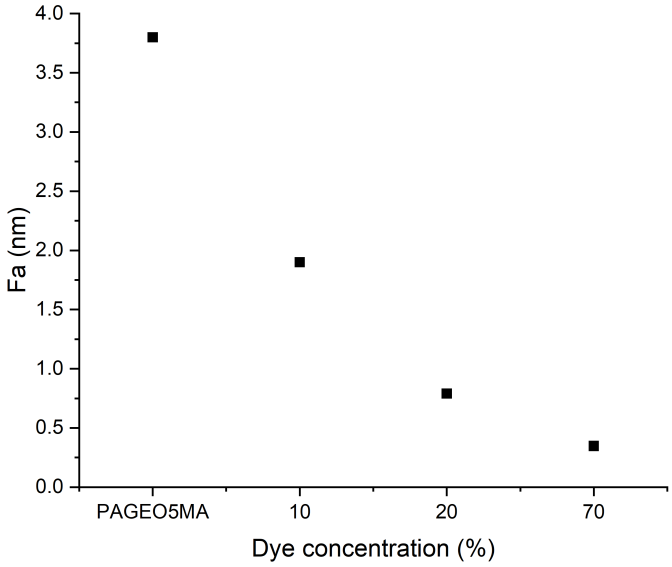

Figure 5.2: Relationship between adhesion forces and dyes concentration in PAGEO5MA brushes.

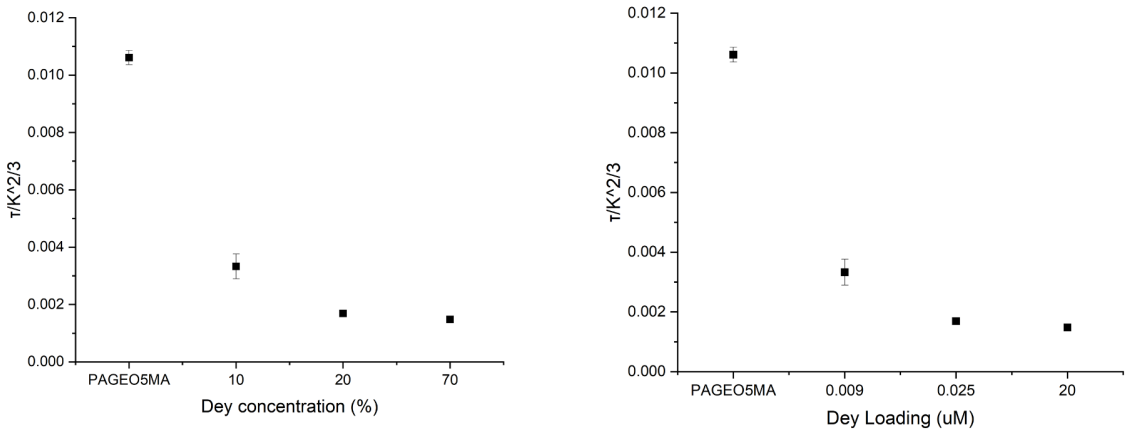

Figure 5.3: Analysis of correlation of surface shear stress calculated using Equation (1) as a function of PAGEO5MA brushes with different grafting density.

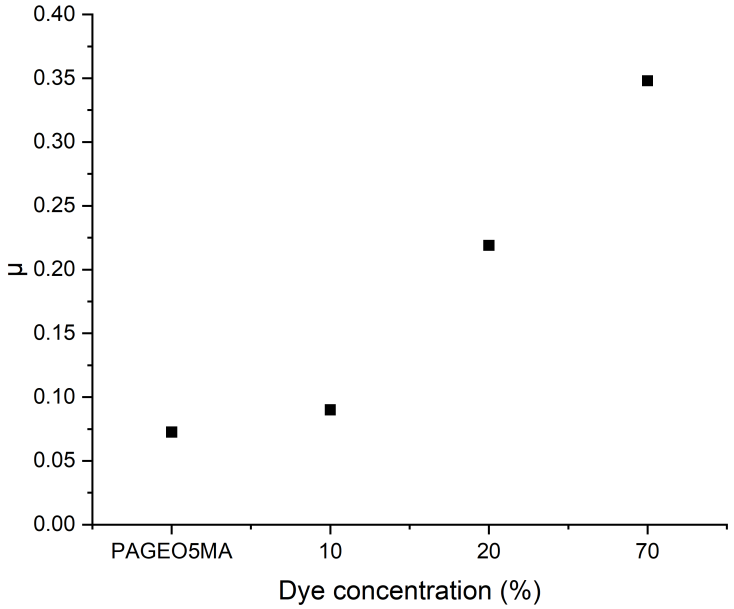

Figure 5.4: Analysis of correlation of friction coefficient as a function of PAGEO5MA brushes with different grafting density.

The friction coefficient (μ) for each configuration was calculated using the Equation (1.31), providing a detailed understanding of how different grafting density affect frictional behaviours (Figure 5.4). Good solvent (methanol) chains are swollen addition of dye creates the homogeneity that causes effective increases in the coefficient of friction. The findings reveal a clear trend: as the grafting density of the PAGEO5MA increases, the friction coefficient decreases. This inverse relationship is attributed to the changes in the density of polymer chains and the contact area between the AFM tip and the polymer surface. Specifically, larger grafting density PAGEO5MA brushes exhibited significantly lower friction coefficients compared to their lower grafting density. This is because larger features provide a more extensive contact area, which distributes the load more evenly and reduces the overall resistance to sliding. Among the lower grafting density, friction coefficients (μ) exhibited a distinct order. Brushes with mid dye concentration demonstrated a lower friction coefficient than those with high dye concentration. The highest dye concentration (70%) recorded the highest friction coefficients. This can be explained by the decrease the contact area of polymer chains within these features, which leads to weaker interactions with the AFM tip. Additionally, the smaller contact area with lower grafting density, results in higher local pressure and greater resistance to movement, Therefore, increasing the friction coefficient.

These results emphasize the importance of grafting density, in determining the frictional properties of PAGEO5MA brushes. In larger grafting density, the friction forces are distributed across a broader area, resulting in a smoother sliding interaction and a lower friction coefficient (μ). Alternatively, in smaller grafting density, the reduced polymer chains and contact area lead to higher frictional forces and greater resistance to sliding.

In summary, the study highlights that the friction coefficient is highly dependent on grafting density of the PAGEO5MA brushes. Larger grafting density tend to have lower friction coefficients (μ) due to better load distribution and less localized pressure, while smaller grafting density exhibit higher friction coefficients (μ) because of increased local resistance. This understanding is crucial for designing polymer surfaces with unique frictional properties for specific applications.

5.4.3 Swelling behaviour of PAGEO5MA brushes in heptane

In contrast, when polymer brushes are immersed in a poor solvent like heptane, the potential for favourable interactions, such as hydrogen bonding between the polymer chains (specifically PAGEO5MA brushes) and the solvent molecules, is significantly reduced. This reduction in interaction leads to a collapse of the polymer brush because the polymer chains prefer to interact with each other rather than with the solvent. This collapsed state often results in the formation of dense, mushroom-like structures. In such a solvent environment, the friction-load relationship tends to remain linear despite variations in grafting density Figure 5.5. This linearity can be explained by examining the structural and interaction dynamics of the polymer brushes in the poor solvent. Unlike in good solvents, where polymer brushes can extend and achieve fully swollen configurations due to favourable solvent-polymer interactions, in heptane, even the most densely grafted polymer chains fail to reach such expanded states. The poor solvent quality leads to the polymer chains collapsing into a more compact and denser form. As the polymer brush collapses, the primary mechanism driving the sliding friction becomes molecular ploughing. Molecular ploughing refers to the process where the moving surface disrubts and deforms the polymer chains during sliding. This interaction causes energy dissipation mainly through the continuous conformational changes and realignment of the polymer chains. As a result, the friction force is directly proportional to the applied load. This is because the extent of molecular ploughing and the degree of chain deformation increase proportionally with the load. Therefore, despite the variations in grafting density, the relationship between friction and load remains consistently linear. This consistency highlights

the critical influence of solvent quality on the conformational state of polymer brushes and their tribological behaviours. In a poor solvent like heptane, the polymer brushes do not achieve a swollen state, leading to a collapsed structure where the frictional force is almost exclusively governed by molecular ploughing.

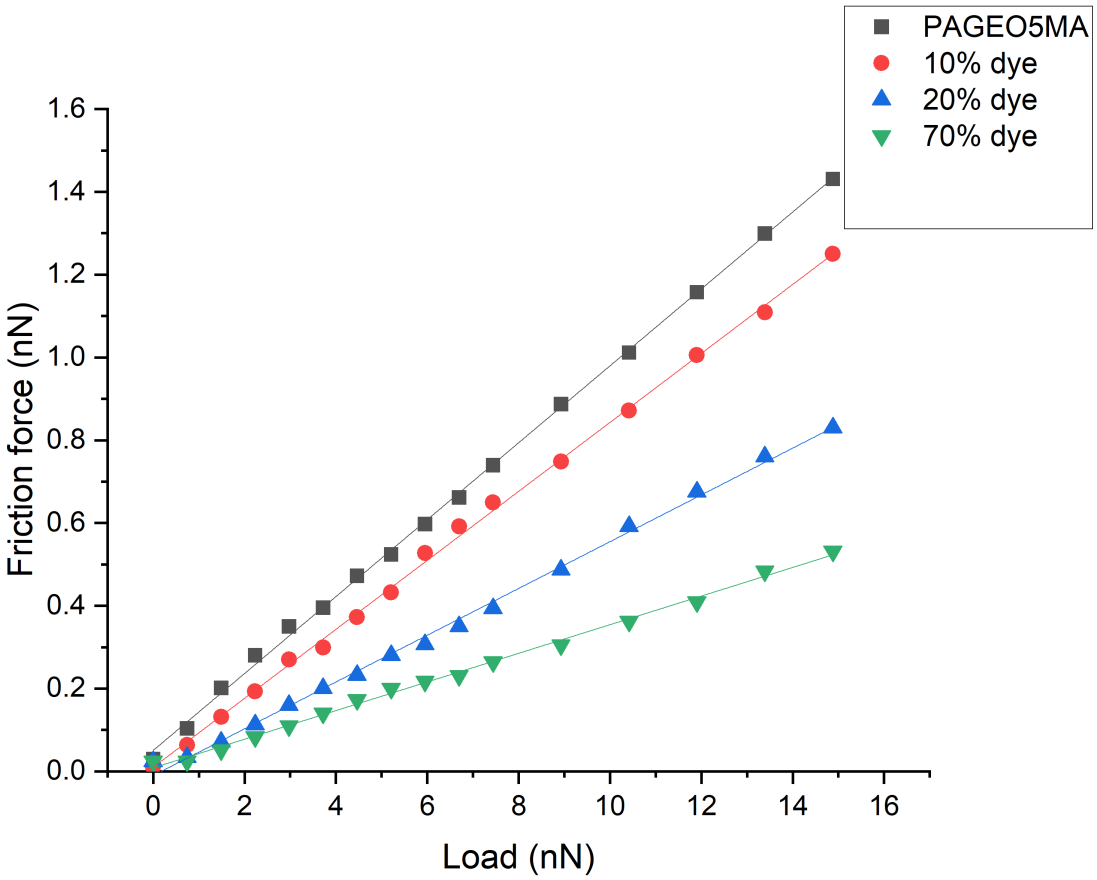

Figure 5.5: illustrates the changes in friction forces relative to applied loads across different grafted PAGEO5MA brushes in a heptane environment.

As a result of this, friction coefficients (μ) were determined from the friction-load graphs, illustrated in Figure 5.6 It has been found that there is a direct correlation between the friction coefficients of PAGEO5MA brushes and the grafting density of their structures. It can be explained by the fact that the number of collapsed PAGEO5MA polymer chains responsible for ploughing reduced as the grafting density became smaller.

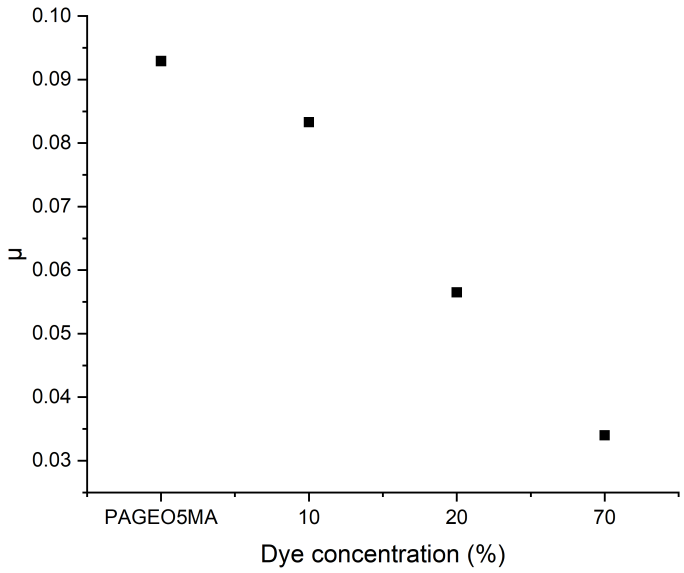

Figure 5.6: Coefficient of friction (μ) measured for PAGEO5MA brushes with varying grafting density in heptane.

Based on the experimental results, the coefficient of friction (μ) was found to be lowest for samples with the lowest grafting density. Specifically, this was observed in the PAGEO5MA brushes with mid and high dye concentration (20% and 70%) respectively. Among these, the PAGEO5MA brushes with 70% dye concentration exhibited the lowest friction coefficient, followed by those with 20% dye concentration. Conversely, the highest coefficient of friction was recorded for the samples with the greatest grafting density, which corresponded to the PAGEO5MA, and brushes attached with 10% dye concentration. In the poor solvent (heptane) chains are collapsed and adding dye molecules reduces pathways for energy dissipation in these collapsed structures. To qualitatively understand this phenomenon, it is essential to consider the concept of molecular ploughing. Molecular ploughing refers to the energy dissipation that occurs between the PAGEO5MA brushes and the scanning tip during frictional interactions. This energy dissipation can be described in terms of the force differences (ΔFF) involved. The amount of energy dissipated during these interactions can be ordered as follows: ΔFF pure PAGEO5MA > PAGEO5MA attached to 10% dye> PAGEO5MA attached to 20% dye> PAGEO5MA attached to 70% dye. In high grafting density, the dense arrangement of polymer chains leads to substantial change in the chain mobility, resulting in a higher degree of molecular ploughing and greater energy dissipation. This increased resistance to sliding rise the friction coefficient for these brushes. In contrast, in PAGEO5MA with lower grafting

densities, the reduced density of polymer chains translates to fewer contact points and less extensive change in the chain mobility. Consequently, the molecular ploughing effect is minimized, leading to lower energy dissipation and a reduced friction coefficient.This extensive knowledge of the relationship between grafting density and frictional behaviour is crucial for designing PAGEO5MA brush surfaces suited to particular purposes. For purposes needing minimal friction, such as in hydraulic systems or biomedical apparatuses, lower grafting densities are recommended due to their reduced energy dissipation and lower friction coefficients. Alternatively, for systems that benefit from higher frictional resistance, such as adhesive surfaces PAGEO5MA with higher grafting densities are more suitable. This facilitates greater energy dissipation and a greater friction coefficient.

In conclusion, the friction coefficient of PAGEOMA brushes is strongly linked to their grafting density. The concept of molecular ploughing and the associated energy dissipation quantitatively explains variations in frictional properties. This data enables the effective fabrication of PAGEOMA brush surfaces with optimized frictional characteristics. This improves their capabilities and usefulness for a wide range of industries.

5.5 Conclusion

In the fabrication of PAGEOMA brushes through Surface-Initiated Activator Regenerated by Electron Transfer Atom Transfer Radical Polymerization (SI-ARGET ATRP) combined with methylaminopyrene molecular polymerizations over a range of grafting densities, substantial influence of the brush conformation on both the grafting density and their surrounding environment was found. This demonstrates the essential relationship between the density of grafted polymer chains and the local environment in determining the physical properties of the PAGEOMA brushes. The friction force produced between the AFM tip and the surface of PAGEOMA brushes can be categorized into two primary factors: the load-dependent term and the shear-dependent term. An AFM tip exerts a normal load on the PAGEOMA surface to determine the load-dependent term. Variations in the normal load strongly influence the friction force generated between the tip and the PAGEOMA surface. Changes in the normal load contribute to proportional friction force variations. Fundamentally, an analysis of the load-dependent term explains how friction forces adjust under fluctuating loads applied by a tip to a PAGEOMA surface.

However, lateral or shear forces between the AFM tip and PAGEOMA surface determine the shear-dependent term of friction force. PAGEOMA brushes generate shear forces through interactions between atoms or molecules at the tip-surface interface. There are several factors that determine the magnitude of the shear-dependent term, including the characteristics of the materials involved, surface features, and the existence of sliding or shearing interactions between them.Using AFM to quantify load-dependent and shear-dependent friction factors facilitates insights into surface morphology, adhesion characteristics, and frictional dynamics of PAGEOMA brushes with different grafting densities. Such studies are essential in various applications across fields like chemical engineering, materials science, and nanoscopic technology. In a favourable solvent, sublinear friction-load correlations were obtained, indicating a complex association between the grafting density and the mechanical behaviours of the PAGEOMA polymer brushes. At high grafting densities, the PAGEOMA chains completely cover the surface, resulting in a significant area of contact between the brush and the tip surface. This extensive contact area, along with the relatively low modulus of the polymer chains, contributes to adhesive sliding behaviours. The softness of the PAGEOMA allows for deformation under load, reducing frictional forces as a result of the applied load. Furthermore, as the grafting density decreases, PAGEOMA chains cover less surface, resulting

in fewer contact points between the brush and the tip surface. Consequently, adhesive sliding diminishes, and ploughing becomes the primary mechanism governing frictional behaviours. Consequently, the reduced density of PAGEOMA chains leads to less extensive contact between the brush and the tip. This results in a transition to a linear friction-load relationship. According to the friction-load model, this conclusion is supported. It was observed that the surface shear strength (τ) exhibited variations corresponding to changes in PAGEOMA grafting density. Specifically, τ increased with higher grafting densities but decreased noticeably at extremely low densities. This observation suggests a potential change in polymer chains' conformations, indicating a shift from brush-like structures to mushroom or pancake configurations in relation to grafting density. These measurements highlight the complicated relationship between grafting density and frictional behaviours in PAGEOMA brushes. Understanding how changes in grafting density influence frictional properties is necessary for the fabrication and optimization of PAGEOMA brush-based materials for various practics, including coating, surface treating, and medical materials. It may be possible to improve polymer brushes' properties by studying the mechanisms governing friction across different grafting densities, providing valuable insights for improving their performance.

CHAPTER 6 SUMMARY OF THESIS

The aim of the research described in this thesis was to create a system based on polymers capable of chemical interactions on the micro and manometer scales. Achieving this objective necessitates meticulous attention to detail about the configuration and behaviour of the polymer chains at a molecular level. In addition, it requires meticulous attention to their performance under physical conditions.

6.1 Fabrication of PDMA micro- and nanostructures and analysis of their behaviour in relation to feature size

Various nanometre- and micrometre-scale structures of PDMA brushes were created using photo-patterned NPPOC-APTES films. Micrometre-scale structures were produced by exposing the silane surface through photomask lithography. Interference lithography at angles of 10° and 25° was employed to create manometer structures, resulting in periodicities of 690 nm and 350 nm, respectively. PDMA brushes were synthesized from the modified areas of the surface using SI-ATRP. Friction force measurements using FFM indicated that the conformation of the PDMA brushes is influenced by the feature dimensions and the characteristics of the surrounding medium. In a solvent that suits PDMA brushes, adhesion interactions primarily govern the contact mechanics at the interface. This results in a sublinear relationship between friction and applied load. The smaller polymer features exhibit reduced adhesion due to less contact area, leading to a decrease in the work of adhesion. Additionally, the behaviour of PDMA brushes is influenced by the solvent, the polymer's intrinsic properties such as free elastic energy, and the degree of lateral stretching of the polymer chains in the patterned areas. In contrast, when a poor solvent for PDMA, is introduced, the behaviour of the PDMA brushes changes significantly. The friction-load relationship becomes linear across all applied loads. This linearity is due to the collapse of the PDMA brush structure in poor solvent, where the polymer chains become densely packed. In this collapsed state, the shear stress is extremely low or nearly non-existent. As a result, molecular ploughing becomes the primary mechanism driving friction in the contact region. The most plausible explanation is that at high grafting densities, friction is primarily dominated by dissipation through shearing. As the grafting density decreases, this shifts to load-dependent ploughing. his suggests that at high density, the polymer chains form a brush structure due to the steric hindrance between chains. As the distance between adjacent grafting points decreases, the PDMA polymer chains begin

to collapse. There was no noticeable change in the polymer chain configuration when the solvent was poor in functionality. Friction-load relationships were linear, regardless of PDMA brush grafting density. Perhaps the polymer chains collapsed, and molecular plowing dominated the interface between tip and PDMA brushes. There is a direct correlation between grafting density and friction coefficient with grafting density being higher. The collapse of polymer chains refers to the compression and entanglement of the chains, which can lead to a reduction in their overall volume and increased surface contact with the substrate. This, in turn, enhances the phenomenon of molecular plowing, where the polymer chains act as "plows" that physically interact with the surface, resulting in higher friction coefficients. As the grafting density increases, there are more polymer chains available for collapse and molecular plowing, leading to a direct correlation between grafting density and friction coefficient.

6.2 Fabrication of PDMA and analysis of their behaviour based on grafting density in various environments

The PDMA brushes were synthesized using bromine-functionalized APTES (3-Aminopropyltriethoxysilane) treated with varying dilutions to generate different surface initiator densities. This ensured a uniform distribution of initiators across the surface. Atom Transfer Radical Polymerization (ATRP) was then employed to grow PDMA chains from these initiators, resulting in brushes with diverse densities. In water, which acts as a good solvent for PDMA, the frictional behaviour was assessed by measuring the friction force as a function of the applied load. The study found that at higher initiator densities, the relationship between friction and load was nonlinear. This can be attributed to the strong solvation and steric repulsion experienced by the polymer chains, causing them to swell away from the surface and form a brush-like structure. The high compressibility of these brushes, due to their low elastic modulus, allows a sharp tip to penetrate deeply, increasing the contact area and leading to significant adhesive interaction. Conversely, at lower initiator densities, the relationship between friction and load became linear. This transition is likely due to the reduced surface chain density, causing the PDMA chains to collapse into "mushroom" conformations. In this state, despite the solvent’s tendency to solvate the polymer, the decreased density leads to less steric repulsion, resulting in a more collapsed structure. The frictional behaviour in this regime was successfully modelled using the Equation, indicating a strong correlation between grafting density, polymer conformation, and frictional properties.

in contrast, when ethanol, a poor solvent for PDMA, was introduced, a significant change in the frictional behaviour was observed. Across all applied loads, the friction-load relationship was consistently linear regardless of the initiator density. This linearity is due to the collapse of the PDMA brush structure in ethanol, where the polymer chains are densely packed and the potential for hydrogen bond interactions with the solvent is greatly reduced. In this collapsed state, the shear stress is extremely low or nearly non-existent, and molecular ploughing becomes the primary mechanism driving friction in the contact region. A comparative analysis of the frictional behaviour in water and ethanol highlighted the critical role of solvent quality. In water, the transition from a nonlinear to a linear friction-load relationship with decreasing grafting density underscores the significant impact of polymer architecture and intermolecular interactions. The study showed that as the distance between grafting points increased, the polymer chains began to collapse, leading to changes in frictional behaviour. In ethanol, the poor solvent quality minimized solvent-induced conformational changes in the polymer brushes. The consistent linear friction-load relationship across different grafting densities indicates that the frictional characteristics primarily reflect the fundamental properties of the polymer chains, rather than being influenced by changes in grafting density.

6.3 Fabrication of PAGEOMA and analysis of their behaviour based on grafting density in various environments

In the study of PAGEOMA brushes fabricated via Surface-Initiated Activator Regenerated by Electron Transfer Atom Transfer Radical Polymerization (SI-ARGET ATRP) combined with methylaminopyrene molecular polymerizations, the relationship between grafting density and local environment significantly affects the brushes' physical properties. The friction force between an AFM tip and PAGEOMA surface is influenced by load-dependent and shear-dependent factors. The load-dependent term is determined by the normal load applied by the AFM tip, with friction force varying proportionally to this load. The shear-dependent term is influenced by interactions at the tip-surface interface, with factors such as material characteristics, surface features, and sliding interactions playing a role. FFM analysis of these friction factors provides insights into the surface morphology, adhesion, and friction dynamics of PAGEOMA brushes at different grafting densities. In a favourable solvent, sublinear friction-load correlations were observed, indicating complex interactions between grafting density and mechanical behaviour. High grafting densities result in extensive contact areas and adhesive sliding due to the soft, deformable polymer chains, leading to reduced friction under

load. Conversely, lower grafting densities reduce contact points, resulting in a transition to ploughing as the primary friction mechanism and a linear friction-load relationship. The surface shear strength (τ) varies with grafting density, increasing at higher densities and decreasing at very low densities, suggesting a shift in polymer chain conformation from brush-like to mushroom or pancake structures. These findings highlight the intricate relationship between grafting density and frictional behavior in PAGEOMA brushes. Understanding these mechanisms is crucial for optimizing the performance of PAGEOMA brush-based materials in applications such as coatings, surface treatments, and medical materials.

6.4 Future Work

A fascinating area for future research would be to investigate the conformation of various micrometer and nanometer PDMA brushes in mixed solvent environments. These mixtures could be composed of both favorable and unfavorable solvents in varying concentrations. The brushes structure may change depending on the solvent concentrations in the mixture. Additionally, examining how the thickness of the brushes influences their behaviours in different environments would be valuable. This can be achieved by fabricating micrometre and nanometre brush structures with varying thicknesses, utilizing FFM to gather friction data, and characterizing the results using contact mechanics models. These studies could provied the fundamental understanding of the behaviours of patterned brushes and serve as a foundation for their potential application in various physiological conditions.

Furthermore, it would be intersting to examine how the morphology, chemistry, and nanomechanics of nanometer patterned PDMA brushes influence the attachment and behavior of different cell types. This investigation could provide valuable insights into the interaction between the patterned brushes and various cells, potentially informing the design of advanced materials for biomedical applications. Understanding these interactions over varying cultivation periods and analyzing the nanomechanical properties could lead to significant advancements in tissue engineering and medicine.

Investigating the conformation of various micrometer and nanometer PAGEOMA brushes in mixed solvent environments is highly beneficial for advancing the understanding of these materials. Studying the behavior of these brushes in solvent mixtures, composed of both good and poor solvents in varying concentrations, can provide valuable insights into their structural dynamics and interactions. This research could discover how different solvent environments

influence the physical properties and stability of PAGEOMA brushes, shedding light on the fundamental principles governing their behavior. Such insights are crucial for optimizing the design and application of PAGEOMA brushes in a wide range of fields, including materials science, nanotechnology, and biomedical engineering. Furthermore, understanding the conformation of these brushes in mixed solvents could inform the development of new materials with tailored properties for specific applications, such as targeted drug delivery systems, responsive surfaces, and advanced coatings. This comprehensive investigation would thus provide a solid foundation for future innovations and practical implementations of PAGEOMA brush technologies.

CHAPTER 7 REFERENCES

[1] W. H. Keesom, "On the deduction of the Equation of State from Boltzmann's Entropy Principle," in *Proceeding of Royal Netherlands Academy of Arts and Sciences (KNAW)*, 1912, pp. 240–256.

[2] P. Debye, "Molecular Forces and Their Electrical Interpretation," *Physikalische Zeitschrift*, vol. 22, pp. 302–308, 1921.

[3] F. London, "Zur Theorie und Systematik der Molekularkräfte," *Zeitschrift für Physik*, vol. 63, pp. 245–279, Mar. 1930, doi: 10.1007/BF01421741.

[4] J. Israelachvili, *Intermolecular and surface forces*. Academic Press, 2011.

[5] H. C. Hamaker, "The London-van der Waals attraction between spherical particles," *Physica*, vol. 4, no. 10, pp. 1058–1072, 1937.

[6] S. woo Lee and W. M. Sigmund, "AFM study of repulsive van der Waals forces between Teflon AF™ thin film and silica or alumina," *Colloids Surf A Physicochem Eng Asp*, vol. 204, no. 1–3, pp. 43–50, 2002.

[7] E. M. Lifshitz, "The theory of molecular attractive forces between solids," 1956.

[8] K. Autumn, "Van der Waals Forces: A Handbook for Biologists, Chemists, Engineers, and Physicists.," in *The Quarterly Review of Biology*, vol. 81, no. 3, Cambridge University Press, 2006, p. 273.

[9] Parsegian, V.A., *Van der Waals Forces: A Handbook for Biologists, Chemists, Engineers, and ... - V. Adrian Parsegian.* Cambridge University Press., 2005.

[10] N. Nikogeorgos and G. J. Leggett, "The relationship between contact mechanics and adhesion in nanoscale contacts between non-polar molecular monolayers," *Tribol Lett*, vol. 50, no. 2, pp. 145–155, 2013.

[11] W. J. Miller and N. L. Abbott, "Influence of van der Waals forces from metallic substrates on fluids supported on self-assembled monolayers formed from alkanethiols," *Langmuir*, vol. 13, no. 26, pp. 7106–7114, 1997.

[12] M. D. Joesten, L. J. Schaad, and M. Tamres, “Hydrogen Bonding,” in *Physics Today*, vol. 28, no. 11, 1975, pp. 72–72.

[13] J. L. Cook, C. A. Hunter, C. M. R. Low, A. Perez-Velasco, and J. G. Vinter, “Solvent effects on hydrogen bonding,” *Angewandte Chemie - International Edition*, vol. 46, no. 20, pp. 3706–3709, 2007.

[14] N. J. Buurma, J. L. Cook, C. A. Hunter, C. M. R. Low, and J. G. Vinter, “The role of functional group concentration in solvation thermodynamics,” *Chem Sci*, vol. 1, no. 2, pp. 242–246, 2010.

[15] N. Nikogeorgos, C. A. Hunter, and G. J. Leggett, “Relationship between molecular contact thermodynamics and surface contact mechanics,” *Langmuir*, vol. 28, no. 51, pp. 17709–17717, 2012.

[16] C. A. Hunter, “Quantifying intermolecular interactions: Guidelines for the molecular recognition toolbox,” *Angewandte Chemie - International Edition*, vol. 43, no. 40, pp. 5310–5324, 2004.

[17] M. H. Abraham and J. A. Platts, “Hydrogen bond structural group constants,” *Journal of Organic Chemistry*, vol. 66, no. 10, pp. 3484–3491, 2001.

[18] K. Busuttil, M. Geoghegan, C. A. Hunter, and G. J. Leggett, “Contact mechanics of nanometer-scale molecular contacts: Correlation between adhesion, friction, and hydrogen bond thermodynamics,” *J Am Chem Soc*, vol. 133, no. 22, pp. 8625–8632, 2011.

[19] C. A. Hunter, “A surface site interaction model for the properties of liquids at equilibrium,” *Chem Sci*, vol. 4, no. 4, pp. 1687–1700, 2013.

[20] T. D and Winterton Rhs, “Direct Measurement of Normal and Retarded Van Der Waals Forces,” vol. 312, no. 1511The measurement of van der Waals dispersion forces in the range 1.5 to 130 nm.pdf, pp. 435–450, 1969.

[21] J. N. Israelachvili and D. Tabor, “The Measurement of Van Der Waals Dispersion Forces in The Range 1.5 to 130 nm,” *Proceedings of the Royal Society of London.*

A. Mathematical and Physical Sciences, vol. 331, no. 1584, pp. 19–38, Nov. 1972, doi: 10.1098/rspa.1972.0162.

[22] J. N. Israelachvili and G. E. Adams, "Measurement of forces between two mica surfaces in aqueous electrolyte solutions in the range 0-100 nm," *Journal of the Chemical Society, Faraday Transactions 1: Physical Chemistry in Condensed Phases*, vol. 74, pp. 975–1001, 1978, doi: 10.1039/F19787400975.

[23] Y. H. Tsao, D. F. Evans, and H. Wennerström, "Long-Range Attraction between a Hydrophobic Surface and a Polar Surface Is Stronger Than That between Two Hydrophobic Surfaces," *Langmuir*, vol. 9, no. 3, pp. 779–785, 1993, doi: 10.1021/la00027a029.

[24] B. Bhushan, J. N. Israelachvili, and U. Landman, "Nanotribology: Friction, wear and lubrication at the atomic scale," *Nature*, vol. 374, no. 6523, pp. 607–616, 1995, doi: 10.1038/374607a0.

[25] Y. Liu, T. Wu, and D. F. Evans, "Lateral Force Microscopy Study on the Shear Properties of Self-Assembled Monolayers of Dialkylammonium Surfactant on Mica," *Langmuir*, vol. 10, no. 7, pp. 2241–2245, 1994, doi: 10.1021/la00019a035.

[26] G. Binnig, C. F. Quate, and Ch. Gerber, "Atomic Force Microscope," *Phys Rev Lett*, vol. 56, no. 9, pp. 930–933, Mar. 1986, doi: 10.1103/PhysRevLett.56.930.

[27] O. Marti, J. Colchero, and J. Mlynek, "Combined scanning force and friction microscopy of mica," *Nanotechnology*, vol. 1, no. 2, pp. 141–144, 1990, doi: 10.1088/0957-4484/1/2/003.

[28] E. W. Van Der Vegte and G. Hadziioannou, "Scanning force microscopy with chemical specificity: An extensive study of chemically specific tip-surface interactions and the chemical imaging of surface functional groups," *Langmuir*, vol. 13, no. 16, pp. 4357–4368, 1997.

[29] W. A. Ducker, T. J. Senden, and R. M. Pashley, "Measurement of forces in liquids using a force microscope," *Langmuir*, vol. 8, no. 7, pp. 1831–1836, 1992, doi: 10.1021/la00043a024.

[30] M. Salmeron, G. Neubauer, A. Folch, M. Tomitori, D. F. Ogletree, and P. Sautet, "Viscoelastic and electrical properties of self-assembled monolayers on gold (111) films," *Langmuir*, vol. 9, no. 12, pp. 3600–3611, 1993, doi: 10.1021/la00036a041.

[31] C. M. Mate, G. M. McClelland, R. Erlandsson, and S. Chiang, "Atomic-Scale Friction of a Tungsten Tip on a Graphite Surface," Springer, Dordrecht., 1987, pp. 226–229. doi: 10.1007/978-94-011-1812-5_35.

[32] J. A. Ruan and B. Bhushan, "Atomic-scale and microscale friction studies of graphite and diamond using friction force microscopy," *J Appl Phys*, vol. 76, no. 9, pp. 5022–5035, 1994, doi: 10.1063/1.357214.

[33] X. Xiao, J. Hu, D. H. Charych, and M. Salmeron, *Chain Length Dependence of the Frictional Properties of Alkylsilane Molecules Self-Assembled on Mica Studied by Atomic Force Microscopy*, vol. 12, no. 2. American Chemical Society, 1996. doi: 10.1021/la950771u.

[34] B. Bhushan and V. N. Koinkar, "Tribological studies of silicon for magnetic recording applications (invited)," *J Appl Phys*, vol. 75, no. 10, pp. 5741–5746, 1994, doi: 10.1063/1.355601.

[35] B. Bhushan and S. Sundararajan, "Micro/nanoscale friction and wear mechanisms of thin films using atomic force and friction force microscopy," *Acta Mater*, vol. 46, no. 11, pp. 3793–3804, 1998.

[36] B. Cappella and G. Dietler, "Force-distance curves by atomic force microscopy," *Surf Sci Rep*, vol. 34, no. 1–3, pp. 1–104, Jan. 1999.

[37] R. L. Jackson, H. Ghaednia, H. Lee, A. Rostami, and X. Wang, "Contact Mechanics," in *Tribology for Scientists and Engineers*, New York, NY: Springer New York, 2013, pp. 93–140.

[38] B. N. J. Persson, O. Albohr, U. Tartaglino, A. I. Volokitin, and E. Tosatti, "On the nature of surface roughness with application to contact mechanics, sealing, rubber friction and adhesion," 2005, *IOP Publishing*.

[39] A. Tiwari, A. Wang, M. H. Müser, and B. N. J. Persson, “Contact Mechanics for Solids with Randomly Rough Surfaces and Plasticity,” *Lubricants*, vol. 7, no. 10, p. 90, Oct. 2019.

[40] A. Johnson, K.L., Kendall, K. and Roberts, “Surface energy and the contact of elastic solids,” in *Proceedings of the Royal Society of London. A. Mathematical and Physical Sciences*, vol. 324, no. 1558, The Royal Society, 1971, pp. 301–313.

[41] I. Szlufarska, M. Chandross, and R. W. Carpick, “Recent advances in single-asperity nanotribology,” *J Phys D Appl Phys*, vol. 41, no. 12, 2008.

[42] G. J. Leggett, N. J. Brewer, and K. S. L. Chong, “Friction force microscopy: Towards quantitative analysis of molecular organisation with nanometre spatial resolution,” *Physical Chemistry Chemical Physics*, vol. 7, no. 6, pp. 1107–1120, 2005.

[43] G. J. Leggett, “Friction force microscopy of self-assembled monolayers: Probing molecular organisation at the nanometre scale,” *Anal Chim Acta*, vol. 479, no. 1, pp. 17–38, 2003.

[44] K. P. Sigdel, L. A. Wilt, B. P. Marsh, A. G. Roberts, and G. M. King, “The conformation and dynamics of P-glycoprotein in a lipid bilayer investigated by atomic force microscopy,” *Biochem Pharmacol*, vol. 156, pp. 302–311, 2018.

[45] R. D. O’Rorke, T. W. J. Steele, and H. K. Taylor, “Bioinspired fibrillar adhesives: A review of analytical models and experimental evidence for adhesion enhancement by surface patterns,” *J Adhes Sci Technol*, vol. 30, no. 4, pp. 362–391, 2016.

[46] D. S. Grierson, E. E. Flater, and R. W. Carpick, “Accounting for the JKR-DMT transition in adhesion and friction measurements with atomic force microscopy,” *J Adhes Sci Technol*, vol. 19, no. 3–5, pp. 291–311, 2005.

[47] J. A. Greenwood, “Adhesion of elastic spheres,” in *Proceedings of the Royal Society A: Mathematical, Physical and Engineering Sciences*, 1997, pp. 1277–1297.

[48] D. V. Vezenov, A. Noy, L. F. Rozsnyai, and C. M. Lieber, “Force titrations and ionization state sensitive imaging of functional groups in aqueous solutions by chemical force microscopy,” *J Am Chem Soc*, vol. 119, no. 8, pp. 2006–2015, 1997.

[49] D. Maugis, “Adhesion of spheres: The JKR-DMT transition using a dugdale model,” *J Colloid Interface Sci*, vol. 150, no. 1, pp. 243–269, 1992.

[50] R. W. Carpick, D. F. Ogletree, and M. Salmeron, “A General Equation for Fitting Contact Area and Friction vs Load Measurements,” *J Colloid Interface Sci*, vol. 211, no. 2, pp. 395–400, Mar. 1999.

[51] T. Ito, S. Ibrahim, and I. Grabowska, “Chemical-force microscopy for materials characterization,” *TrAC - Trends in Analytical Chemistry*, vol. 29, no. 3, pp. 225–233, 2010.

[52] A. Noy, C. D. Frisbie, L. F. Rozsnyai, M. S. Wrighton, and C. M. Lieber, “Chemical Force Microscopy: Exploiting Chemically-Modified Tips To Quantify Adhesion, Friction, and Functional Group Distributions in Molecular Assemblies,” *J Am Chem Soc*, vol. 117, no. 30, pp. 7943–7951, 1995.

[53] J. Chen, Y. Xu, Y. Shi, and T. Xia, “Functionalization of Atomic Force Microscope Cantilevers with Single-T Cells or Single-Particle for Immunological Single-Cell Force Spectroscopy,” *Journal of Visualized Experiments*, vol. 2019, no. 149, pp. 1–9, Jul. 2019, doi: 10.3791/59609.

[54] T. Nakagawa, “Atomic force microscope for chemical sensing,” *Journal of Vacuum Science & Technology B: Microelectronics and Nanometer Structures*, vol. 12, no. 3, pp. 2215–2218, May 1994.

[55] T. Nakagawa, K. Ogawa, T. Kurumizawa, and S. Ozaki, “Discriminating molecular length of chemically adsorbed molecules using an atomic force microscope having a tip covered with sensor molecules (An atomic force microscope having chemical sensing function),” *Jpn J Appl Phys*, vol. 32, no. 2 B, pp. L294–L296, 1993.

[56] T. Ito, M. Namba, P. Bühlmann, and Y. Umezawa, “Modification of silicon nitride tips with trichlorosilane Self-Assembled Monolayers (SAMs) for chemical force microscopy,” *Langmuir*, vol. 13, no. 16, pp. 4323–4332, 1997.

[57] A. Noy, D. V. Vezenov, and C. M. Lieber, “Chemical force microscopy,” *Annual Review of Materials Science*, vol. 27, no. 1, pp. 381–421, 1997, doi: 10.1146/annurev.matsci.27.1.381.

[58] C. R. Hurley and G. J. Leggett, “Influence of the Solvent Environment on the Contact Mechanics of Tip−Sample Interactions in Friction Force Microscopy of Poly(ethylene terephthalate) Films,” *Langmuir*, vol. 22, no. 9, pp. 4179–4183, Apr. 2006, doi: Noob Name.pdfNoob Name.pdf.

[59] N. J. Brewer, B. D. Beake, and G. J. Leggett, “Friction force microscopy of self-assembled monolayers: Influence of adsorbate alkyl chain length, terminal group chemistry, and scan velocity,” *Langmuir*, vol. 17, no. 6, pp. 1970–1974, 2001.

[60] S. Yuan, T. Chu, L. Ma, J. Hou, and J. Wang, “AFM Calibration of Nano-friction through Estimating Meniscus Water Membrane Contour between Single Polystyrene Nano-particle and Silicon Surface,” in *2019 IEEE International Conference on Robotics and Biomimetics (ROBIO)*, IEEE, Dec. 2019, pp. 2351–2356.

[61] B. Bhushan, “Introduction to Scanning Probe Microscopy,” in *Materials Characterization*, ASM International, 2019, pp. 709–724. doi: 10.31399/asm.hb.v10.a0006633.

[62] R. W. Friddle and K. Thürmer, “Mapping ice formation to mineral-surface topography using a micro mixing chamber with video and atomic-force microscopy,” *Atmos Meas Tech*, vol. 13, no. 5, pp. 2209–2218, 2020.

[63] G. J. Leggett, “Scanning probe microscopy,” Surface Analysis–The Principal Techniques, 2009, pp. 479–562.

[64] B. D. Beake and G. J. Leggett, “Friction and adhesion of mixed self-assembled monolayers studied by chemical force microscopy,” *Physical Chemistry Chemical Physics*, vol. 1, no. 14, pp. 3345–3350, 1999.

[65] N. J. Brewer and G. J. Leggett, “Chemical force microscopy of mixed self-assembled monolayers of alkanethiols on gold: Evidence for phase separation,” *Langmuir*, vol. 20, no. 10, pp. 4109–4115, 2004.

[66] J. Gao, W. D. Luedtke, D. Gourdon, M. Ruths, J. N. Israelachvili, and U. Landman, “Frictional forces and Amontons’ law: From the molecular to the macroscopic scale,” *Journal of Physical Chemistry B*, vol. 108, no. 11, pp. 3410–3425, 2004.

[67] Z. Zhang, A. J. Morse, S. P. Armes, A. L. Lewis, M. Geoghegan, and G. J. Leggett, “Nanoscale contact mechanics of biocompatible polyzwitterionic brushes,” *Langmuir*, vol. 29, no. 34, pp. 10684–10692, 2013.

[68] B. Y. Chen, M. K. Yeh, and N. H. Tai, “Accuracy of the spring constant of atomic force microscopy cantilevers by finite element method,” *Anal Chem*, vol. 79, no. 4, pp. 1333–1338, 2007.

[69] P. J. Cumpson, C. A. Clifford, and J. Hedley, “Quantitative analytical atomic force microscopy: A cantilever reference device for easy and accurate AFM spring-constant calibration,” *Meas Sci Technol*, vol. 15, no. 7, pp. 1337–1346, 2004.

[70] P. K. Cleveland, J.P., Manne, S., Bocek, D. and Hansma, “A non-destructive method for determining the spring constant of cantilevers for scanning force microscopy.,” *J Appl Phys*, vol. 64, no. 2, pp. 403–405, 1993.

[71] Tortonese, M. and Kirk, M., “Characterization of application-specific probes for SPMs,” *spiedigitallibrary.org*, vol. 3009, pp. 53–60, 1997.

[72] J. L. Hutter and J. Bechhoefer, “Erratum: ‘“Calibration of atomic-force microscope tips”’ [Rev. Sci. Instrum. 64 , 1868 (1993)],” *Review of Scientific Instruments*, vol. 64, no. 11, p. 3342, 1993.

[73] H. J. Butt and M. Jaschke, “Calculation of thermal noise in atomic force microscopy,” *Nanotechnology*, vol. 6, no. 1, pp. 1–7, 1995.

[74] G. A. Matei, E. J. Thoreson, J. R. Pratt, D. B. Newell, and N. A. Burnham, “Precision and accuracy of thermal calibration of atomic force microscopy cantilevers,” *Review of Scientific Instruments*, vol. 77, no. 8, p. 083703, 2006.

[75] E. Gnecco, R. Bennewitz, T. Gyalog, and E. Meyer, “Friction experiments on the nanometre scale,” *Journal of Physics Condensed Matter*, vol. 13, no. 31, 2001.

[76] N. Wiener, *The Fourier integral and certain of its applications*. 1988.

[77] R. W. Stark, T. Drobek, and W. M. Heckl, “Thermomechanical noise of a free v-shaped cantilever for atomic-force microscopy,” *Ultramicroscopy*, vol. 86, no. 1–2, pp. 207–215, 2001.

[78] A. D. Slattery, A. J. Blanch, V. Ejov, J. S. Quinton, and C. T. Gibson, “Spring constant calibration techniques for next-generation fast-scanning atomic force microscope cantilevers,” *Nanotechnology*, vol. 25, no. 33, p. 335705, Aug. 2014.

[79] M. L. B. Palacio and B. Bhushan, “Normal and lateral force calibration techniques for AFM cantilevers,” *Critical Reviews in Solid State and Materials Sciences*, vol. 35, no. 2, pp. 73–104, 2010.

[80] M. Munz, “Force calibration in lateral force microscopy: a review of the experimental methods,” *J Phys D Appl Phys*, vol. 43, no. 6, p. 063001, 2010.

[81] T. J. Colburn and G. J. Leggett, “Influence of solvent environment and tip chemistry on the contact mechanics of tip - Sample interactions in friction force microscopy of self-assembled monolayers of mercaptoundecanoic acid and dodecanethiol,” *Langmuir*, vol. 23, no. 9, pp. 4959–4964, 2007.

[82] C. R. Hurley and G. J. Leggett, “Quantitative investigation of the photodegradation of polyethylene terephthalate film by friction force microscopy, contact-angle goniometry, and X-ray photoelectron spectroscopy,” *ACS Appl Mater Interfaces*, vol. 1, no. 8, pp. 1688–1697, 2009.

[83] D. F. Ogletree, R. W. Carpick, and M. Salmeron, “Calibration of frictional forces in atomic force microscopy,” *Review of Scientific Instruments*, vol. 67, no. 9, pp. 3298–3306, Sep. 1996.

[84] M. Varenberg, I. Etsion, and G. Halperin, “An improved wedge calibration method for lateral force in atomic force microscopy,” *Review of Scientific Instruments*, vol. 74, no. 7, pp. 3362–3367, 2003.

[85] C. Wendeln and B. J. Ravoo, “Surface patterning by microcontact chemistry,” *Langmuir*, vol. 28, no. 13, pp. 5527–5538, 2012.

[86] A. Ulman, “Formation and Structure of Self-Assembled Monolayers,” *Chem Rev*, vol. 96, no. 4, pp. 1533–1554, Jan. 1996, doi: 10.1021/cr9502357.

[87] J. J. Gooding, F. Mearns, W. Yang, and J. Liu, “Self-assembled monolayers into the 21st century: Recent advances and applications,” *Electroanalysis*, vol. 15, no. 2, pp. 81–96, 2003.

[88] J. C. Love, L. A. Estroff, J. K. Kriebel, R. G. Nuzzo, and G. M. Whitesides, “Self-assembled monolayers of thiolates on metals as a form of nanotechnology,” 2005.

[89] S. Ferretti, S. Paynter, D. A. Russell, K. E. Sapsford, and D. J. Richardson, “Self-assembled monolayers: a versatile tool for the formulation of bio-surfaces,” *TrAC Trends in Analytical Chemistry*, vol. 19, no. 9, pp. 530–540, Sep. 2000.

[90] P. E. Laibinis, G. M. Whitesides, D. L. Aliara, Y. T. Tao, A. N. Parikh, and R. G. Nuzzo, “Comparison of the Structures and Wetting Properties of Self-Assembled Monolayers of n-Alkanethiols on the Coinage Metal Surfaces, Cu, Ag, Au,” *J Am Chem Soc*, vol. 113, no. 19, pp. 7152–7167, 1991.

[91] P. T. Mikulski, L. A. Herman, and J. A. Harrison, “Odd and even model self-assembled monolayers: Links between friction and structure,” *Langmuir*, vol. 21, no. 26, pp. 12197–12206, 2005.

[92] W. Sep-pak, “Lna (1),” vol. 12, no. 11, pp. 4481–4483, 1983, doi: 10.1021/ja028692.

[93] D. Vuillaume, C. Boulas, J. Collet, J. V. Davidovits, and F. Rondelez, “Organic insulating films of nanometer thicknesses,” *Appl Phys Lett*, vol. 69, no. 11, pp. 1646–1648, 1996.

[94] E. Ostuni *et al.*, "Self-assembled monolayers that resist the adsorption of proteins and the adhesion of bacterial and mammalian cells," *Langmuir*, vol. 17, no. 20, pp. 6336–6343, 2001.

[95] R. Kapur and A. S. Rudolph, "Cellular and cytoskeleton morphology and strength of adhesion of cells on self-assembled monolayers of organosilanes," *Exp Cell Res*, vol. 244, no. 1, pp. 275–285, 1998, doi: 10.1006/excr.1998.4156.

[96] Y. Xia, X. M. Zhao, E. Kim, and G. M. Whitesides, "A Selective Etching Solution for Use with Patterned Self-Assembled Monolayers of Alkanethiolates on Gold," *Chemistry of Materials*, vol. 7, no. 12, pp. 2332–2337, 1995.

[97] S. Krämer, R. R. Fuierer, and C. B. Gorman, "Scanning probe lithography using self-assembled monolayers," *Chem Rev*, vol. 103, no. 11, pp. 4367–4418, Nov. 2003.

[98] C. D. Bain and G. M. Whitesides, "Formation of two-component surfaces by the spontaneous assembly of monolayers on gold from solutions containing mixtures of organic thiols," *J Am Chem Soc*, vol. 110, no. 19, pp. 6560–6561, 1988.

[99] H. Sellers, A. Ulman, Y. Shnidman, and J. E. Eilers, "Structure and Binding of Alkanethiolates on Gold and Silver Surfaces: Implications for Self-Assembled Monolayers," *J Am Chem Soc*, vol. 115, no. 21, pp. 9389–9401, 1993.

[100] J. Christopher Love *et al.*, "Formation and structure of self-assembled monolayers of alkanethiolates on palladium," *J Am Chem Soc*, vol. 125, no. 9, pp. 2597–2609, 2003.

[101] M. Manolova *et al.*, "Metal deposition onto thiol-covered gold: Platinum on a 4-mercaptopyridine SAM," *Surf Sci*, vol. 590, no. 2–3, pp. 146–153, 2005.

[102] M. Schlesinger and M. Paunovic, *Modern electroplating*. John Wiley & Sons., 2011.

[103] U. K. Sur and V. Lakshminarayanan, "A study of the hydrophobic properties of alkanethiol self-assembled monolayers prepared in different solvents," *Journal of Electroanalytical Chemistry*, vol. 565, no. 2, pp. 343–350, 2004.

[104] J. Huang and J. C. Hemminger, *Photooxidation of thiols in self-assembled monolayers on gold*, vol. 115, no. 8. 1993.

[105] C. R. Kessel and S. Granick, "Formation and Characterization of a Highly Ordered and Well-Anchored Alkylsilane Monolayer on Mica by Self-Assembly," *Langmuir*, vol. 7, no. 3, pp. 532–538, 1991.

[106] C. D. Lorenz, M. Chandross, G. S. Grest, M. J. Stevens, and E. B. Webb, "Tribological properties of alkylsilane self-assembled monolayers," *Langmuir*, vol. 21, no. 25, pp. 11744–11748, 2005.

[107] S. Onclin, B. J. Ravoo, and D. N. Reinhoudt, "Engineering silicon oxide surfaces using self-assembled monolayers," *Angewandte Chemie - International Edition*, vol. 44, no. 39, pp. 6282–6304, 2005.

[108] D. L. Angst and G. W. Simmons, "Moisture Absorption Characteristics of Organosiloxane Self-Assembled Monolayers," *Langmuir*, vol. 7, no. 10, pp. 2236–2242, 1991.

[109] C. P. Tripp and M. L. Hair, "An Infrared Study of the Reaction of Octadecyltrichlorosilane with Silica," *Langmuir*, vol. 8, no. 4, pp. 1120–1126, 1992.

[110] M. E. McGovern, K. M. R. Kallury, and M. Thompson, "Role of Solvent on the Silanization of Glass with Octadecyltrichlorosilane," *Langmuir*, vol. 10, no. 10, pp. 3607–3614, 1994.

[111] R. P. Dhavale *et al.*, "Monolayer grafting of aminosilane on magnetic nanoparticles: An efficient approach for targeted drug delivery system," *J Colloid Interface Sci*, vol. 529, pp. 415–425, Nov. 2018, doi: 10.1016/j.jcis.2018.06.006.

[112] S. Guha Thakurta and A. Subramanian, "Fabrication of dense, uniform aminosilane monolayers: A platform for protein or ligand immobilization," *Colloids Surf A Physicochem Eng Asp*, vol. 414, pp. 384–392, Nov. 2012, doi: 10.1016/j.colsurfa.2012.08.049.

[113] I. Pang *et al.*, “Aminosilane monolayer-assisted patterning of conductive poly(3,4-ethylenedioxythiophene) source/drain electrodes for bottom contact pentacene thin film transistors,” *Org Electron*, vol. 11, no. 2, pp. 338–343, 2010, doi: 10.1016/j.orgel.2009.10.001.

[114] S. M. Kang *et al.*, “Polarity control of siloxane composite films for triboelectric nanogenerator based self-powered body temperature monitoring,” *Nano Energy*, vol. 127, Aug. 2024, doi: 10.1016/j.nanoen.2024.109742.

[115] J. Advincula, R. C.; Brittain, W. J.; Caster, K. C.; Rühe, *Polymer brushes*. Wiley Online Library, 2004.

[116] S. V. Orski, K. H. Fries, S. K. Sontag, and J. Locklin, “Fabrication of nanostructures using polymer brushes,” *J Mater Chem*, vol. 21, no. 37, pp. 14135–14149, 2011, doi: doi_10.1016_j.progpolymsci.2009.11.002.pdf.

[117] N. Singh, J. Wang, M. Ulbricht, S. R. Wickramasinghe, and S. M. Husson, “Surface-initiated atom transfer radical polymerization: A new method for preparation of polymeric membrane adsorbers,” *J Memb Sci*, vol. 309, no. 1–2, pp. 64–72, 2008.

[118] N. K. Kumar, A.R.S. and Singha, “Reversible Addition-Fragmentation Chain Transfer (RAFT) Polymerization,” in *Synthesis, Fabrication and Characterization*, 2020.

[119] O. Azzaroni, “Polymer brushes here, there, and everywhere: Recent advances in their practical applications and emerging opportunities in multiple research fields,” *J Polym Sci A Polym Chem*, vol. 50, no. 16, pp. 3225–3258, 2012.

[120] T. Pintauer and K. Matyjaszewski, “Atom transfer radical addition and polymerization reactions catalyzed by ppm amounts of copper complexes,” *Chem Soc Rev*, vol. 37, no. 6, pp. 1087–1097, 2008, doi: RSC_CC_C2CC17525H 1..3.pdfRSC_CC_C2CC17525H 1..3.pdfRSC_CC_C2CC17525H 1..3.pdf. Use of alcohols as reducing agents for synthesis of well-defined polymers by AGET-ATRP.

[121] K. Matyjaszewski and J. Xia, *Atom transfer radical polymerization*, vol. 101, no. 9. 2001.

[122] K. Matyjaszewski and J. Xia, *Atom transfer radical polymerization*, vol. 101, no. 9. 2001.

[123] K. Matyjaszewski and N. V. Tsarevsky, "Macromolecular engineering by atom transfer radical polymerization," *J Am Chem Soc*, vol. 136, no. 18, pp. 6513–6533, 2014.

[124] V. A. Ganesh, A. Baji, and S. Ramakrishna, "Smart functional polymers - A new route towards creating a sustainable environment," *RSC Adv*, vol. 4, no. 95, pp. 53352–53364, 2014.

[125] N. V. Tsarevsky, W. A. Braunecker, and K. Matyjaszewski, "Electron transfer reactions relevant to atom transfer radical polymerization," *J Organomet Chem*, vol. 692, no. 15, pp. 3212–3222, 2007.

[126] W. A. Braunecker and K. Matyjaszewski, "Recent mechanistic developments in atom transfer radical polymerization," *J Mol Catal A Chem*, vol. 254, no. 1–2, pp. 155–164, 2006.

[127] T. Pintauer and K. Matyjaszewski, "Structural aspects of copper catalyzed atom transfer radical polymerization," *Coord Chem Rev*, vol. 249, no. 11–12, pp. 1155–1184, 2005.

[128] N. Chan, S. Boutti, M. F. Cunningham, and R. A. Hutchinson, "Continuous atom transfer radical polymerization with low catalyst concentration in a tubular reactor," *Macromol React Eng*, vol. 3, no. 5–6, pp. 222–231, 2009.

[129] T. Pintauer and K. Matyjaszewski, "Atom transfer radical addition and polymerization reactions catalyzed by ppm amounts of copper complexes," *Chem Soc Rev*, vol. 37, no. 6, pp. 1087–1097, 2008, doi: RSC_CC_C2CC17525H 1..3.pdfRSC_CC_C2CC17525H 1..3.pdfRSC_CC_C2CC17525H 1..3.pdf. Use of alcohols as reducing agents for synthesis of well-defined polymers by AGET-ATRP.

[130] Y. Wang, X. Li, F. Du, H. Yu, B. Jin, and R. Bai, "Use of alcohols as reducing agents for synthesis of well-defined polymers by AGET-ATRP," *Chemical Communications*, vol. 48, no. 22, pp. 2800–2802, 2012.

[131] A. M. M. Alswieleh, "Micro- and Nano-Structure of Polymers and Molecular Materials," The University of Sheffield, 2014.

[132] R. Barbey *et al.*, "Polymer brushes via surface-initiated controlled radical polymerization: synthesis, characterization, properties, and applications," *Chem Rev*, vol. 109, no. 11, pp. 5437–5527, 2009.

[133] S. Minko, "Responsive Polymer Brushes," *Journal of Macromolecular Science, Part C*, vol. 46, no. 4, pp. 397–420, Dec. 2006, doi: 10.1080/15583720600945402.

[134] S. Dai, P. Ravi, and K. C. Tam, "pH-Responsive polymers: Synthesis, properties and applications," *Soft Matter*, vol. 4, no. 3, pp. 435–449, 2008.

[135] S. V. Orski, K. H. Fries, S. K. Sontag, and J. Locklin, "Fabrication of nanostructures using polymer brushes," *J Mater Chem*, vol. 21, no. 37, pp. 14135–14149, 2011.

[136] H. il Lee, J. Pietrasik, S. S. Sheiko, and K. Matyjaszewski, "Stimuli-responsive molecular brushes," *Progress in Polymer Science (Oxford)*, vol. 35, no. 1–2, pp. 24–44, 2010.

[137] N. Cheng, A. A. Brown, O. Azzaroni, and W. T. S. Huck, "Thickness-dependent properties of polyzwitterionic brushes," *Macromolecules*, vol. 41, no. 17, pp. 6317–6321, 2008.

[138] E. P. K. Currie, A. B. Sieval, G. J. Fleer, and M. A. C. Stuart, "Polyacrylic acid brushes: Surface pressure and salt-induced swelling," *Langmuir*, vol. 16, no. 22, pp. 8324–8333, 2000.

[139] S. Edmondson, N. T. Nguyen, A. L. Lewis, and S. P. Armes, "Co-nonsolvency effects for surface-initiated poly(2-(methacryloyloxy)ethyl phosphorylcholine)

brushes in alcohol/water mixtures," *Langmuir*, vol. 26, no. 10, pp. 7216–7226, 2010.

[140] D. S. Ginger, H. Zhang, and C. A. Mirkin, "The Evolution of Dip-Pen Nanolithography," 2004, *John Wiley & Sons, Ltd*. doi: 10.1002/anie.200300608.

[141] P. W. Wachulak, M. G. Capeluto, C. S. Menoni, J. J. Rocca, and M. C. Marconi, "Nanopatterning in a compact setup using table top extreme ultraviolet lasers," *Opto-electronics Review*, vol. 16, no. 4, pp. 444–450, 2008.

[142] D. Wouters and U. S. Schubert, "Nanolithography and nanochemistry: Probe-related patterning techniques and chemical modification for nanometer-sized devices," *Angewandte Chemie - International Edition*, vol. 43, no. 19, pp. 2480–2495, 2004.

[143] D. Mijatovic, J. C. T. Eijkel, and A. Van Den Berg, "Technologies for nanofluidic systems: Top-down vs. bottom-up - A review," *Lab Chip*, vol. 5, no. 5, pp. 492–500, 2005.

[144] Y. Xia, J. A. Rogers, K. E. Paul, and G. M. Whitesides, "Unconventional Methods for Fabricating and Patterning Nanostructures," *Chem Rev*, vol. 99, no. 7, pp. 1823–1848, 1999.

[145] Z. Nie and E. Kumacheva, "Patterning surfaces with functional polymers," *Nat Mater*, vol. 7, no. 4, pp. 277–290, 2008.

[146] D. J. Carbaugh, J. T. Wright, R. Parthiban, and F. Rahman, "Photolithography with polymethyl methacrylate (PMMA)," *Semicond Sci Technol*, vol. 31, no. 2, Dec. 2015, doi: 10.1088/0268-1242/31/2/025010.

[147] R. Wei, M. Gryszel, L. Migliaccio, and E. D. Głowacki, "Tuning photoelectrochemical performance of poly(3-hexylthiophene) electrodes: Via surface structuring," *J Mater Chem C Mater*, vol. 8, no. 31, pp. 10897–10906, Aug. 2020, doi: 10.1039/d0tc01477j.

[148] S. A. A. Ahmad, L. S. Wong, E. Ul-Haq, J. K. Hobbs, G. J. Leggett, and J. Micklefield, "Micrometer-and nanometer-scale photopatterning using 2-

nitrophenylpropyloxycarbonyl-protected aminosiloxane monolayers," *J Am Chem Soc*, vol. 131, no. 4, pp. 1513–1522, 2009.

[149] S. Sun, K. S. L. Chong, and G. J. Leggett, "Photopatterning of self-assembled monolayers at 244 nm and applications to the fabrication of functional microstructures and nanostructures," *Nanotechnology*, vol. 16, no. 9, pp. 1798–1808, 2005.

[150] R. Kamitani, K. Niikura, T. Onodera, N. Iwasaki, H. Shimaoka, and K. Ijiro, "Patterned Immobilization of Unprotected Carbohydrates on an Aminooxy Polymer-Grafted Solid Surface," *Bull Chem Soc Jpn*, vol. 80, no. 9, pp. 1808–1813, Sep. 2007.

[151] S. A. Ahmad, G. J. Leggett, A. Hucknall, and A. Chilkoti, "Micro- and Nanostructured Poly[oligo(ethylene glycol)methacrylate] Brushes Grown From Photopatterned Halogen Initiators by Atom Transfer Radical Polymerization," *Biointerphases*, vol. 6, no. 1, pp. 8–15, 2011.

[152] F. Zhou, W. Liu, J. Hao, T. Xu, M. Chen, and Q. Xue, "Fabrication of Conducting Polymer and Complementary Gold Microstructures Using Polymer Brushes as Templates," *Adv Funct Mater*, vol. 13, no. 12, pp. 938–942, 2003.

[153] S. A. A. Ahmad, L. S. Wong, E. Ul-Haq, J. K. Hobbs, G. J. Leggett, and J. Micklefield, "Micrometer-and nanometer-scale photopatterning using 2-nitrophenylpropyloxycarbonyl-protected aminosiloxane monolayers," *J Am Chem Soc*, vol. 131, no. 4, pp. 1513–1522, Feb. 2009, doi: 10.1021/ja807612y.

[154] T. S. Meiron, A. Marmur, and I. S. Saguy, "Contact angle measurement on rough surfaces," *J Colloid Interface Sci*, vol. 274, no. 2, pp. 637–644, 2004.

[155] H. Y. Erbil, "The debate on the dependence of apparent contact angles on drop contact area or three-phase contact line: A review," *Surf Sci Rep*, vol. 69, no. 4, pp. 325–365, 2014.

[156] R. Tadmor, "Line energy and the relation between advancing, receding, and Young contact angles," *Langmuir*, vol. 20, no. 18, pp. 7659–7664, 2004.

[157] J. Zhang, L. Shi, R. Zhang, J. Chen, and G. Wu, “Spectral interference ellipsometry for film thickness measurement on transparent substrate,” *Opt Lasers Eng*, vol. 171, Dec. 2023, doi: 10.1016/j.optlaseng.2023.107819.

[158] C. Chou, H. K. Teng, C. J. Yu, and H. S. Huang, “Polarization modulation imaging ellipsometry for thin film thickness measurement,” *Opt Commun*, vol. 273, no. 1, pp. 74–83, May 2007, doi: 10.1016/j.optcom.2006.12.032.

[159] A. M. C. Ng, K. Y. Cheung, M. K. Fung, A. B. Djurišić, and W. K. Chan, “Spectroscopic ellipsometry characterization of polymer-fullerene blend films,” *Thin Solid Films*, vol. 517, no. 3, pp. 1047–1052, Dec. 2008, doi: 10.1016/j.tsf.2008.05.038.

[160] S. Adam *et al.*, “Quartz crystal microbalance with coupled spectroscopic ellipsometry-study of temperature-responsive polymer brush systems,” *Appl Surf Sci*, vol. 421, pp. 843–851, Nov. 2017, doi: 10.1016/j.apsusc.2017.02.078.

[161] M. P. Seah, I. S. Gilmore, and S. J. Spencer, “Quantitative XPS I. Analysis of X-ray photoelectron intensities from elemental data in a digital photoelectron database,” 2001. [Online]. Available: www.elsevier.nl/locate/elspec

[162] “Fifty Years of X-ray Photoelectron Spectroscopy”.

[163] T. Nakamura *et al.*, “Quick Operando Ambient Pressure Hard X-ray Photoelectron Spectroscopy for Reaction Kinetic Measurements of Polymer Electrolyte Fuel Cells,” *Journal of Physical Chemistry C*, vol. 124, no. 32, pp. 17520–17527, Aug. 2020, doi: 10.1021/acs.jpcc.0c04871.

[164] A. Müller *et al.*, “Determining the Thickness and Completeness of the Shell of Polymer Core-Shell Nanoparticles by X-ray Photoelectron Spectroscopy, Secondary Ion Mass Spectrometry, and Transmission Scanning Electron Microscopy,” *Journal of Physical Chemistry C*, vol. 123, no. 49, pp. 29765–29775, Dec. 2019, doi: 10.1021/acs.jpcc.9b09258.

[165] M. H. Azarian, S. Nijpanich, N. Chanlek, and W. Sutapun, “Probing capping mechanisms and polymer matrix loading of biogenic vaterite CaCO3-Ag hybrid

through X-ray photoelectron spectroscopy (XPS)," *RSC Adv*, vol. 14, no. 21, pp. 14624–14639, May 2024, doi: 10.1039/d4ra01710b.

[166] J. B. Gilbert, M. Luo, C. K. Shelton, M. F. Rubner, R. E. Cohen, and T. H. Epps, "Determination of lithium-ion distributions in nanostructured block polymer electrolyte thin films by X-ray photoelectron spectroscopy depth profiling," *ACS Nano*, vol. 9, no. 1, pp. 512–520, Jan. 2015, doi: 10.1021/nn505744r.

[167] Z. Pei, B. Parvathy Devi, and S. Thiyagu, "Study on the Al-P3HT:PCBM interfaces in electrical stressed polymer solar cell by X-ray photoelectron spectroscopy," *Solar Energy Materials and Solar Cells*, vol. 123, pp. 1–6, Apr. 2014, doi: 10.1016/j.solmat.2013.12.003.

[168] R. W. Carpick and M. Salmeron, "Scratching the surface: Fundamental investigations of tribology with atomic force microscopy," *Chem Rev*, vol. 97, no. 4, pp. 1163–1194, 1997, doi: 10.1021/cr960068q.

[169] S. Yesufu-Rufai *et al.*, "Atomic Force Microscopy (AFM) study of redox conditions in sandstones: Impact on wettability modification and mineral morphology," *Colloids Surf A Physicochem Eng Asp*, vol. 597, no. March, 2020, doi: 10.1016/j.colsurfa.2020.124765.

[170] N. Jalili and K. Laxminarayana, "A review of atomic force microscopy imaging systems: Application to molecular metrology and biological sciences," *Mechatronics*, vol. 14, no. 8, pp. 907–945, 2004.

[171] J. Zhong and J. Yan, "Seeing is believing: Atomic force microscopy imaging for nanomaterial research," *RSC Adv*, vol. 6, no. 2, pp. 1103–1121, 2016, doi: 10.1039/c5ra22186b.

[172] G. Meyer and N. M. Amer, "Erratum: Novel optical approach to atomic force microscopy [Appl. Phys. Lett. 5 3 , 1045 (1988)]," *Appl Phys Lett*, vol. 53, no. 24, pp. 2400–2402, Dec. 1988, doi: 10.1063/1.100425.

[173] F. J. Giessibl, "Advances in atomic force microscopy," *Rev Mod Phys*, vol. 75, no. 3, pp. 949–983, 2003.

[174] M. K. Heljak, A. Chlanda, W. Swieszkowski, and M. Bil, “Multiscale analysis of viscoelastic properties, topography and internal structure of a biodegradable thermo-responsive shape memory polyurethane,” *Polymer (Guildf)*, vol. 191, no. October 2019, 2020, doi: 10.1016/j.polymer.2020.122273.

[175] L. Chen *et al.*, “Friction at single-layer graphene step edges due to chemical and topographic interactions,” *Carbon N Y*, vol. 154, pp. 67–73, 2019, doi: 10.1016/j.carbon.2019.07.081.

[176] S. M. Salapaka, T. De, and A. Sebastian, “A robust control based solution to the sample-profile estimation problem in fast atomic force microscopy,” *International Journal of Robust and Nonlinear Control*, vol. 15, no. 16, pp. 821–837, 2005, doi: Zhong, Q., Inniss, D., Kjoller, K. and Elings, V.B., 1993. Surface Science Letters, 290.

[177] Q. Zhong, D. Inniss, K. Kjoller, and V. B. Elings, “Fractured polymer/silica fiber surface studied by tapping mode atomic force microscopy,” *Surf Sci*, vol. 290, no. 1–2, 1993.

[178] B. Drake *et al.*, “Imaging crystals, polymers, and processes in water with the atomic force microscope,” *Science (1979)*, vol. 243, no. 4898, pp. 1586–1589, Mar. 1989, doi: Y. A. Bobrov, V. A. Bykov, S. I. Leesment, V. V. Polyakov.pdfY. A. Bobrov, V. A. Bykov, S. I. Leesment, V. V. Polyakov.pdf.

[179] Y. Bobrov, V. Bykov, S. Leesment, and V. Polyakov, “Automation of topography and phase contrast measurements in tapping mode,” *In Scanning Probe Microscopy. Russia-China Workshop on Dielectric and Ferroelectric Materials.—Ekaterinburg*, pp. 69–70, 2019.

[180] N. Politakos, E. Diamanti, and S. E. Moya, “Smart, biocompatible, responsive surfaces on pH, temperature and ionic strength of titanium oxide and niobium oxide with polymer brushes of poly(acrylic acid), poly(N-isopropylacrylamide) and poly([2-(methacryloyloxy)ethyl] trimethylammonium chloride),” *Eur Polym J*, vol. 112, no. January, pp. 306–319, 2019.

[181] S. Skiles *et al.*, “Solute- and Temperature-responsive Smart Membranes Formed by Covalent Layer-by-layer Assembly,” in *RSC Smart Materials*, vol. 2019-Janua, no. 35, Royal Society of Chemistry, 2019, pp. 185–201.

[182] B. Zhao, W. J. Brittain, W. Zhou, and S. Z. D. Cheng, “AFM study of tethered polystyrene-b-poly(methyl methacrylate) and polystyrene-b-poly(methyl acrylate) brushes on flat silicate substrates,” *Macromolecules*, vol. 33, no. 23, pp. 8821–8827, 2000, doi: Factors Affecting the Height and Phase Images in Tapping Mode Atomic Force Microscopy. Study of Phase-Separated Polymer Blends of Poly(ethene-co-styrene) and Poly(2,6-dimethyl-1,4-phenylene oxide).pdf.

[183] G. Bar, Y. Thomann, R. Brandsch, H. J. Cantow, and M. H. Whangbo, “Factors affecting the height and phase images in tapping mode atomic force microscopy. Study of phase-separated polymer blends of poly(ethene-co-styrene) and poly(2,6-dimethyl-1,4-phenylene oxide),” *Langmuir*, vol. 13, no. 14, pp. 3807–3812, 1997.

[184] M. Endo, “AFM-based single-molecule observation of the conformational changes of DNA structures,” *Methods*, vol. 169, no. September 2018, pp. 3–10, 2019, doi: AFM for analysis of structure and dynamics of DNA and protein–DNA complexes.pdfAFM for analysis of structure and dynamics of DNA and protein–DNA complexes.pdf.

[185] Y. L. Lyubchenko and L. S. Shlyakhtenko, “AFM for analysis of structure and dynamics of DNA and protein – DNA complexes,” vol. 47, pp. 206–213, 2009, doi: doi_10.1016_j.bpc.2003.09.001.pdfdoi_10.1016_j.bpc.2003.09.001.pdf.

[186] N. C. Santos and M. A. R. B. Castanho, “An overview of the biophysical applications of atomic force microscopy,” *Biophys Chem*, vol. 107, no. 2, pp. 133–149, 2004.

[187] C. Formosa-Dague, R. E. Duval, and E. Dague, “Cell biology of microbes and pharmacology of antimicrobial drugs explored by Atomic Force Microscopy,” *Semin Cell Dev Biol*, vol. 73, pp. 165–176, 2018.

[188] W. Yagi, T. Honda, K. Tamura, and K. Narita, “Study on the quantitative evaluation of the surface force using a scanning probe microscope,” *Lubricants*, vol. 8, no. 6, Jun. 2020, doi: 10.3390/LUBRICANTS8060066.

[189] L. Juhasz, R. D. Ortuso, and K. Sugihara, “Quantitative and Anisotropic Mechanochromism of Polydiacetylene at Nanoscale,” *Nano Lett*, vol. 21, no. 1, pp. 543–549, Jan. 2021, doi: 10.1021/acs.nanolett.0c04027.

[190] B. C. Tran Khac and K. H. Chung, “Quantitative assessment of contact and non-contact lateral force calibration methods for atomic force microscopy,” *Ultramicroscopy*, vol. 161, pp. 41–50, Feb. 2016, doi: 10.1016/j.ultramic.2015.10.028.

[191] T. J. Whittle and G. J. Leggett, “Quantitative kinetic measurements of the esterification of self-assembled monolayers of mercaptoundecanol by trifluoroacetic anhydride using friction force microscopy,” *Langmuir*, vol. 25, no. 16, pp. 9182–9188, Aug. 2009, doi: 10.1021/la900741y.

[192] C. W. Yang *et al.*, “Lateral Force Microscopy of Interfacial Nanobubbles: Friction Reduction and Novel Frictional Behavior,” *Sci Rep*, vol. 8, no. 1, Dec. 2018, doi: 10.1038/s41598-018-21264-6.

[193] D. Dietzel *et al.*, “Interfacial friction obtained by lateral manipulation of nanoparticles using atomic force microscopy techniques,” *J Appl Phys*, vol. 102, no. 8, 2007, doi: 10.1063/1.2798628.

[194] G. J. Leggett, N. J. Brewer, and K. S. L. Chong, “Friction force microscopy: Towards quantitative analysis of molecular organisation with nanometre spatial resolution,” *Physical Chemistry Chemical Physics*, vol. 7, no. 6, pp. 1107–1120, Mar. 2005, doi: 10.1039/b417136p.

[195] F. Marinello, P. Schiavuta, S. Vezzù, A. Patelli, S. Carmignato, and E. Savio, “Atomic force acoustic microscopy for quantitative nanomechanical characterization,” *Wear*, vol. 271, no. 3–4, pp. 534–538, Jun. 2011, doi: 10.1016/j.wear.2010.03.032.

[196] R. Zhang *et al.*, “Entropy-driven segregation of polymer-grafted nanoparticles under confinement,” *Proc Natl Acad Sci U S A*, vol. 114, no. 10, pp. 2462–2467, Mar. 2017, doi: 10.1073/pnas.1613828114.

[197] A. Rastogi, M. Y. Paik, M. Tanaka, and C. K. Ober, “Direct patterning of intrinsically electron beam sensitive polymer brushes,” in *ACS Nano*, Feb. 2010, pp. 771–780. doi: 10.1021/nn901344u.

[198] H. Zhao, T. Chen, T. Wu, L. Xie, Y. Ma, and J. Sha, “Strategy based on multiplexed brush architectures for regulating the spatiotemporal immobilization of biomolecules,” *Biomaterials Advances*, vol. 141, Oct. 2022, doi: 10.1016/j.bioadv.2022.213092.

[199] Q. Yu, J. Cho, P. Shivapooja, L. K. Ista, and G. P. López, “Nanopatterned smart polymer surfaces for controlled attachment, killing, and release of bacteria,” *ACS Appl Mater Interfaces*, vol. 5, no. 19, pp. 9295–9304, Oct. 2013, doi: 10.1021/am4022279.

[200] B. Yu *et al.*, “Nanopatterned Monolayers of Bioinspired, Sequence-Defined Polypeptoid Brushes for Semiconductor/Bio Interfaces,” *ACS Nano*, vol. 18, no. 10, pp. 7411–7423, Mar. 2024, doi: 10.1021/acsnano.3c10204.

[201] R. M. Choueiri *et al.*, “Surface patterning of nanoparticles with polymer patches,” *Nature*, vol. 538, no. 7623, pp. 79–83, Aug. 2016, doi: 10.1038/nature19089.

[202] Q. Yu, L. K. Ista, R. Gu, S. Zauscher, and G. P. López, “Nanopatterned polymer brushes: Conformation, fabrication and applications,” Jan. 14, 2016, *Royal Society of Chemistry*. doi: 10.1039/c5nr07107k.

[203] M. Patra and P. Linse, “Reorganization of nanopatterned polymer brushes by the AFM measurement process,” *Macromolecules*, vol. 39, no. 13, pp. 4540–4546, Jun. 2006, doi: 10.1021/ma0606410.

[204] Q. Yu, P. Shivapooja, L. M. Johnson, G. Tizazu, G. J. Leggett, and G. P. López, “Nanopatterned polymer brushes as switchable bioactive interfaces,” *Nanoscale*, vol. 5, no. 9, pp. 3632–3637, May 2013, doi: 10.1039/c3nr00312d.

[205] R. Kumar, A. Welle, F. Becker, I. Kopyeva, and J. Lahann, “Substrate-Independent Micropatterning of Polymer Brushes Based on Photolytic Deactivation of Chemical Vapor Deposition Based Surface-Initiated Atom-Transfer Radical Polymerization Initiator Films,” *ACS Appl Mater Interfaces*, vol. 10, no. 38, pp. 31965–31976, Sep. 2018, doi: 10.1021/acsami.8b11525.

[206] Z. Zhang, A. J. Morse, S. P. Armes, A. L. Lewis, M. Geoghegan, and G. J. Leggett, “Effect of brush thickness and solvent composition on the friction force response of poly(2-(methacryloyloxy)ethylphosphorylcholine) brushes,” *Langmuir*, vol. 27, no. 6, pp. 2514–2521, Mar. 2011, doi: 10.1021/la1043848.

[207] M. Kobayashi *et al.*, “Friction behavior of high-density poly(2-methacryloyloxyethyl phosphorylcholine) brush in aqueous media,” *Soft Matter*, vol. 3, no. 6, pp. 740–746, 2007, doi: 10.1039/b615780g.

[208] L. J. T. Landherr, C. Cohen, P. Agarwal, and L. A. Archer, “Interfacial friction and adhesion of polymer brushes,” *Langmuir*, vol. 27, no. 15, pp. 9387–9395, Aug. 2011, doi: 10.1021/la201396m.

[209] M. S. Onses *et al.*, “Block copolymer assembly on nanoscale patterns of polymer brushes formed by electrohydrodynamic jet printing,” *ACS Nano*, vol. 8, no. 7, pp. 6606–6613, Jul. 2014, doi: 10.1021/nn5022605.

[210] K. Homma *et al.*, “Autonomous Nanoscale Chemomechanical Oscillation on the Self-Oscillating Polymer Brush Surface by Precise Control of Graft Density,” *Langmuir*, vol. 37, no. 14, pp. 4380–4386, Apr. 2021, doi: 10.1021/acs.langmuir.1c00459.

[211] M. Kaholek, W. K. Lee, B. LaMattina, K. C. Caster, and S. Zauscher, “Fabrication of Stimulus-Responsive Nanopatterned Polymer Brushes by Scanning-Probe Lithography,” *Nano Lett*, vol. 4, no. 2, pp. 373–376, Feb. 2004, doi: 10.1021/nl035054w.

[212] G. V. Redkina, A. S. Sergienko, Y. I. Kuznetsov, and O. Y. Grafov, “Superhydrophobic Anticorrosive Phosphonate–Siloxane Films Formed on Zinc

with Different Surface Morphology," *Materials*, vol. 15, no. 15, Aug. 2022, doi: 10.3390/ma15155360.

[213] A. S. Baikin *et al.*, "The Influence of Fillers on the Structure of Siloxane Films," *Inorganic Materials: Applied Research*, vol. 15, no. 2, pp. 352–357, Apr. 2024, doi: 10.1134/S2075113324020060.

[214] N. Dendane, A. Hoang, L. Guillard, E. Defrancq, F. Vinet, and P. Dumy, "Efficient surface patterning of oligonucleotides inside a glass capillary through oxime bond formation," *Bioconjug Chem*, vol. 18, no. 3, pp. 671–676, 2007, doi: 10.1021/bc060254v.

[215] O. Al-Jaf, A. Alswieleh, S. P. Armes, and G. J. Leggett, "Nanotribological properties of nanostructured poly(cysteine methacrylate) brushes," *Soft Matter*, vol. 13, no. 10, pp. 2075–2084, 2017, doi: 10.1039/c7sm00013h.

[216] Q. Yu, L. K. Ista, R. Gu, S. Zauscher, and G. P. López, "Nanopatterned polymer brushes: Conformation, fabrication and applications," Jan. 14, 2016, *Royal Society of Chemistry*. doi: 10.1039/c5nr07107k.

[217] A. Macior *et al.*, "A New Protocol for Ash Wood Modification: Synthesis of Hydrophobic and Antibacterial Brushes from the Wood Surface," *Molecules*, vol. 27, no. 3, Feb. 2022, doi: 10.3390/molecules27030890.

[218] M. Flejszar *et al.*, "Sequential SI-ATRP in μL-scale for surface nanoengineering: A new concept for designing polyelectrolyte nanolayers formed by complex architecture polymers," *Eur Polym J*, vol. 194, Jul. 2023, doi: 10.1016/j.eurpolymj.2023.112142.

[219] N. Cheng, P. Bao, S. D. Evans, G. J. Leggett, and S. P. Armes, "Facile formation of highly mobile supported lipid bilayers on surface-quaternized pH-responsive polymer brushes," *Macromolecules*, vol. 48, no. 9, pp. 3095–3103, May 2015, doi: 10.1021/acs.macromol.5b00435.

[220] Z. Zhang, A. J. Morse, S. P. Armes, A. L. Lewis, M. Geoghegan, and G. J. Leggett, "Nanoscale contact mechanics of biocompatible polyzwitterionic

brushes," *Langmuir*, vol. 29, no. 34, pp. 10684–10692, Aug. 2013, doi: 10.1021/la4018689.

[221] R. Toomey, J. Mays, and M. Tirrell, "In situ thickness determination of adsorbed layers of poly(2-vinylpyridine)-polystyrene diblock copolymers by ellipsometry," *Macromolecules*, vol. 37, no. 3, pp. 905–911, Feb. 2004, doi: 10.1021/ma034974y.

[222] D. J. Lee, Y. M. Cho, J. H. Kim, I. J. Hwang, Y. Chung, and Y. B. Kang, "Application of k-Means Clustering to Material Research: Measurement of Layer Thickness and Contact Angle," *Metals and Materials International*, vol. 29, no. 9, pp. 2636–2647, Sep. 2023, doi: 10.1007/s12540-023-01411-z.

[223] C. Rodriguez-Emmenegger, S. Janel, A. de los Santos Pereira, M. Bruns, and F. Lafont, "Quantifying bacterial adhesion on antifouling polymer brushes via single-cell force spectroscopy," *Polym Chem*, vol. 6, no. 31, pp. 5740–5751, Aug. 2015, doi: 10.1039/c5py00197h.

[224] E. Csányi *et al.*, "XPS Depth-Profiling Studies of Chlorophyll Binding to Poly(cysteine methacrylate) Scaffolds in Pigment-Polymer Antenna Complexes Using a Gas Cluster Ion Source," *Langmuir*, vol. 40, no. 28, pp. 14527–14539, Jul. 2024, doi: 10.1021/acs.langmuir.4c01361.

[225] A. Kuruly Rajan, I. Sakthinathan, S. Renaudineau, A. Proust, and T. McCormac, "Layer-by-Layer Construction of Hybrid Film Based on PEI Polymer and Preyssler-Type Polyoxometalates: Its Electrochemical and Quartz Crystal Microbalance Measurement," *ChemElectroChem*, vol. 11, no. 15, Aug. 2024, doi: 10.1002/celc.202400102.

[226] M. Müller *et al.*, "Surface-Initiated Polymerizations Mediated by Novel Germanium-Based Photoinitiators," *ACS Appl Mater Interfaces*, vol. 15, no. 26, pp. 31836–31848, Jul. 2023, doi: 10.1021/acsami.3c05528.

[227] E. A. Smith *et al.*, "Lipid bilayers on polyacrylamide brushes for inclusion of membrane proteins," *Langmuir*, vol. 21, no. 21, pp. 9644–9650, Oct. 2005, doi: 10.1021/la051116h.

[228] M. Delcea and C. A. Helm, “X-ray and Neutron Reflectometry of Thin Films at Liquid Interfaces,” *Langmuir*, vol. 35, no. 26, pp. 8519–8530, Jul. 2019, doi: 10.1021/acs.langmuir.8b04315.

[229] M. Li *et al.*, “Brush conformation of polyethylene glycol determines the stealth effect of nanocarriers in the low protein adsorption regime,” *Nano Lett*, vol. 21, no. 4, pp. 1591–1598, Feb. 2021, doi: 10.1021/acs.nanolett.0c03756.

[230] Y. Wu *et al.*, “Mushroom-brush transitional conformation of mucus-inert PEG coating improves co-delivery of oral liposome for intestinal metaplasia therapy,” *Biomaterials Advances*, vol. 136, May 2022, doi: 10.1016/j.bioadv.2022.212798.

[231] T. Wang, X. Wang, Y. Long, G. Liu, and G. Zhang, “Ion-specific conformational behavior of polyzwitterionic brushes: Exploiting it for protein adsorption/desorption control,” *Langmuir*, vol. 29, no. 22, pp. 6588–6596, Jun. 2013, doi: 10.1021/la401069y.

[232] N. Verimli, A. Demiral, H. Yılmaz, M. Çulha, and S. S. Erdem, “Design of Dense Brush Conformation Bearing Gold Nanoparticles as Theranostic Agent for Cancer,” *Appl Biochem Biotechnol*, vol. 189, no. 3, pp. 709–728, Nov. 2019, doi: 10.1007/s12010-019-03151-6.

[233] S. Varma, L. Bureau, and D. Débarre, “The Conformation of Thermoresponsive Polymer Brushes Probed by Optical Reflectivity,” *Langmuir*, vol. 32, no. 13, pp. 3152–3163, Apr. 2016, doi: 10.1021/acs.langmuir.6b00138.

[234] L. Xie *et al.*, “Study of poly(acrylamidoxime) brushes conformation with uranium adsorption by neutron reflectivity,” *Mater Lett*, vol. 220, pp. 47–49, Jun. 2018, doi: 10.1016/j.matlet.2018.02.102.

[235] S. Varma, L. Bureau, and D. Débarre, “The Conformation of Thermoresponsive Polymer Brushes Probed by Optical Reflectivity,” *Langmuir*, vol. 32, no. 13, pp. 3152–3163, Apr. 2016, doi: 10.1021/acs.langmuir.6b00138.

[236] “The Effect of [CuI]:[CuII] Ratio on the Kinetics and Conformation of Polyelectrolyte Brushes by Atom”.

[237] M. Koenig *et al.*, “Adsorption of enzymes to stimuli-responsive polymer brushes: Influence of brush conformation on adsorbed amount and biocatalytic activity,” *Colloids Surf B Biointerfaces*, vol. 146, pp. 737–745, Oct. 2016, doi: 10.1016/j.colsurfb.2016.07.015.

[238] R. M. Espinosa-Marzal, P. C. Nalam, S. Bolisetty, and N. D. Spencer, “Impact of solvation on equilibrium conformation of polymer brushes in solvent mixtures,” *Soft Matter*, vol. 9, no. 15, pp. 4045–4057, Apr. 2013, doi: 10.1039/c3sm27726g.

[239] “Effect of the Density of ATRP Thiol Initiators in the Yield and Water Content of Grafted-From PMETAC”.

[240] “Spatially Resolving Polymer Brush Conformation: Opportunities Ahead”.

[241] X. S. Yan and F. L. Jen, “Effect of fluctuations in the brush conformation on the interaction between polymer brushes in a good solvent,” in *Journal of Applied Mechanics, Transactions ASME*, Sep. 2008, pp. 0510091–0510097. doi: 10.1115/1.2937155.

[242] Y. Pei, J. Travas-Sedjic, and D. E. Williams, “Electrochemical switching of conformation of random polyampholyte brushes grafted onto polypyrrole,” *Langmuir*, vol. 28, no. 37, pp. 13241–13248, Sep. 2012, doi: 10.1021/la302202k.

[243] I. E. Apata, B. V. Tawade, S. P. Cummings, N. Pradhan, A. Karim, and D. Raghavan, “Comparative Study of Polymer-Grafted BaTiO3 Nanoparticles Synthesized Using Normal ATRP as Well as ATRP and ARGET-ATRP with Sacrificial Initiator with a Focus on Controlling the Polymer Graft Density and Molecular Weight,” *Molecules*, vol. 28, no. 11, Jun. 2023, doi: 10.3390/molecules28114444.

[244] W. Zhao *et al.*, “Controlling the ethylene polymerization parameters in iron pre-catalysts of the type 2-[1-(2,4-dibenzhydryl-6-methylphenylimino)ethyl]-6-[1-(arylimino) ethyl] pyridyliron dichloride,” *Polymer (Guildf)*, vol. 53, no. 1, pp. 130–137, Jan. 2012, doi: 10.1016/j.polymer.2011.11.024.

[245] K. Ishihara, S. Yanokuchi, K. Fukazawa, and Y. Inoue, “Author Correction: Photoinduced self-initiated graft polymerization of methacrylate monomers on

poly(ether ether ketone) substrates and surface parameters for controlling cell adhesion (Polymer Journal, (2020), 52, 7, (731-741), 10.1038/s41428-020-0318-9),” Jul. 01, 2020, *Springer Nature*. doi: 10.1038/s41428-020-0336-7.

[246] A. Olivier, F. Meyer, J. M. Raquez, P. Damman, and P. Dubois, “Surface-initiated controlled polymerization as a convenient method for designing functional polymer brushes: From self-assembled monolayers to patterned surfaces,” 2012, *Elsevier Ltd*. doi: 10.1016/j.progpolymsci.2011.06.002.

[247] C. J. Biermann and R. Narayan, “Grafting of partially hydrolysed poly(methyl methacrylate) onto mesylated cellulose acetate,” 1987.

[248] Y. F. Lee and T. M. Wu, “Investigation on the Photodegradation Stability of Acrylic Acid-Grafted Poly(butylene carbonate-co-terephthalate)/Organically Modified Layered Zinc Phenylphosphonate Composites,” *Polymers (Basel)*, vol. 15, no. 5, Mar. 2023, doi: 10.3390/polym15051276.

[249] X. Man, R. Wu, X. Jiang, S. Xu, and W. Wang, “Organo-montmorillonite supported titania nanocomposite synthesized by using poly(methyl methacrylate) grafted cellulose as template and its application in photodegradation,” *Cellulose*, vol. 22, no. 5, pp. 3189–3198, Oct. 2015, doi: 10.1007/s10570-015-0704-1.

[250] S. Yamamoto, M. Ejaz, Y. Tsujii, and T. Fukuda, “Surface interaction forces of well-defined, high-density polymer brushes studied by atomic force microscopy. 2. Effect of graft density,” *Macromolecules*, vol. 33, no. 15, pp. 5608–5612, Jul. 2000, doi: 10.1021/ma991988o.

[251] J. Zhao, M. Chen, Y. An, J. Liu, and F. Yan, “Preparation of polystyrene brush film by radical chain-transfer polymerization and micromechanical properties,” *Appl Surf Sci*, vol. 255, no. 5 PART 1, pp. 2295–2302, Dec. 2008, doi: 10.1016/j.apsusc.2008.07.099.

[252] M. A. Brady, F. T. Limpoco, and S. S. Perry, “Solvent-dependent friction force response of poly(ethylenimine)- graftpoly(ethylene glycol) brushes investigated by atomic force microscopy,” *Langmuir*, vol. 25, no. 13, pp. 7443–7449, Jul. 2009, doi: 10.1021/la900371k.

[253] F. T. Limpoco, R. C. Advincula, and S. S. Perry, “Solvent dependent friction force response of polystyrene brushes prepared by surface initiated polymerization,” *Langmuir*, vol. 23, no. 24, pp. 12196–12201, Nov. 2007, doi: 10.1021/la701272a.

[254] E. L. P. Dumont, H. Belmas, and H. Hess, “Observing the mushroom-to-brush transition for kinesin proteins,” *Langmuir*, vol. 29, no. 49, pp. 15142–15145, Dec. 2013, doi: 10.1021/la4030712.

[255] X. Song *et al.*, “High-density zwitterionic polymer brushes exhibit robust lubrication properties and high antithrombotic efficacy in blood-contacting medical devices,” *Acta Biomater*, vol. 178, pp. 111–123, Apr. 2024, doi: 10.1016/j.actbio.2024.02.032.

[256] M. Kobayashi *et al.*, “Wettability and antifouling behavior on the surfaces of superhydrophilic polymer brushes,” *Langmuir*, vol. 28, no. 18, pp. 7212–7222, May 2012, doi: 10.1021/la301033h.

[257] K. Speyer and C. Pastorino, “Pressure responsive gating in nanochannels coated by semiflexible polymer brushes,” *Soft Matter*, vol. 15, no. 5, pp. 937–946, 2019, doi: 10.1039/c8sm02388c.

[258] Q. A. Besford *et al.*, “Molecular Transport within Polymer Brushes: A FRET View at Aqueous Interfaces,” *Molecules*, vol. 27, no. 9, May 2022, doi: 10.3390/molecules27093043.

[259] Z. Zhang and P. Raffa, “Anti-freezing conductive zwitterionic composite hydrogels for stable multifunctional sensors,” *Eur Polym J*, vol. 199, Nov. 2023, doi: 10.1016/j.eurpolymj.2023.112484.

[260] H. Wang *et al.*, “Low hysteresis zwitterionic supramolecular polymer ion-conductive elastomers with anti-freezing properties, high stretchability, and self-adhesion for flexible electronic devices,” *Mater Horiz*, vol. 11, no. 11, pp. 2628–2642, Mar. 2024, doi: 10.1039/d4mh00174e.

[261] B. Yameen, M. Ali, R. Neumann, W. Ensinger, W. Knoll, and O. Azzaroni, “Single conical nanopores displaying pH-tunable rectifying characteristics.

manipulating ionic transport with zwitterionic polymer brushes," *J Am Chem Soc*, vol. 131, no. 6, pp. 2070–2071, Feb. 2009, doi: 10.1021/ja8086104.

[262] J. Anthi, V. Kolivoška, B. Holubová, and H. Vaisocherová-Lísalová, "Probing polymer brushes with electrochemical impedance spectroscopy: A mini review," Nov. 21, 2021, *Royal Society of Chemistry*. doi: 10.1039/d1bm01330k.

[263] H. Jiang and F. J. Xu, "Biomolecule-functionalized polymer brushes," *Chem Soc Rev*, vol. 42, no. 8, pp. 3394–3426, Mar. 2013, doi: 10.1039/c2cs35453e.

[264] A. M. Alswieleh, N. Cheng, G. J. Leggett, and S. P. Armes, "Spatial control over cross-linking dictates the pH-responsive behavior of poly(2-(tert - butylamino)ethyl methacrylate) brushes," *Langmuir*, vol. 30, no. 5, pp. 1391–1400, Feb. 2014, doi: 10.1021/la403666y.

[265] N. Cheng, P. Bao, S. D. Evans, G. J. Leggett, and S. P. Armes, "Facile formation of highly mobile supported lipid bilayers on surface-quaternized pH-responsive polymer brushes," *Macromolecules*, vol. 48, no. 9, pp. 3095–3103, May 2015, doi: 10.1021/acs.macromol.5b00435.

[266] S. B. Lee, R. R. Koepsel, S. W. Morley, K. Matyjaszewski, Y. Sun, and A. J. Russell, "Permanent, nonleaching antibacterial surfaces, 1. Synthesis by atom transfer radical polymerization," *Biomacromolecules*, vol. 5, no. 3, pp. 877–882, May 2004, doi: 10.1021/bm034352k.

[267] R. Barbey and H. A. Klok, "Room temperature, aqueous post-polymerization modification of glycidyl methacrylate-containing polymer brushes prepared via surface-initiated atom transfer radical polymerization," *Langmuir*, vol. 26, no. 23, pp. 18219–18230, Dec. 2010, doi: 10.1021/la102400z.

[268] Y. Zou, P. Y. J. Yeh, N. A. A. Rossi, D. E. Brooks, and J. N. Kizhakkedathu, "Nonbiofouling polymer brush with latent aldehyde functionality as a template for protein micropatterning," *Biomacromolecules*, vol. 11, no. 1, pp. 284–293, Jan. 2010, doi: 10.1021/bm901159d.

[269] E. E. Brotherton, E. C. Johnson, M. J. Smallridge, D. B. Hammond, G. J. Leggett, and S. P. Armes, "Hydrophilic Aldehyde-Functional Polymer Brushes: Synthesis,

Characterization, and Potential Bioapplications," *Macromolecules*, vol. 56, no. 5, pp. 2070–2080, Mar. 2023, doi: 10.1021/acs.macromol.2c02471.

[270] T. Bilgic and H. A. Klok, "Oligonucleotide Immobilization and Hybridization on Aldehyde-Functionalized Poly(2-hydroxyethyl methacrylate) Brushes," *Biomacromolecules*, vol. 16, no. 11, pp. 3657–3665, Nov. 2015, doi: 10.1021/acs.biomac.5b01116.

[271] K. Glinel, A. M. Jonas, T. Jouenne, J. Leprince, L. Galas, and W. T. S. Huck, "Antibacterial and antifouling polymer brushes incorporating antimicrobial peptide," *Bioconjug Chem*, vol. 20, no. 1, pp. 71–77, 2009, doi: 10.1021/bc800280u.